Stefano Sanvito

Giant Magnetoresistance and Quantum Transport in Magnetic Hybrid Nanostructures

A thesis submitted for the degree of Doctor of Philosophy

ProQuest Number: 11003639

All rights reserved

INFORMATION TO ALL USERS
The quality of this reproduction is dependent upon the quality of the copy submitted.

In the unlikely event that the author did not send a complete manuscript
and there are missing pages, these will be noted. Also, if material had to be removed,
a note will indicate the deletion.

ProQuest 11003639

Published by ProQuest LLC (2018). Copyright of the Dissertation is held by the Author.

All rights reserved.
This work is protected against unauthorized copying under Title 17, United States Code
Microform Edition © ProQuest LLC.

ProQuest LLC.
789 East Eisenhower Parkway
P.O. Box 1346
Ann Arbor, MI 48106 – 1346

PACS:

72 Electron transport in condensed matter

72.10 Bg General formulation of transport theory

73.23 Ad Ballistic Transport

73.50-h Electron transport phenomena in thin film and low dimensional strucures

75.50 Pa Giant Magnetoresistance

73.40 Gk Tunneling

74.80 Fp Point contacts, SN, SNS junctions

74.80 Dm Superconducting layer structures: superlattices, heterojunctions and multilayers

72.80 Rj Fullerenes and related Materials

Abstract

Technological advances in device micro- and nano-fabrication over the past decade has enabled a variety of novel heterojunction device structures to be made. Among these, magnetic multilayers, superconductor/normal metal junctions and carbon nanotubes exhibit a rich variety of features, with the potential for future generations of electronic devices with improved sensitivity and higher packing density. The modeling of such structures in a flexible and accurate way, with a predictive capability is a formidable theoretical challenge.

In this thesis I will present a very general numerical technique to compute transport properties of heterogeneous systems, which can be used together with accurate *spd* tight-binding Hamiltonians or simpler models. I will then apply this technique to several transport problems in the mesoscopic regime.

Firstly I will review the material dependence of CPP GMR in perfect crystalline magnetic multilayers, analyze their conductance oscillations and discuss some preliminary results of magnetic tunneling junctions. In the contest of the conductance oscillations I will introduce a simple Krönig-Penney model which gives a full understanding of the relevant periods involved in the oscillations. I will then present a simple model, which can be used to study disordered magnetic systems and the cross-over from ballistic to diffusive transport. This model explains recent experiments on CPP GMR, which cannot be understood within the usual Boltzmann transport framework. Then I will present results for superconducting/normal metal and for superconducting/multilayer junctions. In the case of multilayers I will show that in both the ballistic and diffusive regimes the GMR is expected to vanish if a superconducting contact is added and go on to show why this is not the case in practice. Finally I will present features of ballistic transport in multiwall carbon nanotubes and show how the inter-tube interaction can, not only block some of the scattering channels but also re-distribute non-uniformly the current across the tubes. The results explain an old open question concerning ballistic transport in Carbon nanotubes.

Acknowledgment

A PhD work is always a team-work and nothing would have been possible without the collaboration and the patience of many people. All my gratitude goes to my two supervisors **Prof. John Jefferson** from the DERA Malvern and **Prof Colin Lambert** from the University of Lancaster, for their continuous support and interest. In particular, I want to thank John for the never-ending late night discussions in which I always discovered that physics is just simple solutions for difficult problems, and Colin for his contagious enthusiasm and curiosity and for having taught to me that what is interesting is also possible.

There are also a lot of other persons who helped me and collaborated with me during all these three years. Special thanks go to my friends **Fabio Taddei** for his energy in the stimulating conversations about superconductivity and **Mike Fearn** for bearing all my questions about computers, compilers and rescuing me during my frequent paralyzing computer crashes. I also have had great benefits from the collaboration with experimentists at DERA Malvern and I am debited with **Dr. Peter Wright**.

One of the great pleasures of this work has been to travel around the world for learning from the best persons and absorbing their knowledge and experience. I am really grateful to **Dr. Alex Bratkovsky** from HP Laboratories in Palo Alto for his teachings on transport in magnetic materials, to **Prof. David Tománek** and **Young-Kwon Kyun** from Michigan State University for having shown me the fascinating world of Carbon nanotubes and to **Dr. Jáime Ferrer** from University of Oviedo for having introduced me to the local density functional theory.

One of the great aspects of belonging to a group is to realize through discussions that your problem has been already solved by someone else in a different form. For this I want to thank **George, Agapi, Rob, Vince, Carol, Val, Steve** and **Paul** from Lancaster, **Denver**, **Mohammed** and **Phil** from Malvern and **Pedro** and **Savas** from East Lansing.

Finally, no thanks will be never enough for my family, my dad **Roberto**, my mum **Maria Luisa** and my sister **Simona** because their trust and proud of me never rest, and for my girlfriend **Stefania**, who never fails to remind me that there is more to life than physics alone.

From this thesis the following papers have been published

- S. Sanvito, C.J. Lambert, J.H. Jefferson and A.M.Bratkovsky, J. Phys.C: Condens. Matter **10**, L691 (1998)
- S. Sanvito, C.J. Lambert, J.H. Jefferson and A.M. Bratkovsky, Phys. Rev. **B 59**, 11936 (1999)
- S. Sanvito, C.J. Lambert and J.H. Jefferson, J. Magn. Magn. Mater **197**, 101 (1999)
- S. Sanvito, C.J. Lambert and J.H. Jefferson, J. Magn. Magn. Mater **201-203**, 105 (1999)
- S. Sanvito, C.J. Lambert and J.H. Jefferson, Phys. Rev. **B 60**, 7385 (1999)
- F. Taddei, S. Sanvito, C.J. Lambert and J.H. Jefferson, Phys. Rev. Lett. **82**, 4938 (1999)
- S. Sanvito, C.J. Lambert and J.H. Jefferson, submitted to Phys. Rev. Lett., also cond-mat/9903190
- S. Sanvito, Y.-K. Kwon, D. Tománek and C.J. Lambert, submitted to Phys. Rev. Lett., also cond-mat/9808154
- S. Sanvito, Y.-K. Kwon, D. Tománek and C.J. Lambert, "Quantum Transport in inhomogeneous multi-wall nanotubes" (to appear in *Science and application of Nanotubes*, Kluwer Academic Publishing/Plenum Press)

Questa così vana presunzione d'intendere il tutto non può avere principio altro che dal non avere inteso mai nulla, perchè, quando altri avesse esperimentato una volta sola a intender perfettamente una cosa sola e avesse gustato veramente come è fatto il sapere, conoscerebbe come dell'infinità dell'altre cose niuna ne intende.

Galileo Galilei

Da "Dialogo Sopra i due Massimi Sistemi del Mondo"

The vain effrontery of understanding every thing can only be due to not understanding anything, because if one has experienced for only one time the full understanding of one thing only and has enjoyed the pleasure of the knowledge, he would know how big is the universe of things which he does not understand.

Galileo Galilei

From "Dialogo Sopra i due Massimi Sistemi del Mondo"

Contents

1 Introduction

1.1 The Spin Transport Era

Since 1988 with the discovery of the Giant Magnetoresistance (GMR) in metallic magnetic multilayers [1, 2] a revolution in the world of electronics has begun. GMR is the drastic change of the resistance of a multilayer composed of alternating magnetic and non-magnetic layers when a strong magnetic field is applied. This effect is the result of a change in the magnetic configuration of the multilayer. In fact the thickness of the non-magnetic layers can be tuned in such a way that the exchange coupling between magnetic layers through the non-magnetic layer makes adjacent magnetizations antiparallel [3, 4, 5, 6]. This results in a global antiferromagnetic (AF) configuration of the multilayer. If a magnetic field strong enough to rotate the magnetizations toward the field direction is applied, a ferromagnetic (FM) configuration may be achieved. This latter configuration turns out to possess a lower resistance, with the relative difference being larger than 100%.

The impact of this discovery was enormous, particularly for two reasons. First it paved the way for a new generation of devices and sensors with sensitivity far beyond the existing structures based on conventional anisotropic magnetoresistance (AMR). Secondly it brought the "spin" to the attention of the scientific community as a possible degree of freedom to use in electronics [7]. The first aspect has been largely explored. At present magnetometers based on GMR elements have been produced [8, 9] and in the catalogues of the major computer manufacturers [10] it is possible to find high density hard-disks with reading heads based on GMR. The second aspect generated a renewed interest in the transport properties of magnetic systems and in the subtle interplay between spin and transport. Although the initial problem of, whether GMR was a surface or a bulk effect has not been completely solved, it was clear from the very beginning that a fundamental ingredient for GMR to occur was the total, or at least partial spin-polarization of the current in a ferromagnetic metal. The original idea of Mott [11] of the current as two independent spin-fluids, and the pioneering work of Tedrow and Meservey (for a review see reference [12]) on the spin-polarization of the current in transition metals have been rediscovered and GMR is now regarded as a new fundamental tool.

The earlier GMR experiments [1, 2] have been conducted with the so-called current in the planes configuration (CIP) in which the current flows in the plane of the layers and in which the resistance is measured with a conventional four-probe technique. In these experiments the typical cross sections are of the order of 1 mm^2 and the transport is mainly diffusive. A further important breakthrough was the possibility to study the transport of a multilayer with the current flowing perpendicular to the planes (CPP GMR). This has been achieved either by using superconducting contacts [13] or by shaping the samples to very small cross sections [14]. In these experiments the electrons have to cross the entire multilayer over distances smaller than 1 μm. The spin filtering is more effective and the transport is largely phase-coherent. Estimates of the spin-polarization of the conductance were made and material specific modeling became possible (for a large review on CPP GMR see [15, 16]). Despite the indisputable success of the CPP GMR either as scientific tool and as building block for devices, it presents some disadvantages. Firstly, since the resistances involved are rather small there is the need to grow samples comprising many layers and to measure the resistance with sophisticated techniques. Secondly it is difficult to magnetically decouple the layers, large magnetic fields are needed and complex micromagnetic effects are unavoidable. Both these complications create severe limitations to possible applications. Moreover the complexity of the system (large number of interfaces often with different quality, presence of superconducting contacts, non-homogeneous disorder due to the confinement, non-homogeneous distribution of the current across the cross-section) makes the polarization of an individual magnetic layer a quite indirect quantity and difficult to infer.

To overcome both these problems a new kind of device has been introduced, namely the tunnel spin valve [17, 18]. In this case only two magnetic layers with different coercive fields are employed. They are separated by an insulator and the different magnetic configurations (the FM and the AF) can be obtained by applying a magnetic field with variable intensity. This results in a tunneling magnetoresistance effect (TMR) analogous to that measured in GMR experiments. Because of the presence of only two magnetic layers this device gives a direct information on the spin-polarization of the current through the barrier. Nevertheless in this case the current is a tunneling current, whose polarization may differ from the one of the direct current measured with GMR

experiments. In particular the tunneling current is related to the DOS at the Fermi energy [17] while the direct current is also strongly dependent on the dispersion of the bands. Furthermore the insulator used is often non-crystalline and tunneling through impurity states in the barrier is important [19, 20]. Finally very recently it has been shown [21] that TMR junctions made by different insulators but the same magnetic materials possess different spin-polarizations, which may differ even in the sign. The importance of this result is twofold. On the one hand it shows that the definition of spin-polarization of the current is not unique and depends on the system measured, on the other hand it makes clear that to make reliable predictions real material modeling is needed.

Another attempt to measure the spin-polarization of magnetic metals has been recently done using ballistic Ferromagnet/Superconductor junctions [22]. In such a case the quantity measured is the suppression of Andreev reflection [23] due to the ferromagnetism. The magnitude of the spin-polarization can be measured but not its sign. Typically the measured spin-polarization is not completely consistent with the one measured with other methods (GMR or TMR). This highlights the intrinsic impossibility to isolate the measurement of the spin-polarization of an individual magnetic metal from the measurement of the spin-polarization of the whole structure in which it is embedded. In particular in the case of ballistic F/S junctions the transport is completely phase-coherent and the definition of the spin-polarization of an individual layer becomes meaningless.

From this brief overview it is clear that, despite the fact that spin-transport is not a new field, it continues to provide interesting problems and issues. To understand most of the present experiments (particularly with the continuous shrinking of the dimensions) both a phase-coherent description of the transport and an accurate material modeling capability is fundamental. Moreover a new generation of materials like carbon nanotubes and magnetic semiconductors is opening new and almost unexplored fields, where theoretical modeling can drive new experiments.

The main aim of this thesis therefore is to study and understand the main mechanisms governing the spin-transport in various metallic magnetic nanostructures, to develop the capability of making predictions of the fundamental material characteris-

tics, and to predict and design new structures with novel properties. To this end I have developed a very flexible numerical calculation technique with which to study transport properties. I will concentrate the attention solely on two-probe measurements and phase coherent systems. The technique is based on the Landauer-Büttiker formalism [24], that will be briefly reviewed in the next section, and is capable to deal both with realistic material-specific systems and with more simple models. The first give important insights into the material properties and the second provide a more transparent understanding of the main phenomena. I will present the main results obtained by either numerical simulations and simple models, keeping continuous contact both with experiments and other theoretical models. From this work a complete picture of the spin-polarized transport in different structure will emerge and novel effects will be predicted.

1.2 Landauer-Büttiker Formalism

One of the purposes of this thesis is to relate the transport properties of a magnetic system to its electronic structure. To this aim it is useful to map the transport calculation onto a scattering problem, then to solve the scattering problem including both band structures and structural details. Furthermore, since most of the measurements involving mesoscopic magnetic junctions are carried out at low bias and temperature, the Landauer-Büttiker [24, 25, 26] formalism is the most appropriate theoretical ground on which to build up a scattering theory. I this section I will briefly introduce the main idea of such a formalism. The final result will be a formula that relates the conductance of a system comprising a scattering region attached to two semi-infinite crystalline leads to the S matrix of the correspondent scattering problem.

Consider the situation of figure 1.1 for a mono-dimensional system (I will later generalize the problem to higher dimensions). A scattering region is connected to two semi-infinite crystalline leads. The fundamental assumption is that the two leads inject completely non-correlated electrons into the scattering region (the leads act as a thermal bath). This means that the phases between the electrons that enter the scattering region do not possess any relation.

Moreover suppose the chemical potentials of the two leads to be respectively μ_1 and μ_2 with $(\mu_1 - \mu_2) \to 0^+$ (zero-bias limit and current flowing from left to right).

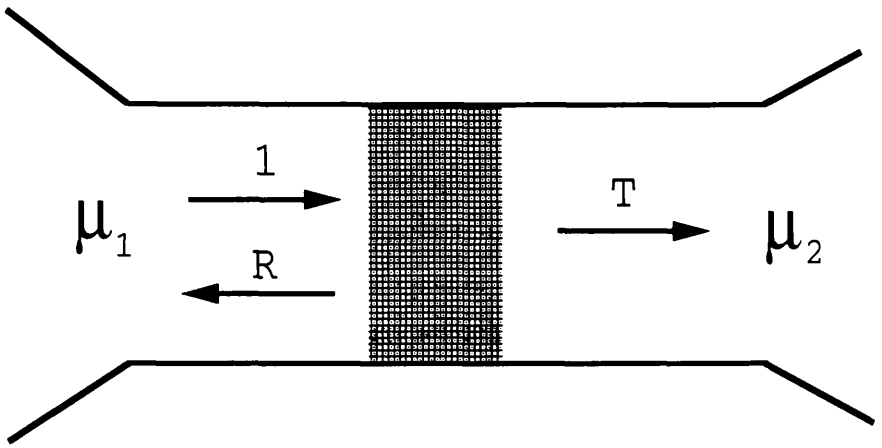

Figure 1.1: Scattering region connected to semi-infinite crystalline leads. An electron carrying unit flux is transmitted with probability T and reflected with probability R $(T + R = 1)$.

The current I emitted from the left lead is therefore

$$I = ev\left(\frac{\partial n}{\partial E}\right)(\mu_1 - \mu_2)\,, \tag{1.1}$$

where e is the electronic charge, v is the group velocity and $\partial n/\partial E$ the density of states. Since $\partial n/\partial E = \partial n/\partial k \cdot \partial k/\partial E = \partial n/\partial k \cdot 1/v\hbar$ and in one dimension $\partial n/\partial k = 1/2\pi$ the equation (1.1) can be written as

$$I = \frac{e}{h}(\mu_1 - \mu_2)\,. \tag{1.2}$$

From the (1.2), by considering the relation between the difference in chemical potential $\Delta\mu$ and the bias voltage $\Delta V = e\Delta\mu$, the conductance $(\Gamma = I/\Delta V)$ of the system is easily evaluated

$$\Gamma = \frac{e^2}{h} = \frac{1}{2}G_0\,, \tag{1.3}$$

where the quantum conductance $G_0 = 2e^2/h$ has been introduced. Finally, since each carrier has a finite probability T to be transmitted and to be reflected R (with $T + R = 1$) by the scattering region sandwiched between the two leads, the total net current flowing from the left to the right lead is

$$I = \frac{e}{h}T(\mu_1 - \mu_2) = \frac{e^2}{h}T\Delta V\,. \tag{1.4}$$

The equation (1.4) is the famous Landauer-Büttiker formula [24, 25, 26] which relates the conductance of a system to its scattering probability. Note that in the case of a perfectly transmitting scattering region equation (1.4) reduces to equation (1.2). Note

also that equation (1.4) is for a single-spin system, in the case of spin-degeneracy this should be multiplied by a factor 2.

The above result may be generalized to the case of many scattering channels. To this aim consider the same physical situation of before, with the only exception that the number of independent scattering channels in the leads is N. This takes into account for the degrees of freedom in the plane transverse to the direction of the current. The scattering channels, independent in the leads, may be scattered into each other in the scattering region. For instance, an electron propagating in the i-th channel in the left-hand side lead has a probability to be transmitted into the j-th channel of the right-hand side lead equal to $T_{ji} = |t_{ji}|^2$, where t is the transmission matrix. To extend the formalism valid in one dimension to the multichannel case the following assumptions are made. The electrons injected from the left-hand side lead feel the same chemical potential μ_1, and in the same way the electrons collected at the right-hand side lead feel the same chemical potential $\mu_2 < \mu_1$. An electron coming from the scattering region and absorbed from the leads is instantaneously thermalized. The incident electrons have no phase-relation and hence they are incoherent. Under these assumptions the current injected into the leads in the j-th scattering channel is $ev_j(\partial n_j/\partial E)(\mu_1 - \mu_2)$. The density of state is given by $\partial n_j/\partial E = 1/2\pi\hbar v_j$, and this means that the current fed into the j-th channel is independent of the group velocity v_j. The current transmitted from the j-th channel to the i-th channel is $(e/h)T_{ij}(\mu_1 - \mu_2)$ and the total current is obtained by summing over all the incoming and outgoing channels. This leads to a total conductance

$$\Gamma = \frac{e^2}{h}\sum_{ij}^{N} T_{ij} = \frac{e^2}{h}\mathrm{Tr}\; tt^{\dagger}\,. \tag{1.5}$$

In the second equality I have introduced the transmission matrix t which is related with the S matrix through the relation

$$S = \begin{pmatrix} r & t' \\ t & r' \end{pmatrix}\,, \tag{1.6}$$

with r the reflection matrix and t' and r' the same quantities for electron approaching from the right. The equation (1.5) expresses the conductance of a scattering region sandwiched between to semi-infinite crystalline leads solely in terms of the S matrix of the system. This fundamental result is valid in general and forms a fundamental link with the scattering theory I will develop in the next chapter.

1.3 Thesis Outline

This thesis is organized as follows. In Chapter 2 I will present a general scattering technique based on tight-binding Hamiltonians to calculate the transport coefficients in a two-probe measurement. I will provide, together with a general approach, a simple example where the calculation can be carried out explicitly. The central result of the technique is a semi-analytic formula which allows the direct calculation of the surface Green functions for semi-infinite leads. The treatment is very general and does not refer to any particular tight-binding models.

In Chapter 3 I will apply such a technique to the calculation of the conductance and the GMR ratio of magnetic multilayers and tunneling spin valves. I will use an *spd* tight-binding Hamiltonian with parameters fitted from *ab initio* calculations. As far as GMR is concerned I will analyze the dependence of the GMR ratio from the materials forming the multilayers and identify the main sources of scattering. The results are presented for Co and Ni as magnetic materials and a large number of $3d, 4d$ and $5d$ transition metals as non-magnetic materials. From this analysis some prescriptions on how to maximize the GMR ratio will be given. As far as tunneling spin valves are concerned, the main result will be to show that in the case of a disorder-free barrier the polarization of the tunneling current through the junction depends strongly on the material characteristics of the insulator. This result will shed some light on a long-living debate on how to measure the polarization of a magnetic material. I will come back on this point in Chapter 6, when discussing Ferromagnet/Superconductor ballistic junctions. Most of the material presented in Chapter 2 and Chapter 3 can be found in reference [27].

In Chapter 4 I will discuss the problem of conductance oscillations in transition metal multilayers. The calculation is motivated by a controversial experiment [28] in which the resistance of a multilayer oscillates as a function of the layer thicknesses with periods extending over many monolayers. The experiments have been carried out in the CIP geometry and I will make some predictions regarding analogous new experiments in the CPP geometry. First I will approach the problem using the realistic *spd* tight-binding Hamiltonian and then I will consider a simpler effective mass model. The main advantage of the latter is that it provides a full understanding of the nature

of the oscillations and a complete analytic treatment is possible. Finally I will extend the effective mass approach to re-interpret the results obtained in Chapter 3, namely the dependence of the GMR ratio on the material characteristics. In this last part it will be clear what the rôle of the very different Fermi surfaces of the materials forming the multilayer is and a two-band model will emerge as the minimal model to capture all the phenomenology of transport in transition metal multilayers. Part of the results of Chapter 4 have been published in references [29, 30, 31].

All the calculations presented in the first four chapters deal with disorder-free systems, where translational invariance is always satisfied. In Chapter 5 I will introduce disorder and discuss its effects. Since the *spd*-Hamiltonian in the case of disorder leads immediately to unmanageably large matrices, I will introduce a simpler model, namely a two-band simple-cubic tight-binding model. Several kinds of disorder are introduced, including random on-site potentials, lattice distortions, vacancies and impurities. Moreover in the case of narrow multilayered wires [32] the effects of cross-section fluctuations and confinement will be considered. From a more technical point of view I will discuss the implementations of the scattering technique in the case of disorder and introduce a "diagrammatic" scheme ("decimation diagrams") for the treatment of the scattering region. From this chapter two main results will emerge. First I will be able to describe the crossover between the ballistic, diffusive and localized regime of the conductance in magnetic multilayers. Secondly I will show in which limit a fully diffusive approach to transport, based onto the Boltzmann equation [33, 34], breaks down. This last result is very important to the interpretation of very recent experiments [35, 36] in which an extremely long electronic mean free path requires a phase-coherent description of the transport. Some of the results of this chapter are published in references [37, 38].

Chapter 6 is focused on the introduction of superconducting contacts in two-probe GMR experiments and on the description of ballistic Normal/Superconductor (N/S) and Ferromagnet/Superconductor (F/S) junctions. The main result of considering superconducting contacts in a two-probe GMR experiment is to completely suppress the spin-polarization of the current, resulting in a vanishing GMR ratio. This dramatic suppression raises interesting questions regarding existing experiments, where the rôle of disorder and spin-flip scattering will turn out to be crucial. Finally ballistic N/S and F/S junctions will be considered. As well as tunneling spin valves they are an important

probe into the spin-polarization of the current in ferromagnetic transition metals, and therefore an accurate model is of interest. I will show that a detailed description of the Fermi surfaces of both the normal and the superconductor metal can reproduce the typical I-V curves found in experiments in the case of N/S junctions. Conversely the inclusion of spin-flip and of enhanced magnetic moment at the interface is fundamental to a description of the F/S junctions. Some of the results can be found in references [39, 40].

The final chapter lies somewhat outside the structure of the previous work. I will consider transport in carbon nanotubes where to-date only one experiment has shown spin-polarized transport [41]. Most of the chapter will be devoted to the calculation of the transport properties of multi-wall nanotubes, where the inter-tube interaction may change completely the transport properties [42, 43] with respect to individual isolated tubes. This result explains a recent experiment in which multi-wall nanotubes show conductances respectively of 1/2 and 1 quantum conductance [44]. From a more technical point of view I will introduce a way to deal with a periodic system in which the hopping matrix between adjacent cells is singular. The use of the "decimation diagrams" will be very useful to give prescriptions on how to construct the unit cell and how to make the contacts with the scattering region. Important considerations on the distribution of the chemical potential across the structure and the efficiency of the electrons feeding from the reservoirs will also be discussed. Finally I will consider the possibility of the injection of spin-polarized electrons into carbon nanotubes by contacting the tubes with magnetic metals. The interplay between the spin-asymmetric Fermi surface of a magnetic metal and the point-like Fermi surface of a carbon nanotube can make spin-injection possible. Moreover the absence of disorder at microscopic level and of an efficient spin-flip process in carbon nanotubes are very promising for long-living spin states, with possible applications in magnetoelectronics and quantum computation. Finally in Chapter 8 I will make some conclusions.

2 A New Scattering Technique

2.1 A Simple example

In the introduction I pointed out that the great advantage of the Landauer-Büttiker approach to transport [25, 26] is to map the calculation of the conductance onto a scattering problem. This is strictly valid in the limit of small bias and temperature, a condition that is matched in a typical MR experiment. In this chapter I will develop a novel technique to evaluate the transport coefficients of a heterostructure described by a tight-binding model. The technique is general and can deal with multi-orbital models with a large number of degrees of freedom.

In a scattering problem the important elements are the asymptotic wave-functions far from the scattering region ("quantum channels" in the Landauer-Büttiker formalism) and the scattering potential. Information regarding the value of the wave-function within the scattering region are not important, because the asymptotic states determine the current. Therefore it is natural to divide the calculation of the S matrix into three fundamental steps: 1) the calculation of the asymptotic states in the leads, 2) the construction of an effective coupling matrix between the surfaces of the leads (the scattering potential), 3) the evaluation of the S matrix. From a numerical point of view it is convenient to decouple the first and the second stages, because the same leads can be used with different scatterers, saving the computation time of re-evaluating the asymptotic states. This point will be more clear in Chapter 5, when disorder will require a large ensemble average and hence the evaluation of the S matrix for many scatterers.

Before going to a detailed analysis of the general scattering technique, I present a simple example in which the main ideas are introduced. Consider two semi-infinite linear chains described by a tight-binding model with one degree of freedom per atomic site (see figure 2.1). The on-site energy of the left- (right-) hand side linear chain is set to zero (ϵ_0) and the hopping is γ_1 (γ_2). Note that setting one of the on-site energies to zero is completely general because the system is invariant under a total energy shift. The left-hand side chain is terminated at the atomic position $l = 0$ and the right-hand side chain starts at the position $l = 1$. The chains are coupled with a coupling element α.

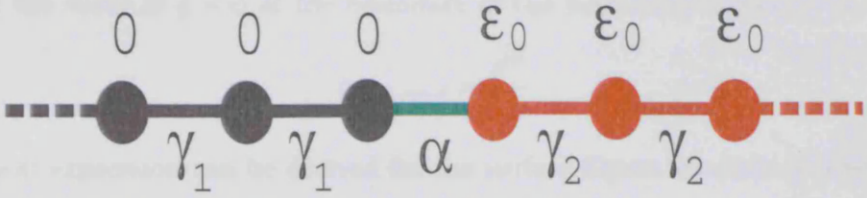

Figure 2.1: Linear tight-binding chains connected through the hopping α. ϵ_0 and 0 are the values of the on-site energies and γ_1 and γ_2 the hopping parameters.

For an infinite chain with on-site energy ϵ_0 and hopping γ it is easy to show that the wave-function is simply a plane-wave with momentum k given by the tight-binding dispersion relation

$$E = \epsilon_0 + 2\gamma \cos k \,, \tag{2.1}$$

with E the energy. In a scattering problem it useful to consider the retarded Green functions instead of the wave-functions. For the above infinite linear chain it is easy to show that the retarded Green function is simply (see for example reference [45])

$$g_{jl} = \frac{e^{ik|j-l|}}{i\hbar v} \,, \tag{2.2}$$

with v the group velocity given by

$$\hbar v = \frac{\partial E}{\partial k} = -2\gamma \sin k \,. \tag{2.3}$$

The equation (2.2) describes the Green function of an infinite system. In the scattering problem one is interested in knowing how an electron approaches the scattering region, therefore one requires the Green function for a semi-infinite system evaluated at the terminating surface. It is possible to compute this from the retarded Green function for the double-infinite system of equation (2.2) and by using the appropriate boundary conditions. Suppose the infinite system is terminated at the position $i = i_0 - 1$ in such a way that the site $i = i_0$ is absent. Therefore the Green function g_{jl} with source at $i = l < i_0$ must vanish for $j = i_0$ (ie the plane-waves are approaching the boundaries from the left). This is achieved by adding to the expression in equation (2.2) the following wave-function

$$\psi_j(l, i_0) = -\frac{e^{-ik(j-2i_0+l)}}{i\hbar v} \tag{2.4}$$

and noting that adding a wave-function to a Green function results in a new Green function with the same causality. Finally the surface Green function can be obtained

by taking the value of $g + \psi$ at the boundary of the scattering region $j = l = i_0 - 1$

$$g_{i_0-1,i_0-1} = \frac{e^{ik}}{\gamma} . \tag{2.5}$$

An identical expression can be derived for the surface Green function of a semi-infinite linear chain starting at $i = i_0$ and extending to infinite to the right. Going back to the initial problem, the surface Green function for two chains facing through the sites $i = 0$ and $i = 1$ but decoupled ($\alpha = 0$) is simply

$$g = \begin{pmatrix} \frac{e^{ik_1}}{\gamma_1} & 0 \\ 0 & \frac{e^{ik_2}}{\gamma_2} \end{pmatrix} , \tag{2.6}$$

with obvious notation for k_1 and k_2. Note that g has vanishing off-diagonal terms, which reflects the fact that the two chains are decoupled.

Let us now switch on the coupling α between the two chains. This can be easily done by solving the Dyson equation

$$G = (g^{-1} - V)^{-1} , \tag{2.7}$$

where G is the new surface Green function for the two coupled chains and V is a 2×2 matrix with α in the off-diagonal positions and zero elsewhere. In the present example with a little algebra one obtains

$$G = \frac{1}{\gamma_1\gamma_2 e^{-i(k_1+k_2)} - \alpha^2} \begin{pmatrix} e^{-ik_2}\gamma_2 & \alpha \\ \alpha & e^{-ik_1}\gamma_1 \end{pmatrix} . \tag{2.8}$$

Before continuing with this pedagogic example it is useful to summarize the structure of the calculation done so far. The starting point was to evaluate the surface Green function for two decoupled leads. This has been achieved by considering an infinite system and by using the appropriate boundary conditions. Then the total Green function for the coupled leads has been calculated by solving the Dyson equation. The coupling between the lead surfaces enters into the calculation only at this point. This approach is still valid in the case in which the scattering region extends over many atomic planes and includes a large number of degrees of freedom. In fact I will show in the following sections that it is always possible to reduce the Hamiltonian describing the scattering region to an effective coupling matrix H_{eff} between the surfaces of the leads. In a general case such a matrix will also include diagonal terms which represent the self-coupling within the surfaces.

The remaining task is to extract from the total Green function G the S matrix. First note that the general wave-function for an electron approaching the scattering region from the left has the form

$$\psi_l = \begin{cases} \frac{e^{ik_1 l}}{{v_1}^{1/2}} + \frac{r}{{v_1}^{1/2}} e^{-ik_1 l} & l \leq 0 \\ \\ \frac{t}{{v_2}^{1/2}} e^{ik_2 l} & l \geq 1 \end{cases} , \tag{2.9}$$

where the transmission t and reflection r coefficients are introduced and where the incoming wave-function $\frac{e^{ik_1 l}}{{v_1}^{1/2}}$ has been normalized in order to carry unit flux (open scattering channel). This last convention guarantees the unitarity of the S matrix $|t|^2 + |r|^2 = 1$. The final step is to project the total Green function G over the wave-function of equation (2.9). It is possible to show (see Appendix C) that the projector that projects the retarded Green function for an infinite system over the unitary flux wave-function $\frac{e^{ikl}}{v^{1/2}}$, projects also the total Green function G over the (2.9). Such projector is easily calculated through the relation

$$g_{lj} P(j) = \frac{e^{ikl}}{v^{1/2}} \quad \text{for} \quad l \geq j \, , \tag{2.10}$$

and is simply

$$P(j) = i e^{ikj} v^{1/2} \, . \tag{2.11}$$

Now I can now use $P(j)$ to extract t and r. In fact by applying $P(j)$ to G_{lj} and by taking the limit $l \to 0$ I obtain

$$G_{00} P(0) = \frac{1}{{v_1}^{1/2}} + \frac{r}{{v_1}^{1/2}} \, , \tag{2.12}$$

from which the reflection coefficient is easily calculated

$$r = G_{00} P(0) {v_1}^{1/2} - 1 \, . \tag{2.13}$$

In the same way the transmission coefficient is simply

$$t = G_{10} P(0) {v_2}^{1/2} e^{-ik_2} \, . \tag{2.14}$$

Note that the same technique can be used to calculate t and r for electrons incoming the scattering region from the right.

To conclude this section I want to summarize the calculation scheme presented in this example. First I calculated the Green function for an infinite system and from it

derived the surface Green function for the corresponding semi-infinite leads by using the appropriate boundary conditions. Secondly I switched on the interaction between the leads by solving the Dyson equation with a given coupling matrix between the two lead surfaces. Finally I calculated the S matrix by introducing a projector that maps the total Green function onto the total scattered wave-function. The advantage of this technique is twofold. On the one hand the calculation of the Green function for the infinite system enables us to obtain useful information regarding the leads (density of state, conductance) and on the other the scattering region is treated separately and added to the leads only before evaluating the S matrix. As noted above this latter aspect is particularly useful in the case in which a large number of computations of different scatterers with the same leads are needed.

In the following sections I will generalize this approach (previously introduced in the case of cubic lattice [46]) to an arbitrary tight-binding Hamiltonian.

2.2 Structure of the Green Functions

In this section I discuss the general structure of the Green function that I will use for calculating the S matrix. To do so consider a two-dimensional nearest-neighbour simple-cubic model with a tight-binding Hamiltonian. The system is briefly sketched in figure 2.2. Consider z to be the direction of the transport and x the transverse direction. Let the system be infinite in the direction of transport and consist of M atomic sites in the transverse direction. I assign as before the on-site energy to be ϵ_0, and the hopping between nearest neighbours γ.

The Green function for such a system can be shown to be

$$g(z,x;z',x') = \sum_{n=1}^{M} \left(\frac{2}{M+1}\right) \sin\left(\frac{n\pi}{M+1}x\right) \sin\left(\frac{n\pi}{M+1}x'\right) \frac{e^{ik_z^n(E)|z-z'|}}{i\hbar v_z^n(E)} , \qquad (2.15)$$

where $k_z^n(E)$ is the longitudinal momentum that satisfies the dispersion law

$$E = \epsilon_o + 2\gamma \left[\cos\left(\frac{n\pi}{M+1}\right) + \cos k_z^n(E)\right] , \qquad (2.16)$$

and $v_z^n(E)$ is the group velocity

$$\frac{\partial E(k_z^n)}{\partial k_z^n} = \hbar v_z^n(E) . \qquad (2.17)$$

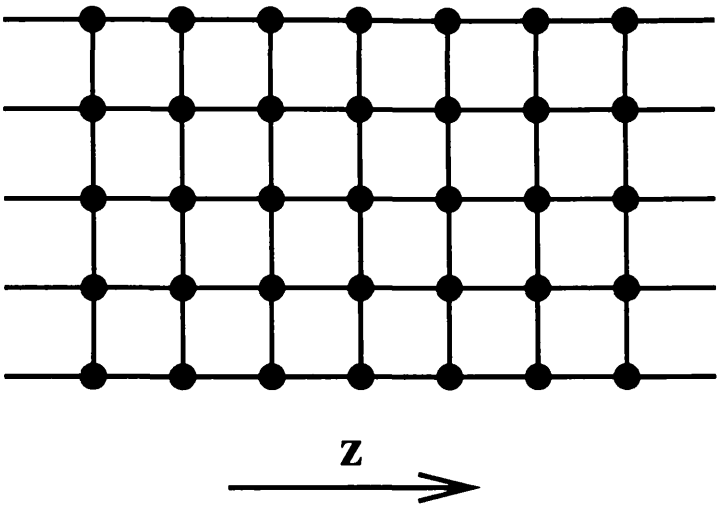

Figure 2.2: 2D Simple cubic lattice.

Since (2.15) will be the starting point for the construction of a more general Green function in the next section, it is important to understand its structure. The expression of equation (2.15) can be schematically written

$$g(z,x;z',x') = \sum_{n=1}^{M} \beta_n(x) \frac{e^{ik_z^n(E)|z-z'|}}{i\hbar v_z^n(E)} \beta_n^*(x') \ . \tag{2.18}$$

$g(z,x;z',x')$ consists of the sum of all the allowed plane-waves $e^{ik_z^n(E)z}$ (with $k_z^n(E)$'s both real and imaginary) weighted with the corresponding transverse wave-function $\beta_n(x)$ of momentum $k_{||}^n$ ($k_{||}^n = n\pi/(M+1)$ in the present case) with $k_z^n(E)$ defined by the generalized dispersion relation

$$E = E(k_{||}^n, k_z^n) \ . \tag{2.19}$$

Since the transport is in the z direction it is easy to identify the plane-waves $\frac{e^{ik_z^n(E)z}}{v_z^n(E)}$ with the scattering channels defined in the previous section. Note that in the case of a one-dimensional linear chain the equation (2.18) reduces to the expression given by equation (2.2), where the β's are only numbers.

The possible scattering channels can be divided into four classes. The left-moving open scattering channels *lm* (right-moving open scattering channels *rm*) are propagating states (k_z^n is a real number) having negative (positive) group velocity. Similarly the left-decaying closed scattering channels *ld* (right-decaying closed scattering channels *rd*) are states whose wave-functions have a real exponential decay, with k_z^n possessing a negative (positive) imaginary part. Note that in the case in which time-reversal symmetry is

valid, the number of left- and right-moving scattering channels must be the same, as well as the number of left- and right-decaying scattering channels. Schematic pictures of all the scattering channels is given in figure 2.3.

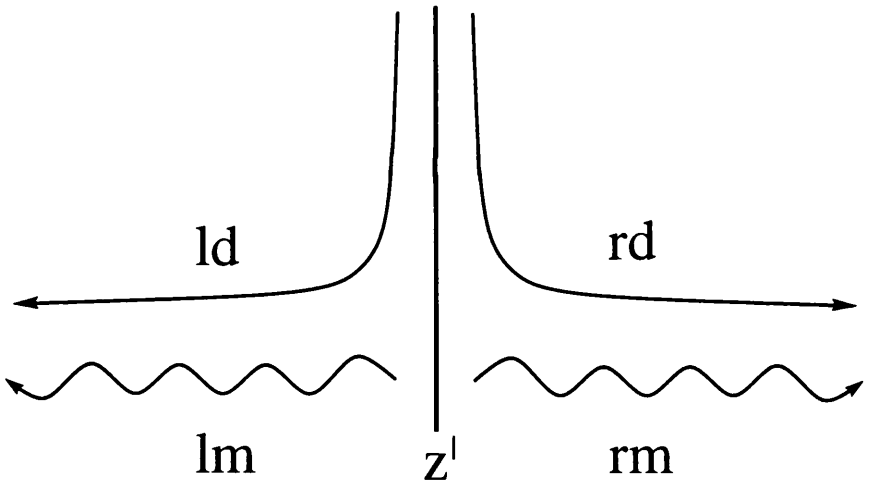

Figure 2.3: Green function structure. *lm* (*rm*) denotes the left- (right-) moving channels, *ld* (*rd* the left- (right-) decaying channels.

Clearly there are M scattering channels and the retarded Green function of equation (2.15) is obtained by by summing up the channels, either left- and right-moving and left- and right-decaying, with their relative transverse wave-components. This structure is the starting point for a more general approach that will be presented in the remaining sections of this chapter.

2.3 General Surface Green Function

In this section I present the first step of a general scattering technique, namely the construction of the surface Green function of the arbitrary crystalline leads. An important feature of this section is that the Green function will be defined by a semi-analytic formula, which avoids the adding of an infinitesimal imaginary part to the energy. As explained in the first section of this chapter, to compute the Green function for a semi-infinite crystalline lead of finite cross-section I first calculate the Green function of a doubly infinite system and then derive the semi-infinite case by applying the boundary conditions at the end of the lead. To this end, consider the doubly infinite system shown in figure 2.4.

If z is the direction of transport, the system comprises a periodic sequence of slices,

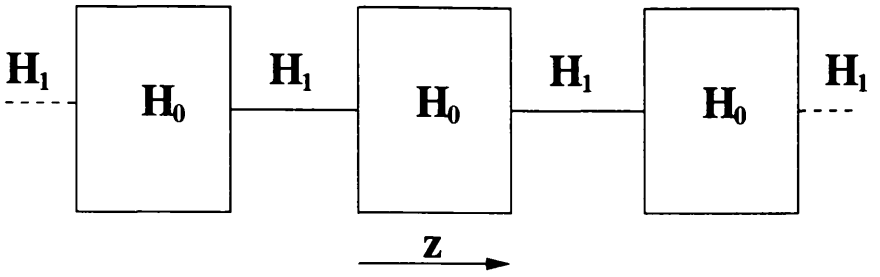

Figure 2.4: Infinite system formed from periodically repeated slices. H_0 describes the interaction within a slice and H_1 describes the coupling between adjacent slices.

described by an intra-slice matrix H_0 and coupled by a nearest neighbour inter-slice hopping matrix H_1. The nature of the slices need not be specified at this stage. They can describe a single atom in an atomic chain (as in the example of the introduction), an atomic plane or a more complex cell. For such a general system, the total Hamiltonian H can be written as an infinite matrix of the form

$$H = \begin{pmatrix} \cdots & \cdots & \cdots & \cdots & \cdots & \cdots & \cdots & \cdots \\ \cdots & H_0 & H_1 & 0 & \cdots & \cdots & \cdots & \cdots \\ \cdots & H_{-1} & H_0 & H_1 & 0 & \cdots & \cdots & \cdots \\ \cdots & 0 & H_{-1} & H_0 & H_1 & 0 & \cdots & \cdots \\ \cdots & 0 & 0 & H_{-1} & H_0 & H_1 & 0 & \cdots \\ \cdots & \cdots & \cdots & \cdots & \cdots & \cdots & \cdots & \cdots \\ \cdots & \cdots & \cdots & \cdots & \cdots & \cdots & \cdots & \cdots \end{pmatrix} , \tag{2.20}$$

where H_0 is Hermitian and $H_{-1} = H_1^\dagger$. The Schrödinger equation for this system is of the form

$$H_0\psi_z + H_1\psi_{z+1} + H_{-1}\psi_{z-1} = E\psi_z , \tag{2.21}$$

where ψ_z is a column vector corresponding to the slice at the position z with z an integer measured in units of inter-slice distance. Let the quantum numbers corresponding to the degrees of freedom within a slice be $\mu = 1, 2, \ldots, M$ and the corresponding components of ψ_z be ψ_z^μ. For example in an *spd* tight-binding Hamiltonian, these enumerate the atomic sites within the slice and the valence orbitals (*spd*) at a site, while in the example at the beginning of this chapter $\mu = 1$ and $\psi_z = \psi_z^\mu$ is a c-number. The Schrödinger equation may then be solved by introducing the Bloch state,

$$\psi_z = n_{k_\perp}^{1/2} e^{ik_\perp z}\phi_{k_\perp} , \tag{2.22}$$

where $\phi_{k_\perp}$ is a normalized M-component column vector and $n_{k_\perp}^{1/2}$ an arbitrary constant. Note that throughout all the thesis I will use the symbol "$\perp$" to indicate the direction

of the current and the symbol "||" to label the transverse plane. Substituting (2.22) into the equation (2.21) gives

$$\left(H_0 + H_1 e^{ik_\perp} + H_{-1} e^{-ik_\perp} - E\right) \phi_{k_\perp} = 0 \,. \tag{2.23}$$

The task is now to compute the Green function g of such a system, for all real energies, using the general Green function structure discussed in the previous section. For a given energy E, the first goal is to determine all possible values (both real and complex) of the wave-vectors $k_\perp$ by solving the secular equation

$$\det(H_0 + H_1 \chi + H_{-1}/\chi - E) = 0 \,, \tag{2.24}$$

where $\chi = e^{ik_\perp}$. Note that the equation (2.24) reduces to the well known formulae of equations (2.1) and (2.16) respectively for a linear chain, and for a two-dimensional simple-cubic lattice.

In contrast to conventional band-theory, where the problem is to compute the M values of E for a given (real) choice of $k_\perp$, my aim is to compute the complex roots χ of the polynomial (2.24) for a given (real) choice of E (remember that both open and closed scattering channels enter in the definition of the Green function). Consider first the case where H_1 is not singular. Note that for real $k_\perp$, conventional band-theory yields M energy bands $E_n(k_\perp)$, $n = 1, \ldots, M$, with $E_n(k_\perp + 2\pi) = E_n(k_\perp)$. As a consequence, for a given choice of E, to each real solution $k_\perp = k$, for which the group velocity

$$v_k = \frac{1}{\hbar} \frac{\partial E(k)}{\partial k} \tag{2.25}$$

is positive (right-moving channel), there exists a second solution $k_\perp = \bar{k}$ for which the group velocity

$$v_{\bar{k}} = \frac{1}{\hbar} \frac{\partial E(\bar{k})}{\partial \bar{k}} \tag{2.26}$$

is negative (left-moving channel). In the simplest case, where $H_1 = H_{-1}$, one finds $k = -\bar{k}$. I also note that to each solution $k_\perp$ the Hermitian conjugate of (2.23) shows that $k_\perp^*$ is also a solution. Hence to each right-decaying solution k possessing a positive imaginary part, there is a left-decaying solution $\bar{k}$ with a negative imaginary part. For the purpose of constructing the Green function, this suggests dividing the roots of (2.23) into two sets: the first set of M wave-vectors labeled k_l ($l = 1, ..., M$) correspond to

right-moving and right-decaying plane-waves and the second set labeled $\bar{k}_l$ ($l = 1, ..., M$) correspond to left-moving and left-decaying plane-waves.

Although the solutions to (2.24) can be found using a root tracking algorithm, for numerical purposes it is more convenient to map (2.23) onto an equivalent eigenvalue problem by introducing the matrix $\mathcal{H}$

$$\mathcal{H} = \begin{pmatrix} -H_1^{-1}(H_0 - E) & -H_1^{-1}H_{-1} \\ \mathcal{I} & 0 \end{pmatrix}, \tag{2.27}$$

where $\mathcal{I}$ is the M dimensional identity matrix. The eigenvalues of $\mathcal{H}$ are the $2M$ roots e^{ik_l}, $e^{i\bar{k}_l}$ and the upper M components of the eigenvectors of $\mathcal{H}$ are the corresponding eigenvectors $\phi_{k_l}, \phi_{\bar{k}_l}$. It is clear that in the case in which H_1 is singular, the matrix $\mathcal{H}$ is not defined. Since H_1 describes the coupling between unit cells, it can be singular if some of the degrees of freedom of adjacent cells are not coupled. Furthermore it can also be singular if there is "over-coupling" between cells. Suppose one considers a two-dimensional simple-cubic lattice with one degree of freedom per site. Consider an infinite strip two atomic site wide. If the coupling extends to second nearest neighbours and is the same for the first and the second nearest neighbors, then H_1 is a 2×2 matrix in which all the elements are the same, therefore it is a singular matrix. Nevertheless in most of the practical cases H_1 is not singular, or can be reduced to a non-singular matrix. In fact it is possible to remove the singularities of H_1 with a procedure completely analogous to the one used for computing the effective coupling matrix of the scatterer. More details of this procedure are given in Chapter 7, where dealing with carbon nanotubes.

To construct the retarded Green function $g_{zz'}$ of the doubly infinite system, note that except at $z = z'$, g is simply a wave-function and hence must have the form

$$g_{zz'} = \begin{cases} \sum_{l=1}^{M} \phi_{k_l} e^{ik_l(z-z')} \mathbf{w}_{k_l}^{\dagger} & z \geq z' \\ \sum_{l=1}^{M} \phi_{\bar{k}_l} e^{i\bar{k}_l(z-z')} \mathbf{w}_{\bar{k}_l}^{\dagger} & z \leq z' \end{cases} \tag{2.28}$$

where the M-component vectors $\mathbf{w}_{k_l}$ and $\mathbf{w}_{\bar{k}_l}$ are to be determined. At this point it is important to observe that the structure of the Green function of equation (2.28) is identical to the one discussed in the previous section, and that the vectors ϕ_k and $\mathbf{w}_k$ (equivalent to β_n and β_n^*) include all the degrees of freedom of the transverse direction. Since $g_{zz'}$ is retarded both in z and z', it satisfies the Green function equation corresponding to (2.21) and is continuous at the point $z = z'$ (see Appendix A for a detailed

calculation), one obtains

$$g_{zz'} = \begin{cases} \sum_{l=1}^{M} \phi_{k_l} e^{ik_l(z-z')} \tilde{\phi}^{\dagger}_{k_l} \mathcal{V}^{-1} & z \geq z' \\ \sum_{l=1}^{M} \phi_{\bar{k}_l} e^{i\bar{k}_l(z-z')} \tilde{\phi}^{\dagger}_{\bar{k}_l} \mathcal{V}^{-1} & z \leq z' \end{cases} . \tag{2.29}$$

The matrix $\mathcal{V}$ is defined by

$$\mathcal{V} = \sum_{l=1}^{M} H_{-1} \left[\phi_{k_l} e^{-ik_l} \tilde{\phi}^{\dagger}_{k_l} - \phi_{\bar{k}_l} e^{-i\bar{k}_l} \tilde{\phi}^{\dagger}_{\bar{k}_l} \right] , \tag{2.30}$$

and the set of vectors $\tilde{\phi}^{\dagger}_{k_l}$ ($\tilde{\phi}^{\dagger}_{\bar{k}_l}$) are the duals of the set ϕ_{k_l} ($\phi_{\bar{k}_l}$), defined by

$$\tilde{\phi}^{\dagger}_{k_l} \phi_{k_h} = \tilde{\phi}^{\dagger}_{\bar{k}_l} \phi_{\bar{k}_h} = \delta_{lh} , \tag{2.31}$$

from which follows the completeness conditions

$$\sum_{l=1}^{M} \phi_{k_l} \tilde{\phi}^{\dagger}_{k_l} = \sum_{l=1}^{M} \phi_{\bar{k}_l} \tilde{\phi}^{\dagger}_{\bar{k}_l} = \mathcal{I} . \tag{2.32}$$

Equation (2.29) is the retarded Green function for a doubly infinite system. For a semi-infinite lead, this must be modified to satisfy the boundary conditions at the end of the lead. Consider first the left lead, which extends to $z = -\infty$ and terminates at $z = z_0 - 1$, such that the position of the first missing slice is $z = z_0$. To satisfy the boundary condition that the Green function must vanish at $z = z_0$, one must subtract from the right hand side of (2.29) a wave-function of the form

$$\Delta_z(z', z_0) = \sum_{lh}^{M} \phi_{\bar{k}_h} e^{i\bar{k}_h z} \Delta_{hl}(z', z_0) , \tag{2.33}$$

where $\Delta_{hl}(z', z_0)$ is a complex matrix, determined from the condition that the Green function vanishes at z_0, which yields

$$\Delta_z(z', z_0) = \Delta_{z'}(z, z_0) =$$

$$\sum_{l,h=1}^{M} \phi_{\bar{k}_h} e^{i\bar{k}_h(z-z_0)} \tilde{\phi}^{\dagger}_{\bar{k}_h} \phi_{k_l} e^{ik_l(z_0-z')} \tilde{\phi}^{\dagger}_{k_l} \mathcal{V}^{-1} . \tag{2.34}$$

For the purpose of computing the scattering matrix, I will require the Green function of the semi-infinite left-lead $\tilde{g}_{zz'}(z_0) = g_{zz'} - \Delta_z(z', z_0)$ evaluated on the surface of the lead, namely at $z = z' = z_0 - 1$. Note that in contrast with the Green's function

of a doubly infinite lead, which depends only on the difference between z and z', the Green's function $\tilde{g}$ of a semi-infinite lead for arbitrary z, z' is also a function of the position z_0 of the first missing slice beyond the termination point of the lead. Writing $g_{\rm L} = g_{(z_0-1)(z_0-1)}(z_0)$ yields for this surface Green function

$$g_{\rm L} = \left[\mathcal{I} - \sum_{l,h} \phi_{\bar{k}_h} e^{-i\bar{k}_h} \tilde{\phi}^{\dagger}_{\bar{k}_h} \phi_{k_l} e^{ik_l} \tilde{\phi}^{\dagger}_{k_l}\right] \mathcal{V}^{-1} \ . \tag{2.35}$$

Similarly on the surface of the right lead, which extends to $z = +\infty$, the corresponding surface Green function is

$$g_{\rm R} = \left[\mathcal{I} - \sum_{l,h} \phi_{k_h} e^{ik_h} \tilde{\phi}^{\dagger}_{k_h} \phi_{\bar{k}_l} e^{-i\bar{k}_l} \tilde{\phi}^{\dagger}_{\bar{k}_l}\right] \mathcal{V}^{-1} \ , \tag{2.36}$$

which has been obtained by subtracting from g the following wave-function

$$\Delta_z(z', z_0) = \Delta_{z'}(z, z_0) =$$

$$\sum_{l,h=1}^{M} \phi_{k_h} e^{ik_h(z-z_0)} \tilde{\varphi}^{\dagger}_{k_h} \phi_{\bar{k}_l} e^{i\bar{k}_l(z_0-z')} \tilde{\phi}^{\dagger}_{\bar{k}_l} \mathcal{V}^{-1} \ , \tag{2.37}$$

and considering $g_{\rm R} = g_{(z_0+1)(z_0+1)}(z_0)$ (z_0+1 is the position of the first slice of the right lead).

The expressions (2.35) and (2.36), when used in conjunction with (2.27) form a versatile method of determining lead Green functions, without the need to perform k-space integrals or a contour integration. As a consequence of translational invariance of the doubly infinite system, the surface Green functions are independent of the position of the surface z_0. Furthermore as noted below, in the case of different vectors ϕ_k corresponding to the same real k-vector k, the current operator is not diagonal. Hence it is convenient to perform a unitary rotation in such a degenerate sub-space to ensure the unitarity of the S-matrix. I will discuss in more details such a point in the section regarding the S matrix and in Appendix B.

2.4 The effective Hamiltonian of the scattering region

I have shown in the introduction that given the coupling matrix between the surfaces of the external leads, the Green function of the scatterer plus leads can be computed via

Dyson's equation. Generally the scattering region is not simply described by a coupling matrix between surfaces, but is a complex Hamiltonian involving all the degrees of freedom of the scatterer. Therefore it is useful to develop a method that transforms such a detailed Hamiltonian into an effective coupling matrix between the two surfaces. For structures, which possess a quasi-one dimensional geometry and a Hamiltonian which is block tri-diagonal, this can be achieved by projecting out the internal degrees of freedom of the scatterer. In the literature, depending on the context or details of implementation, this procedure is sometimes referred to as "the recursive Green function technique" or "the decimation method", but is no more than an efficient implementation of Gaussian elimination.

Consider a scatterer composed on $N - 2M$ degrees of freedom. Then the Hamiltonian for the scatter plus semi-infinite leads is of the form $H = H_L + H_R + \tilde{H}$, where H_L, H_R are the Hamiltonians of the left and right isolated leads and $\tilde{H}$ a $N \times N$ Hamiltonian describing the scattering region and any additional couplings involving surface sites of the leads induced by the presence of the scatterer. The aim of the decimation (i.e. recursive Green function) method is to successively eliminate the internal degrees of freedom of the scatterer, which I label i, $i = 1, 2, ..., N - 2M$, to yield a $(2M)\times(2M)$ effective Hamiltonian H_{eff}. After eliminating the degree of freedom $i = 1$, $\tilde{H}$ is reduced to a $(N-1)\times(N-1)$ matrix with elements

$$H_{ij}^{(1)} = \tilde{H}_{ij} + \frac{\tilde{H}_{i1}\tilde{H}_{1j}}{E - \tilde{H}_{11}} \,. \tag{2.38}$$

Repeating this procedure l times one obtains the "decimated" Hamiltonian at l-th order

$$H_{ij}^{(l)} = H_{ij}^{(l-1)} + \frac{H_{il}^{(l-1)} H_{lj}^{(l-1)}}{E - H_{ll}^{(l-1)}} \,, \tag{2.39}$$

and after $N - 2M$ such steps, an effective Hamiltonian $H_{\text{eff}} = H^{N-2M}$ of the form

$$H_{\text{eff}}(E) = \begin{pmatrix} H_{\text{L}}^{*}(E) & H_{\text{LR}}^{*}(E) \\ H_{\text{RL}}^{*}(E) & H_{\text{R}}^{*}(E) \end{pmatrix} . \tag{2.40}$$

In this expression, $H_{\text{L}}^{*}(E)$ ($H_{\text{R}}^{*}(E)$) describes intra-surface couplings involving degrees of freedom belonging to the surface of the left- (right-) hand side lead and $H_{\text{LR}}^{*}(E) = H_{\text{RL}}^{*}(E)^{\dagger}$ describes the effective coupling between the surfaces of the left-hand side and the right-hand side leads.

Since the effective Hamiltonian is energy dependent, this procedure is particularly useful when one wishes to compute the Green function at a given energy. It is also very efficient in the presence of short range interactions, because only matrix elements involving degrees of freedom coupled to the decimated one, are redefined. This latter aspect is very useful in the case that the scatterer has some periodicity and allows clever numerical optimizations. More about this will be discussed in the case of disordered multilayers in Chapter 5.

Since the problem now involves only $(2M)\times(2M)$ matrices, it is straightforward to obtain the surface Green function for the whole system (i.e. the scattering region attached to semi-infinite leads) by solving Dyson's equation

$$G(E) = [g(E)^{-1} - H_{\rm eff}(E)]^{-1} , \tag{2.41}$$

where

$$g(E) = \begin{pmatrix} g_{\rm L}(E) & 0 \\ 0 & g_{\rm R}(E) \end{pmatrix} , \tag{2.42}$$

with g_L and g_R given by equations (2.35) and (2.36).

2.5 The S matrix and the transport coefficients

To extract the transport coefficients from the Green function, I generalize the method described in reference [47] (in particular see A.26 of [47]) to the case of non-orthogonal scattering channels. The same method has been used in the introduction of this chapter to calculate the S matrix for two linear chains. For a system of Hamiltonian H, the S matrix is defined to connect incoming to outgoing propagating states in the external leads (see equation (1.6)). If k, (k') are real incoming (outgoing) wave-vectors of energy E, then an incident plane-wave in one of the leads, with longitudinal wave-vector k, will scatter into outgoing plane-waves k' with amplitudes $s_{k'k}(E,H)$. If all plane-waves are normalized to unit flux, (by dividing by the square-root of their group velocities) then provided the plane-wave basis diagonalizes the current operator in the leads, the outgoing flux along channel k' is $|s_{k'k}(E,H)|^2$ and S will be unitary. If H is real, then S will be symmetric, but more generally time reversal symmetry implies $s_{k'k}(E,H) = s_{kk'}(E,H^*)$. For convenience, if k,k' belong to the left (right) lead, then I define reflection coefficients via $r_{k'k} = s_{k'k}$ ($r'_{k'k} = s_{k'k}$), whereas if k,k' belong to

left and right leads respectively (right and left leads respectively) I define transmission coefficients $t_{k'k} = s_{k'k}$ ($t'_{k'k} = s_{k'k}$).

To extract the transport coefficients, consider the probability current for an electron in the Bloch state (2.22)

$$J_k = n_{k_\perp} v_{k_\perp} \ , \tag{2.43}$$

where $n_{k_\perp}$ is the probability of finding an electron in a slice and $v_{k_\perp}$ is the corresponding group velocity. It follows that the vector

$$\psi_z = \frac{1}{\sqrt{v_k}} e^{ikz} \phi_k \ , \tag{2.44}$$

is normalized to unit flux. To compute the group velocity note that if $|\psi_k\rangle$ is an eigenstate (2.20), whose projection onto slice z is ψ_z, then

$$v_k = \frac{1}{\hbar} \frac{\partial}{\partial k} \langle \psi_k | H | \psi_k \rangle =$$

$$= \frac{1}{\hbar} \frac{\partial}{\partial k} \left[\phi_k^\dagger \left(H_0 + H_1 e^{ik} + H_{-1} e^{-ik} \right) \phi_k \right] = \tag{2.45}$$

$$= \frac{i}{\hbar} \phi_k^\dagger \left(H_1 e^{ik} - H_{-1} e^{-ik} \right) \phi_k \qquad , \tag{2.46}$$

where the last step follows from equation (2.23) and normalization of ϕ_k.

It can be shown that the states (2.44) diagonalize the current operator only if they correspond to distinct k values. In the case of degenerate k's, the current is in general non-diagonal. Nevertheless it is always possible to define a rotation in the degenerate subspace for which the current operator is diagonal and in what follows, when a degeneracy is encountered, I assume that such a rotation has been performed (see Appendix B). With this convention, the current carried by a state of the form

$$\psi_z = \sum_l a_l \frac{e^{ik_l z}}{\sqrt{v_l}} \phi_{k_l} \ , \tag{2.47}$$

is simply $\sum_l |a_l|^2$.

It is now straightforward to generalize the analysis of [47] (and of paragraph 2.1) to the case of non-orthogonal scattering channels. Consider first a doubly infinite periodic

structure, whose Green function is given by equation (2.29). For $z \geq z'$, acting on $g_{zz'}$ from the right with the following projector

$$P_l(z') = \mathcal{V}\phi_{k_l}\frac{e^{ik_l z'}}{\sqrt{v_l}} , \tag{2.48}$$

yields the normalized plane-wave (2.44). Similarly by acting on the Green function $g_{zz'}(z_0)$ of a semi-infinite left-lead terminating at z_0, one obtains for $z \geq z'$, $z_0 \geq z$, an eigenstate of a semi-infinite lead arising from a normalized incident wave along channel k_l. Note that the projector introduced through the (2.48) is the generalization of the one defined in the simple example at the beginning of this chapter. In Appendix C I will formally show that the projector that projects the Green function for a double infinite system onto its corresponding wave-function, projects also the total Green function.

Thus the operator $P_l(z')$ and its left-moving counterpart $\bar{P}_l(z')$ allow one to project-out wave-functions from the Green function of a given structure. For example, following the same procedure of the introduction, if $G_{zz'}$ is the retarded Green function for a scattering region sandwiched between two perfect leads whose surfaces are located at the points $z = 0$ and $z = L$, then for $z' \leq 0$, the projected wave-function is of the form

$$\psi_z = \begin{cases} \frac{e^{ik_l z}}{\sqrt{v_l}}\phi_{k_l} + \sum_h \frac{r_{hl}}{\sqrt{v_h}} e^{i\bar{k}_h z}\phi_{\bar{k}_h} & z \leq 0 \\ \sum_h \frac{t_{hl}}{\sqrt{v_h}} e^{ik_h z}\phi_{k_h} & z \geq L \end{cases} , \tag{2.49}$$

where $r_{hl} = r_{\bar{k}_h,k_l}$, $t_{hl} = t_{k_h,k_l}$ are reflection and transmission coefficients associated with an incoming state from the left. In particular for $z = L$, $z' = 0$, one obtains

$$\sum_h \frac{t_{hl}}{\sqrt{v_h}} e^{ik_h L}\phi_{k_h} = G_{L0}P_l(0) , \tag{2.50}$$

and hence

$$t_{hl} = \tilde{\phi}^\dagger_{k_h} G_{L0}\mathcal{V}\phi_{k_l}\sqrt{\frac{v_h}{v_l}}e^{-ik_h L} , \tag{2.51}$$

where I used the definition of the dual vector $\tilde{\phi}$ given in equation (2.31). With the same method one evaluates all the other elements of the S matrix

$$t'_{hl} = \tilde{\phi}^\dagger_{\bar{k}_h} G_{0L}\mathcal{V}\phi_{\bar{k}_l}\sqrt{\frac{v_h}{v_l}}e^{i\bar{k}_h L} , \tag{2.52}$$

$$r_{hl} = \tilde{\phi}^\dagger_{\bar{k}_h}(G_{00}\mathcal{V} - \mathcal{I})\phi_{k_l}\sqrt{\frac{v_h}{v_l}} , \tag{2.53}$$

$$r'_{hl} = \tilde{\phi}^{\dagger}_{k_h}(G_{LL}\mathcal{V} - \mathcal{I})\phi_{\tilde{k}_l}\sqrt{\frac{v_h}{v_l}} \ . \tag{2.54}$$

Since the right-hand sides of (2.51-2.54) involve only the surface Green function of equation (2.41) the transport coefficients are determined. Moreover, since the above analysis is valid for any choice of the Hamiltonians H_0 and H_1, this approach is completely general.

3 The Material-Dependence of GMR and TMR

3.1 Introduction

The aim of this chapter is to analyze the dependence of GMR and TMR on the materials composing respectively a multilayer and a spin-tunneling junction. I will focus attention solely on the case in which the current flows perpendicular to plane of the layers (CPP), where the full power of the scattering technique developed in the previous chapter can be used.

Consider first the case of CPP GMR. The main difference with respect to its CIP counterpart is twofold. On the one hand there is the fact that an electron must cross the whole structure before being collected at the leads, and on the other hand the dimensions on which the transport occurs are mesoscopic, the typical multilayer length being smaller than 1μm. This means that, particularly at low temperature, the transport is largely phase coherent. Despite the evidence of such an important aspect, early theoretical work was based on spin-dependent scattering at interfaces and/or magnetic impurities and completely neglected quantum interference [48]. In 1995 Schep, Kelly and Bauer [49, 50] challenged this conventional picture and showed that for Co/Cu multilayers large values of GMR (of order 120%) exist even in absence of impurity scattering. Their calculations are based on local density functional theory and the Sharvin resistance of a small constriction formed from a pure crystalline magnetic multilayer is calculated. Since then several methods have been used to take into account the contributions of realistic band structures in CPP GMR. These includes *ab initio* density functional methods [51, 52] and tight-binding methods [53, 54]. The use of the second is also motivated by the possibility to deal with disordered systems, even if some severe limitations are still present (see also the introduction to Chapter 5). Despite the availability of numerical techniques able to deal with realistic band structures, very little theoretical work has been done to study systematically the dependence of GMR on the materials forming the multilayers. The aim of this chapter is to fill this gap and to provide some prescriptions on how to build multilayers showing large GMR [27].

From an experimental point of view Co/Cu [55, 56, 57, 58] and Fe/Cr [14, 59] are the most largely studied multilayered systems and also the ones that present the largest effect. Part of the success of these two systems is due to the fact that multilayers may

be deposited in relatively simple conditions, producing samples of good quality with small inter-diffusion at the interface. As far as the magnetic materials are concerned, Ni has been also employed in conjunction with non-magnetic materials with fcc lattice structure [60, 61, 62], but to date all the measurements have been conducted with the CIP configuration and only a small GMR ratio has been found. This is believed to be related to the smaller exchange field of Ni with respect to Co. Moreover Ni has been also employed in forming alloys [63, 64, 65]. This is useful in dual magnetic element multilayers in which one wants to engineer the coercive fields of the different materials. One of the more widely-used alloys is $Ni_{80}Fe_{20}$ which grows with an fcc lattice onto Cu. $Ni_{80}Fe_{20}$/Cu multilayers have been successfully grown [64, 65] with a quite large CPP GMR. The limitation of these systems seems to be the large spin-flip scattering in the alloy and at the interfaces between the alloy and Cu. As far as the non-magnetic metals are concerned Ag has been used in conjunction with Co [13, 66, 67] showing quite large CPP GMR. In contrast other heavy elements like Rh [68, 69], Ru [70], Au [71] and Ir [72, 73] possess very small GMR, even if at present the only measurement carried out are in the CIP configuration (with the only exception of reference [71]). The absence of large GMR in these materials is believed to be connected with the usually large inter-diffusion at the interfaces resulting in large spin-flip scattering, and for some materials in a poor antiferromagnetic alignment in zero magnetic field. In this chapter I will perform a systematic study of disorder-free Co/A and Ni/A multilayers, where A is a $3d$, $4d$ an $5d$ transition metal with fcc lattice structure and analyze the optimal conditions for GMR. From this analysis it will be clear that the different alignment between the band structures of the magnetic and non-magnetic metals forming the multilayer may result in very different spin-polarizations of the current and GMR.

Turning the attention to TMR, the main difference with respect to GMR is that the current involved is a tunneling current. From the point of view of the scattering theory this means that not only the match between the asymptotic wave-functions through the scattering region is important, but also how these wave-functions decay within the tunneling barrier. Early theoretical work on magneto-tunneling attributed the degree of polarization of a tunneling junction either to the different spin-dependent DOS of the magnetic leads [17], or to the different Fermi wave-vectors of the two spin-bands [74].

These models were based on a free electron model in the effective mass approximation. In a more realistic description of real metals the details of the band structure are important and deviations from the simple theories may be found. Realistic band structures have been introduced in the calculation of the tunneling current either through *ab initio* density functional methods [75, 76, 77] or through tight-binding models [78, 79]. These calculations give rise to a controversy regarding the actual polarization of a tunneling junction and on the relevant factors which affect the tunneling. The common starting point is that for Co the polarization of the *s*-electrons at the Fermi energy is positive, while for the *d*-electrons it is negative. Therefore, if the barrier acts selectively on the *s*- and *d*-electrons, different polarizations of the tunneling junction are expected. MacLaren and co-workers, using a KKR Green function approach to the tunneling transport [76], have found that the polarization of a Co-based tunneling junction is positive for several insulators and concluded that it is always positive. Their argument is based on the fact that the decay of the wave-function within the barrier is faster if the wave-function has a strong *d*-component with respect to the case in which the wave-function has a large *s*-component. In contrast Tsymbal [78] and Wang [77] independently have found that the polarization may be changed by changing the kind of coupling between the magnetic electrodes and the tunneling barrier. For instance Tsymbal showed that in a Co-based tunneling junction with an *s*-insulator, the polarization is positive if one considers only ssσ coupling at the interface and becomes negative if sdσ is also included.

In the last paragraph of this chapter I will consider a Cu/Co/INS/Co/Cu junction (INS is an insulator) described by *spd* tight-binding Hamiltonian and show that, if the thickness of the insulator is large enough the polarization of the junction is negative, otherwise it is positive. This highlights the transition between a regime in which direct transport and tunneling co-exist to one involving pure tunneling. An important feature of the calculation is that in the pure tunneling regime the transmission coefficient for the minority electrons shows sharp resonances at certain $k_{\|}$'s in the 2D transverse Brillouin zone. Resonances can be reproduced with a simple effective-mass model with parabolic band, even if the position of the resonances in the 2D Brillouin zone is a characteristic of the realistic band structure used. All the calculations deal with ballistic transport and disorder-free junctions and important aspects like impurity- [19], phonon- and

magnon-assisted tunneling [80] have been neglected.

In all the calculations of the following sections the magnitude of the GMR and TMR effect is measured by means of the MR ratio defined as

$$\mathrm{MR} = \frac{\Gamma_{\mathrm{FM}}^{\uparrow} + \Gamma_{\mathrm{FM}}^{\downarrow} - 2\Gamma_{\mathrm{AF}}^{\uparrow\downarrow}}{2\Gamma_{\mathrm{AF}}^{\uparrow\downarrow}} , \tag{3.1}$$

where $\Gamma_{\mathrm{FM}}^{\sigma}$ is the conductance of a given spin channel σ in the ferromagnetic (FM) configuration and $\Gamma_{\mathrm{AF}}^{\uparrow\downarrow}$ is the corresponding conductance (for either spin) in the anti-ferromagnetic (AF) state. In the equation (3.1) it is implicitly assumed the current is carried by two decoupled spin-fluids [11]. In what follows I also assume a perfect match at the interface between the fcc lattices of the different materials. This assumption is particularly good in the case of Co, Cu, and Ni which possess almost identical lattice constants. I will consider crystalline systems with smooth interfaces, where $k_{||}$ is a good quantum number. The Hamiltonian can then be diagonalized in the Bloch basis $k_{||}$ to yield a spin-dependent conductance

$$\Gamma^{\sigma} = \sum_{k_{||}} \Gamma^{\sigma}(k_{||}) = \frac{e^2}{h} \sum_{k_{||}} T^{\sigma}(k_{||}) , \tag{3.2}$$

where the sum over $k_{||}$ is extended over the two-dimensional Brillouin zone in the case of infinite cross section and over the allowed discrete $k_{||}$'s in the case of finite cross section.

3.2 Tight-Binding Model: Slater-Koster Parameterization

In this paragraph I will introduce the parameterization I have used to produce the tight-binding Hamiltonian describing real materials. The method is based on the famous Slater-Koster Local Combination of Atomic Orbitals (LCAO) method in the two-centre approximation [81]. The general idea of the tight-binding method is to reproduce the band structure of real materials using a minimal number of parameters, which can be either directly calculated or simply fitted. The main advantage of this method is that usually the number of parameters necessary to capture the main features of the band structure is quite small. This allows one to deal with disordered systems and to perform molecular dynamics simulations, both of which are hardly accessible using more fundamental methods.

Consider a generic Hamiltonian H for a crystal. The Slater-Koster method involves expanding such an Hamiltonian in an atomic orbital basis using only a small number of orbitals. Let $\phi_n(\mathbf{r}-\mathbf{R_i})$ be an atomic orbital located on an atom at the position $\mathbf{R_i}$ with a quantum number n. The main purpose of the LCAO method is to express the Hamiltonian H in term of Bloch states formed from the atomic orbital basis, namely states of the form

$$\psi_n(\mathbf{r}) = \sum_{\mathbf{R_i}} e^{i\mathbf{k}\cdot\mathbf{R_i}} \phi_n(\mathbf{r}-\mathbf{R_i}) \,, \tag{3.3}$$

where $\mathbf{R_i}$ spans the atoms in equivalent positions in all the unit cells of the crystal. The approximate solution of the periodic potential problem defined by the Hamiltonian H can be set up as follows. First take a finite set of atomic orbitals on each of the atoms of the unit cell (going up in energy from the lowest one). Secondly construct Bloch sums of the kind of equation (3.3). Finally for a given $\mathbf{k}$-vector, set up a wave function consisting of a linear combination of these Bloch sums and calculate the matrix elements between the states given by the equation (3.3).

This procedure has immediately a complication. The problem is that the Bloch sums of equation (3.3) are not orthogonal each other. The reason is that atomic orbitals belonging to different atoms are not orthogonal. Even though the construction of a tight-binding model using non-orthogonal basis is possible [82], it is more convenient to set up a new orthogonal atomic orbital basis. This can be done systematically by the Löwdin method [83]. In what follows I assume that such an orthogonalization procedure has always been performed and I consider the new orthogonal basis φ_n. It is important to note that these new Löwdin functions φ_n possess the same symmetry properties as the atomic orbitals ϕ_n from which they were derived. For instance, if I start with a p_x atomic orbital and construct the orthogonalized atomic orbitals according to Löwdin's prescription, I will find that the orthogonalized atomic orbital formed from p_x and from contributions of other orbitals on adjacent atoms, will still have the symmetry of a p_x function.

I can now build up Bloch sums using these Löwdin's functions

$$\psi_n(\mathbf{r}) = \frac{1}{\sqrt{N}} \sum_{\mathbf{R_i}} e^{i\mathbf{k}\cdot\mathbf{R_i}} \varphi_n(\mathbf{r}-\mathbf{R_i}) \,, \tag{3.4}$$

where I have assumed to have only one atom in the unit cell, and where the sum runs over the N available unit cells. The next step is to find the matrix elements

corresponding to the states ψ_n, namely

$$H_{nm} = \frac{1}{N} \sum_{\mathbf{R_i R_j}} e^{i\mathbf{k}\cdot(\mathbf{R_j}-\mathbf{R_i})} \times \int \varphi_n^*(\mathbf{r}-\mathbf{R_i}) H \varphi_m(\mathbf{r}-\mathbf{R_j})\, dV \,. \tag{3.5}$$

One of the two sums in equation (3.5) can be eliminated using translational symmetry giving rise to a factor N and to the final equation

$$H_{nm} = \sum_{\mathbf{R}} e^{i\mathbf{k}\cdot\mathbf{R}} \times \int \varphi_n^*(\mathbf{r}-\mathbf{R}) H \varphi_m(\mathbf{r})\, dV \,. \tag{3.6}$$

The structure of the (3.6) is very simple and H_{nm} does involve only atomic orbitals belonging to atoms in neighbouring positions. Nevertheless the calculation of the integral may be extremely difficult and the number of matrix elements H_{nm} may be very large. This is because, first one has to find the orthogonalized Löwdin's functions φ_n and secondly because a linear combination of integral of the form $\int \phi_n^*(\mathbf{r}-\mathbf{R}) H \phi_m(\mathbf{r})\, dV$ must be calculated. Therefore it is convenient to approximate (3.6) and express all the matrix elements H_{nm} by means of a small set of parameters.

First of all it is important to note that, despite the fact that the Löwdin's functions are not atomic orbitals, it is reasonable to expect that the integral (3.6) will vanish unless the two atoms are close enough so that their orbitals overlap to an appreciable extent. A general procedure is to arbitrary set to zero the matrix elements involving atoms with a distance larger than some fixed cut-off distance. This will result in considering first nearest neighbours, first and second nearest neighbours, first, second and third nearest neighbours, and so on, depending on the cut-off distance. It is clear that the larger is the number of neighbours, the better the tight-binding Hamiltonian will reproduce the correct band structure. Unfortunately an interaction extending to a large number of neighbours will result in an Hamiltonian with a large number of parameters. In all the calculations presented in this thesis I will always consider first nearest neighbours coupling.

A further simplification can be to consider only atomic orbitals whose energy is somewhere near that of the energy bands one is interested in. For a 3*d* transition metal for instance, if one is only interested in the description of the conduction and the valence band, it is reasonable to consider the 3*d*, 4*s* and 4*p* orbitals and disregard the rest. In the same way I will consider only 4*d*, 5*s* and 5*p*, and 5*d*, 6*s* and 6*p*, respectively for 4*d* and 5*d* transition metals.

Finally note that the integral of equation (3.6) involves a Löwdin's function $\varphi_n^*(\mathbf{r} - \mathbf{R})$ located on an atom at the position $\mathbf{R}$, another Löwdin's function $\varphi_m(\mathbf{r})$ located at the origin, and a spherical potential function, given by the potential part of the Hamiltonian, located on a third atom. In other words the integral of equation (3.6) is a three-center integral. A useful simplification is to disregard three-center integrals and to retain in the equation (3.6) the sum of the spherical potentials located only on the two atoms on which the atomic orbitals are located. Thus the integral becomes similar to the type which one should have in a diatomic molecule. If one considers the vector $\mathbf{R_j} - \mathbf{R_i}$, stretching from one atom to the other, to be an axis like that of a diatomic molecule, it is possible to express each of the functions φ as a sum of functions quantized with respect to that axis. Then to set up the integral of equation (3.6) one needs contributions consisting of a product of an atomic orbital located at $\mathbf{R_i}$, another atomic orbital located at $\mathbf{R_j}$ and a spherical potential centered on the two atoms. Let the direction of the the vector $\mathbf{R_j} - \mathbf{R_i}$ be specified by the direction cosines l, m, n. With this notation the integral denoted with $E_{\alpha,\beta}(l, m, n)$ is the integral between the functions φ_α and φ_β. For instance $E_{x,xy}(l, m, n)$ is the integral between the function φ_x with a p_x-like symmetry, and the d-function φ_{xy} with a symmetry xy. Therefore this particular integral can be written approximately as the sum of two integrals: that between a pσ orbital on the first atom and a dσ orbital on the second, and that between a pπ orbital on the first atom and a dπ orbital on the second. As a matter of notation the first of these is indicated like pdσ and the second like pdπ. With this notation the first index labels the atomic orbital of the first atom, the second index the atomic orbital of the second atom and the third index the angular momentum of the bond formed between the two atoms measured along their axis. The above mentioned integral for instance turns out to be $E_{x,xy}(l, m, n) = \sqrt{3}l^2 m(\mathrm{pd}\sigma) + m(1 - 2l^2)(\mathrm{pd}\pi)$. The full parameterization in the two-center limit is provided in the original Slater-Koster paper of reference [81].

Finally the approximated Hamiltonian can be written as

$$H = \sum_{i,\alpha} E^i_{\alpha\alpha} c^\dagger_{\alpha i} c_{\alpha i} + \sum_{i,j,\alpha\beta} E^{ij}_{\alpha\beta} c^\dagger_{\beta j} c_{\alpha i} \,, \tag{3.7}$$

where α and β label the two orbitals and i, j denote the atomic sites. $E_{\alpha\alpha}$ is the on-site energy and $E^{ij}_{\alpha\beta}$ the hopping energy between the orbital α at the position i and the

orbital β at the position j. $c^{\dagger}_{\alpha i}$ and $c_{\alpha i}$ are respectively the creation and annihilation operator for an electron in the orbital α at the atomic position i. In what follows I will always consider *spd*-Hamiltonians with nine degrees of freedom per atomic site and first nearest neighbours coupling. According to the Slater-Koster parameterization I need thirteen parameters to define one single material, namely one on-site energy per atomic orbital (E_{s}, E_{p} and E_{d}) and ten hopping parameters (ssσ, spσ, sdσ, ppσ, ppπ, pdσ, pdπ, ddσ, ddπ and ddδ). Note that the dependence on the lattice constant is included in the definition of the thirteen parameters, since they are defined with respect to the vector joining the two atoms forming the bond. The parameters used in the simulations are obtained by fitting the band structures calculated with plane-wave local density functional theory and are tabulated [84]. The only exception is for Co, Cu and Pb where I have performed a new fit in order to better reproduce the features around the Fermi surface (more about this will be discussed in Chapter 6 and in the Appendix D). As a matter of convention I always shift all the on-site energies in order to have the Fermi energy equal to zero ($E_{\mathrm{F}} = 0\mathrm{eV}$). Finally the ferromagnetism is taken into account by introducing a shift in the on-site energy between the *d*-orbitals of the up and down spin sub-bands. This simple model can reproduce the correct magnetic moment and the correct DOS at the Fermi energy.

3.3 GMR for disorder-free systems

Using the technique developed in the previous chapter I have studied the transport properties of multilayers formed from Co and Ni as magnetic materials and several $3d$, $4d$ and $5d$ transition metals as non-magnetic materials. All of these metals possess fcc lattice structure with the following lattice constants (Table 3.1). It is clear that Co, Ni and Cu have a good lattice match, while for the other metals the lattice mismatch is large and may introduce strain, defects and inter-diffusion at the interfaces. All these sources of disorder generate additional scattering, which is neglected in the present calculations. A fully realistic description of an interface involving metals with very different lattice constants requires *ab initio* methods implemented with molecular dynamics approach which is beyond the aim of this thesis. Nevertheless I will show that large values of the GMR ratio can be obtained, in agreement with the largest experimental values, which suggests that CPP GMR is a bulk effect, whose main features

Metal	Lattice Constant (Å)
Co	3.55
Ni	3.52
Cu	3.61
Ag	4.09
Pd	3.89
Au	4.08
Pt	3.92
Rh	3.80
Ir	3.84
Pb	4.95
Al	2.70

Table 3.1: Lattice constants of the metals considered in the calculation. Note that Co, Ni and Cu present very similar lattice constants.

are contained in a ballistic quantum description of the conductance with an accurate band structure. In what follows the hopping parameters at the heterojunctions between different materials are assigned to be the geometric mean of the pure metal values. This is a standard, widely-used [53, 54] procedure for estimating the hopping between unlike elements in a heterojunction. It is worth noting that different averaging procedures used to obtain the hopping coefficients in the heterojunctions yield small changes in the calculated conductances of the multilayers. Nonetheless, a more realistic approach to the heterojunctions between different metals, based on *ab initio* calculations and molecular dynamics, would be useful to clarify the role of coupling across the interfaces in such structures.

3.3.1 Density of electronic states and conductance of pure metals

I begin my analysis by examining the DOS and conductance of pure metals. Since the Hamiltonians include *spd* hybridization, the atomic orbital states are not eigenstates of the system. Nevertheless to understand the relative role of the angular symmetry on inter-band and intra-band scattering, it is useful to project the DOS and conductance onto an atomic orbital basis. I will label as an *s*-like electron and simply call *s*-electron (and similarly for the *p*- and *d*-electrons) an electron whose *s*-component $|\langle s|\psi\rangle|^2$ of the wave function $|\psi\rangle$ is much larger than the *p*- and *d*-components. The DOS ρ for pure materials are calculated by evaluating the retarded Green function for an infinite

system at the same point

$$\rho(E) = -\frac{1}{\pi} \sum_{k_{||}} \Im \, \mathrm{Tr} \, g_{zz}(E, k_{||}) \; . \tag{3.8}$$

The DOS's for the two spin sub-bands of Co and Ni are very similar (see figure 3.1). As

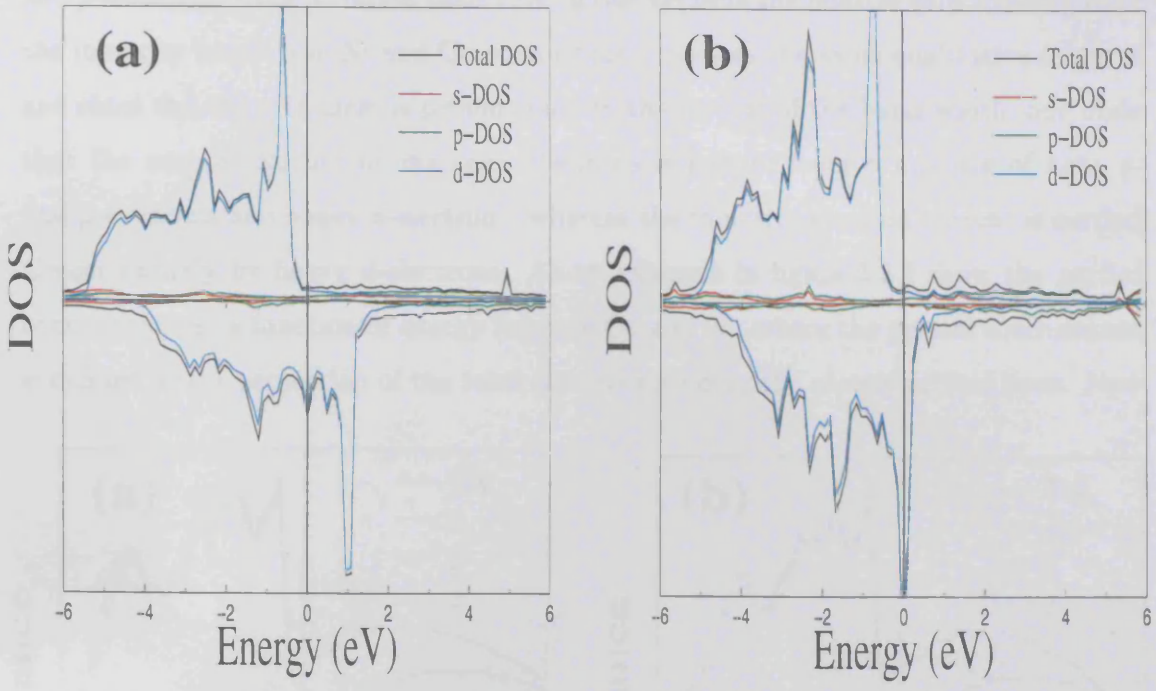

Figure 3.1: DOS for pure Co (a) and Ni (b). The vertical line denotes the position of E_F that is chosen to be 0 eV.

in all the d-transition metals, the DOS is formed from a localized d-band embedded in a broad nearly parabolic sp-band. The width of the bands is roughly the same in Co and Ni, as well as the position of the majority band with respect to the Fermi energy. In both materials, the Fermi energy lies just above the edge of the majority d-band, while the minority band is almost rigidly shifted with respect to the majority band towards higher energies, the shift being larger in Co than in Ni. In both the minority bands of Co and Ni the Fermi energy lies well within the d-band and the DOS is completely dominated by d-electrons. A rough estimate of the mismatch between the minority d-bands of Co and Ni can be obtained from the on-site energies of the d-electrons in the minority band. As shown in the tables in Appendix D, the difference between the on-site energies of the d minority electrons in Co and Ni is about 0.7eV and corresponds to the relative shift of the bands.

The conductance of pure Co and Ni is determined solely by the DOS. For majority electrons at the Fermi energy, the current is carried by the s-, p- and d-electrons, which give almost equal contributions. On the other hand the current carried by minority electrons is completely dominated by the d-electrons, with the contributions from s- and p-electrons being no larger than 10%. If one neglects the relative shift in energies of the minority bands, the Ni and Co conductances possess the same qualitative features and since the effective mass is proportional to the inverse of the band width, one finds that the current carried by majority electrons is formed from a mixture of light s- and p-electrons and heavy d-electrons, whereas the minority-electron current is carried almost entirely by heavy d-electrons. As an example in figure 3.2 I show the partial conductance as a function of energy for pure Co and Ni, where the partial conductance is defined as the projection of the total conductance over the atomic orbital basis. Now

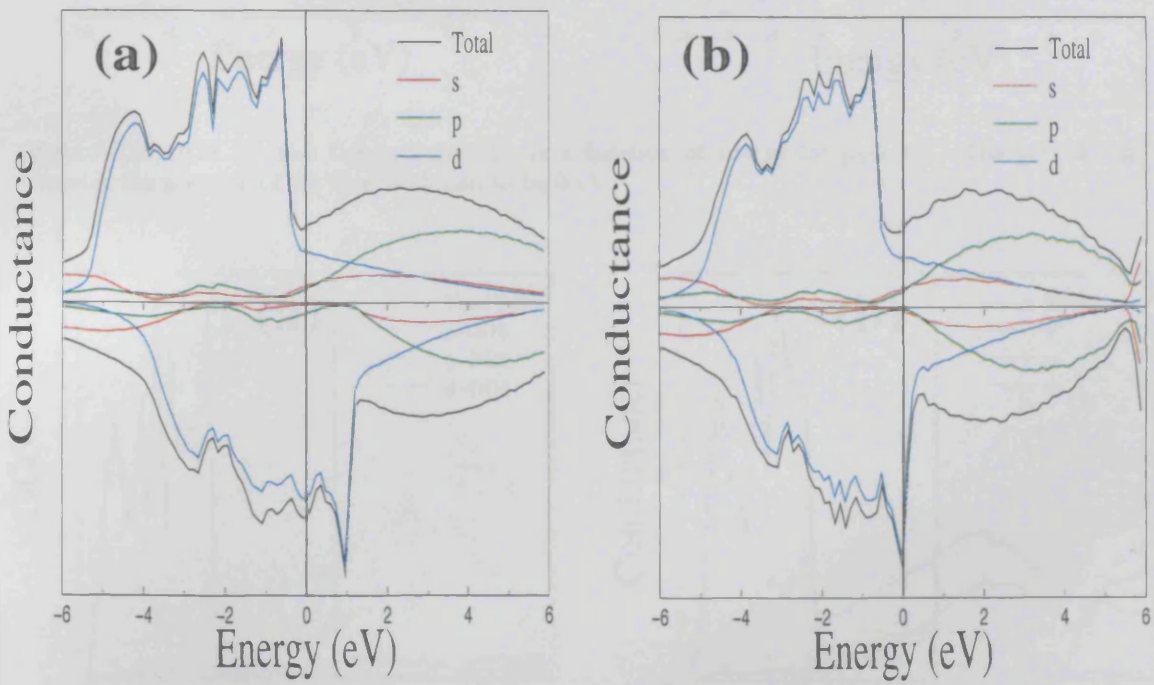

Figure 3.2: Conductance as a function of energy for pure Co (a) and Ni (b). The vertical line denotes the position of E_F that is chosen to be 0 eV.

consider the non-magnetic $3d$, $4d$ and $5d$ transition metals with fcc lattices. A glance at the DOS of these materials reveals four types of band structure: i) the DOS closely matches the DOS of the majority spin sub-band of Co and Ni (e.g. Cu and Au), ii) the DOS has only sp-components at the Fermi energy, with the d-component highly

suppressed (as in Ag), iii) the DOS is composed of an almost pure d-component at the Fermi energy (e.g. for Pd, Pt, Rh and Ir), iv) the DOS shows a $\sqrt{E}$-dependence, typical of free electron-like metals (Al and Pb).

Examples of each of these cases are given in figures 3.3, 3.4, 3.5 and 3.6, which show the DOS of Cu, Ag and Pd and Al together with their corresponding conductances.

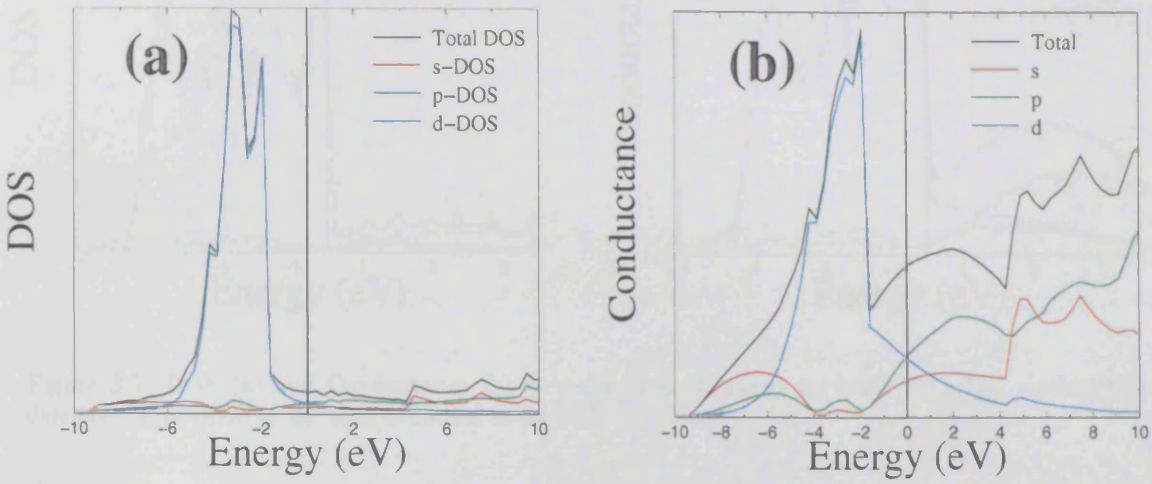

Figure 3.3: DOS (a) and Conductance (b) as a function of energy for pure Cu. The vertical line denotes the position of E_F that is chosen to be 0 eV.

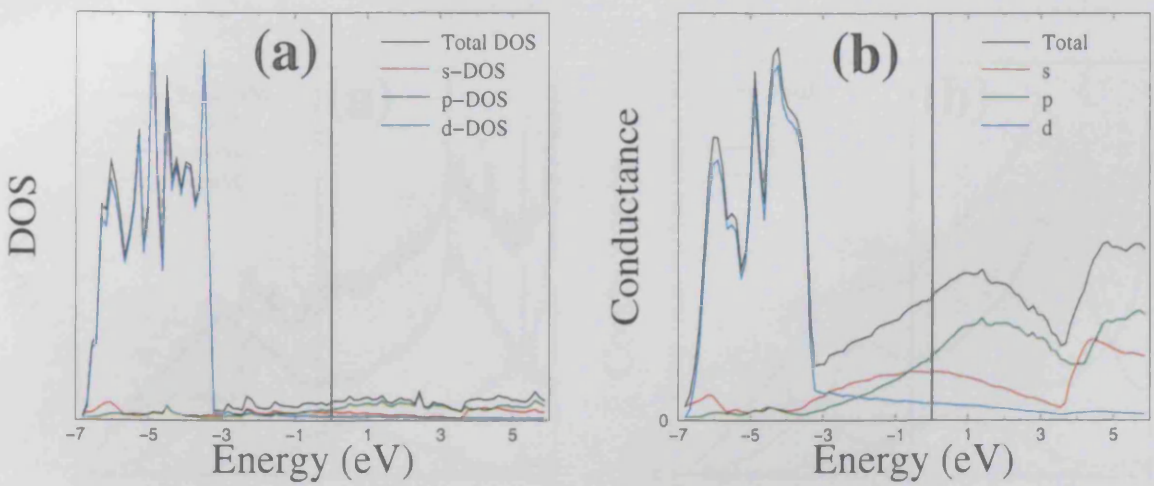

Figure 3.4: DOS (a) and Conductance (b) as a function of energy for pure Ag. The vertical line denotes the position of E_F that is chosen to be 0 eV.

For ballistic structures, in absence of defects and impurities, the mismatch between the bands of the magnetic and non-magnetic metals forming the multilayer is the key feature which determines the conductance. Moreover, although the positions of the

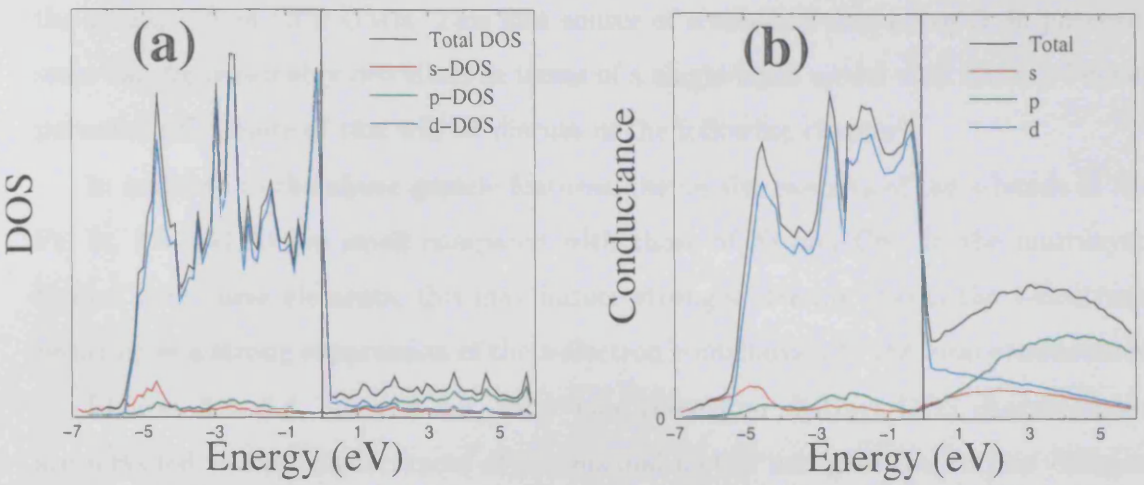

Figure 3.5: DOS (a) and Conductance (b) as a function of energy for pure Pd. The vertical line denotes the position of E_F that is chosen to be 0 eV.

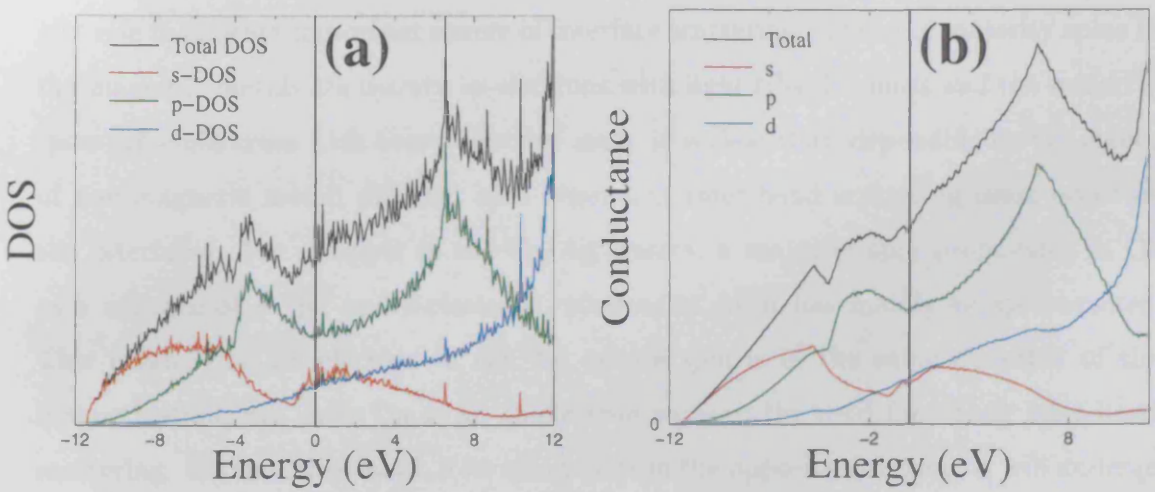

Figure 3.6: DOS (a) and Conductance (b) as a function of energy for pure Al. The vertical line denotes the position of E_F that is chosen to be 0 eV.

s- and *p*-bands are the same for both spins, for *d*-electrons the two spin sub-bands possess a different mismatch at the interface and this mismatch largely determines the magnitude of CPP GMR. This first source of scattering that arises from potential steps can be reasonably described in terms of a single-band model with Krönig-Penney potential [29] (more of this will be discuss in the following chapter).

In addition to the above generic features, the on-site energies of the *s*-bands of Au, Pt, Ir, Pb and Al are small compared with those of Ni and Co. In the multilayers formed with these elements, this may induce strong scattering also of the *s*-electrons, resulting in a strong suppression of the *s*-electron contribution to the total conductance.

Figures 3.3, 3.4, 3.5 and 3.6, show how these four distinct DOS characteristics are reflected in the conductances of the normal metals and give rise to four different scenarios for charge transport: i) the contributions to the current at the Fermi energy from *s*-, *p*- and *d*-electrons are almost equal (e.g. in Cu and Au), ii) the current at the Fermi energy has a strong *sp*-character (e.g. in Ag), iii) the current at the Fermi energy has a strong *d*-character (e.g. Pd, Pt, Rh and Ir), iv) the current at the Fermi energy is dominated by electrons with a parabolic dispersion and scales linearly with respect to the energy (Al and Pb).

These different characteristics of the current carriers in the non-magnetic metals give rise to another important source of interface scattering. Since the majority spins in the magnetic metals are mainly *sp*-electrons with light effective mass and the minority spins are *d*-electrons with heavy effective mass, it is clear that, depending on the choice of non-magnetic metal, different spin-dependent inter-band scattering must occur at the interfaces. For example in the Co/Ag system, a majority spin propagates in Co as a mixture of *s*-, *p*-, and *d*-electrons, whereas in Ag it has mainly an *sp*-character. This means that an electron in the Ag, whose spin is in the same direction of the magnetization, can enter Co as an *sp*-electron without the need for strong inter-band scattering. On the other hand, if its spin points in the opposite direction, it will undergo inter-band scattering because in the minority band the electron must propagate as a *d*-electron. Note that this second source of scattering has primarily to do with the very different dispersion relations of the *sp*-electrons with respect to the *d*- electrons. This feature is hardly describable by a single-band model and a more sophisticate approach is needed. In this thesis I will introduce two models capable to capture this aspect. The

first is a parabolic model with different spin- and material-dependent effective masses [30], and the second is a simple-cubic two-band tight-binding model [37].

The above observations suggest that the key mechanisms affecting transport are i) a strong band mismatch and ii) a strong inter-band scattering, reflecting respectively large step potentials and different dispersions. The best GMR multilayers must be able to maximize the electron propagation in one of the two spin-bands and to minimize it in the another. To achieve this result, the high conduction spin-band should have a small band mismatch and weak inter-band scattering at the heterojunctions, while the low conduction band should have a large band mismatch and strong inter-band scattering. Note that at this stage there are no general predictions on the total polarization of a multilayer, being dependent on the band structure details of both the magnetic and non-magnetic materials and their match.

3.3.2 Comparison between Co-based and Ni-based multilayers

To clarify how the spin-polarization of the magnetic material affects the properties of the GMR multilayers, I begin by examining GMR in Cu-based multilayers, in which the magnetic metals are either Ni or Co. All the multilayers consist of ten bilayers of the form A/Cu where A is Co or Ni, attached to two semi-infinite Cu leads (i.e. $Cu/[Co/Cu]_{\times 10}/Cu$ and $Cu/[Ni/Cu]_{\times 10}/Cu$). The Fermi energy is fixed by the semi-infinite leads which is taken as zero. After calculating the different spin conductances in the ferromagnetic and antiferromagnetic configurations, the GMR ratio is obtained from equation (3.1). In all the calculations the current flows in the (110) crystalline direction and the structures are translationally invariant within the layers. Below I consider 8100 $k_{||}$ points (90 × 90) in the plane of the layers. I have estimated that the GMR ratio calculated with 2×10^4 $k_{||}$ points on average differs by $\sim 3\%$, from that calculated using 8100 $k_{||}$ points ($\frac{GMR(8100)-GMR(2\times 10^4)}{GMR(8100)} \sim 3\%$). Since the oscillations of the GMR ratio with respect to the layer thicknesses are larger than 3%, the choice of 8100 $k_{||}$ points allows investigation of the oscillating behaviour of the conductance and the GMR, and is a good compromise between the accuracy of the calculation and the required computer time. Initially I fix the magnetic layer thickness to 5 atomic planes (AP), and calculate the conductance and GMR as a function of the Cu layer thickness.

I normalize the conductance by dividing it by the conductance of a single spin in

the pure metallic leads, which is a natural choice for the present work. For the results shown in figure 3.7 this means that the normalization factor is one half of the total Cu conductance, because of spin degeneracy. In this case the conductances of different multilayers are independent of the number of open channels in the leads and can be compared directly. From Figure 3.7 it is clear that the Co based multilayers possess

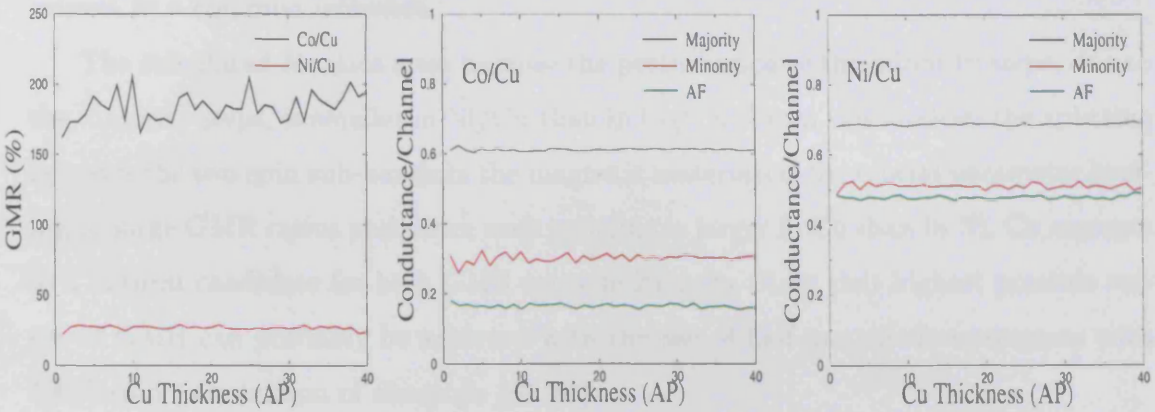

Figure 3.7: GMR and spin conductance for Co/Cu and Ni/Cu systems as a function of the Cu layers thickness. The first graph is the GMR, the second is the conductance for the Co/Cu system normalized to the conductance of pure Cu and the third is the conductance of the Ni/Cu system with the same normalization.

larger GMR ratios. In the ferromagnetic configuration, the majority electrons possess high conductances in both cases, reflecting the good match between the majority bands of Co and Ni, and the Cu band. Moreover the better match of the s and p majority bands of Ni with Cu, compared with those of Co, gives rise to a slightly higher conductance in majority channel for Ni than for Co. A similar argument explains the difference in the conductances of the minority channel. As one can see from the table in Appendix D, the minority d-band of Ni has a better match to Cu than that of Co, as indicated by the difference in the on-site energies of about 0.7 eV. Hence for the minority band, the interface scattering between Co/Cu is greater than for Ni/Cu. In the antiferromagnetic configuration, both spins undergo the same scattering sequence, belonging alternately to the majority and to the minority bands. The total spin conductance in the antiferromagnetic configuration is found to be close to that of the minority band in the ferromagnetic configuration, because the minority band mismatch is larger than the majority band, and dominates the scattering.

The ratio R between the conductance Γ of the AF configuration and of the minority

band in the FM configuration ($R = \Gamma^{\uparrow\downarrow}_{AF}/\Gamma^{\downarrow}_{FM}$) is ~ 0.6 for Co/Cu and ~ 0.9 for Ni/Cu. This difference can be understood by modeling the interface scattering through the step potential discussed previously, whose magnitude is equal to the band mismatch [29]. The effective scattering potential in the antiferromagnetic configuration will be a sequence of high steps (for minority band) and low steps (for majority band) with respect to a common reference.

The calculated R ratios arise because the perturbation of the minority steps, due to the majority steps, is smaller in Ni/Cu than in Co/Cu. From this analysis the splitting between the two spin sub-bands in the magnetic materials is the crucial parameter leading to large GMR ratios and, since such splitting is larger in Co than in Ni, Co emerges as a natural candidate for high GMR ratio multilayers. Note that highest possible values of GMR can probably be achieved with the use of half-metallic ferromagnets with 100% spin polarization of electrons [80, 85].

Having examined the dependence of transport properties on the normal-metal layer thickness, I now examine the dependence on the magnetic-layer thickness. For a fixed Cu layer-thickness of 5 atomic planes, figure 3.8 shows results for Co/Cu and Ni/Cu multilayers. A key result in this figure is that for thin magnetic layers, GMR in both Ni/Cu and Co/Cu multilayers is suppressed. This can be understood in term of an effective scattering potential. The large off-sets between the minority d-bands of the different materials create an effective barrier in the d-band, for channels with high transverse momentum $k_{||}$. When the width of such a barrier is small, tunneling across the magnetic metal within the d-band is possible, and this results in an enhancement of the conductance in the minority spin channel and hence in a reduction of GMR. Thus I predict a lower limit of approximately 4 atomic planes (~ 10Å) to the magnetic-layer thickness, in order to achieve the highest possible GMR ratio. In what follows I will only consider thicknesses larger than this value.

3.3.3 Dependence of GMR on non-magnetic spacer material

I now consider the dependence of GMR on the choice of non-magnetic material in Co- and Ni-based multilayers. In all calculations with Co I fix the Co thickness either at 5 or 10 atomic planes and in the calculations with Ni only at 10 atomic planes. The thickness of the non-magnetic layers always varies from 1 to 40 atomic planes.

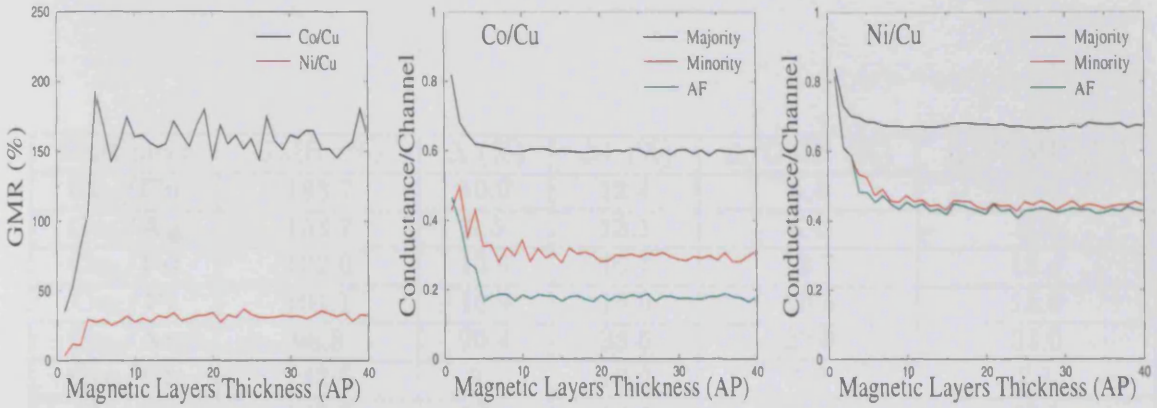

Figure 3.8: GMR and spin conductance for Co/Cu and Ni/Cu systems as a function of Co and Ni layers thicknesses. The first graph is the GMR, the second is the conductance for the Co/Cu system normalized to the conductance of pure Cu and the third is the conductance of the Ni/Cu system with the same normalization.

The material in the external leads is the same non-magnetic material used for the multilayers (e.g. Ag in Co/Ag multilayers). Tables 3.2 and 3.3 show the average value of the GMR ratio and the root mean square amplitude of oscillation around such value (Δ) for Co-based and Ni-based multilayers. To highlight the fact that GMR is an oscillatory function of the normal-metal thickness with an amplitude which decreases with increasing thickness, the tables also show the mean square oscillation calculated for non-magnetic metal layers thicknesses between 1-10 ($\Delta 1$). In the tables the subscripts indicate the number of atomic planes of the magnetic material layers. From the tables some general considerations can be made. The first important aspect is that the Co-based multilayers always present a GMR larger than their Ni-based counterparts. This confirms the result of the previous paragraph obtained for Cu and extends it to all the transition metals examined. It is important to note that the difference between Co/A and Ni/A multilayers is large when A belongs to the first two classes of non-magnetic materials (the ones represented by Cu, and Ag respectively), and is quite small when A is a *d*-conductor (ie Pd, Pt, Rh and Ir). Finally when A is a parabolic-like metal (Pb and Al) the GMR ratio is quite large for both Co-based and Ni-based multilayers, but also the oscillations are very large. The reasons for all these differences will be more clear when I present the conductances for the above multilayers in the different magnetic configurations.

Multilayer	GMR (%)	Δ (%)	Δ1 (%)	Δ/GMR (%)	Δ1/GMR (%)
Co_5/Cu	183.7	10.0	12.4	5.4	6.7
Co_5/Ag	153.7	9.5	13.1	6.1	8.5
Co_5/Pd	102.0	13.9	16.7	13.7	13.4
Co_5/Pt	104.1	10.9	15.6	10.5	15.0
Co_5/Au	98.8	20.4	33.6	20.6	34.0
Co_5/Rh	142.6	9.9	10.2	6.9	7.1
Co_5/Ir	143.6	12.8	14.4	8.9	10.1
Co_5/Pb	124.0	29.1	52.2	23.5	42.1
Co_5/Al	197.6	35.8	60.6	18.2	30.6
Co_{10}/Cu	150.7	9.2	9.2	6.1	6.1
Co_{10}/Ag	131.0	7.6	5.3	5.8	4.1
Co_{10}/Pd	165.2	31.1	32.2	18.8	19.4
Co_{10}/Pt	175.7	14.8	21.1	8.4	12.5
Co_{10}/Au	138.8	20.1	26.4	14.5	17.8
Co_{10}/Rh	171.9	15.1	18.7	8.7	10.9
Co_{10}/Ir	175.4	13.6	16.0	7.7	9.1
Co_{10}/Pb	154.7	25.2	40.9	16.3	26.4
Co_{10}/Al	169.6	35.7	56.4	21.1	33.3

Table 3.2: GMR ratio and GMR oscillations for different Co-based metallic multilayers.

Multilayer	GMR (%)	Δ (%)	Δ1 (%)	Δ/GMR (%)	Δ1/GMR (%)
Ni_{10}/Cu	29.1	2.9	3.3	10.1	11.3
Ni_{10}/Ag	35.8	2.8	2.0	7.9	5.6
Ni_{10}/Pd	100.2	10.8	16.2	10.8	16.2
Ni_{10}/Pt	94.3	10.6	18.4	11.2	19.5
Ni_{10}/Au	26.9	3.3	4.1	12.37	15.2
Ni_{10}/Rh	131.3	6.4	6.7	4.9	5.1
Ni_{10}/Ir	107.3	6.0	5.3	5.6	4.9
Ni_{10}/Pb	97.8	12.1	10.9	12.4	11.1
Ni_{10}/Al	107.7	19.7	29.4	18.3	27.3

Table 3.3: GMR ratio and GMR oscillations for different Ni-based metallic multilayers.

It is clear from table 3.2 that the GMR ratios depend quite sensitively on the multilayer geometry, i.e. on the layer thicknesses. This can be seen both from the values of Δ and from the fact that the GMR for Co thickness fixed at 5 atomic planes is generally larger than that obtained for a Co thickness of 10 atomic planes, with a relative difference up to 30%. As examples, figure 3.9 shows plots of the GMR ratio as a function of the non-magnetic metal layer thickness for the Co/Ag and Co/Pd systems. Nevertheless in all the cases (excluding Au, Al and Pb) the oscillations are small com-

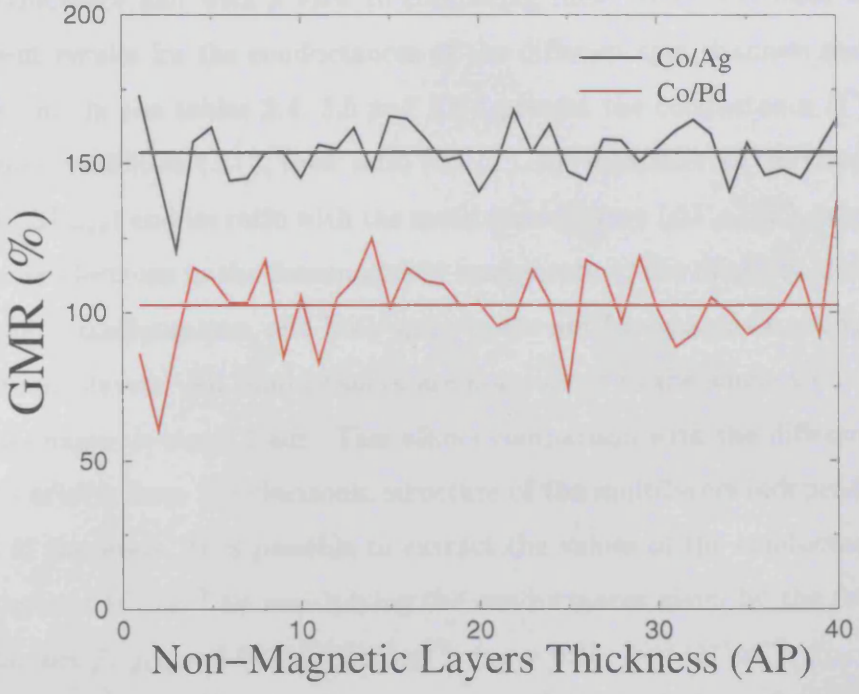

Figure 3.9: GMR as a function of the non-magnetic metal layer thickness for Co/Ag and Co/Pd. The horizontal lines denote the position of the average GMR.

pared to the long range oscillations observed experimentally [56, 86], suggesting that an additional contribution must be considered. This is most likely to arise from a periodic deviation from a perfect antiferromagnetic configuration, the possibility of which is neglected in the calculations. It is important to point out that perfect antiferromagnetic alignment of the multilayer in zero magnetic field is a consequence of the exchange coupling of the adjacent magnetic layers through the non-magnetic layer. The strength and phase of such coupling depends critically on the Fermi surface of the non-magnetic metal [3, 4, 5, 6]. To the best of my knowledge few experimental data are available for

the d-conductor multilayers Co/Pd and Co/Pt, for which the antiferromagnetic configuration may not be achievable. Nevertheless, even in the case that the exchange coupling is very weak, in a spin valve system an antiferromagnetic configuration can be always obtained by tuning the coercive fields of the different magnetic layers. This is achieved for instance by an appropriate choice of the spin valve geometry, or by using some magnetization pinning technique. Hence the theoretical predictions on Co/Pd and Co/Pt multilayers can in principle be tested in the spin valves.

The above results for the GMR ratio hide the material dependence of the electrical conductance and with a view to comparing these with their band structures, I now present results for the conductances of the different spin channels and of the AF configuration. In the tables 3.4, 3.5 and 3.6 I present the conductance (Γ), the mean conductance oscillation ($\Delta\Gamma$), their ratio ($\Delta\Gamma/\Gamma$), the maximum of the conductance oscillations ($\Delta\Gamma_{max}$) and its ratio with the mean conductance ($\Delta\Gamma_{max}/\Gamma$), respectively for the majority electrons in the ferromagnetic configuration, the minority electrons in the ferromagnetic configuration, and both spins in the antiferromagnetic configuration, for Co-based multilayers. All conductances are normalized to the single-spin conductance of the non-magnetic-metal leads. This allows comparison with the different scattering properties arising from the electronic structure of the multilayers independently of the material of the leads. It is possible to extract the values of the conductance per unit area in units of $\Omega^{-1}m^{-2}$ by multiplying the conductances given by the following conversion factors f: $f_{Cu} = 0.61 \cdot 10^{15}\ \Omega^{-1}m^{-2}$, $f_{Ag} = 0.45 \cdot 10^{15}\ \Omega^{-1}m^{-2}$, $f_{Au} = 0.47 \cdot 10^{15}\ \Omega^{-1}m^{-2}$, $f_{Pd} = 0.73 \cdot 10^{15}\ \Omega^{-1}m^{-2}$, $f_{Pt} = 0.83 \cdot 10^{15}\ \Omega^{-1}m^{-2}$, $f_{Rh} = 1.18 \cdot 10^{15}\ \Omega^{-1}m^{-2}$, $f_{Ir} = 0.97 \cdot 10^{15}\ \Omega^{-1}m^{-2}$, $f_{Al} = 1.49 \cdot 10^{15}\ \Omega^{-1}m^{-2}$, $f_{Pb} = 0.52 \cdot 10^{15}\ \Omega^{-1}m^{-2}$. Note that the absolute values of conductance per unit area are consistent with *ab initio* calculations for infinite superlattices in the ballistic regime [49, 50]. The tables 3.4-3.6 illustrate that, with some exceptions, materials belonging to the same class have similar normalized conductances. For Cu and Ag the majority (minority) band is a high (low) transmission band, leading to a large GMR ratio for such materials. The majority bands of these two materials match that of Co and there is little interband scattering (even less in Ag where the electrons at the Fermi energy are completely sp). By contrast, the minority carriers are subject to a large scattering potential due to the difference between the on-site energies of the d-band. They are also subject to large

inter-band scattering because of almost pure d-character of the minority carriers in Co. The presence of an high transmission band together with a low transmission one is the reason for the large GMR in those systems.

Multilayer	Γ	$\Delta\Gamma$	$\Delta\Gamma/\Gamma$ (%)	$\Delta\Gamma_{max}$	$\Delta\Gamma_{max}/\Gamma$ (%)
Co_{10}/Cu	0.59	$5.33 \cdot 10^{-3}$	0.90	$1.06 \cdot 10^{-2}$	1.81
Co_{10}/Ag	0.63	$4.37 \cdot 10^{-3}$	0.69	$1.31 \cdot 10^{-2}$	2.06
Co_{10}/Pd	0.33	$8.89 \cdot 10^{-3}$	2.67	$2.05 \cdot 10^{-2}$	6.14
Co_{10}/Pt	0.37	$5.02 \cdot 10^{-3}$	1.37	$1.25 \cdot 10^{-2}$	3.41
Co_{10}/Au	0.24	$1.05 \cdot 10^{-2}$	4.42	$3.69 \cdot 10^{-2}$	15.53
Co_{10}/Rh	0.17	$6.13 \cdot 10^{-3}$	3.61	$2.63 \cdot 10^{-2}$	15.47
Co_{10}/Ir	0.17	$9.91 \cdot 10^{-3}$	5.73	$4.00 \cdot 10^{-2}$	23.17
Co_{10}/Pb	0.15	$6.90 \cdot 10^{-3}$	4.54	$1.56 \cdot 10^{-2}$	10.30
Co_{10}/Al	0.12	$1.07 \cdot 10^{-2}$	9.26	$4.64 \cdot 10^{-2}$	40.17

Table 3.4: Conductance and conductance oscillations for different Co-based metallic multilayers: majority band. The conductance of each multilayer is normalized to the conductance of the corresponding non-magnetic metal, which composes the leads.

Multilayer	Γ	$\Delta\Gamma$	$\Delta\Gamma/\Gamma$ (%)	$\Delta\Gamma_{max}$	$\Delta\Gamma_{max}/\Gamma$ (%)
Co_{10}/Cu	0.32	$1.08 \cdot 10^{-3}$	3.38	$2.82 \cdot 10^{-2}$	8.80
Co_{10}/Ag	0.32	$1.75 \cdot 10^{-2}$	5.54	$5.73 \cdot 10^{-2}$	18.15
Co_{10}/Pd	0.16	$1.56 \cdot 10^{-2}$	9.78	$3.50 \cdot 10^{-2}$	21.14
Co_{10}/Pt	0.19	$9.02 \cdot 10^{-3}$	4.71	$2.63 \cdot 10^{-2}$	13.73
Co_{10}/Au	0.16	$9.60 \cdot 10^{-3}$	5.95	$2.34 \cdot 10^{-2}$	14.53
Co_{10}/Rh	0.25	$6.36 \cdot 10^{-3}$	2.50	$1.60 \cdot 10^{-2}$	6.29
Co_{10}/Ir	0.31	$8.46 \cdot 10^{-3}$	2.75	$3.41 \cdot 10^{-2}$	11.14
Co_{10}/Pb	0.17	$8.66 \cdot 10^{-3}$	4.95	$1.97 \cdot 10^{-2}$	11.24
Co_{10}/Al	0.16	$1.49 \cdot 10^{-2}$	9.08	$7.55 \cdot 10^{-2}$	45.98

Table 3.5: Conductance and conductance oscillations for different Co-based metallic multilayers: minority band. The conductance of each multilayer is normalized to the conductance of the corresponding non-magnetic metal, which composes the leads.

Turning the attention to the d-conductors it is easy to note that Pd and Pt have almost identical behaviour, which differs from the behaviour of Rh and Ir. The general feature of all the d-conductors is that the conductances in the majority spin band are highly suppressed with respect to the case of Ag and Cu. The on-site energies of the majority band of Co, Pd, Pt, Rh and Ir are roughly the same, ensuring a

Multilayer	Γ	$\Delta\Gamma$	$\Delta\Gamma/\Gamma$ (%)	$\Delta\Gamma_{max}$	$\Delta\Gamma_{max}/\Gamma$ (%)
Co_{10}/Cu	0.18	$6.40 \cdot 10^{-3}$	3.51	$1.62 \cdot 10^{-2}$	8.94
Co_{10}/Ag	0.21	$5.10 \cdot 10^{-3}$	2.46	$1.06 \cdot 10^{-2}$	5.17
Co_{10}/Pd	$9.41 \cdot 10^{-2}$	$1.09 \cdot 10^{-2}$	11.62	$3.15 \cdot 10^{-2}$	33.45
Co_{10}/Pt	0.10	$4.77 \cdot 10^{-3}$	4.69	$1.43 \cdot 10^{-2}$	14.12
Co_{10}/Au	$8.40 \cdot 10^{-2}$	$6.95 \cdot 10^{-3}$	8.27	$1.66 \cdot 10^{-2}$	19.77
Co_{10}/Rh	$7.81 \cdot 10^{-2}$	$4.14 \cdot 10^{-3}$	5.30	$8.76 \cdot 10^{-3}$	11.21
Co_{10}/Ir	$8.73 \cdot 10^{-2}$	$4.75 \cdot 10^{-3}$	5.43	$1.59 \cdot 10^{-2}$	18.30
Co_{10}/Pb	$6.47 \cdot 10^{-2}$	$6.29 \cdot 10^{-3}$	9.72	$2.04 \cdot 10^{-2}$	31.50
Co_{10}/Al	$5.28 \cdot 10^{-2}$	$8.01 \cdot 10^{-3}$	15.15	$3.05 \cdot 10^{-2}$	57.80

Table 3.6: Conductance and conductance oscillations for different Co-based metallic multilayers: AF configuration. The conductance of each multilayer is normalized to the conductance of the corresponding non-magnetic metal, which composes the leads.

good band match. Nevertheless, the width of the *d*-majority band of Co is associated with hybridization of *s*-, *p*-, and *d*-electrons, while the *d*-conductor bands are only *d*-like. Hence, a strong inter-band scattering is present in the majority band of Co/Pd, Co/Pt, Co/Rh and Co/Ir superlattices. As far as the minority bands are concerned, the behaviour of Pd and Pt is quite different from that of Rh and Ir. Co/Pt and Co/Pd multilayers present a small conductance in the minority band, while it is quite large in Co/Rh and Co/Ir multilayers. This leads to the remarkable fact that the spin polarization of the carriers has opposite sign in Co/Pd and Co/Pt than in Co/Rh and Co/Ir. The spin-polarization is usually defined as

$$P = \frac{\Gamma^{\uparrow}_{FM} - \Gamma^{\downarrow}_{FM}}{\Gamma^{\uparrow}_{FM} + \Gamma^{\downarrow}_{FM}} , \tag{3.9}$$

where Γ^{σ} is the spin σ conductance. For the above materials, the spin-polarizations are $P_{Co/Pd} = 0.35$, $P_{Co/Pt} = 0.32$, $P_{Co/Rh} = -0.20$ and $P_{Co/Ir} = -0.28$. This result is quite important because it shows that the spin-polarization of a multilayer does not depend solely on the spin-polarization of the magnetic layers, but is a general property of the whole structure. The reason of the different conductances in the minority bands of multilayers formed from *d*-conductors is in the details of the band structure. In general one would expect the minority band to be an high transmission band in *d*-conductor based multilayers. Nevertheless the position of the Fermi energy with respect to the band center of the *d*-band is quite different in the different materials. In the minority band of Co, Rh and Ir (see figure 3.10 for Rh and Ir) the Fermi energy is well within the *d*-band and in particular it lies to the left of the large peak in the density of states

at the d-band edge. On the contrary the Fermi energy in Pd and Pt lies to the right of the d-band edge. This means that the curvature of the d-band at the Fermi energy is very different for Rh and Ir and for Pd and Pt. This explains the differences in the conductances. The multilayers formed from the parabolic-like conductors and from

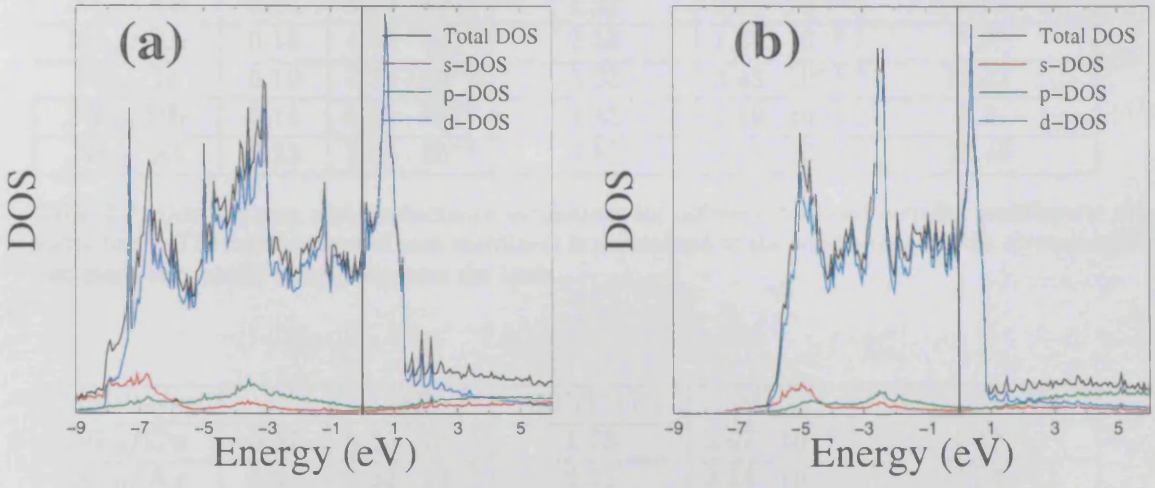

Figure 3.10: Partial DOS for Ir (a) and Rh (b). Note the position of the Fermi energy with respect to the peak of the d-band.

Au lie somewhat outside the above picture. All the conductances are usually quite small (particularly for Pb and Al) and the oscillations are very large. This is not surprising if one considers the tight-binding parameters used. Both the on-site energies and the hopping integrals of Au, Al and Pb are quite different with respect to Co. This leads to large scattering potentials and therefore to large oscillations. Two important aspects must be pointed out. First the large difference between hopping parameters can break down the geometric mean approximation that I have used to describe an interface between different materials. Secondly Co/Au, Co/Al and Co/Pb are multilayers formed from materials with quite large lattice mismatch. In reality the interfaces are likely to present a large amount of defects and a more realistic description would be useful.

Attention is now turned to the Ni-based multilayers. The conductances for all the multilayers are presented in the tables 3.7, 3.8 and 3.9, where I used the same normalization as before.

Multilayer	Γ	$\Delta\Gamma$	$\Delta\Gamma/\Gamma$ (%)	$\Delta\Gamma_{max}$	$\Delta\Gamma_{max}/\Gamma$ (%)
Ni_{10}/Cu	0.66	$4.26 \cdot 10^{-3}$	0.64	$9.51 \cdot 10^{-3}$	1.43
Ni_{10}/Ag	0.69	$5.81 \cdot 10^{-3}$	0.84	$2.27 \cdot 10^{-2}$	3.27
Ni_{10}/Pd	0.26	$9.26 \cdot 10^{-3}$	3.51	$2.16 \cdot 10^{-2}$	8.19
Ni_{10}/Pt	0.28	$6.01 \cdot 10^{-3}$	2.15	$1.88 \cdot 10^{-2}$	6.74
Ni_{10}/Au	0.64	$8.35 \cdot 10^{-3}$	1.31	$2.80 \cdot 10^{-2}$	4.41
Ni_{10}/Rh	0.18	$4.58 \cdot 10^{-3}$	2.53	$1.31 \cdot 10^{-2}$	7.27
Ni_{10}/Ir	0.19	$7.76 \cdot 10^{-3}$	3.93	$3.43 \cdot 10^{-2}$	17.37
Ni_{10}/Pb	0.14	$6.25 \cdot 10^{-3}$	4.43	$1.19 \cdot 10^{-2}$	8.5
Ni_{10}/Al	0.13	$1.04 \cdot 10^{-2}$	7.87	$3.50 \cdot 10^{-2}$	26.46

Table 3.7: Conductance and conductance oscillations for different Ni-based metallic multilayers: majority band. The conductance of each multilayer is normalized to the conductance of the corresponding non-magnetic metal, which composes the leads.

Multilayer	Γ	$\Delta\Gamma$	$\Delta\Gamma/\Gamma$ (%)	$\Delta\Gamma_{max}$	$\Delta\Gamma_{max}/\Gamma$ (%)
Ni_{10}/Cu	0.47	$8.35 \cdot 10^{-3}$	1.78	$2.07 \cdot 10^{-2}$	4.42
Ni_{10}/Ag	0.43	$9.32 \cdot 10^{-3}$	2.15	$3.14 \cdot 10^{-2}$	7.23
Ni_{10}/Pd	0.54	$2.75 \cdot 10^{-2}$	5.07	$7.81 \cdot 10^{-2}$	14.40
Ni_{10}/Pt	0.52	$2.15 \cdot 10^{-2}$	4.15	$5.35 \cdot 10^{-2}$	10.36
Ni_{10}/Au	0.49	$7.96 \cdot 10^{-3}$	1.62	$2.51 \cdot 10^{-2}$	5.10
Ni_{10}/Rh	0.51	$8.26 \cdot 10^{-3}$	1.62	$1.96 \cdot 10^{-2}$	3.84
Ni_{10}/Ir	0.49	$7.90 \cdot 10^{-3}$	1.59	$2.76 \cdot 10^{-2}$	5.57
Ni_{10}/Pb	0.16	$9.07 \cdot 10^{-3}$	5.51	$2.71 \cdot 10^{-2}$	16.49
Ni_{10}/Al	0.11	$9.29 \cdot 10^{-3}$	8.67	$3.61 \cdot 10^{-2}$	33.69

Table 3.8: Conductance and conductance oscillations for different Ni-based metallic multilayers: minority band. The conductance of each multilayer is normalized to the conductance of the corresponding non-magnetic metal, which composes the leads.

Multilayer	Γ	$\Delta\Gamma$	$\Delta\Gamma/\Gamma$ (%)	$\Delta\Gamma_{max}$	$\Delta\Gamma_{max}/\Gamma$ (%)
Ni_{10}/Cu	0.44	$8.07 \cdot 10^{-3}$	1.84	$1.88 \cdot 10^{-2}$	4.30
Ni_{10}/Ag	0.42	$8.18 \cdot 10^{-3}$	1.97	$2.19 \cdot 10^{-2}$	5.28
Ni_{10}/Pd	0.20	$6.18 \cdot 10^{-3}$	3.07	$1.81 \cdot 10^{-2}$	8.98
Ni_{10}/Pt	0.20	$6.16 \cdot 10^{-3}$	3.00	$2.73 \cdot 10^{-2}$	13.34
Ni_{10}/Au	0.44	$7.95 \cdot 10^{-3}$	1.79	$2.27 \cdot 10^{-2}$	5.11
Ni_{10}/Rh	0.15	$3.87 \cdot 10^{-3}$	2.59	$7.84 \cdot 10^{-3}$	5.25
Ni_{10}/Ir	0.17	$4.47 \cdot 10^{-3}$	2.67	$1.51 \cdot 10^{-2}$	9.06
Ni_{10}/Pb	$7.74 \cdot 10^{-2}$	$5.04 \cdot 10^{-3}$	6.51	$1.36 \cdot 10^{-2}$	17.55
Ni_{10}/Al	$5.83 \cdot 10^{-2}$	$7.61 \cdot 10^{-3}$	13.06	$2.59 \cdot 10^{-2}$	44.40

Table 3.9: Conductance and conductance oscillations for different Ni-based metallic multilayers: AF configuration. The conductance of each multilayer is normalized to the conductance of the corresponding non-magnetic metal, which composes the leads.

Most of the features of Co-based multilayers can also be found in Ni-based multilayers. From the tables it is very clear that the conductances for the Ni-based multilayers are generally higher than the conductances for their Co-based counterparts. This is particularly true for the majority band of Ni/Cu, Ni/Ag and Ni/Au and for the minority band of Ni/Pd, Ni/Pt, Ni/Ir and Ni/Rh. Moreover in the case of Ni/Cu, Ni/Ag and Ni/Au also the conductance of the minority band is quite large giving rise to a small spin-polarization ($P_{\mathrm{Ni/Cu}} = 0.17$, $P_{\mathrm{Ni/Ag}} = 0.23$, $P_{\mathrm{Ni/Au}} = 0.13$) and consequently to small a GMR ratio (see table 3.2). In the case of *d*-conductors Ni/Pd and Ni/Pt have the same spin-polarization as Ni/Rh and Ni/Ir and in all the four cases it is negative ($P_{\mathrm{Ni/Pd}} = -0.34$, $P_{\mathrm{Ni/Pt}} = -0.30$, $P_{\mathrm{Ni/Rh}} = -0.48$, $P_{\mathrm{Ni/Ir}} = -0.43$). This reflects the fact that in the minority band of Ni the Fermi energy lies exactly at the peak of the *d*-region of the DOS (close to the band edge). Therefore the dispersion of the *d*-band is not largely different from that of both Pd, Pt and Rh, Ir. This is an important result and suggests that Ni can be used in conjunction with *d*-conductors to form multilayers with large GMR ratio. Finally one can note that also in the case of Ni, multilayers formed from Al and Pb present low conductances and large oscillations. The same considerations made for Co-based multilayers are still valid.

To conclude this section I will discuss the relevance of the present calculations to experiments. The results obtained for Co/Cu and Co/Ag multilayers are well consistent with the largest experimental values for CPP GMR [13, 58, 67] and also with *ab initio* calculations [49, 50]. This result is surprisingly good if one considers that in actual multilayers a perfect antiferromagnetic configuration is difficult to achieve [87]. Nevertheless it is important to bear in mind that the calculations are for ballistic disorder-free systems and that the disorder can alter the present picture. The effect of disorder will be discussed in the Chapter 5.

CPP GMR measurements exist also for Co/Au point contacts [71] where one expects to reproduce closely the results obtained from a ballistic calculation. Nevertheless in such a measurement the point contacts yield I/V curves which are typical of a diffusive regime. Moreover the system appears granular with the presence of paramagnetic clusters. All this information suggests that in such a system inelastic scattering dominates, and therefore the conductance regime is very far from ballistic.

As far as multilayers based on *d*-conductors are concerned very little experimental work has been done [69, 72, 86] and none in the CPP configuration or with Ni. On the theoretical side *ab initio* transport calculations have been carried out [68]. The GMR ratios found for Co/Pd and Co/Rh are smaller than the ones computed here. The reason is that in reference [68] very thin magnetic layers are considered and therefore the spin filtering is not efficient (see the dependence of GMR on the magnetic layers thickness of figure 3.8). More experimental work on multilayers based on *d*-conductors, particularly built with Ni as magnetic materials would be welcome.

3.4 TMR

In this last section I will discuss some preliminary calculations on tunneling junctions. My aim is to show that the scattering technique developed in the previous chapters is able to deal with a tunneling problem and to show that a realistic description of ballistic tunnel junctions may be given. The structure I want to simulate is a Co-based tunnel junction attached to two semi-infinite crystalline Cu leads, namely the structure Cu/Co/INS/Co/Cu, where INS denotes the insulator. The magnetizations of the Co layers may have either a perfect ferromagnetic or antiferromagnetic alignment. Note that the presence of the Cu leads reproduces correctly the typical experimental situation in which the magnetic layers do not form the electrical contacts.

I used for Cu and Co the same parameterization used for the case of GMR, while for INS I have taken the parameterization shown in the tables of Appendix D (see figure 3.11). For all the simulations I considered perfect translational invariance in the transverse plane and used 150×150 $k_{||}$-points in the 2D Brillouin zone. An important problem that one has to face when calculating the tunneling current is that, due to the small value of the transmission coefficient, the violation of the unitarity of the S matrix due to numerical errors may be of the same order of the transmission coefficient itself. If this happens the error in the calculated tunneling current is larger than the current itself and the calculation is meaningless. To avoid this problem I performed the following test. For each $k_{||}$-point I compared the transmission coefficient $T(k_{||})$ with the following measurement of violation of unitarity $\delta(k_{||}) = |N(k_{||}) - R(k_{||}) - T(k_{||})|$, where $R(k_{||})$ and $N(k_{||})$ are respectively the reflection coefficient and the number of open scattering channels. In the case $\delta > 1/10T$ I rejected the corresponding T. Surprisingly

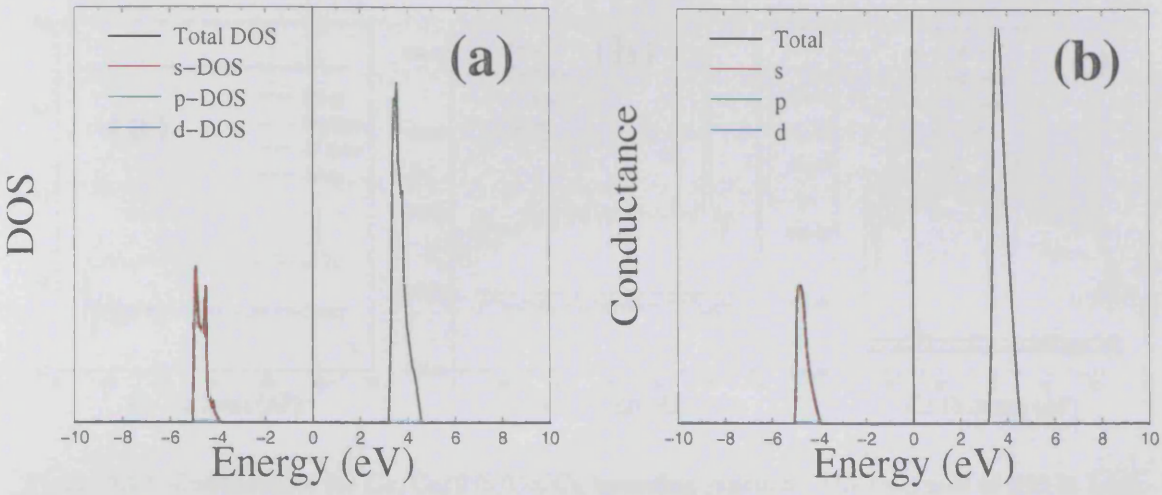

Figure 3.11: Partial DOS (a) and partial conductance (b) for the fcc insulator used in the calculation. The vertical line denotes the position of the Fermi energy.

the conductance obtained with this procedure differs by less than 1% with respect to the conductance calculated keeping all the transmission coefficients. This means that the transmission coefficients which significantly contribute to the conductance are calculated with good accuracy.

In figure 3.12 I present the different spin conductances for a junction in which the thickness of the first Co layer is fixed to 50 atomic planes, the thickness of the insulator is respectively 1,2, and 3 atomic planes and the thickness of the second Co layer is varied between 5 and 55 atomic planes. In the antiferromagnetic case I present either the majority or the minority electrons (with respect to the magnetization of the first Co layer), which show very similar conductances even if the oscillating patterns are quite different. The most important feature of figure 3.12 is that, on the one hand when the thickness of the insulator is one atomic plane the conductance in the ferromagnetic configuration is dominated by the majority electrons with a polarization of $P_1 = 0.34$ (the subscript labels the INS thickness), on the other hand when the INS thickness is larger than one atomic plane, the minority electrons dominate the conductance with polarizations $P_2 = -0.33$ and $P_3 = -0.7$. The polarization for one atomic plane of INS is close to the polarization found for Co/Cu multilayers ($P_{Co/Cu} = 0.30$) and, since the conductance is large (the normalized conductance is $\Gamma = 0.45$ for the majority spins), I conclude that the transport is mainly via direct current and the tunneling component is very suppressed.

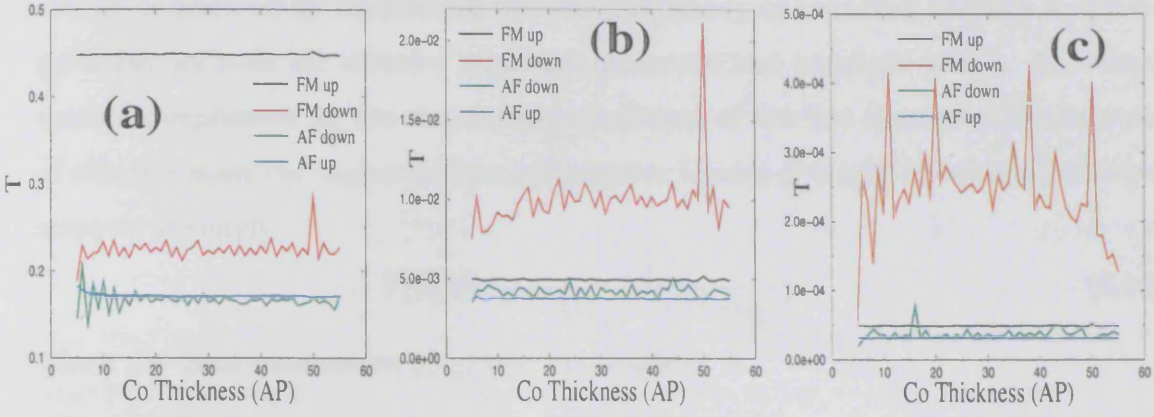

Figure 3.12: Conductance for Cu/Co/INS/Co/Cu tunneling junction. The thickness of INS is 1 (a), 2 (b) and 3 (c) atomic planes. In the AF configuration the spin-direction is given with respect to the first Co layer.

The situation when the thickness of the insulator is larger than one atomic plane is very different. In such a case the transmission is generally very small and decays exponentially with the INS thickness (as expected from the elementary tunneling theory). In figure 3.13 I present the normalized transmission coefficient for the majority and minority spins as a function of the thickness of the insulator and the corresponding spin-polarization of the tunneling junction. Note that while the transmission coefficient decays exponentially (the scale is logarithmic) the polarization first increases (becomes more negative) and finally saturates at a value close to -1 for thick barriers. This effect

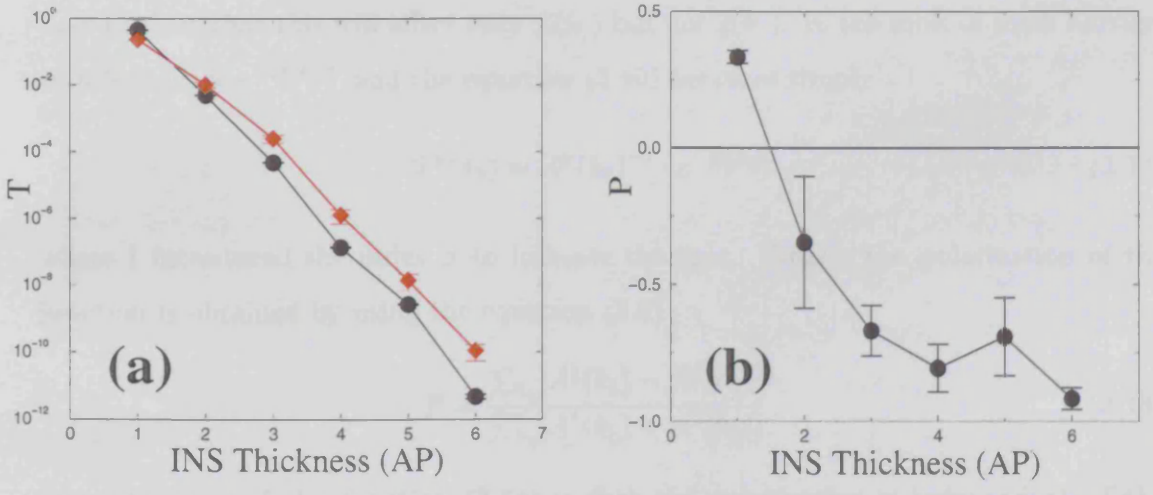

Figure 3.13: Transmission coefficient (a) and polarization (b) of Cu/Co/INS/Co/Cu tunneling junctions as a function of INS thickness. The thickness of the right-hand side Co layer is varied from 1AP to 55AP and each point corresponds to the average value over these thicknesses.

can be understood by considering the standard theory of tunneling through a rectangular barrier with the effective mass approximation and parabolic bands. The usual textbook expression for the transmission coefficient of two free electron normal metals of effective mass $m_{\rm N}$ separated by a rectangular barrier of height U_o with an effective mass $m_{\rm I}$ is simply

$$T(k_{||}) = \frac{1}{1 + A(k_{||}) \cdot \sinh^2[q(k_{||})l]} , \tag{3.10}$$

where the quasi-momentum $q(k_{||})$ into the insulator is

$$q(k_{||}) = \frac{1}{\hbar}\sqrt{2m_{\rm I}^*(U_o - E_{\rm F}) + k_{||}^2} , \tag{3.11}$$

and the coefficient $A(k_{||})$

$$A(k_{||}) = \frac{\left[2m_{\rm I}m_{\rm N}^2(U_o - E_{\rm F}) + 2m_{\rm I}^2 m_{\rm N}E_{\rm F} - k_{||}^2(m_{\rm I}^2 + m_{\rm N}^2)\right]^2}{4m_{\rm I}^2m_{\rm N}^2\left[2m_{\rm N}E_{\rm F} - k_{||}^2\right]\left[2m_{\rm I}(U_o - E_{\rm F}) - k_{||}^2\right]} . \tag{3.12}$$

The total conductance is simply given by the sum of all the transmission coefficients $T(k_{||})$ over the 2D transverse Brillouin zone. The important point of equation (3.10) is that the decay of the transmission coefficient with the insulator thickness l is solely determined by the quasi-momentum q. In the present case this yields to the well known fact that the transmission is largest at the Γ point and decays exponentially far away from it (note that in the parabolic case the quasi-momentum q is a function only of $k_{||}^2$). Moreover if one introduces an exchange field between the two spin sub-bands it is easy to show that this will affect only $A(k_{||})$ but not $q(k_{||})$. In the limit of thick barriers $\sinh^2[q(k_{||})l] \propto e^{-2q(k_{||})l}$ and the equation (3.10) becomes simply

$$T^\sigma(k_{||}) = A^\sigma(k_{||})^{-1} \cdot e^{-2q(k_{||})l} , \tag{3.13}$$

where I introduced the index σ to indicate the spin. Finally the polarization of the junction is obtained by using the equation (3.9)

$$P = \frac{\sum_{k_{||}}[A^\downarrow(k_{||}) - A^\uparrow(k_{||})]}{\sum_{k_{||}}[A^\uparrow(k_{||}) + A^\downarrow(k_{||})]} . \tag{3.14}$$

The key point of the equation (3.14) is that the polarization is independent of the thickness of the barrier and this reflects the fact the the same decaying factor $e^{-2q(k_{||})l}$ is present both for the majority and the minority spin-current.

Nevertheless the model considered is highly ideal and the band structure of real transition metals can be very different from parabolic. The crucial point is that in general the quasi-momentum q can be a complicated function of $k_{||}$, which depends on the insulator. In particular q can be different for electrons with different atomic orbital components. Note that different values of q for different atomic orbital components means that there are different effective barriers for different bands. For instance one can imagine the situation in which q for electrons with a strong s-component is larger than q for electrons with a strong d-component. In this case of a thick enough barrier the contribution to the current will come mainly from the d-electrons and consequently it will be given by the d-electrons only. Moreover the polarization will change by changing the barrier thickness because the cancellation of the exponential terms, yielding the equation (3.14), will not occur. Finally for very thick barriers the polarization will saturate to either the value 1 or -1, depending on which of the two spin-electrons has the largest exponential decay. This last result is crucial because it means that for disorder-free tunnel junctions the polarization increases with the barrier thickness and it is complete for very thick barriers. Therefore I predict that for large disorder-free barriers the TMR ratio of a tunneling junction is either $+\infty$ or $-\infty$. Nevertheless it is also important to note that if the barrier is disordered, tunneling through localized states in the barrier is possible. This process may be largely spin-independent [19, 20] resulting in a global reduction of the polarization of the junction.

To prove that q can be a non-trivial function of $k_{||}$ in figure 3.14 and 3.15 I show the transmission coefficient $T(k_x, k_y)$ for the Cu/Co/INS/Co/Cu junction as a function of k_x and k_y in the first Brillouin zone, respectively for the majority and minority spin. The two distributions of T in the Brillouin zone look very different. On the one hand the one for majority spins shows spherical symmetry around the Γ point, highlighting a quasi-parabolic behaviour. On the other hand the distribution for the minority spins shows a remarkable resonant signature of the intricate band structure of the d-band at the Fermi energy. This very different behaviour of the transmission coefficient is a property of the insulator that therefore affects in a crucial way the polarization of the junction.

To conclude this section I want to compare the result obtained above with other existing theories. In particular Tsymbal and Pettifor [78] showed that the polarization

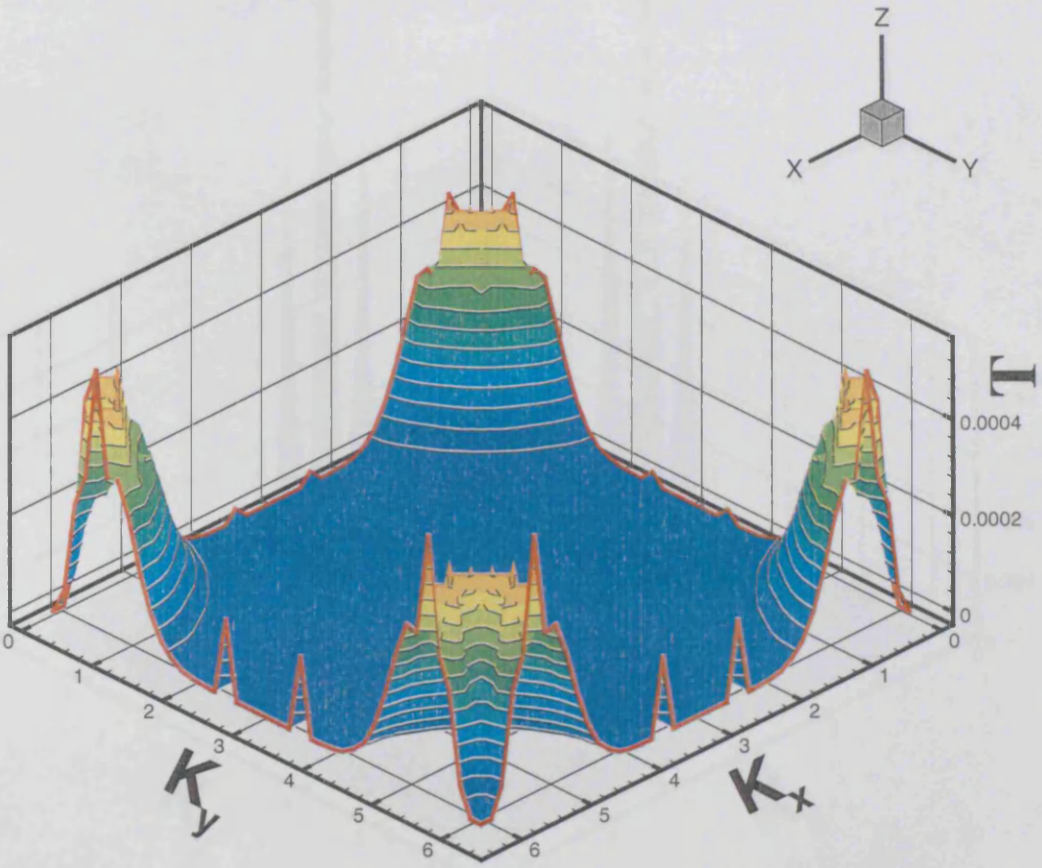

Figure 3.14: $T(k_x, k_y)$ for Cu/Co/INS/Co/Cu tunneling junction: majority spins.

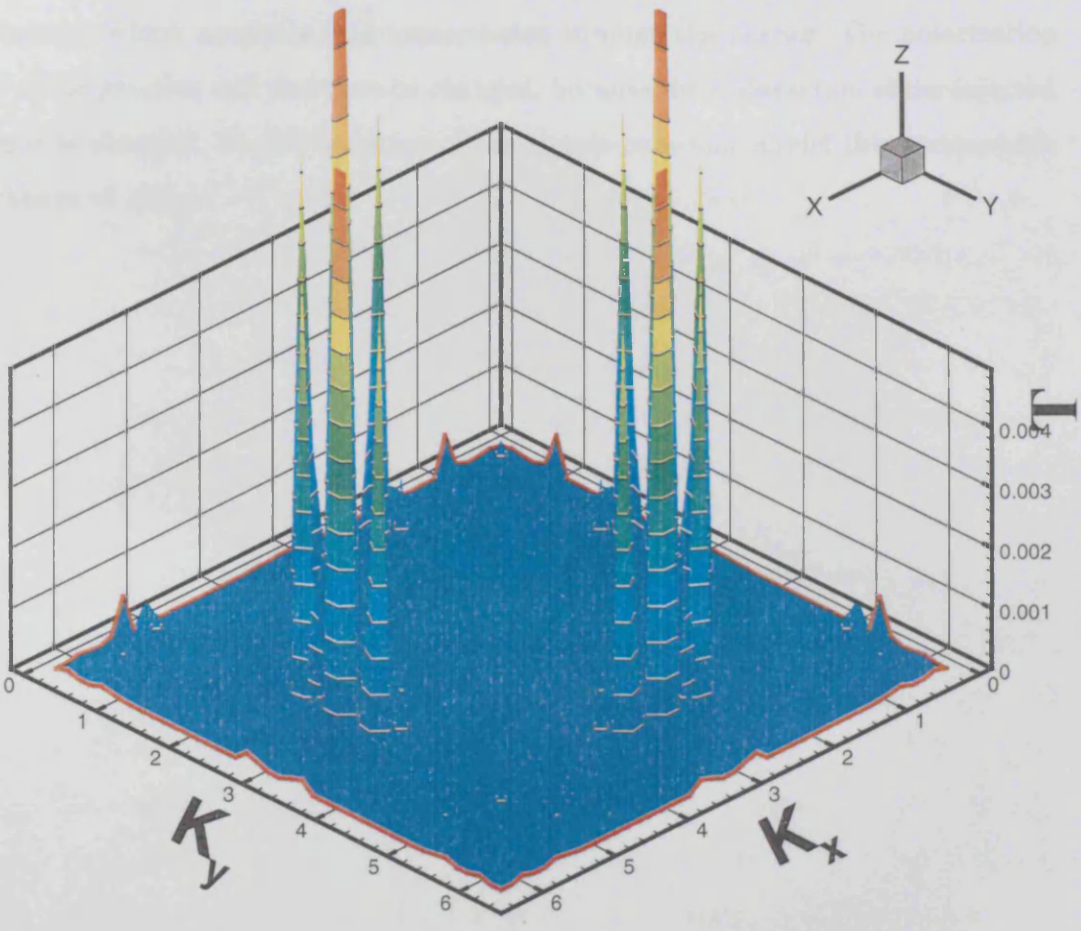

Figure 3.15: $T(k_x, k_y)$ for Cu/Co/INS/Co/Cu tunneling junction: minority spins.

can be changed by varying the coupling between the insulator and the magnetic electrodes while keeping constant the parameters of the insulator itself. In that case the barrier is not changed and the decay of the wave-function within the barrier will not vary. Nevertheless by changing the coupling between the magnetic electrodes and the barrier, the local density of state at the surface of the barrier is changed. This results in a change of the polarization of the electrons approaching the barrier, or at least of that fraction which possesses high transmission through the barrier. The polarization of the whole junction will therefore be changed, because the polarization of the injected electrons is changed. In the language of the simple-parabolic model this corresponds to a change of $A(k_{||})$.

4 Conductance Oscillations

4.1 Introduction

One of the results of the previous chapter was that the spin-conductance and the GMR ratio are oscillating functions of the thickness of the layers forming the multilayer. These oscillations are larger when large scattering is present even if they cannot take into account the large-amplitude long-period oscillations of GMR found in experiments. These latter are due to a periodic variation of the exchange coupling between adjacent magnetic layers, which results in the absence of the antiferromagnetic alignment of the multilayer for certain layers thicknesses. The magnetic configuration in zero magnetic field will not always be antiferromagnetic and the corresponding conductance will not be that of the antiferromagnetic configuration. In the extreme case in which in zero magnetic field a ferromagnetic configuration is present instead of an antiferromagnetic one, the GMR ratio will vanish. Therefore the oscillations of the GMR ratio only reflect the fact that for some layer thicknesses the antiferromagnetic configuration does not exist.

Recently a new set of measurements on Ni/Co [88, 89, 90, 91] multilayers revealed the possibility of long-period oscillations of the conductance of a different origin, whereas, measurements on Ag/Pd [91], Ag/Au and Ag/Cu [92] multilayers have not shown any long-period oscillations. On the one hand, the Ag based multilayers are entirely non-magnetic. On the other, the Ni/Co multilayers were measured in high magnetic field, far above the coercive field of the structure, which rules out magnetic misalignment between magnetic layers as source of the oscillations. In these experiments, all the measurements were conducted with the current in plane (CIP) configuration and to-date, no measurements have been carried out in the CPP configuration.

One of the possible explanations of such puzzling experiments is the formation of quantum wells in all or only few of the bands due to the multilayer structure. The quantum well theory has been used in the past for describing the oscillations of the exchange coupling [5, 6, 93], and to correlate such oscillations with the oscillations of the CPP conductance [94, 95]. All the calculations have been carried out by considering a trilayer because in this case the treatment is simplified and analytic calculations can be carried out. The central result of this approach is that the conductance and the

exchange coupling oscillate with periods that depend only on the Fermi surface of the materials involved, the superlattice structure being neglected.

In this chapter I will study in detail the oscillations of the conductance in a multilayer and show that the oscillation periods are not only a function of the Fermi surface of the materials forming the multilayer, but also a function of the geometry of the multilayer. The calculations are carried out in the CPP configuration where at present no experimental data exist and predictions for future experiments will be made. First I will calculate the conductance for disorder-free Ni/Co and Ag/Pd multilayers, where the layer thickness fluctuates randomly. This will provide quantitative description of the conductance fluctuations in the CPP geometry for real multilayers.

Secondly I will introduce a free electron model within the effective mass approximation and Krönig-Penney potential. This simple model has the advantage of giving a clear interpretation of the numerical results and provides a simple expression for the relevant oscillation periods. The long period oscillations of the conductance will emerge to be the result of beating between the Fermi wave-vector and a class of wave-vectors characteristic of the superlattice structure. A completely analytic description of the system and a formula to calculate the conductance will be given.

Finally, leaving the problem of the oscillations, I will use the simple model to rediscuss the material dependence of GMR and in particular on the different dispersion relations between different materials. Even in this case the model gives a good qualitative understanding of the general mechanism leading to the scattering, even though it will not capture all the details of the transition metals. This leads to a better model which will be developed in the next chapter.

4.2 Real Material Simulations

In this section I consider the conductance of Ni/Co and Ag/Pd multilayers in the CPP configuration. I use the same tight-binding parameterization used in the previous chapter [84] and assume that in the case of Ni/Co a perfect ferromagnetic alignment of both Co and Ni is achieved. Furthermore I consider complete translational invariance and completely clean interfaces. Note that this assumption is particularly good in the case of Co and Ni which do not mix at the interface, but breaks down in the case of Ag and Pd which are quite miscible [91]. The conductance is therefore given by summing

up the spin-dependent, $k_{||}$-dependent transmission coefficients $T^{\sigma}(k_{||})$ as indicated in equation (3.2). In what follows, I employ as in the previous chapter 8100 $k_{||}$-points, which is sufficient to render effects due to the finite number of $k_{||}$-points negligible compared with the oscillations of interest.

The same analysis used in Chapter 3 to interpret the conductance results in term of band structures mismatch can also be used here. It should be noted that the majority bands of Ni and Co are dominated by *sp*-electrons and are closely aligned (see figure 3.1). On the other hand the minority bands are *d*-like and possess a relative shift in energy of about 0.7 eV. Hence one expects a large contribution to the conductance from the majority channel and a small contribution from the minority channel. For the same reason the oscillations of the conductance are expected to be larger in the minority spin sub-bands than in the majority.

For Ag/Pd the situation is qualitatively different (see figures 3.4 and 3.5), because at the Fermi energy the DOS of Ag is dominated by *sp*-electrons, while in Pd it is dominated by *d*-electrons. As a consequence one expects at the interfaces, together with a scattering potential in the *d*-band, a strong inter-band scattering. In summary, despite the scattering mechanisms at the interface looking different, both Ni/Co and Ag/Pd multilayers are constituted by two metals whose band match gives rise to an effective periodic scattering potential.

Following reference [54, 96], I consider a pseudorandom layer arrangement, in which a finite A/B multilayer, attached to semi-infinite leads of material A, possesses B-layers of fixed thickness l_B and A-layers of random thicknesses l_A which are allowed to fluctuate by ± 1 atomic planes (AP) around a mean value $\bar{l}_A$ (with equal probability for $\bar{l}_A$, $\bar{l}_A \pm 1$). In all the following simulations, I consider multilayers consisting of 10 A/B bilayers and for each l_B show results for the average conductance of 10 random configurations of the A-layers.

For Ni/Co and Ag/Pd respectively, figures 4.1 and 4.2 show the mean conductance as a function of l_B, along with error bars for the standard deviation of the mean σ_m. While σ_m is smaller than the underlying conductance fluctuations, it should be noted that this is not the case for the standard deviation σ in the distribution of the individual conductances, which for an ensemble of m realization satisfies $\sigma_m = \sigma/\sqrt{m}$, where $m = 10$ for figures 4.1 and 4.2. For small m, σ is of the order of the conductance

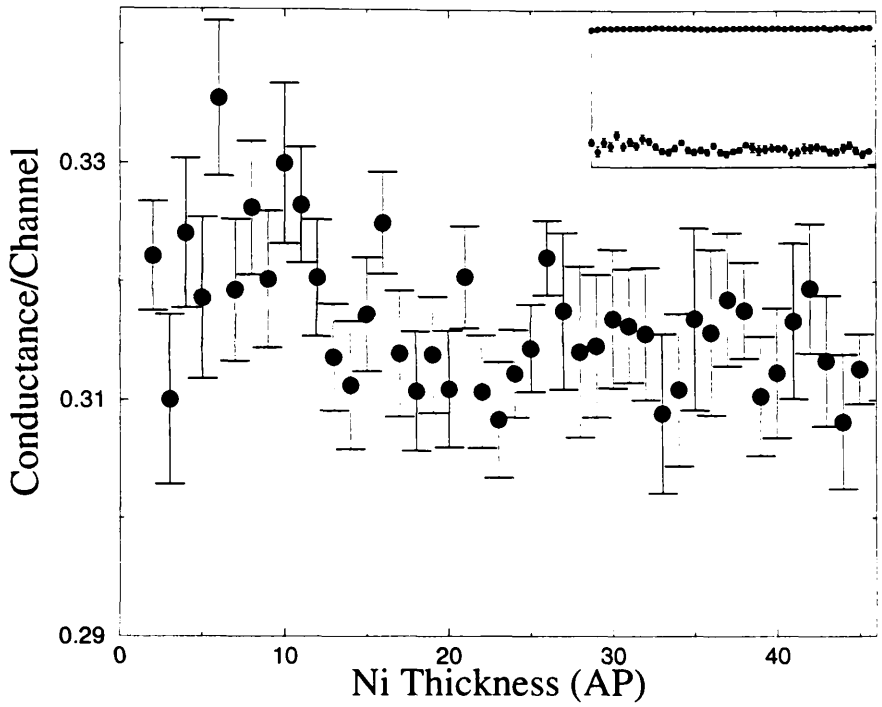

Figure 4.1: Conductance of Ni/Co multilayers as a function of the Ni thickness. The Co thickness is 10 atomic planes. The inset shows the two spin conductances on the same scale with the upper plot for majority spin and the lower for minority spin. The error bars correspond to the root-mean-square deviation of the mean.

oscillations themself, thereby masking any underlying trend. In experiments involving a large number n of bilayers, such that the total length $l = n(l_A + l_B)$ is larger than the phase braking length l_ϕ (due to incoherent scattering processes), the sample may be viewed as comprising l/l_ϕ samples in series and therefore the total resistance is the sum of l/l_ϕ statistically independent resistances. This suggests that multilayers with a large number of bilayers are needed in order to detect reproducible conductance oscillations, as pointed out in several experiments [88, 89, 90, 91]. The figures suggest the presence of long-period oscillations on a scale greater than the atomic spacing, with amplitudes not exceeding 25% of the mean conductance, though the period does not seem constant. Moreover the Ni/Co system shows smaller oscillations than the Ag/Pd system, and despite the fact that the conductance of the majority spin channel is almost double that of the minority, the oscillations arise predominantly from the minority spins, where the scattering is strongest. This is consistent with the scattering mechanisms pointed out in the previous chapter. Although the results of figures 4.1 and 4.2 are important because represent a quantitative calculation involving real materials,

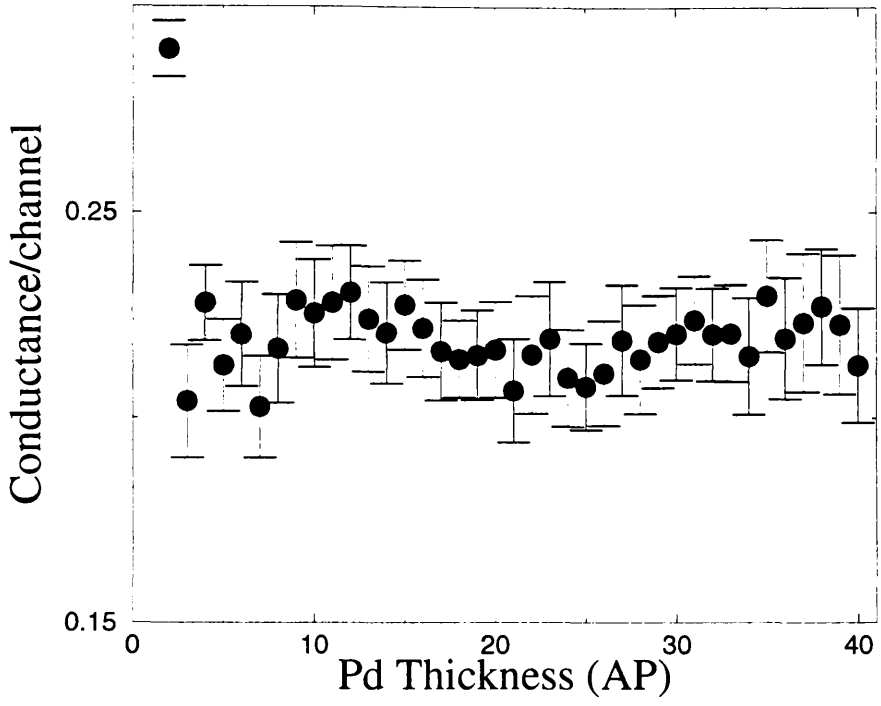

Figure 4.2: Conductance of Ag/Pd multilayers as a function of the Pd thickness with an average Ag thickness of 5 atomic planes.

in order to understand how quantum interference of the conduction electron wave-functions might give rise to long period oscillations. it useful to develop a simple model which capture most of the relevant physics. This is done in the next section.

4.3 Effective Mass Model and Conductance for an Infinite System

The model consists in a 3D free-electrons gas with parabolic band, effective mass and Krönig-Penney potential [97]. The potential is along the z-direction only (the direction of the current in the CPP configuration) and describes the off-sets between the bottom of the bands of different materials. The masses of the different materials are allowed to be different reflecting the different band dispersions. For instance, if one wants to describe a *d*-conductor (Pd) in contact with an *sp*-conductor (Ag), two parabolic bands with respectively large and small effective masses will be considered. The Hamiltonian for such a system can be written as

$$H^{\sigma}(\mathbf{r}) = -\frac{\hbar^2}{2}\left[\frac{\nabla_{xy}^2}{m^*(z)} + \frac{\partial}{\partial z}\frac{1}{m^*(z)}\frac{\partial}{\partial z}\right] + V^{\sigma}(z)\,. \tag{4.1}$$

where ∇^2_{xy} is the 2D I aplacian. Since the structure considered possesses translational invariance in the x-y directions, the spin-dependent Krönig-Penney potential $V^\sigma(z)$ and the effective mass $m^*(z)$ are functions of z only. Consequently the problem can be mapped onto a $k_{||}$-dependent 1D problem, whose Hamiltonian is

$$H^\sigma(z;k_{||}) = -\frac{\hbar^2}{2}\frac{\mathrm{d}}{\mathrm{d}z}\frac{1}{m^*(z)}\frac{\mathrm{d}}{\mathrm{d}z} + \frac{\hbar^2 k_{||}^2}{2m^*(z)} + V^\sigma(z). \tag{4.2}$$

For each $k_{||}$ and spin σ, an eigenstate at the Fermi energy contributes e^2/h to the conductance of this infinite periodic structure. The open scattering channels of the Hamiltonian (4.2) can be found with an ordinary transfer matrix technique (see Appendix E). Nevertheless in the case in which the effective mass is constant, the calculations can be carried out analytically and a good description of the relevant oscillation periods can be given. It is therefore useful to introduce a general formula for the conductance (more precisely for the conductance per unit area) of an infinite system in the case in which the Schrödinger equation can be solved by separating the variables. This is the case of the Hamiltonian of equation (4.1) when $m^*(z) = m^*$.

The starting point is the Landauer-Büttiker formula for an infinite system. In this case there is no reflection and the total conductance is

$$\Gamma = \frac{e^2}{h} N(E_\mathrm{F}) , \tag{4.3}$$

where $N(E_\mathrm{F})$ is the total number of open channels at the Fermi energy. Suppose the total energy can be written as a sum of a transverse component $E_{||}$ and a component along the direction z of the transport $E_\perp$. The total number of open channels at the Fermi energy is simply the number of states of the form $e^{ik_\perp z}$ whose corresponding energies $E_\perp$ satisfy the relation

$$E_\perp = E_\mathrm{F} - E_{||} , \tag{4.4}$$

for some allowed $E_{||}$. If the potential is periodic along z the states $e^{ik_\perp z}$ will form one dimensional bands E_n and the number of open channels will be the number of states satisfying the equation (4.3) with $E_\perp$ belonging to one of the bands

$$N(E_\mathrm{F}) = \sum_n N_n , \tag{4.5}$$

where N_n is the number of open channels corresponding to the n-th band and the sum runs over all the occupied bands up to the Fermi energy. The number of states between an energy window $E_\perp$ and $E_\perp + dE_\perp$ within an allowed band is simply given by

$$dN_n = \rho(E_\parallel)dE_\parallel = \rho(E_F - E_\perp)dE_\perp \,, \tag{4.6}$$

where ρ is the two-dimensional density of state in the plane orthogonal to z (this can be substituted by a one-dimensional density of states if one deals with a two-dimensional transport problem). Given (4.6), the total conductance can be easily evaluated

$$\Gamma = \frac{e^2}{h} \sum_n \int_{E_n}^{E_n + \Delta_n} dE \rho(E_F - E) \,, \tag{4.7}$$

where the sum spans all the occupied n-bands, E_n is the position of the bottom of the n-th band and Δ_n is the correspondent band width. The expression (4.7) is completely general and can be applied to every system in which the energy can be written in the form of equation (4.4).

In the free-electron case introduced above the equation (4.7) can be further simplified. In fact for a system with finite cross section $A = L \times L$ and with periodic boundary conditions the two-dimensional density of states is simply

$$\frac{dN}{dE} = \frac{2\pi A m^*}{h^2} \,, \tag{4.8}$$

with m^* the effective mass. Note that the two-dimensional DOS does not depend on the energy. Therefore the integral of equation (4.7) is trivial and the conductance assumes the following expression

$$\Gamma = \frac{2\pi e^2 m^* A}{h^3} \sum_n \Delta_n \,. \tag{4.9}$$

Note that in the case of an infinite system also in the transverse direction Γ diverges because $A \longrightarrow \infty$. It is possible to eliminate such a divergence by defining the conductance per unit area Γ/A (note that this is proportional to the normalized conductance used throughout the first chapters).

It is also important to note that in this simple case the problem of calculating the conductance is mapped onto the problem of calculating the total bandwidth of a one-dimensional periodic potential. In the next section I will use the formula (4.9) to evaluate the conductance of an infinite multilayer and to calculate the oscillation periods.

4.4 The Oscillation Periods

In the previous section I have shown that the calculation of the conductance in a three-dimensional infinite multilayer consists of evaluating the total bandwidth up to the Fermi energy of the mono-dimensional problem defined by the Hamiltonian

$$H^{\sigma}(z) = -\frac{\hbar^2}{2m^*}\frac{\mathrm{d}^2}{\mathrm{d}z^2} + V^{\sigma}(z)\,. \tag{4.10}$$

Consider an infinite superlattice composed of materials A and B, with layer-thicknesses l_{A} and l_{B} ($l_{\mathrm{A}} + l_{\mathrm{B}} = L$). The correspondent Krönig-Penney potential assumes values $V = V_o$ ($E_{\mathrm{F}} > V_o$) in the metal A and $V = 0$ in the metal B. The Hamiltonian (4.10) yields immediately the Kröning-Penney secular equation

$$\cos(k_{\perp}L) = \cos(k_{\mathrm{A}}l_{\mathrm{A}} + k_{\mathrm{B}}l_{\mathrm{B}}) - \frac{(k_{\mathrm{A}} + k_{\mathrm{B}})^2}{k_{\mathrm{A}}k_{\mathrm{B}}}\sin(k_{\mathrm{A}}l_{\mathrm{A}})\sin(k_{\mathrm{B}}l_{\mathrm{B}}), \tag{4.11}$$

with $k_{\mathrm{A}}(E) = \sqrt{2m^*(E - V_o)}/\hbar$ and $k_{\mathrm{B}}(E) = \sqrt{2m^*E}/\hbar$. Based on this expression, I now argue that the bandwidths exhibit several periods of oscillation as the layer thicknesses are varied.

To describe Ni/Co (Ag/Pd) multilayers, I vary the thickness of metal B keeping fixed the thickness of metal A. To understand the oscillatory behaviour of the bandwidths, note that equation (4.11) cannot be satisfied at energies for which

$$k_{\mathrm{A}}(E)l_{\mathrm{A}} + k_{\mathrm{B}}(E)l_{\mathrm{B}} = m\pi\,, \tag{4.12}$$

where m is an integer. Hence at $E = E_{\mathrm{F}}$ and fixed l_A, successive bandgaps appear at the Fermi energy E_{F} when l_{B} changes by

$$l_{\mathrm{B}}^{m} = \frac{\pi}{k_{\mathrm{B}}(E_{\mathrm{F}})}m = \frac{\pi\hbar}{\sqrt{2m^*E_{\mathrm{F}}}}m = l_{\mathrm{B}}^{\mathrm{F}}m\,. \tag{4.13}$$

Equation (4.13) introduces the first period of oscillation $l_{\mathrm{B}}^{\mathrm{F}}$. The second period corresponds to the presence of narrow gaps below the Fermi energy. From equations (4.11) and (4.12) narrow bandgaps appear at the energies

$$E_{\mathrm{A}}^{(n)} = \frac{\hbar^2\pi^2n^2}{2m^*l_{\mathrm{A}}^2} + V_o\,, \tag{4.14}$$

whenever the lengths l_{B} equal

$$l_{\mathrm{B}}^{(n)} = \frac{\pi\hbar}{\sqrt{2m^*E_{\mathrm{A}}^{(n)}}}\,. \tag{4.15}$$

This last result can be easily proved as follows. Consider a general choice of $k_A(E)l_A$ and $k_B(E)l_B$ which satisfies the equation (4.12)

$$k_A(E)l_A = m\pi + \phi\,, \tag{4.16}$$

$$k_B(E)l_B = -\phi\,, \tag{4.17}$$

with $0 \leq \phi < \pi$. By substituting the equations (4.16) and (4.17) into the equation (4.12) one obtains

$$\cos(k_\perp L) = \pm 1 \pm \frac{(k_A + k_B)^2}{k_A k_B}\sin^2(\phi)\,, \tag{4.18}$$

where the sign "+" ("-") corresponds to even (odd) m. It is now clear that narrow gaps are obtained when the second term of the left-hand side of the equation (4.18) is small. This occurs when $\phi = n'\pi$, which yields the relation

$$k_A l_A = n\pi \tag{4.19}$$

and the condition (4.14). The total bandwidth Δ and hence the conductance per unit of area (4.9) are oscillating functions with periods l_B^F and the $l_B^{(n)}$'s. All these periods are of order λ_F (ie few Å), but beating between them can give rise to long-period oscillations. It is important to note that the Fermi period is defined only through the Fermi energy, while the periods $l_B^{(n)}$ depend critically on the superlattice geometry. In particular, because the energies corresponding to periods (4.15) depend on $1/l_A^2$ and must not exceed the Fermi energy, the number of $l_B^{(n)}$'s depends on the thickness of the metal A. If l_A is large, a large number of $l_B^{(n)}$ periods will be present and the beating pattern will be complex. On the other hand, if l_A is small, few $l_B^{(n)}$'s will be present, giving rise to a simple beating pattern. A numerical evaluation of the equation (4.9) is shown in figure 4.3. For the chosen parameter in this plot, I expect only one $l_B^{(n)}$ and clear beats are observed, with period $2l_B^{(1)}l_B^F/(l_B^{(1)} - l_B^F)$. Since the $l_B^{(n)}$ periods are characteristic of the superlattice structure I predict that the period of the long oscillations can be set by choosing the appropriate superlattice geometry. Of course in a real superlattice, the B-metal thickness can only be changed in units of the inter-atomic spacing. The solid dots in figure 4.3 highlight the conductance associated with such a discrete set of thicknesses.

The above dependence of oscillations on the multilayer structure is missed by a trilayer quantum well approach to conductance oscillations and GMR [93], where only

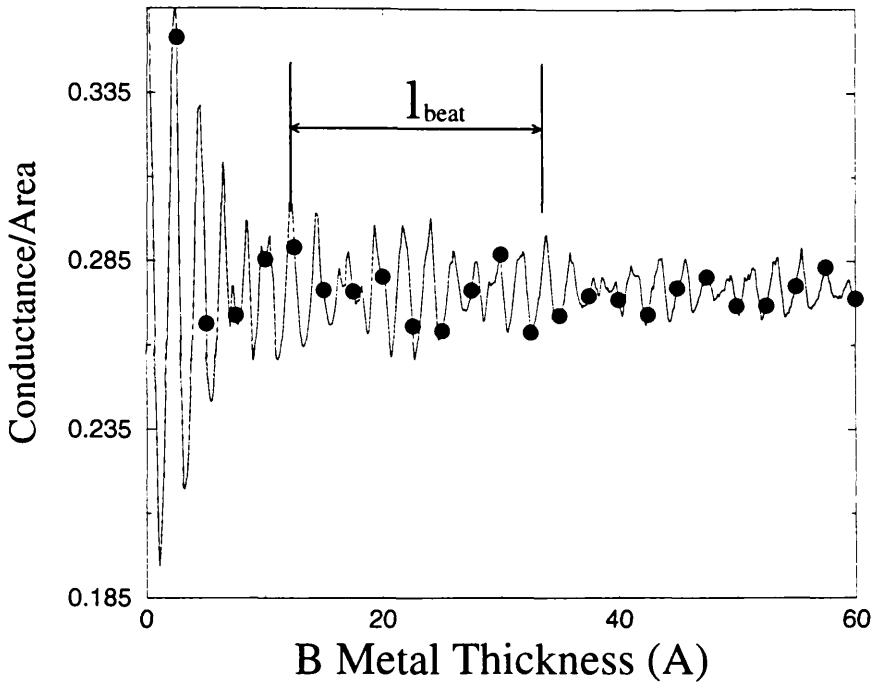

Figure 4.3: Conductance per unit area in the effective mass approximation. The parameters are E_F = 10eV, V_o = 6eV, m^* = 0.5MeV, l_A = 8Å. The dots correspond to the conductance calculated at integer values of the lattice spacing of Ni. The vertical lines show the beating period $l_{beat} = 2l_B^{(1)}l_B^F/(l_B^{(1)} - l_B^F)$.

two periods have been identified. The first of these p^{FS} depends on the extremal Fermi surface radius of the spacer forming the well, and in the parabolic band approximation corresponds exactly to the period l_B^F. The second period p^{cp} depends on the cut-off of the sum over the $k_{||}$'s, and in the parabolic approximation, on the energy difference between the Fermi energy and the step potential V_o. In the superlattice description given, this period is replaced by the class of periods $l_B^{(n)}$, which are a function of the superlattice structure itself. This structural dependence of the oscillation periods is the key to understanding the apparent non-reproducibility of the long period oscillations from sample to sample, observed in some of the experiments [92]. It may be shown that these beating features are preserved when a more realistic material-dependent effective mass is used and therefore may be considered general.

Bearing in mind that the above analysis describes the CPP configuration, I can also speculate on the absence of the oscillations in other recent experiments [92, 91]. Ag/Cu [92] exhibits very good phase separation between the different metals and hence it should be a good candidate for observing conductance oscillations. However the band

match between Ag and Cu is very good, resulting in a very small scattering potential at the interface. In the effective mass approach this means a very small step potential V_o with respect to the Fermi energy. A large number of periods $l_B^{(n)}$ will be present and the beats will be difficult to detect. The same argument is valid for Ag/Au [92]. In addition the high miscibility of Ag and Au results in dirty interfaces. Ag/Pd [91] is in theory a good candidate to show conductance oscillations because of the large mismatch between the Ag and Pd bands. Unfortunately interdiffusion at the interface is difficult to avoid and the elastic mean free path will be quite short. Finally, note that for Ni/Co [88, 89, 90, 91, 92], the majority band reproduces roughly the situation of Ag/Cu, while the scattering in the minority band is quite large. According to the effective mass model the minority band will possess a low conductance with large oscillations, while the conductance of the majority band will be large and the oscillations small. This is precisely what I obtain from the material specific tight-binding calculations. The absence of oscillations found in reference [92] for Ni/Co multilayers may be due to the diffusive nature of the multilayers. In fact in such experiments the resistances involved are about five times larger than the ones of references [88, 89, 90, 91], and the mean free path is much shorter. This suggests that the transport is not only non-ballistic, but also that the absolute error in the resistance measurements may become comparable to the observed magnitude of the oscillations.

This concludes the part of this chapter concerning the conductance oscillations. In the next section I will revisit the dependence of the GMR on the materials forming the multilayer by using the effective mass model.

4.5 The rôle of the effective mass

In this section I extend the effective mass model to the case of different effective masses for different materials and consider an infinite multilayer described by the Hamiltonian (4.1). Note that the kinetic operator possesses the following term $\frac{\partial}{\partial z}\frac{1}{m^*(z)}\frac{\partial}{\partial z}$ which ensures the Hamiltonian to be hermitian. In the case of a multilayer composed of different materials the effective mass $m^*(z)$ can be a step function assuming the values m_A^* and m_B^* respectively in the metal A and B. Whether or not this model is well-founded and the consequent envelope-function approximated wave-function represents the real wave-function is a matter of debate [99]. There is more or less general agreement

that this approximation is valid in the case in which the Fermi wave-length is much larger than the typical interface region between different materials ($\mathbf{p}\cdot\mathbf{k}$ theory [100]). This is the case of semiconductors. In the case of metals the typical Fermi wave-lengths are of the order of the lattice spacing and questions on the validity of such an approximation are legitimate. I do not want to enter into this debate and I will use the above model only as phenomenological model to understand some general features of the transport of metallic multilayers. At the end of this paragraph it will be clear that a free-electron model is too crude to account for some features of the transport.

The conductance is calculated using the general transfer matrix technique presented in Appendix E. The problem one has to face is to select correctly the parameters for the Krönig-Penney potential and the effective masses. In what follows I assume that the bottom of the band of the non-magnetic material A (say Cu) is 0eV and the Fermi energy is 7eV. The remaining parameters to set are the Krönig-Penney potential for the two spin-bands of the magnetic material (say Co) $V^{\uparrow}$ and $V^{\downarrow}$, the spin-dependent effective masses in Co $m^{\uparrow}$ and $m^{\downarrow}$, and the effective mass in Cu m. I leave m to be a free parameter. This is because I want to study the dependence of the conductivity and the GMR on the dispersion of the non-magnetic material. The only parameters left are therefore the ones regarding Co. The criterion I adopted was to reproduce the correct DOS at the Fermi energy $\rho^{\sigma}(E_{\mathrm{F}}) = \rho_{\mathrm{F}}$ and the integrated DOS up to the Fermi energy N^{σ} of Co, calculated with the *spd* tight-binding model. In a free electron model these two quantities are respectively

$$\rho(E) = \frac{m^{3/2}}{\hbar^3\pi^2}\sqrt{2E} \tag{4.20}$$

and

$$N = \int_0^{E_{\mathrm{F}}} \rho(E)dE = \frac{m^{3/2}}{\hbar^3\pi^2}\frac{2\sqrt{2}}{3}E_{\mathrm{F}}^{3/2} \ . \tag{4.21}$$

From the tight-binding model I obtain the following estimates $\rho_{\mathrm{F}}^{\downarrow}/\rho_{\mathrm{F}}^{\uparrow} = 6.3$ and $N^{\downarrow}/N^{\uparrow} = 0.94$, which yield the relations $(E_{\mathrm{F}}-V^{\downarrow})/(E_{\mathrm{F}}-V^{\uparrow}) \sim 0.15$ and $m^{\downarrow}/m^{\uparrow} \sim 6.4$. These two equations can be solved for several choices of $V^{\downarrow}$, $V^{\uparrow}$, $m^{\downarrow}$ and $m^{\uparrow}$. I performed several calculations aimed at reproducing the normalized conductances of Co/Cu multilayers. One of the typical results is presented in figure 4.4 where the conductances of the two spins and the antiferromagnetic configuration, and the consequent GMR are plotted as a function of the Cu effective mass. Figure 4.4 presents some interesting features.

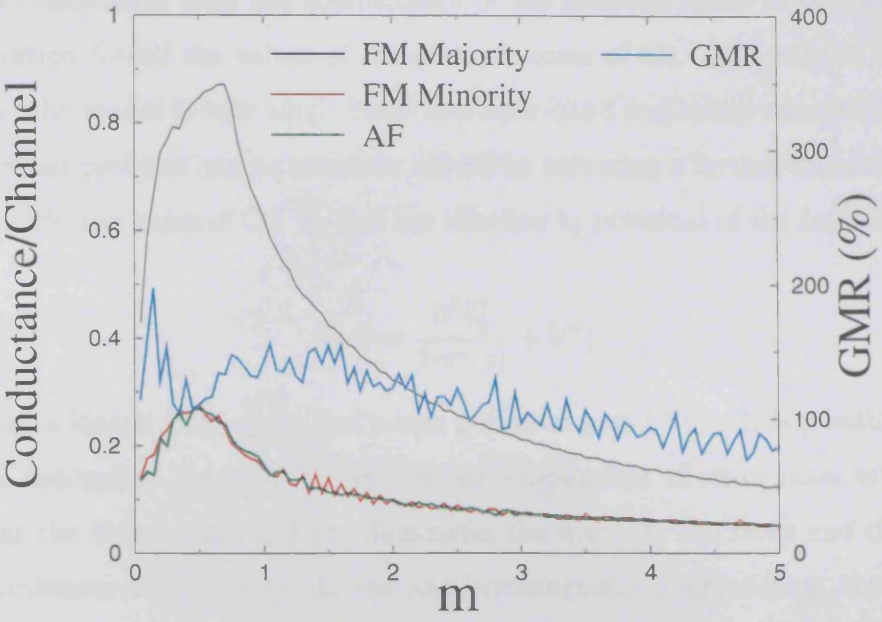

Figure 4.4: Conductance per channel in the effective mass approximation. The parameters are E_F = 7eV, $V^{\uparrow} = 1.9$eV, $V^{\downarrow} = 6.4$eV, $m^{\uparrow} = 16\, m_e$, $m^{\downarrow} = 2\, m_e$, with m_e the electron mass.

Assume the "true" effective mass of Cu is the one which maximizes the GMR, i.e. it is about 1.4 m_e. If the effective mass of the non-magnetic metal decreases from the value of Cu, all the spin conductances increase, but the GMR decreases. This reflects correctly the behaviour of Co/Ag with respect to Co/Cu, where the presence of a full *sp*-like band at the Fermi energy is simulated by an Ag effective mass lighter than that of Cu. On the other hand if one moves the non-magnetic metal effective mass towards large effective masses, all the conductances decrease. Moreover, because an increase of the effective mass results in an improved band match of the minority band with the non-magnetic band, and in a degraded match of the majority band, the majority spin conductance turns out to decrease faster. This gives rise to a decreasing of the GMR. Pd and Pt show this situation, and the *d*-like behaviour at the Fermi energy can be simulated by a large effective mass.

Therefore this qualitative behaviour seems to reproduce correctly the results obtained with the *spd* tight-binding model for Co-based multilayers. Nevertheless there are two problems. First the spin-dependent effective mass for Co assumes very large values that, despite the fact they should include the large curvature of the *d*-band, seem largely non-realistic. Secondly the conductance of the antiferromagnetic configuration

is almost coincident with the conductance of the minority spins in the ferromagnetic configuration for all the values of the effective mass of Cu. This reflects directly the fact that the model is only single-band and inter-band scattering cannot be described.

This last problem can be somehow solved by assuming a further mismatch between the spin-effective mass of Co. In fact the effective $k_{||}$ potential of the total Hamiltonian (4.2)

$$U(z) = \frac{\hbar^2 k_{||}^2}{2m^*(z)} + V^\sigma(z), \tag{4.22}$$

comprises a kinetic part $\frac{\hbar^2 k_{||}^2}{2m^*(z)}$ and a true potential part $V^\sigma(z)$. It is possible to choose the spin-dependent potential V^σ and the spin-dependent effective mass $m^{*\sigma}$ in such a way that the kinetic part of $U(z)$ dominates the majority electrons and the potential part dominates the minority. In the antiferromagnetic configuration, this will result in two different sources of scattering for electrons moving into regions with different magnetizations. In figure 4.5 I plot the conductance and the GMR for one of these possible choices of parameters. It is interesting to note that now the antiferromagnetic

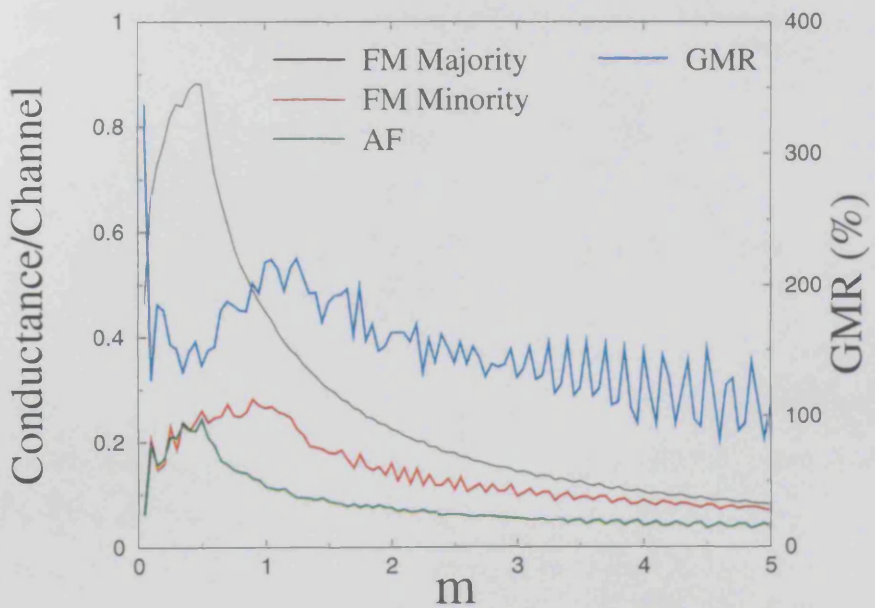

Figure 4.5: Conductance per channel in the effective mass approximation. The parameters are E_F = 7eV, $V^\uparrow = 1.9$eV, $V^\downarrow = 6.4$eV, $m^\uparrow = 28\, m_e$, $m^\downarrow = 1.4\, m_e$, with m_e the electron mass. Note that the large difference between $m^\uparrow$ and $m^\downarrow$ yields the conductance in the AF configuration to be smaller than the conductances in both spin-channels in the FM configuration.

conductance is lower than the conductance for the minority spins in the ferromagnetic

alignment. Nevertheless the parameters and in particular the effective masses are very large.

To conclude, although a single-band model provides a good qualitative description of the spin-conductance in magnetic multilayers, it leads to unrealistic parameters. This suggests that a realistic minimal model must include two bands with different dispersions and possible hybridation. This model can describe both a scattering potential and inter-band scattering.

5 GMR, Disorder and the Breakdown of the Boltzmann Description

5.1 Introduction

In the previous chapters I have considered disorder-free systems with translational invariance in the direction orthogonal to the current. The main aim of this chapter is to investigate the effects of breaking this hypothesis and to study how disorder affects the spin transport. This is particularly relevant for magnetic systems produced with non-MBE techniques, where structural defects or impurities are largely present. In particular in magnetic multilayers made by electrodeposition techniques [32, 101, 102] the quality of the interfaces is not as good as in the MBE-made counterparts and large interdiffusion between the multilayer constituents is present. Moreover, because of the dual bath technique usually employed, the magnetic layers are contaminated by non-magnetic impurities with concentration as large as 15%. Nevertheless, despite all these sources of disorder, such disordered multilayers show large GMR ratios sometimes larger than 100%. It is therefore natural to ask what are the effects of disorder on spin-transport.

On the theoretical side two fundamentally different approaches have been used to describe CPP GMR in disordered systems. The first assumes that all the transport is diffusive and is based on the semi-classical Boltzmann's equation within the relaxation time approximation. This model has been developed by Valet and Fert [33, 34], and has the great advantage that the same formalism describes both CIP and CPP experiments. It identifies the characteristic lengths of the problem and can include the effects of disorder into the definition of the spin σ dependent mean free path λ_σ and the spin diffusion length l_{sf}. Moreover it can be extended to describe the temperature dependence of GMR [102]. In the limit that the spin diffusion length is much larger than the layer thicknesses (infinite spin diffusion length limit), this model reduces to a classical two current resistor network, in which additional spin-dependent scattering at the interfaces is considered. The resistor network model has been used since the early days of CPP GMR by the Michigan State University group [66], and describes most of the experimental data. The parameters of the model are the magnetic (non-magnetic) metal resistivity ρ^*_M (ρ^*_N), the spin asymmetry parameter β introduced

through the spin-dependent resistivity of the magnetic metal $\rho_{\uparrow(\downarrow)} = 2\rho^*_{\rm M}[1-(+)\beta]$, the magnetic/normal metal interface resistance per unit area $r^*_{\rm b}$ and the interface scattering spin asymmetry γ introduced through the spin-dependent interface resistance per unit area $r_{\uparrow(\downarrow)} = 2r^*_{\rm b}[1-(+)\gamma]$. A good fit of the parameters has been shown to be possible, and the same values can fit reasonably well both the CIP and the CPP data [66]. The limitation of such a model is that it neglects the band structure of the system, and all the parameters are phenomenological. An extension of the model to include band structure has been made recently [51, 52], implementing the above transport theory within the framework of density functional theory in the local spin density approximation. In this calculation, the scattering due to impurities is treated quantum mechanically, while transport is described semi-classically using the Boltzmann equation. The same method has been previously used to describe the spin-polarization of the current in diluted Ni- [103] and Co- [104] alloys. The polarization is generally reproduced correctly for light impurities, while the absence of spin-orbit interaction seems to be a strong limitation in the case of heavy impurities.

The second theoretical approach to CPP GMR in disordered systems is based on the quantum theory of scattering. Full *ab initio* calculations based on density functional theory [49, 50] in this case cannot be used because of the massive computer overheads. Tight-binding methods are more promising even if the use of accurate *spd* Hamiltonians leads quickly to unmanageably large matrices. The only calculations carried out to date involve either infinite superlattices in the diffusive regime [53] where small unit cells can be used, or finite superlattices in which disorder is introduced without breaking translational symmetry in the direction perpendicular to the current [29, 54]. In the latter case the system is an effective quasi 1D system, whereas real multilayers are 3D systems with roughness at the interfaces which breaks translational invariance.

From this short overview it is clear that with exception of references [29, 54] the transport in disordered magnetic multilayers is always assumed to be diffusive. The main expectation from this assumption is that interference effects can be neglected and that transport is completely local. As a consequence of this assumption both the spin-polarization of the current and the GMR do not change with the length of the systems. This picture is generally consistent with experiments. Nevertheless very recently it has been shown [35, 36, 105] that in magnetic multilayers the GMR increases with

the number of magnetic/non-magnetic layers period, and depends critically on the order of the layers. Although in the case of reference [36] these data are explained by considering a very short spin-diffusion length, this argument is hardly applicable to the experiments of references [35, 105] where the use of MBE-grown Co/Cu and Co/Cu/Fe/Cu multilayers assure long spin-diffusion lengths. These results suggest that the relevant length scale for CPP GMR is not only the spin-diffusion length but also the elastic mean free path, and that non-local contributions to the conductance are important. For these reasons the strictly local description of the transport based on the Boltzmann's equation is not valid and a quantum approach to transport is needed.

The aim of the present chapter is twofold. First I will study three-dimensional GMR multilayers and investigate the effect of disorder on the spin-transport in both the ballistic and diffusive regimes and the crossover between them. Secondly I will present a few examples in which the resistor network model is clearly violated and a phase coherent theory of transport is needed. To address these problems I consider a reduced tight-binding model with two degrees of freedom (*s-d*) per atomic site. I use the same technique as in Chapter 2 to compute the zero-bias zero-temperature conductance in the framework of the Landauer-Büttiker formalism. The calculation is optimized such that it scales sub-linearly with the multilayer length. This is crucial to study phase coherent transport in long but finite multilayers, where a large ensemble average is also needed. Several models of disorder are introduced in order to mimic defects, impurities, vacancies and lattice imperfections. In the case of electrodeposition-made multilayered nanowires [32, 101, 102] where the phase breaking length is comparable with the wire cross-section, I also consider the effects of rough boundaries and confinement.

The main result of this analysis is to show that phase coherent transport in disordered magnetic multilayers may give rise to behaviours not describable by the Boltzmann approach and I will discuss the relevance of these "non-diffusive" effects in several new experiments [35, 36, 105]. Most of the results of this chapter have been published already in references [37, 38].

The chapter is organized as follows: in the next section I will describe an implementation of the numerical scattering technique capable of handling large systems and performing efficient averages over large ensembles. In this section I introduce a "diagrammatic" approach to decimation, which will also be useful in Chapter 7 to describe

carbon nanotubes. In the section 5.3 I discuss a two *s-d* band model which is the minimal Hamiltonian capable of capturing inter-band scattering and reproducing the correct density of state of transition metals. Then I present the main results of this chapter and discuss the effect of different sources of disorder. Finally I consider examples where a phase coherent approach to transport gives rise to completely different results with respect to the resistor network model. It will be clear that this approach is more appropriate for describing new experiments where the elastic mean free path may be very long.

5.2 Implementation of decimation in the case of disorder: "Decimation Diagrams"

The numerical technique used in the present calculation is entirely equivalent to that presented in Chapter 2 and reference [27]. Here I want only to discuss some numerical optimizations which are useful in the case of disordered systems. I always consider finite disordered multilayers sandwiched between two semi-infinite perfectly crystalline leads. With this setup all the disorder is included into the scattering region. Therefore the only difference to the completely disorder-free case is that one needs to decimate a region where the matrices describing the atomic planes are different. Nevertheless, since I want to consider arbitrary long disordered multilayers and perform averages over a large number of ensembles, it is crucial to optimize the decimation technique. This is achieved by recalling that the decimation technique, in the case of nearest neighbour coupling, only redefines the matrix element coupled with the decimated one. For instance in the decimated Hamiltonian at l-th order

$$H_{ij}^{(l)} = H_{ij}^{(l-1)} + \frac{H_{il}^{(l-1)} H_{lj}^{(l-1)}}{E - H_{ll}^{(l-1)}} , \tag{5.1}$$

only the matrix elements coupled to the element $H_{ll}^{(l-1)}$ of the $(l-1)$-th order Hamiltonian are redefined. Consider now a disordered multilayer composed of alternating magnetic (M) and non-magnetic (N) layers of thicknesses t_{M} and t_{N} respectively. Suppose that the multilayer consists of μ repeated (N/M/N/M) units, that I call double bilayers. Since I consider only short range interactions, it is possible to decimate the Hamiltonian of the whole multilayer by building up the following intermediate Hamil-

tonian

$$H_{\mathrm{M}} = \begin{pmatrix} \cdots & \cdots & \cdots & \cdots & \cdots & \cdots & \cdots & \cdots \\ V_0^{\dagger} & H_{\mathrm{Li}} & H_{\mathrm{LRi}} & 0 & \cdots & \cdots & \cdots & \cdots \\ \cdots & H_{\mathrm{RLi}} & H_{\mathrm{Ri}} & V_0 & 0 & \cdots & \cdots & \cdots \\ \cdots & 0 & V_0^{\dagger} & H_{\mathrm{L(i+1)}} & H_{\mathrm{LR(i+1)}} & 0 & \cdots & \cdots \\ \cdots & 0 & 0 & H_{\mathrm{RL(i+1)}} & H_{\mathrm{R(i+1)}} & V_0 & 0 & \cdots \\ \cdots & \cdots & \cdots & \cdots & \cdots & \cdots & \cdots & \cdots \\ \cdots & \cdots & \cdots & \cdots & \cdots & \cdots & \cdots & \cdots \end{pmatrix}, \tag{5.2}$$

where H_{Li} (H_{Ri}) describes the coupling within the left- (right-) hand surfaces of the i-th cell (N/M/N/M) (i=1,..,μ), H_{LRi} ($H_{\mathrm{RLi}} = H_{\mathrm{LRi}}^{\dagger}$) describes the coupling between the left and right surfaces of the i-th cell, and V_0 is the "bare" coupling between the first right-hand atomic plane of the i-th cell and the first left-hand atomic plane of the $(i+1)$-th cell, which is assumed to be the same for every cell (this last condition is easily satisfied if the first left-hand and the last right-hand atomic plane of every (N/M/N/M) cell is disorder-free). Equation (5.2) suggests a very convenient implementation in which multilayers consisting of μ (N/M/N/M) cells are built using the following procedure. Firstly one decimates a certain number ν, of cells (N/M/N/M) in which disorder is introduced everywhere except in the first and last atomic plane. Secondly the matrix H_{M} of equation (5.2) is built, choosing randomly the order of the μ (N/M/N/M) cells. Finally the matrix H_{M} is further decimated to yield the coupling matrices between the lead surfaces $H_{\mathrm{eff}}(E)$ of equation (2.40), which has the structure

$$H_{\mathrm{eff}}(E) = \begin{pmatrix} H_{\mathrm{L}}^{*}(E) & H_{\mathrm{LR}}^{*}(E) \\ H_{\mathrm{RL}}^{*}(E) & H_{\mathrm{R}}^{*}(E) \end{pmatrix}. \tag{5.3}$$

In this expression, $H_{\mathrm{L}}^{*}(E)$ ($H_{\mathrm{R}}^{*}(E)$) describes intra-surface couplings involving degrees of freedom belonging to the surface of the left- (right-) hand side lead and $H_{\mathrm{LR}}^{*}(E) = H_{\mathrm{LR}}^{*}(E)^{\dagger}$ describes the effective coupling between the surfaces of the left-hand side and the right-hand side leads. Note that μ^{ν} possible different multilayers can be built from a set of ν disordered unit cells, and that the computation time scales as the number of (N/M/N/M) cells and not as the total length of the scatterer. This procedure can be further optimized, for instance by building ν' new cells (N/M/N/M)×2, and using these to form the multilayers.

To conclude this section it is instructive and useful to introduce a "diagrammatic" way to describe the decimation procedure. Consider as an example figure 5.1. In the figure I represent an atomic plane described by the intra-plane matrix A_0 by a

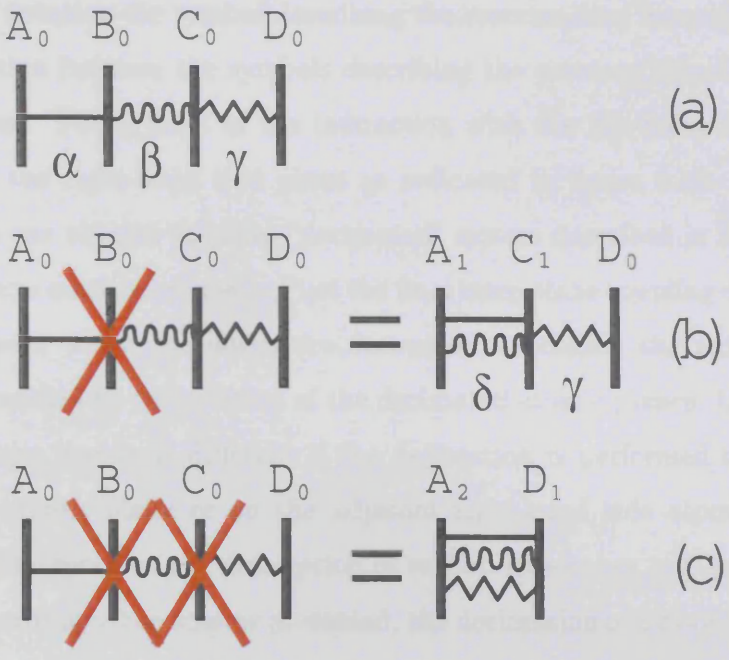

Figure 5.1: "Decimation diagrams".

vertical line labeled with the index A_0. The coupling between different atomic planes is represented by horizontal lines with different shapes for different coupling matrices, which are denoted with Greek letters. For instance the quadri-layer of figure 5.1a consists of four atomic planes described by the matrices A_0, B_0, C_0 and D_0 respectively, and coupled by mean of the matrices α, β and γ. The Hamiltonian describing this structure is a block-trigonal matrix H of the form

$$H = \begin{pmatrix} A_0 & \alpha & 0 & 0 \\ \alpha^\dagger & B_0 & \beta & 0 \\ 0 & \beta^\dagger & C_0 & \gamma \\ 0 & 0 & \gamma^\dagger & D_0 \end{pmatrix} . \tag{5.4}$$

Suppose now that one decimates all the degrees of freedom of the atomic plane labelled with B_0 (I denote the decimation with a red cross over the plane to eliminate). Figure 5.1b shows the result of such a decimation. On the one hand the in-plane matrices of the layers adjacent to B_0 have been redefined (A_1 and C_1 respectively) as well as the coupling between the two. On the other hand the atomic plane D_0 and the interaction between D_0 and C_0 are not redefined because they are decoupled from B_0. Therefore the new matrix describing the right-hand side of figure 5.1b is

$$H = \begin{pmatrix} A_1 & \delta & 0 \\ \delta^\dagger & C_1 & \gamma \\ 0 & \gamma^\dagger & D_0 \end{pmatrix} . \tag{5.5}$$

As a matter of notation the symbol describing the renormalized inter-plane interaction is the composition between the symbols describing the previous interactions with the decimated plane. The symbol of the interaction with the left-hand side plane is on top of that of the right-hand side plane as indicated in figure 5.1b. By continuing the decimation one obtains the final "decimated" system described in figure 5.1c. Two important aspects must be stressed. First the final inter-plane coupling does not depend on the order with which the layers are decimated. Secondly the redefined in-plane matrices are sensitive to the position of the decimated atomic planes. In general a new redefined in-plane matrix is different if the decimation is performed on the adjacent left-hand side atomic plane or on the adjacent right-hand side atomic plane. This difference will be crucial in the description of carbon nanotubes in Chapter 7.

Finally according to the scheme presented, the decimation of a disordered (N/M/N/M) cell is shown in figure 5.2. Note that in this case the coupling between adjacent (N/M/N/M) cells (terminal coupling symbols) is not redefined.

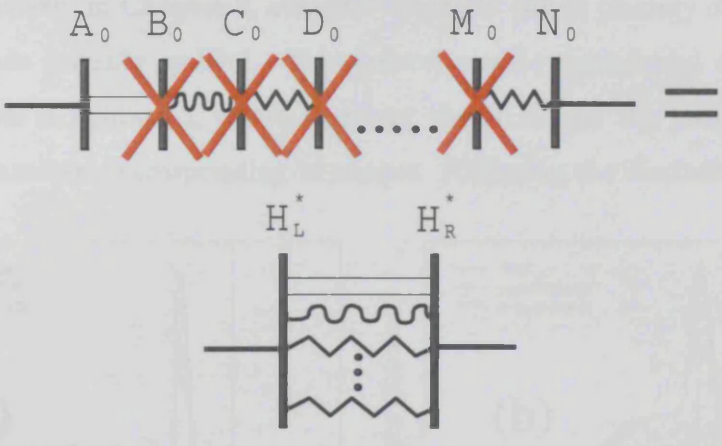

Figure 5.2: Scheme of the decimation of a (N/M/N/M) cell. Note that the coupling between adjacent cells is not redefined.

5.3 The two-band model and the models for disorder

The technique for computing transport properties, is based on a three dimensional tight-binding model with nearest neighbour couplings on a simple cubic lattice and two degrees of freedom (*s*-*d*) per atomic site. I have chosen this simple model because it provides a good description of the density of state of transition metals and of the inter-band scattering, and at the same time allows disordered unit cells to be dealt

with. The general spin-σ-dependent Hamiltonian is

$$H^{\sigma} = \sum_{i,\alpha} \epsilon_i^{\alpha\sigma} c_{\alpha i}^{\sigma\dagger} c_{\alpha i}^{\sigma} + \sum_{i,j,\alpha\beta} \gamma_{ij}^{\alpha\beta\sigma} c_{\beta j}^{\sigma\dagger} c_{\alpha i}^{\sigma} , \tag{5.6}$$

where α and β label the two orbitals (which for convenience we call s and d), i, j denote the atomic sites and σ the spin. $\epsilon_i^{\alpha\sigma}$ is the on-site energy which can be written as $\epsilon_i^{\alpha} = \epsilon_0^{\alpha} + \sigma h \delta_{\alpha d}$ with h the exchange energy and $\sigma = -1$ ($\sigma = +1$) for majority (minority) spins. In equation (5.6), $\gamma_{ij}^{\alpha\beta\sigma} = \gamma_{ij}^{\alpha\beta}$ is the hopping between the orbitals α and β at sites i and j, and $c_{\alpha i}^{\sigma}$ ($c_{\alpha i}^{\sigma\dagger}$) is the annihilation (creation) operator for an electron at the atomic site i in an orbital α with a spin σ. h vanishes in the non-magnetic metal, and $\gamma_{ij}^{\alpha\beta}$ is zero if i and j do not correspond to nearest neighbour sites. Hybridization between the s and d orbitals is taken into account by the non-vanishing term γ^{sd}. I consider two orbitals per site in order to give an appropriate description of the density of states of transition metals and to take into account inter-band scattering occurring at interfaces between different materials. The DOS of a transition metals, as discussed extensively in Chapter 3, consists of narrow bands (mainly d-like) embedded in broader bands (mainly sp-like). This feature can be reproduced in the two-band model, as shown in figure 5.3, where I present the DOS and the partial conductance for a set of parameters corresponding to copper. Following the discussion of Chapter 3

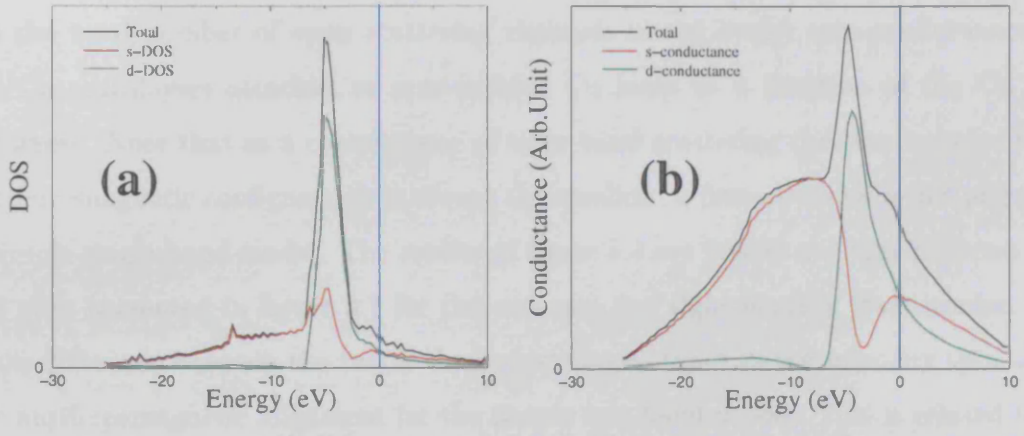

Figure 5.3: DOS (a) and partial conductance (b) obtained for the two-band model. The parameters used are the ones corresponding to Cu in the Table 5.1. The vertical line denotes the position of the Fermi energy used in the calculation.

I note that the position of the Fermi energy with respect to the edge of the d-band largely determines the transport properties of pure transition metals. For instance the

current in silver is carried almost entirely by light effective mass *sp*-electrons with a small DOS, while in the minority band of Co or Ni it is carried by heavy *d*-electrons with a large DOS. The hybridization at the Fermi energy can also be important and for instance in copper the current consists of an equal mixture of *sp*- and *d*-electrons. In the analysis of Chapter 3 I have identified the large inter-band scattering as one of the main sources of GMR. In particular it has been shown that due to inter-band scattering the conductance of a multilayer in the antiferromagnetic configuration is always smaller than both spin conductances in the ferromagnetic configuration. It is possible to capture this feature by choosing the parameters of the two-band model to yield conductances as close as possible to those obtained for the full *spd* model (see Chapter 3 and reference [27]). In the case of a heterojunction, like for the *spd* model, the hopping parameters between different materials are chosen to be the geometric mean of the hopping elements of the bulk materials. The parameters for Cu and Co and FeV are presented in Table 5.1. In figure 5.4 I show the corresponding normalized

Material	ϵ_s (eV)	ϵ_d (eV)	ssσ (eV)	dd(σ, π, δ) (eV)	sdσ (eV)	h (eV)
Cu	-7.8	-4.0	-2.7	-0.85	1.1	0.0
Co	-4.6	-2.0	-2.7	-0.85	0.9	1.6
FeV	-4.6	3.25	-2.7	-0.95	1.1	1.75

Table 5.1: Parameters used in the calculations.

(to the total number of open scattering channels in the leads) spin-conductances for Co/Cu multilayers attached to semi-infinite Cu leads as a function of the Cu layer thickness. Note that as a consequence of inter-band scattering the conductance in the antiferromagnetic configuration is always the smallest, a feature which is not present in a simple single-band model. The results of figure 5.4 are indeed not very different from the ones presented in figure 3.7 for the accurate *spd* tight-binding Hamiltonian. The main difference between the two is the largest conductance in the minority spin and in the antiferromagnetic alignment for the simple two band model. This is related to the different degeneracy of the *s*- (no degeneracy) and *d*-band (fivefold degeneracy), which is neglected in the simple two band model. I believe that this simple two-band model is the minimal model capable of describing in a semi-quantitative way the behaviour of transition metals. It includes the correct DOS and the possibility of scattering electrons between high dispersion (s) and low dispersion bands (d).

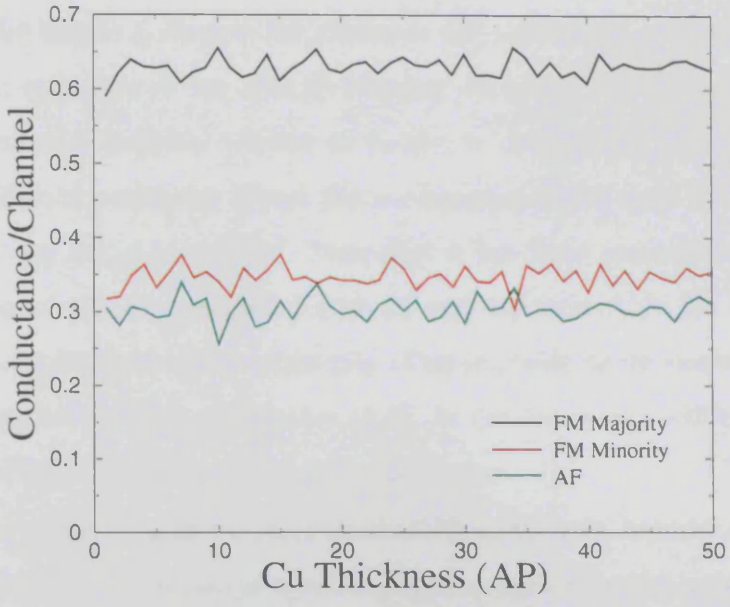

Figure 5.4: Conductances normalized to the number of open channels for Co/Cu multilayers with Cu semi-infinite leads as a function of the Cu layers thickness. This gives rise to a GMR of about 60%. This results should be compared with those of figure 3.7 obtained for an accurate *spd* tight-binding Hamiltonian.

Figure 5.5 shows the different models of disorder analyzed below. The simplest model was introduced by Anderson within the framework of the localization theory [106] and consists of adding a random potential V to each on-site energy, with a uniform distribution of width W $(-W/2 \leq V \leq W/2)$, centered on $V = 0$

$$\tilde{\epsilon}_i^{\alpha\sigma} = \epsilon_i^{\alpha\sigma} + V \ . \tag{5.7}$$

This generic model of disorder can yield arbitrary mean free paths and significant spin-asymmetry in the conductance. To obtain a more realistic description of disorder I also consider the rôle of lattice distortions, which are known to be present at the interfaces between materials with different lattice constants. Moreover in the case of electrodeposited nanowires, contamination by impurities is unavoidable, and lattice distortions occur in the vicinity of such point defects. In what follows I model lattice distortions by scaling the hopping parameters between nearest neighbours. It has been proposed [107] and confirmed numerically [84] that the following scaling law for the tight-binding hopping $\gamma^{\alpha\beta}$ is valid

$$\gamma^{\alpha\beta} = \gamma_0^{\alpha\beta} \cdot (1 + \delta r)^{-(1+\alpha+\beta)} \ , \tag{5.8}$$

where $\gamma_0^{\alpha\beta}$ is the hopping element for atoms at the equilibrium positions r_0, α and β are the angular momenta of the orbitals forming the bond, and δr is the displacement from the equilibrium position relative to r_0 ($\delta r = \Delta r/r_0$ with Δr the displacement from the equilibrium position). Hence the *s-s* hopping scales as $(1+\delta r)^{-1}$, the *d-d* as $(1+\delta r)^{-5}$ and the *s-d* as $(1+\delta r)^{-3}$. Note that it has been recently proved [108] that in 3*d* transition metals contaminated with 3*d* and 4*sp* impurities the variation of the nearest neighbour distance in the proximity of an impurity never exceeds $\sim 5\%$, which is within the limit of validity of equation (5.8). In the following I will consider uniform distributions of lattice displacements with zero mean.

As mentioned above, in electrodeposited GMR nanowires, because of the dual-bath deposition technique, the magnetic layers are contaminated by non-magnetic impurities up to 15% in concentration [109], while a negligible concentration of magnetic impurity atoms is present in the non-magnetic layers. To describe this feature I have introduced non-magnetic impurities in the magnetic layers of the multilayer. An impurity is modeled by substituting a magnetic ion by a non-magnetic ion (ie Cu instead of Co for the materials considered) at an atomic site. The on-site energy of the impurity is assumed to be the same of the bulk material forming the impurity (ie bulk Cu for Cu impurities), and the hopping tight-binding parameters depend on the type of sites surrounding the impurity. I do not introduce correlation between impurities and hence there are no clustering effects. Although this model is quite primitive and does not take into account perturbations of atoms in the proximity of the impurity, density functional calculations [103, 104] have shown that a good estimate of the resistivity of transition metal alloys in the low concentration limit is possible by considering only perturbations of the first nearest neighbours of the impurity. This suggests that this simple model should give a correct qualitative description of a 3*d* impurity in 3*d* transition metals.

As a third source of disorder I have considered the possibility of vacancies. A vacancy is introduced simply by setting an on-site energy to a large number (10^3eV in the present case), with all the hoppings to nearest neighbours set to zero. I do not consider aggregation of vacancies and assume a uniform distribution across the whole multilayer. Finally I model cross-section fluctuations of GMR nanowires by examining a wire of finite cross-section which is not repeated periodically in the transverse direction and mimics the fluctuations along the wire by introducing vacancies in the first monolayer

at the wire surface.

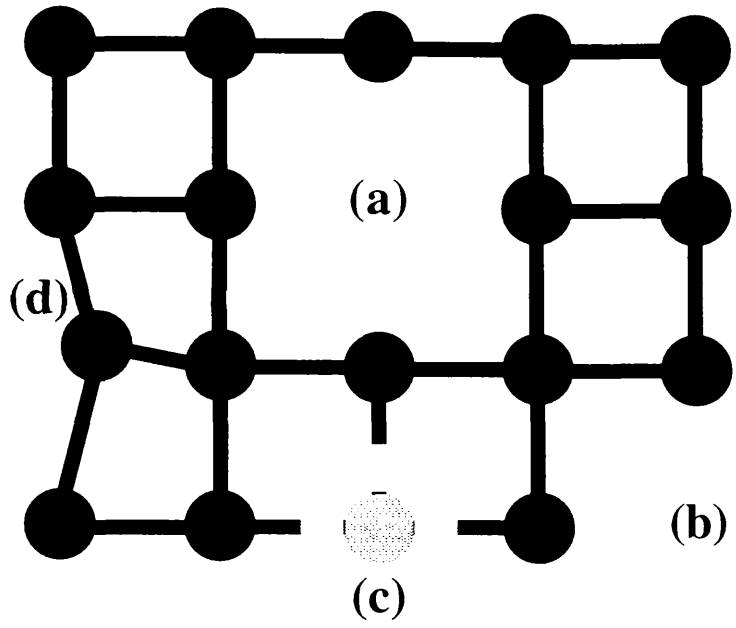

Figure 5.5: Schematic illustration of the disorder models considered: (a) vacancy, (b) vacancy at the boundary of the cell (cross-section fluctuation), (c) impurity (with hopping parameters the geometric mean of those for bulk and the impurity), (d) lattice distortion.

In all the calculations with disorder, I consider finite cross-sections involving 5×5 atomic sites, which I repeat periodically using up to 100 k -points in the 2D Brillouin zone. In the case of cross-section fluctuations I compute the ensemble-averaged conductance of wires with finite cross-sections as large as 15×15 atomic sites. It is important to note that in sputtered or MBE multilayers the typical cross-sections vary between $1\mu\text{m}^2$ and 1mm^2, which is several times larger than the typical phase breaking length l_{ph}. On the other hand in the case of electrodeposited nanowires the diameter of the wires is usually between 20nm and 90nm, but several wires are measured at the same times thereby yielding the mean conductance of an array of phase coherent nanowires, each with a cross-section of the order of l_{ph}^2.

5.4 Results and Discussion

5.4.1 Disorder-induced enhancement of the spin-polarization of the current

In this section I consider effects produced by Anderson-type disorder, impurities and lattice distortions. Despite the fact that the disorder in each of these cases is spin-independent the effect on transport is spin-dependent. In order to investigate the

different conductance regimes that may occur and their dependence on the magnetic state of the system it is convenient to consider as a scaling quantity the average spin conductance $\langle \Gamma^\sigma \rangle$ multiplied by the total multilayer length L and divided by the number of open scattering channels in the leads. I define the resulting "reduced" conductance g by means of the equation

$$g^\sigma = \frac{h}{e^2} \frac{\langle \Gamma^\sigma \rangle}{N_{\text{open}}} \cdot L \,, \tag{5.9}$$

where the number of open channels in the leads N_{open} in the case of a finite system is proportional to the multilayer cross-section. In the ballistic limit g increases linearly with a coefficient proportional to the conductance per unit area, in the diffusive (metallic) limit g is constant, and in the localized regime g decays as $g \propto \exp(-L/\xi)$ with ξ the localization length [110, 111]. Consider first the case of a random on-site potential. For Co/Cu multilayers with a width of disorder $W = 0.6$eV, figure 5.6 shows

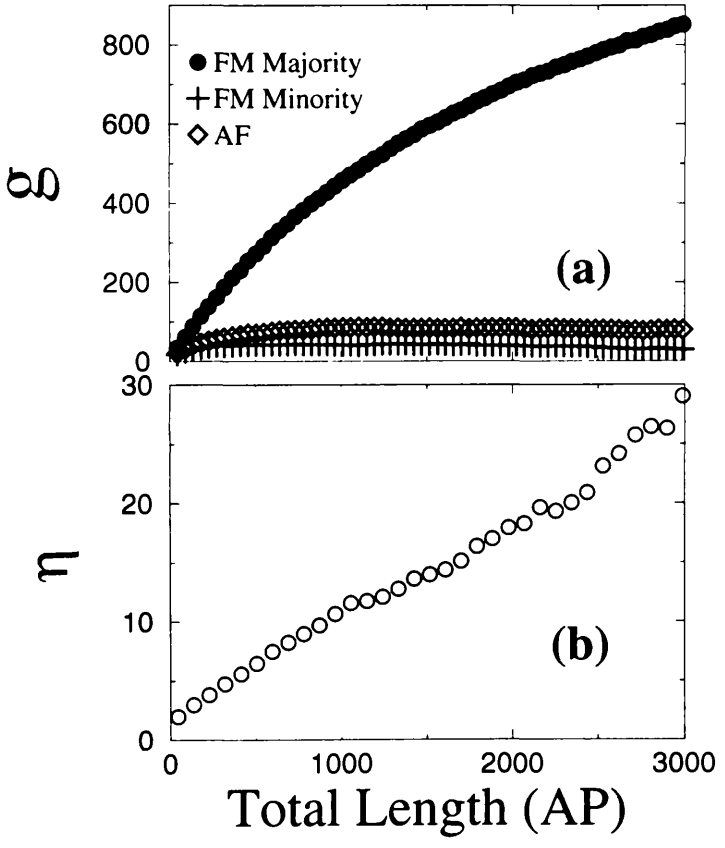

Figure 5.6: Reduced conductance g^σ and spin asymmetry $\eta = g^\uparrow_{\text{FM}}/g^\downarrow_{\text{FM}}$ as a function of the multilayer length for Cu/Co multilayers with random on-site potential. The random potential has a normal distribution of width 0.6eV, and the layer thicknesses are $t_{\text{Cu}} = 8$AP and $t_{\text{Co}} = 15$AP. Each point corresponds to a cell Co/Cu/Co/Cu of total thickness 46AP.

the quantity g for the two spin sub-bands in the FM and AF configurations along with the ratio $\eta = g^{\uparrow}_{\rm FM}/g^{\downarrow}_{\rm FM}$. These results were obtained for a cross-section of 5×5 atoms, and layer thicknesses of $t_{\rm Cu} = 8$ atomic planes (AP) and $t_{\rm Co} = 15$AP. In figure 5.6 the standard deviation of the mean is negligible on the scale of the symbols, and each point corresponds to an additional Cu/Co double bilayer. From the figure it is immediately clear that the spin-asymmetry of g (ie of the conductance) is increased by the disorder, which as a consequence of the band structure, turns out to be more effective in the minority band and in the AF configuration. In fact the disorder has the effect of spreading the DOS beyond the band edge, but does not affect the center of the band. The relevant quantity is the disorder strength defined as the ratio r_α between the width of the distribution of random potentials and the band width $r_\alpha = W/\gamma_\alpha$. For the set of parameters chosen the disorder strength of the s- and d-band is respectively $r_d = 0.7$ and $r_s = 0.22$. Since the current in the majority band of the FM configuration is carried mostly by s-electrons, for which the disorder strength is weak, the majority spin sub-band will not be strongly affected by the disorder. In contrast in the minority band and in both bands in the AF configuration, the current is carried by d-electrons, for which the scattering due to disorder is strong.

A second remarkable result is that in the FM configuration the almost ballistic majority electrons can co-exist with diffusive minority carriers. In the regime of phase coherent transport the definition of spin-dependent mean free paths for individual materials within the multilayer is not meaningful, and one must consider the spin-dependent mean free path for the whole multilayered structure. Hence I introduce the elastic mean free path for the majority (minority) spin sub-band in the FM configuration $\lambda^{\uparrow}_{\rm FM}$ ($\lambda^{\downarrow}_{\rm FM}$) and for both spins in the AF configuration $\lambda^{\uparrow\downarrow}_{\rm AF}$. This is defined as the length at which the corresponding conductance curve $g(L)$ changes from linear to constant (ie the length L^* corresponding to the crossing point between the curve $g(L)$ and the tangent to g in the region where g is constant). For the calculation in figure 5.6 it is possible to estimate $\lambda^{\uparrow}_{\rm FM} > 3000$AP, $\lambda^{\downarrow}_{\rm FM} \sim 500$AP and $\lambda^{\uparrow\downarrow}_{\rm AP} \sim 1000$AP. All of these results are obtained at zero temperature and voltage. At finite temperature, when the phase breaking length $l_{\rm ph}$ is shorter than the elastic mean free path, $l_{\rm ph}$ becomes the relevant length scale. The system can be considered as a series of phase coherent scatterers of length $l_{\rm ph}$ added in series through reservoirs [113]. The scattering properties of such a structure are solely

determined by elastic transport up to a length l_{ph}.

Turning now the attention to GMR, it is clear from figure 5.6 and the definition of the GMR ratio (3.1) that enhanced spin asymmetry will increase the GMR ratio because of the high transmission in the majority band. In figure 5.7 I present the GMR ratio as a function of the total multilayer length for different values of the width of the distribution of the random potential. From the figure it is possible to conclude that GMR strongly increases as a function of the disorder strength and that this is due to the increasing of the spin polarization of the conductance. Note also that the standard deviation of the mean GMR increases as a function of disorder and of the multilayer length. This is due to the approaching of the AF conductance to the localized regime, in which the fluctuations are expected to be large. The results of figures 5.7 seem

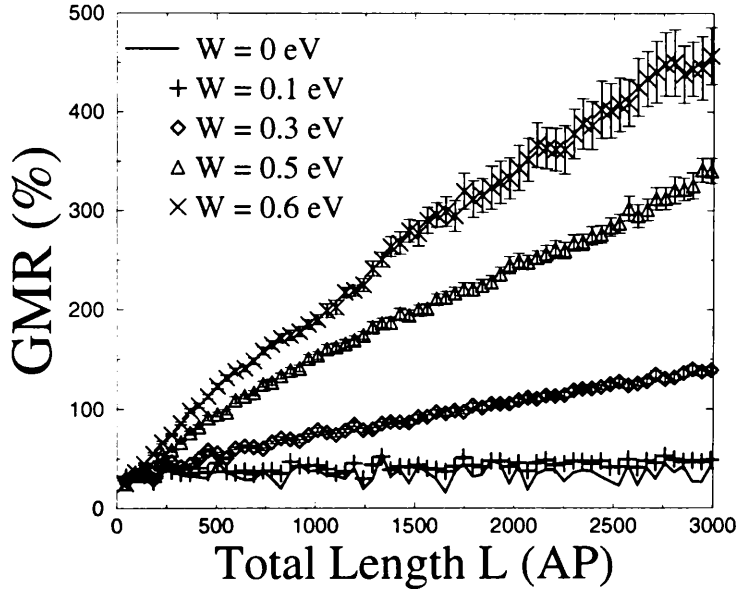

Figure 5.7: GMR as a function of the total multilayer length for different values of the on-site random potential. The layer thicknesses are t_{Cu} = 8AP and t_{Co} = 15AP and each point corresponds to a cell Co/Cu/Co/Cu of total thickness 46AP.

to be in contradiction with the published results of Tsymbal and Pettifor [53, 112]. In that case an analogous kind of disorder was employed together with an accurate *spd* tight-binding model, and the GMR ratio turned out to decrease with increasing disorder. They calculated the conductance for an infinite diffusive system using a small disordered unit cell in the direction of the current, namely a Co_4/Cu_4 cell (the subscripts indicate the number of atomic planes). To check this apparent contradiction

I have calculated the conductances and the GMR ratio for a $Co_5/Cu_5/Co_5/Cu_5$ unit cell attached to pure crystalline Cu leads. Apart from the resistances of the interfaces with the leads, the conductance for this system is proportional to the conductance calculated in reference [53] and figure 5.8 shows that the GMR ratio for such a short system does indeed decrease with disorder strength. This shows that for small cells, when the mean free path is much longer than the cell itself, the increase of all the resistances is not fully compensated by an increase of their spin-asymmetry, and this gives rise to a decrease of GMR. In contrast for thicker layers, provided the transport remains phase coherent, asymmetry builds up with increasing L and the resulting GMR ratio increases.

Consider now the effect produced by Cu impurities in the Co layers and by lattice distortions. The main features of both these kinds of disorder are very similar to the case of a random on-site potential: the GMR ratio increases as a function of disorder because of an increase in spin-asymmetry. Again the quantity g behaves quasi-ballistically for small lengths, followed by a diffusive region and finally by a localized regime. The mean free path at any disorder turns out to be longer for the majority spins in the FM configuration and the co-existence of ballistic majority electrons with diffusive minority electrons is still possible. This means that even in these cases spin-independent disorder produces spin-dependent effects. Similar arguments to the one used for the on-site random potential can be applied. In fact, in the case of impurities, we note from Table 5.1 that the alignment between the majority band of Co and the conduction band of Cu is better than that of the minority band of Co. Hence impurities are less effective in the majority band than in the minority. For lattice distortions, it is important to observe that the scaling of the hopping coefficients with the displacement from the equilibrium position is more severe for the d orbitals (see equation (5.8)). Since the current in the majority band is s-like while in the minority band and in the AF configuration it is d-like, this different scaling will result in larger disorder-induced scattering for the minority channel and for the AF configuration. Figure 5.9 shows the reduced conductances g for all the the spins in the case of uniform distributions of lattice displacements with different widths. From the figures I can conclude that: i) the spin-conductance asymmetry increases with increasing disorder ii) all the mean free paths decrease, iii) the contrast between $g^{\downarrow}_{\mathrm{FM}}$ and $g^{\uparrow\downarrow}_{\mathrm{FM}}$ increases with disorder.

I wish to conclude this section with some final remarks about length scales involved.

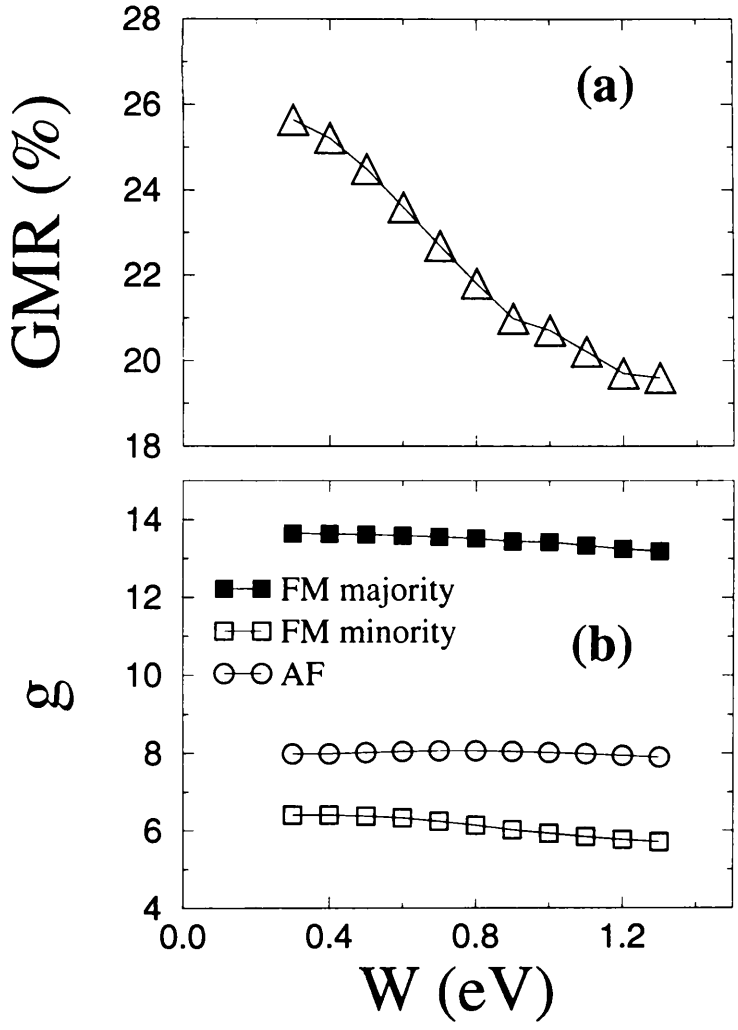

Figure 5.8: GMR and reduced spin conductances as a function of the width W of the normal distribution of on-site random potentials for a single Co/Cu/Co/Cu cell with Co and Cu thicknesses of 5AP. In this case, according with the results of reference [53] the GMR ratio decreases with the disorder strength. This is due to a general reduction of the mean free paths, which is not compensated by the enhancement of the spin-asymmetry of the conductance.

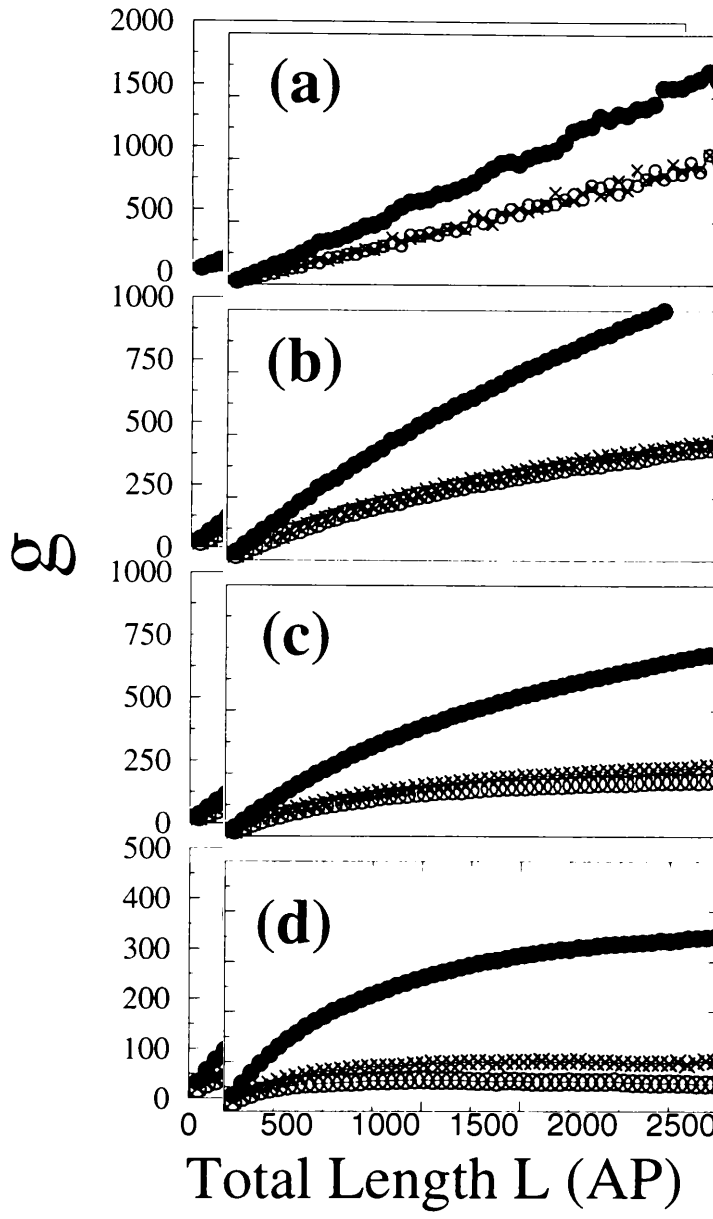

Figure 5.9: Reduced spin conductances g for different width of a normal distribution of lattice distortion: (a) $\delta r = 0$. (b) $\delta r = 0.02\%$, (c) $\delta r = 0.03\%$, (d) $\delta r = 0.05\%$. The symbols • (○) represent the majority (minority) spins in the FM configuration, and × the AF configuration. The layer thicknesses are $t_{Cu} = 8$AP and $t_{Co} = 15$AP and each point corresponds to a cell Co/Cu/Co/Cu of total thickness 46AP. Note the different vertical scales for the different disorders.

As mentioned above, since one is dealing with phase coherent transport, the concept of mean free path within the individual layers loses meaning, and one can only speak about the spin-dependent mean free path of the whole multilayer (ie $\lambda^{\uparrow}_{\rm FM}$, $\lambda^{\downarrow}_{\rm FM}$ and $\lambda^{\uparrow\downarrow}_{\rm AF}$). Nevertheless, if the mean free paths of both the spin sub-bands in the FM configuration extend over a length scale comparable with the cell Co/Cu ($\lambda^{\uparrow}_{\rm FM}, \lambda^{\downarrow}_{\rm FM} \sim t_{\rm Co} + t_{\rm Cu}$), the mean free path of the AF configuration is simply given by

$$\lambda^{\uparrow\downarrow}_{\rm AF} = \frac{\lambda^{\uparrow}_{\rm FM} + \lambda^{\downarrow}_{\rm FM}}{2}\,, \tag{5.10}$$

and a resistor network approach becomes valid at the length scale of the Co/Cu cell. I have checked this prediction by calculating the GMR ratio as a function of the number of double bilayers for multilayers with different Co layer thicknesses but the same concentration of impurities (8%). By increasing the Co thickness one can cross over from a regime in which the resistor network is not valid at the scale of the bilayer thickness to a regime in which the resistances of bilayers add in series. In the first case the GMR ratio will increase as the number of bilayers increases and in the second one expects a constant GMR. The result for a Co thicknesses of respectively 150AP, 50AP and 15AP is presented in figure 5.10. Note that for a phase-coherent structure the increase of GMR with the number of bilayers is different from the increase of GMR in diffusive systems when the total multilayer length is kept constant (as predicted by the Boltzmann approach [33] and observed experimentally [66, 101, 102]). In the latter case the effect is due to an interplay between the resistances of the different materials while in the former it is due to an increase of the spin asymmetry of the current. It is crucial to observe that the second effect is strictly connected with the non-local nature of the transport in high-quality magnetic multilayers. To date a massive increase of the GMR ratio with the number of bilayers has been observed in the CIP configuration [114, 115], while a systematic study of this effect in the CPP configuration is still lacking, although there is some evidence of a similar trend [35, 105] (see also last section of this chapter).

5.4.2 Reduction of mean free path

In this section I consider the effect of vacancies and cross-section fluctuations and their interplay with the other sources of disorder discussed in the previous section. I recall

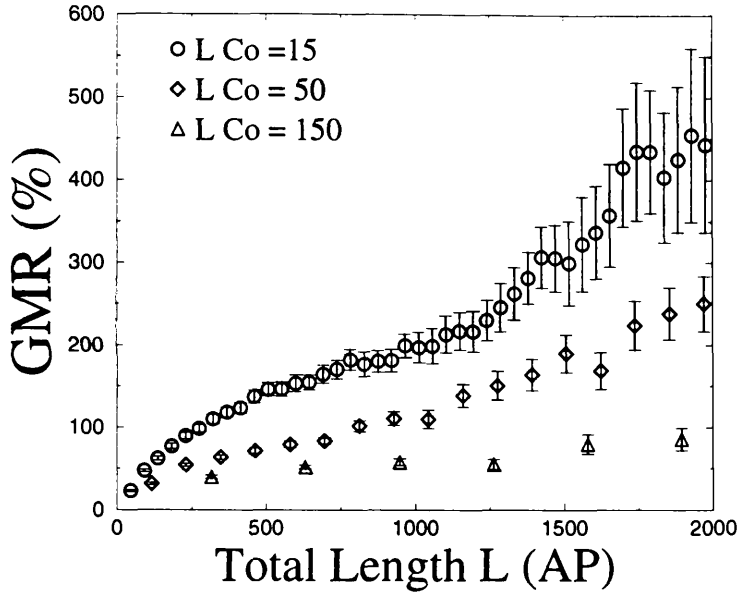

Figure 5.10: GMR as a function of the number of double bilayers for an impurity concentration of 8%. The Cu thickness is fixed to 8AP and the Co thickness is varied in order to show the crossover from a phase coherent regime to a regime in which a resistor network model is valid. Note that in the case of t_{Co} =150AP the GMR is almost independent of the total multilayer length.

that cross-section fluctuations are modeled as vacancies with a distribution concentrated at the boundaries of a finite cross-section multilayer (see figure 5.5). Hence it is natural to expect the qualitative behaviour of vacancies and cross-section fluctuations to be the same. As main feature these sources of disorder do not act on the two spin sub-bands in a selective way and produce only a small spin asymmetry. The largest effect is to drastically reduce the elastic mean free paths of all the spins. In figure 5.11 I present the reduced spin-conductances g^σ, the spin asymmetry η and the GMR ratio for a Co/Cu multilayer (t_{Cu} = 8AP, t_{Co} = 15AP) with a vacancy concentration of 1%. The results obtained for cross-section fluctuations are very similar and presented in figure 5.12. Figures 5.11 and 5.12 show that (in contrast with figure 5.6b) the spin asymmetry of the conductance is not greatly enhanced by the presence of vacancies and cross section fluctuations. For instance in the case of vacancies with the parameters used in the present simulation η varies from 1.6 to 3.5 for multilayers with a total thickness ranging from 46 to 3000 atomic planes. In contrast for the case of a random on-site potential of 0.6eV figure 5.6 shows that η varies from 2 to about 30 for the same range of multilayer lengths. Moreover it is important to note that in the case of a

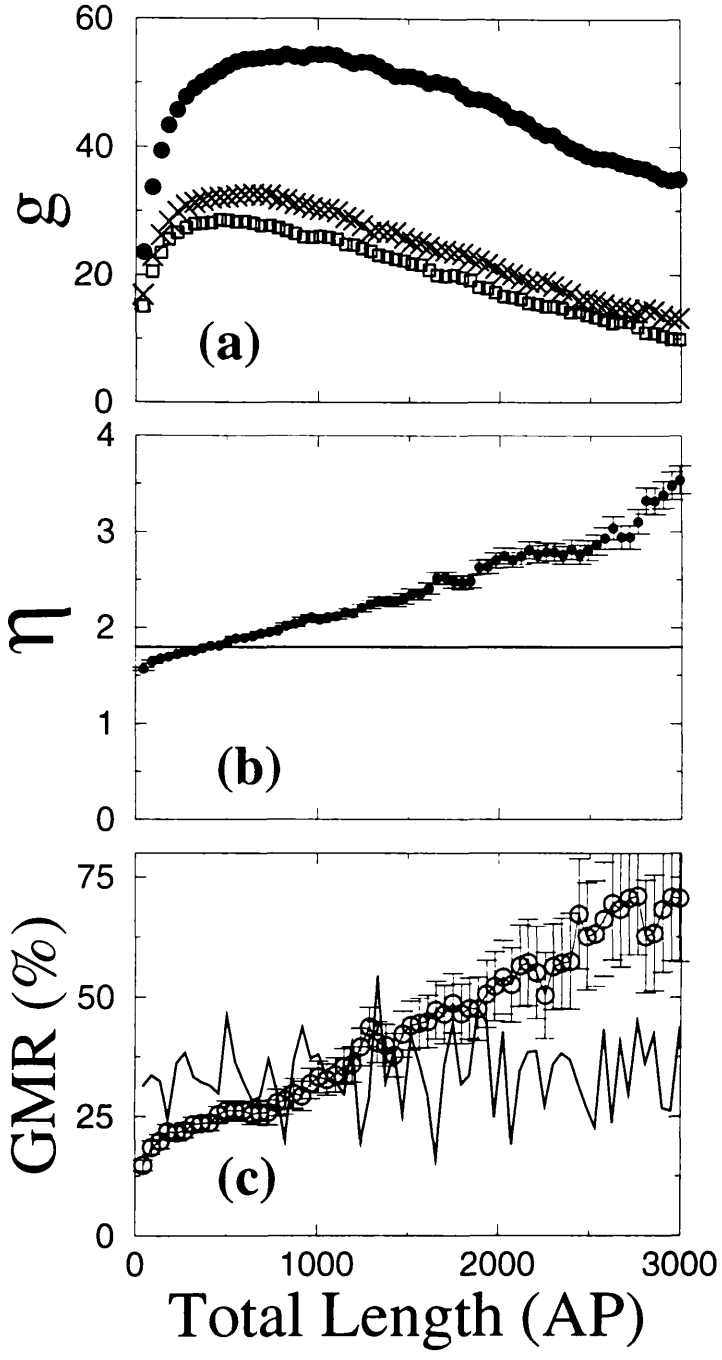

Figure 5.11: Effects of vacancies on Co/Cu multilayers. Figure (a) shows the reduced spin conductance for majority spin in the FM configuration (•), for minority spins in the FM configuration (□), and for the AF configuration (×). Figure (b) shows the spin asymmetry of the conductance and figure (c) the GMR. The horizontal line of (b) represents the average spin asymmetry of the conductance for the clean system. In figure (c) the symbols ○ represent the system with vacancies and the solid line the disorder-free system. The vacancy concentration is 1% and the thicknesses are t_{Cu} =8AP and t_{Co} =15AP.

random on-site potential the spin asymmetry of the current is always larger than in the disorder-free case. In contrast, when vacancies are present, the spin asymmetry of the current is smaller than the disorder-free case for short multilayers and becomes larger for longer multilayers. From figure 5.11 one can see that the crossover length (that I denote l_{cr}), defined as the length at which η for a system with vacancies equalizes η for the disorder-free case, is comparable with the mean free path of the minority spins in the FM configuration and of the AF configuration. It is important to note that the reduction of all the mean free paths with respect to both the vacancy concentration and the cross-section fluctuations is very severe. The reduced spin conductances g exhibit quasi-ballistic behaviour for lengths up to l_{cr}, and an almost localized behaviour for lengths larger than l_{cr}. The diffusive region is strongly suppressed and there is a small difference between all the spin-dependent elastic mean free paths. The spin asymmetry of the current can be enhanced by increasing the vacancy concentration, but this produces a further decreasing of the mean free paths and a further suppression of the diffusive region, resulting in a global reduction of GMR for lengths shorter than l_{cr}. For lengths longer than l_{cr} GMR is enhanced and this is due to the approach of $g_{AF}^{\uparrow\downarrow}$ to the localized regime. To date there is no evidence of localization effects in metallic magnetic multilayers and I believe that the results shown here are currently important only for lengths shorter than l_{cr}. To summarize, the main effects of vacancies are, on the one hand to reduce the spin asymmetry of the current for lengths shorter than l_{cr} and to enhance it for lengths larger than l_{cr}, and on the other to reduce drastically the mean free paths for all the spins in both magnetic configurations. The crossover length is comparable with the mean free path of the minority spin in the FM configuration and GMR is always reduced in the limit of quasi-ballistic transport. The qualitative results obtained for vacancies are broadly mirrored by those of cross-section fluctuations as it can be seen by comparing figure 5.11 and 5.12. Nevertheless some differences must be discussed. The simulations with cross-section fluctuations have been carried out with a finite cross-section, whereas for the case of vacancies I have considered a wire repeated periodically in the transverse direction. When cross-section fluctuations are introduced, the disorder-induced scattering scales as $P/S \propto 1/L$ with P the perimeter, S the area of the cross-section and $L = \sqrt{S}$. This introduces a new length scale, namely the cross-section linear dimension $l_{cs} = \sqrt{S}$. If this length is shorter than the mean free

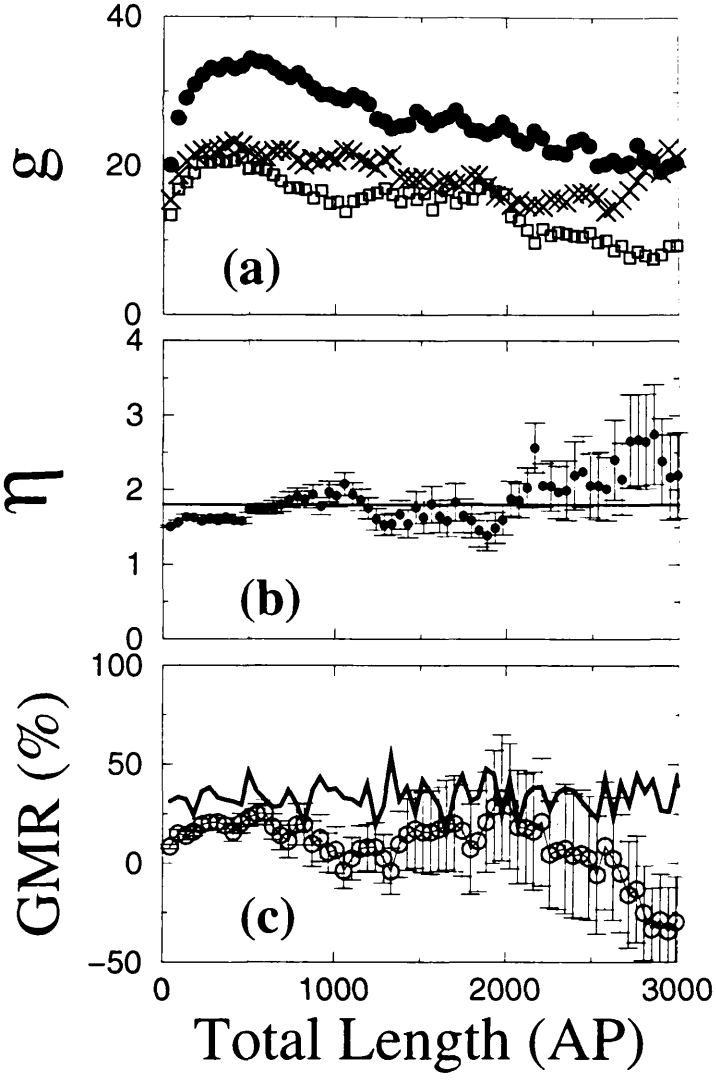

Figure 5.12: Effects of cross-section fluctuations on Co/Cu multilayers. Figure (a) shows the reduced spin conductance for majority spin in the FM configuration (•), for minority spins in the FM configuration (□), and for the AF configuration (×). Figure (b) shows the spin asymmetry of the conductance and figure (c) the GMR. The horizontal line of (b) represents the average spin asymmetry of the conductance for the clean system. In figure (c) the symbols ○ represent the system with cross section fluctuations and the solid line the disorder-free system. The cross section fluctuation concentration is 5% and the thicknesses are t_{Cu} =8AP and t_{Co} =15AP. The cross section in this calculation is 10 × 10 atomic sites.

paths, then a reduction of GMR will take place for the same reasons as in the case of vacancies, whereas if the mean free paths are shorter than l_{cs}, the effect of the cross-section fluctuations will be weak and no further reduction of the GMR will take place. Unfortunately, even with the optimized technique presented in the previous section it is very difficult to investigate the limit $\lambda \leq l_{cs}$. I have performed simulations with cross-sections up to 15×15 atomic sites, which is far below this limit, and have found no important deviations from the case of vacancies. A cross-section of 15×15 atomic sites corresponds to P/S of $0.26a_o^{-1}$ with a_o the lattice constant. This is comparable with the values of experiments [32, 101, 102] which can be estimated to range between $0.005a_o^{-1}$ and $0.025a_o^{-1}$. This suggests that the disorder strength in the present simulations is larger than the experimental values and that the effects of the cross-section fluctuations on GMR nanowires should be weak. On the other hand the model used for cross-section fluctuations involves only the first monolayer at the boundaries while in real systems the roughness extends over several monolayers. Moreover long range correlated surface roughness along the wires is likely to be present in real systems because of the structure of the nano-holes in which the wires are deposited. All these effects may result in a drastic enhancement of the disorder strength due to surface roughness and therefore a reduction of GMR.

A key result of the above simulations is that the reduction of GMR due to vacancies and cross-section-fluctuations may be compensated by a large increase of the spin asymmetry of the conductance. To address this issue I have performed simulations with both vacancies and non-magnetic impurities in the magnetic layers. The GMR ratios and spin asymmetries of the conductances are presented in figure 5.13 for Co/Cu multilayers with different impurities and vacancies concentrations. The figures show very clearly that competing effects due to impurities and vacancies can give rise to large values of GMR even for very disordered systems. The same value of GMR obtained in presence of impurities and vacancies can be obtained for a system with only impurities, but at a lower concentration. The fundamental difference between the two cases is that when impurities and vacancies co-exist, all the mean free paths are very small and the large GMR is solely due to the large spin asymmetry of the current. In this limit, despite the GMR ratio is large, a description of spin-transport based on the resistor network model is possible. More about this will be presented in the next section.

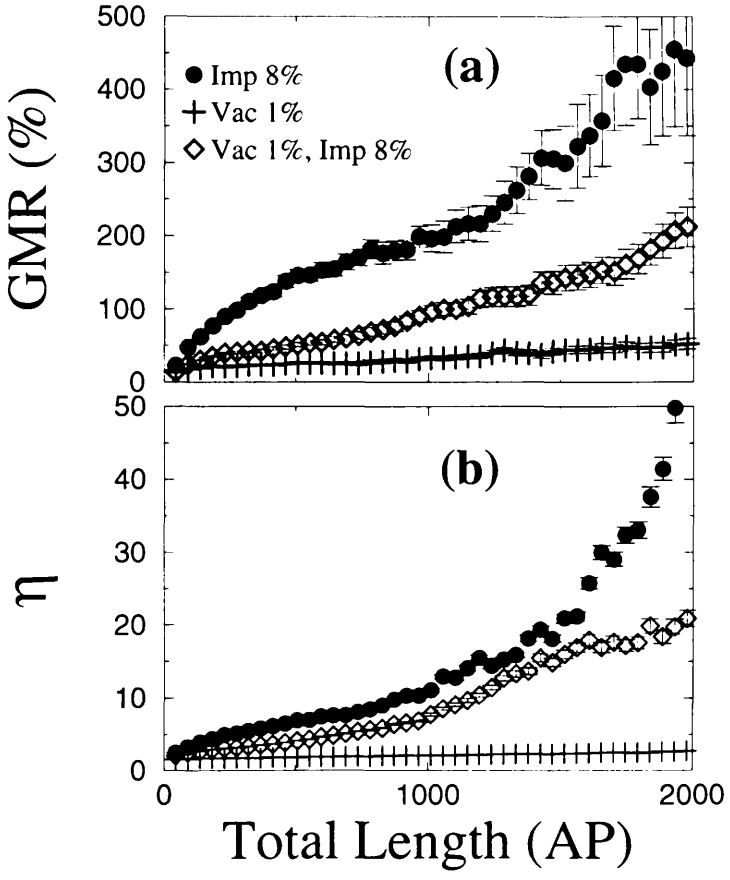

Figure 5.13: Competition between vacancies and impurities. Figure (a) shows the GMR ratio for Co/Cu multilayers with only impurities (•), only vacancies (+) and impurities and vacancies together (◇). Figures (b) shows the spin asymmetry of the current for the same samples. The layer thicknesses are t_{Cu} =8AP and t_{Co} =15AP.

5.5 Breakdown of the resistor model

In the introduction of this chapter I pointed out that one of the most successful models to describe CPP GMR in magnetic multilayers is the resistor network model, which can be derived from the Boltzmann's equation in the limit of infinite spin-diffusion length. Two important and central predictions of this model are that the CPP GMR ratio is independent of the number of bilayers in the case that the total multilayer length is not constrained to be constant, and furthermore is independent of the order of the magnetic layers in the case of different magnetic species. These two predictions arise directly from the fact that the transport is assumed to be local, which in the framework of quantum transport means that the phase breaking length is shorter than the layer thicknesses. An apparent violation of the first prediction has been observed in CIP and CPP measurements [35, 105, 114, 115], and of the second prediction in CPP measurements [35, 36, 105].

The aim of this section is to provide a quantitative description of the breakdown of the resistor model in diffusive CPP multilayers in the limit of infinite spin-relaxation length. To illustrate this breakdown, consider a multilayer consisting of two independent building blocks, namely a (N/M) and a (N/M′) bilayer, where M and M′ represent magnetic layers of different materials or of the same material but with different thicknesses and N represents normal metal 'spacer' layers. This is the experimental setup of references [35, 36, 105]. From an experimental point of view M and M′ must possess different coercive fields, in order to allow AF alignment. In the case of references [36, 105] this is achieved by considering Co and respectively $Ni_{84}Fe_{16}$ layers with Ag as non-magnetic spacer (reference [36]), and Fe layers with Cu as non-magnetic spacer (reference [105]). On the contrary in the case of reference [35] all the magnetic layers are made from Co (with Cu as spacer) but with different thicknesses (respectively 1nm and 6nm). Two kinds of multilayer can be deposited. The first, that I call type I ("interleaved" in the notation of reference [105]), consists of a $(N/M/N/M')\times\mu$ sequence where the species M and M′ are separated by an N layer and the group of four layers is repeated μ times. The second, that I call type II ("separated"), consists of a $(N/M)\times\mu(N/M')\times\mu$ sequence, where the multilayers $(N/M)\times\mu$ and $(N/M')\times\mu$ are arranged in series. If the coercive fields of M (H_M) and M′ ($H_{M'}$) are different (eg

$H_M < H_{M'}$) and if N is long enough to decouple adjacent magnetic layers, the AF configuration can be achieved in both type I and type II multilayers by applying a magnetic field H whose intensity is $H_M < H < H_{M'}$. The AF configuration is topologically different in the two cases, because in type I multilayers it consists of AF alignment of adjacent magnetic layers (conventional AF alignment), while in type II multilayers it consists of the AF alignment between the (N/M)$\times\mu$ and (N/M')$\times\mu$ portions of the multilayer, within which the alignment is parallel (see figure 5.14a and figure 5.14c). In other words the magnetization profile for the two types of multilayers is very different. This is not the case of the FM configuration, where the type I and type II differs only because of the different kind of layers M and M' (see figure 5.14b and figure 5.14d). From the point of view of a resistor network description of transport, the two types of multilayers are equivalent, because they possess the same number of magnetic and non-magnetic layers, and the same number of N/M and N/M' interfaces. Hence the GMR ratio must be the same. In contrast the GMR ratio of type I multilayers is found experimentally to be larger than that of type II multilayers [35, 36, 105], and the difference between the two GMR ratios increases with the number of bilayers. In reference [36] this effect is attributed to loss of coherence due to the short spin-diffusion length of permalloy. This explanation is not however applicable to the case of reference [35, 105] because of the well-known long spin-diffusion length of MBE-deposited Co and Fe. Moreover, in such a case the GMR ratio of both type I and type II multilayers increases with the number of bilayers, which again lies outside the resistor network model.

In this section I demonstrate that a description which incorporates phase-coherent transport over long length scales can account for such experiments. To illustrate this I have simulated type I and type II multilayers using a Co/Cu system with different thicknesses for the Co layers, namely $t_{\mathrm{Cu}} = 10\mathrm{AP}$, $t_{\mathrm{Co}} = 10\mathrm{AP}$, $t'_{\mathrm{Co}} = 40\mathrm{AP}$. The model I used is the two band-model discussed in this chapter with random on-site potentials to mimic generic disorder and to study the difference between type I and type II multilayers in different transport regimes. In the present calculation I consider disordered cubic supercells containing 100 atoms in the plane perpendicular to the current, and as many atomic planes as the total length of the multilayer. Such supercells are repeated periodically in the irreducible 2D Brillouin zone using 100 k-points. I

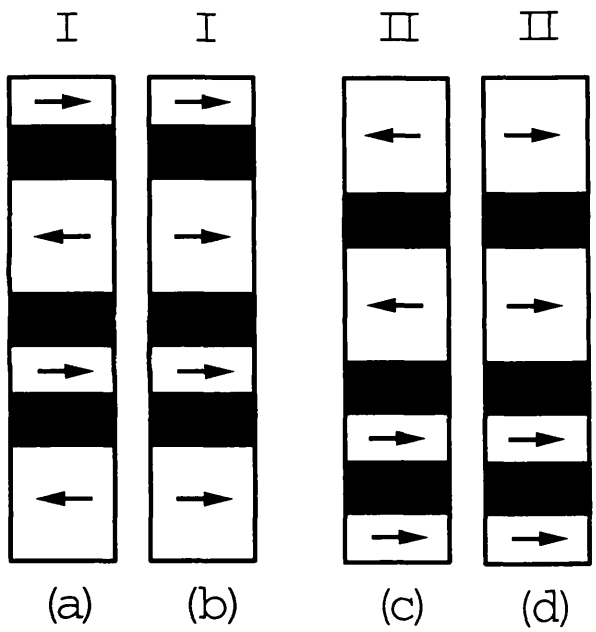

Figure 5.14: AF and FM configuration for type I and type II multilayers described in the text. Figures (a) and (c) refer to the AF configuration in the case of thick and thin Co layers with different coercive fields. Figures (b) and (d) are the corresponding FM configurations. The black blocks represent Cu, the white Co and the arrows indicate the direction of the magnetizations. Note that in the case of figure (c) the AF alignment occurs between the two halves of the multilayer.

checked the convergency of the calculation with respect to both disorder and cell size. Conductance per channel did not change by more than a few percent for cells containing more than 20 atoms and, due to the weak disorder considered, larger ensembles were not needed. In figure 5.15 I present the mean GMR ratio for type I (type II) multilayers GMR_I (GMR_{II}) and the difference between the GMR ratios of type I and type II multilayers $\Delta GMR = GMR_I - GMR_{II}$, as a function of μ for different values of the on-site random potential. The average has been taken over 10 different random configurations except for very strong disorder where I have considered 60 random configurations. In the figure I display the standard deviation of the mean only for ΔGMR because for GMR_I and GMR_{II} it is negligible on the scale of the symbols. It is clear that type I multilayers possess a larger GMR ratio than type II multilayers, and that both the GMR ratios and their difference increase for large μ. These features are in agreement with experiments [35, 36, 105] and cannot be explained within the resistor network model of CPP GMR. The increase of the GMR ratio as a function of the number of bilayers is a consequence of enhancement of the spin asymmetry of the current due to disorder, as I discussed in the previous section. In fact I recall that, even though

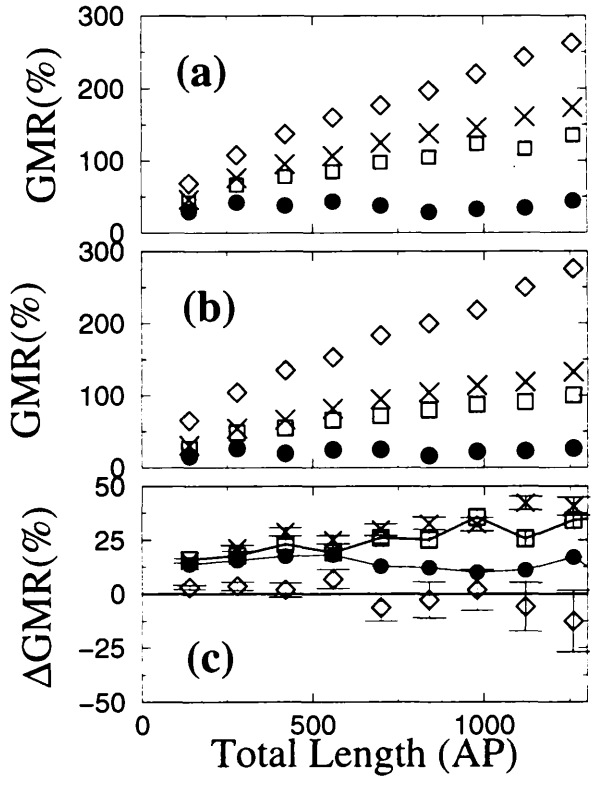

Figure 5.15: GMR for type I (a) and type II (b) multilayers, and ΔGMR (c) in the case of thin (10AP) and thick (40AP) Co layers, as a function of the number of double bilayers Co/Cu/Co/Cu for different values of disorder. The symbols represent respectively $W = 0$ (•), $W = 0.3$eV (□), $W = 0.6$eV (×), $W = 1.5$eV (◇). As an example the calculated mean free paths for $W = 0.6$eV are $l_{\mathrm{FM}}^{(\mathrm{I})\uparrow} \geq 4000$AP, $l_{\mathrm{FM}}^{(\mathrm{I})\downarrow} = 1300$AP, $l_{\mathrm{AF}}^{(\mathrm{I})\uparrow\downarrow} = 1800$AP, $l_{\mathrm{FM}}^{(\mathrm{II})\uparrow} \geq 4000$AP, $l_{\mathrm{FM}}^{(\mathrm{II})\downarrow} = 1700$AP, $l_{\mathrm{AF}}^{(\mathrm{II})\uparrow\downarrow} = 2300$AP.

the Anderson potential is spin-independent it is more effective on the d-band than on the s-band, because the former possesses a smaller bandwidth. Since the minority spin sub-band is dominated by the d-electrons and the majority by the s-electrons, the disorder will suppress the conductance more strongly in the minority band than in the majority. Moreover, since transport is phase-coherent, the asymmetry builds up with the length, resulting in a length-dependent increase of the GMR ratio. These features are shown in figure 5.16, where I present the reduced conductance g for both the multilayers and different values of disorder. It is important to note that, with the only exception of the disorder-free case, the g's of type I and type II multilayers are very similar in the FM configuration while they are rather different in the AF configuration. In the FM configuration in fact the conductance is largely dominated by the majority electrons, while in the AF configuration both the spin-electrons give the same contribution. Moreover the majority electrons undergo weak scattering either at the Co/Cu interfaces and due to disorder, while the opposite is the case for the minority electrons. Therefore the majority electrons and consequently the conductance in the FM configuration are not very sensitive to the order of the layers. In contrast in the AF configuration the conductance of type I multilayers is smaller than the one of type II multilayers and this is what gives rise to the different GMR ratios. The different GMR ratios of type I and type II multilayers are a consequence of the inter-band scattering, which occurs whenever an electron phase-coherently crosses a region where two magnetic layers have AF magnetizations. This occurs in each (N/M/N/M') cell for type I multilayers, while only in the central cell for type II multilayer (see figure 5.14a and 5.14c). Hence the contribution to the conductance in the AF alignment due to inter-band scattering is smaller in type I than in type II multilayers, as shown in figure 5.16. Eventually when the elastic mean free path is comparable with a single Co/Cu cell one expects the resistor model to become valid. To illustrate this feature, figure 5.15 shows that in the case of very large disorder ($W = 1.5$eV), ΔGMR vanishes within a standard deviation. In this regime the mean free path for the minority spins and the AF configuration is smaller than 100AP, while the mean free path of the majority spins is still large ($\sim$ 1000AP). This means that the resistor model is applicable only to the minority spins and to the AF configuration and that a phase-coherent approach is needed for the majority spins. Nevertheless, as pointed out above, the conductance

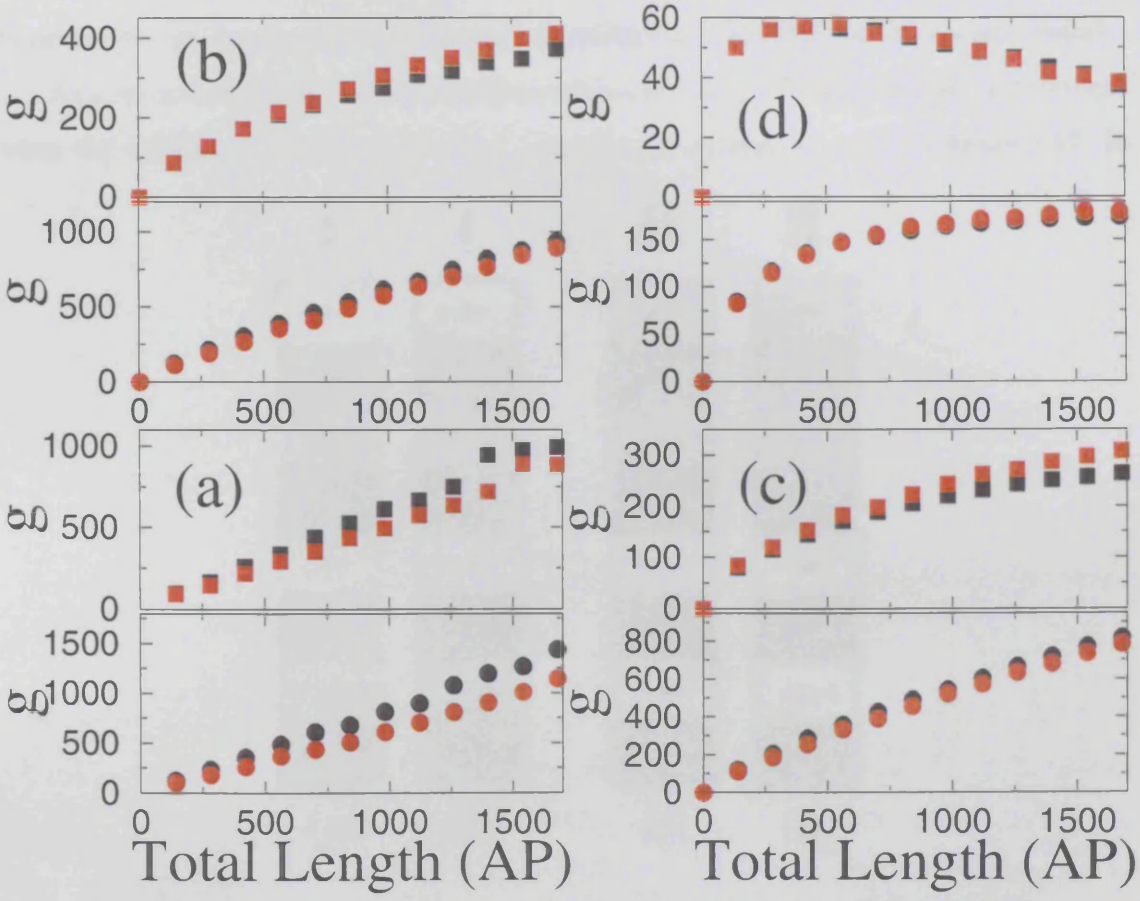

Figure 5.16: Reduced conductance g for type I and type II multilayers, in the case of thin (10AP) and thick (40AP) Co layers, as a function of the number of double bilayers Co/Cu/Co/Cu for different values of disorder: (a) $W = 0$, (b) $W = 0.3$eV, (c) $W = 0.6$eV and (d) $W = 1.5$eV. The upper plots ($\square$ symbol) represent the AF configuration while the bottom plots ($\bullet$ symbol) the FM configuration. Black and red symbols are for type I and type II multilayers respectively.

of the majority spins is only weakly dependent on the order of the layers. For these reasons, although the individual GMR ratios of type I and type II multilayers are still increasing with the number of bi-layers, their difference vanishes. Figure 5.16 shows very clearly this point. If one considers the highly disordered limit ($W = 1.5eV$), from figure 5.16d it is easy to see that the reduced conductance is the same for type I and type II multilayers in both the FM and AF configurations. This eliminates any difference between the two kinds of geometry and therefore the two GMR ratios become equal.

As a second example in which the dependence of the GMR ratio on disorder changes when the multilayer geometry is varied, consider the system sketched in figure 5.17. In

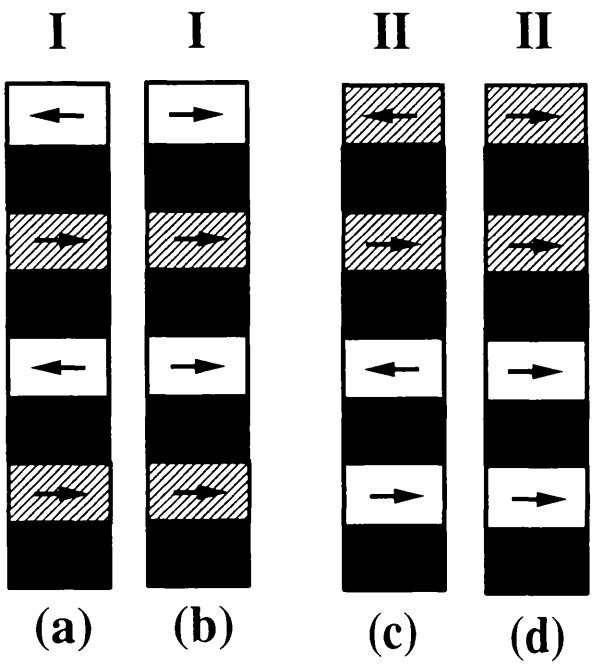

Figure 5.17: AF and FM configuration for type I and type II multilayers of the second example described in the text. Figures (a) and (c) refer to the AF configurations, figures (b) and (d) are the corresponding FM configurations. The black blocks represent Cu, the white Co and the hatched $Fe_{72}V_{28}$. The arrows indicate the direction of the magnetizations.

this case M and M′ are different materials chosen in such a way that the minority (majority) band of M possesses a good alignment with the majority (minority) band of M′. Moreover the thickness of the N layers has been chosen in order to allow an AF alignment of the magnetizations of adjacent magnetic layers in both type I and type II multilayers. In this case both type I and type II multilayers exhibit conventional FM and AF alignments, but their potential profile is quite different. In figure 5.18 I present a schematic view of the potential profiles for type I and type II multilayers for both the

spins in the FM and AF configuration. A high barrier corresponds to large scattering and a small barrier corresponds to weak scattering. The dashed line represents the effective potential for material M and and the continuous line for material M′. Figure 5.18 illustrates that type I multilayers possess a high transmission spin-channel in the AF alignment, and hence the resulting GMR ratio will be negative. In contrast type

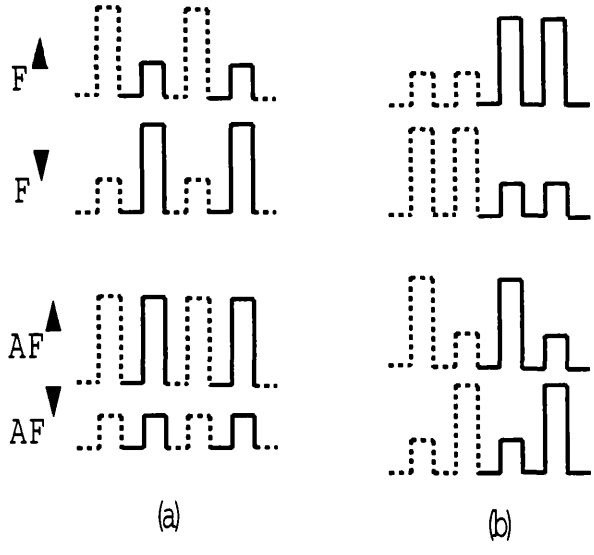

Figure 5.18: Heuristic scattering profiles for type I (a) and type II (b) multilayers of the second example discussed in the text. The dashed and continuous lines represent respectively scattering potentials of material M and M′.

II multilayers do not possess a high transmission channel (there are large barriers for all spins in both the FM and AF configuration) and the sign of the GMR ratio will depend on details of the band structure of M and M′. Consider the effects of disorder on these two kinds of multilayers. Using the same heuristic arguments as above one should expect that the GMR ratio of type I multilayers will increase (become more negative) as disorder increases, in the case of disorder that changes the spin asymmetry of the current. This is a consequence of the fact that, in common with the conventional single-magnetic element, one of the spin sub-bands in the AF alignment is dominated by weak scattering *s*-electrons (small barrier), which are only weakly affected by disorder. It is clear that this system is entirely equivalent to conventional single-magnetic element multilayers discussed above. In contrast for type II multilayers there are no spin sub-bands entirely dominated by the weak scattering (small barriers) *s*-electrons, and all spins in either the FM and AF configuration will undergo scattering by the same number of high barriers. In this case the effect of disorder will be to increase all the resistances

and this will result in a suppression of GMR. Moreover it is important to note that in the completely diffusive regime, where the resistances of the different materials may be added in series, the GMR ratio will vanish if $R_{\mathrm{M}}^{\uparrow(\downarrow)} \sim R_{\mathrm{M}'}^{\downarrow(\uparrow)}$, where $R_{\mathrm{A}}^{\uparrow(\downarrow)}$ is the spin-dependent resistance of the material A. To verify this prediction I have simulated both type I and type II multilayers using the parameters corresponding to Co and $Fe_{72}V_{28}$ respectively for M and M', and corresponding to Cu for N, taken from table 5.1. This choice was motivated by the fact that a reverse CPP-GMR has been obtained for $(Fe_{72}V_{28}/Cu/Co/Cu)\times\mu$ multilayers [116, 117]. The GMR ratio for type I and type II multilayers is shown in figure 5.19, which illustrates the remarkable result that the GMR ratio of type I multilayers increases with disorder, while for type II structures it decreases. As explained above this is due to an enhanced asymmetry between the conductances in the FM and AF alignment for type I multilayers, and to a global increase of all the resistances for type II multilayers. As far as I know there are no experimental studies of the consequences of the geometry-dependent effect described above, and further investigation will be of interest, in order to clarify the rôle of the disorder in magnetic multilayers.

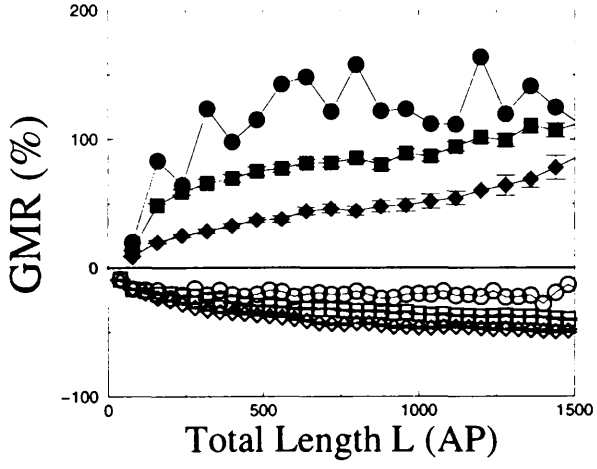

Figure 5.19: Different geometry-induced behaviour of the GMR ratio as a function of disorder in multilayers composed of Co and $Fe_{72}V_{28}$. In this case all the layer thicknesses are fixed at 10AP. The open (closed) symbols represent type I (type II) multilayers discussed in the text. The circles are the disorder free case, squares and diamonds are for random on-site potentials of 0.6eV and 1.2eV respectively.

6 GMR with Superconducting Contacts and FS Junctions

6.1 Introduction

In previous chapters I have considered spin-transport in a typical two-probe measurement, in which the current/voltage probes are made by ordinary non-magnetic transition metals. The aim of this chapter is to complete this analysis by considering the effects of superconducting contacts. This is relevant for understanding the transport of spin-polarized systems in contact with superconductors and the rôle of spin-flip scattering at the interface. The use of superconducting contacts will also highlight the need for a better understanding of the transport across Ferromagnet/Superconductor (F/S) ballistic junctions, which will be considered in the last section of this chapter.

Turn the attention to the case of two probe GMR measurements using superconducting contacts. The interest of these systems is twofold. On the one hand superconducting contacts have been always used by the group at Michigan State University [13] to achieved a uniform distribution of the current across the cross-section of the magnetic multilayers, and to perform squid measurements of the resistance. On the other hand, at a fundamental level, new physics associated with such structures arises from the proximity of two electronic ground states with different correlations (ferromagnetism and superconductivity), which can reveal novel scattering processes not apparent in the separate materials. The basic feature of the transport in ferromagnetic/superconductor and ferromagnetic-multilayer/superconductor systems is that the current is spin-polarized in the magnetic material, but it is not spin-polarized in the superconductor. Below the superconducting gap the current is solely determined by Andreev reflection [23], which involves electrons and holes with different spin orientations. In view of the spin-imbalance in a ferromagnet due to the exchange field, one may expect that Andreev reflection will be generally suppressed in the case of F/S junctions [118]. Moreover, since the Andreev reflection is a spin-polarized process, one may also expect a severe suppression of the GMR ratio when superconducting contacts are considered. Despite these important features past theoretical treatments of GMR have always neglected the presence of Andreev reflection at the leads. In this chapter I

will fill this gap and consider the GMR of a magnetic multilayer in which one contact is a superconductor and the other is a normal metal. This situation corresponds to the case in which the phase breaking length is shorter than the entire multilayer length. The analysis, carried out by considering both the realistic *spd* tight-binding model and the two-band model, will show the surprising result that the GMR is completely suppressed by the presence of a superconducting contact. Such a result, completely in contradiction with the measurements at Michigan State University, opens important questions on the nature of the interfaces with the superconductor. Agreement with experiments is achieved by postulating a large amount of spin-flip scattering at the surface of the superconducting contact. This appears to be consistent with recent experimental observations [119].

A better understanding of these issues can be achieved by considering ballistic N/S and F/S junctions. Recent nano-fabrication technology enables N/S and F/S ballistic point contacts to be made [22, 120, 121]. Transport in these structures has been shown to be ballistic and therefore its description is directly accessible by the calculation technique developed so far. I calculate the transport properties of several junctions and found that the I-V curve can be reproduced very accurately in the case of N/S (ie Cu/Pb) junctions, while this is not the case of F/S (ie Co/Pb) junctions. In particular the calculations underestimate the sub-gap conductance at very small bias. Possible sources of this discrepancy are the neglecting of spin-flip scattering and the local enhancement of the magnitude of the magnetization at the F/S interface. Several scenarios will be considered and a consistent picture of the spin dynamics of F/S heterojunctions will be given.

6.2 GMR and Superconducting Contacts

As pointed out in the introduction, although superconducting contacts have been largely employed in CPP GMR measurements [13], a complete theoretical description has never been given. In this chapter I will address this problem and show that as superconductivity is induced in one of the contacts (eg by lowering the temperature) CPP GMR is largely suppressed. The suppression is total in the case of diffusive and ballistic systems, even though for the latter case the GMR ratio is very sensitive to the

multilayer geometry and small GMR (either positive and negative) can be found. In an intermediate regime, when the majority spins are quasi-ballistic and the minority are diffusive, the GMR ratio can be different from zero. Nevertheless I will show that the GMR possesses an upper bound of 100% and larger GMR ratios cannot be achieved. This is strongly in contradiction with most of the experiments, where GMR ratios much larger than such a value have been found. Before going to describe the calculations and

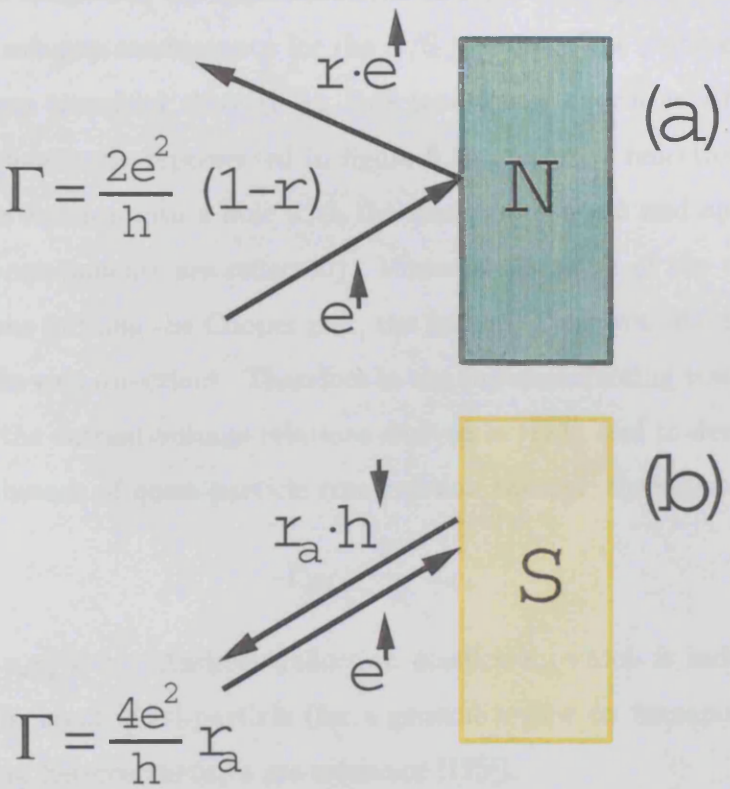

Figure 6.1: Schematic picture of N/N (a) and N/S (b) junctions and relative scattering processes. Note that the Andreev reflection is a spin-flip process, where the spin direction of the incoming electron and the reflected hole are opposite.

the results, I will briefly introduce the basic modification of the transport theory in the case of superconductivity. Consider for example a junction between a normal metal and a superconductor (N/S junction), as sketched in figure 6.1. In the case in which superconductivity is switched off, this reduces to a junction between two normal metals (N/N junction), whose conductance Γ_{NN} is simply given by the Landauer-Büttiker formula [24, 25, 26]

$$\Gamma_{NN} = \frac{e^2}{h}\left(T^{\uparrow} + T^{\downarrow}\right) , \tag{6.1}$$

where $T^\sigma = \mathrm{Tr}\, t^\sigma t^{\sigma\dagger}$, with t^σ the multi-channel transmission matrix for the spin σ. In this case every electron with spin σ crossing the interface with a transmission amplitude T^σ gives a contribution $\frac{e^2}{h}T^\sigma$ to the conductance. When one of the normal metal is replaced by a superconductor the situation is drastically different. In fact, because of the presence of the superconducting gap, free electrons with an energy $E < \Delta$ (Δ is the superconducting gap) cannot propagate within the superconductor. Nevertheless electrons can propagate in the superconductor in form of Cooper pairs, giving rise to a non-vanishing sub-gap conductance for the N/S junction. The pairing process responsible for sub-gap transport through an N/S junction is known as Andreev reflection [23] and is schematically represented in figure 6.1b. Andreev reflection consists in the reflection of an electron into a hole with the same momentum and opposite group velocity (all the components are reflected). Moreover, because of the opposite spins of the two electrons forming the Cooper pair, the incoming electron and the reflected hole possess opposite spin directions. Therefore in the superconducting state, equation (6.1) is replaced by the current-voltage relations derived in [123], and re-derived in [47, 124], which in the absence of quasi-particle transmission through the superconductor yields

$$\Gamma_{\mathrm{NS}} = \frac{4e^2}{h} R_{\mathrm{a}} \,, \tag{6.2}$$

where $R_{\mathrm{a}} = r_{\mathrm{a}} r_{\mathrm{a}}^\dagger$ is the Andreev reflection coefficient, which is independent on the spin σ of the incident quasi-particle (for a general review on transport in mesoscopic superconducting heterostructures see reference [125]).

For what follows it is important to note that the Andreev reflection is a process which does not conserve spin and in which the two spin-bands are coupled. This reflects the fact that the supercurrent in the superconductor is not spin-polarized. Therefore when a superconductor is brought into contact with a material in which the current is spin-polarized, one expects extra resistance at the interface [118, 126, 127] and the presence of depolarizing effects. Since the GMR in magnetic multilayers is an effect which arises from the spin-polarization of the current, it is reasonable to expect strong modifications by adding superconducting contacts.

To understand the rôle of superconducting contacts on the CPP GMR consider first the case of ballistic transport in which there is no disorder within the layers, nor at the interface. I have used the same *spd* tight-binding Hamiltonian introduced in Chapter 3,

with parameters corresponding to Cu, Co and Pb. Superconductivity is introduced by doubling the Hilbert space in order to take into account the degrees of freedom of the holes, and by coupling electrons and holes with the superconducting order parameter Δ. Δ assumes the value of the superconducting gap in bulk Pb (Δ_{Pb} =1.331·10^{-3} eV). The resulting Bogoliubov-De Gennes [128] Hamiltonian has the form

$$H_{BG} = \begin{pmatrix} H_0^{\uparrow} & 0 & \underline{\Delta} & 0 \\ 0 & H_0^{\downarrow} & 0 & -\underline{\Delta} \\ \underline{\Delta}^* & 0 & -H_0^{\downarrow *} & 0 \\ 0 & -\underline{\Delta}^* & 0 & -H_0^{\uparrow *} \end{pmatrix}, \tag{6.3}$$

where H_0^{σ} is the spin-dependent Hamiltonian describing the normal state and $\underline{\Delta} = \Delta \times \mathcal{I}$ with $\mathcal{I}$ the unit matrix. Note that if one considers the *spd* tight-binding model, the Hamiltonian H_{BG} is a $(36M) \times (36M)$ matrix, with M the number of atoms in the unit cell.

The system simulated consists in a Co/Cu multilayer with the Co and Cu layers respectively of 7 and 10 atomic planes, and in which the Co/Cu period is repeated 10 times. Such a structure is attached on one side to a Cu lead and on the other to a Pb lead. I represent such a system with the notation $Cu/[Co_7/Cu_{10}]_{\times 10}/Pb$. Figure 6.2a

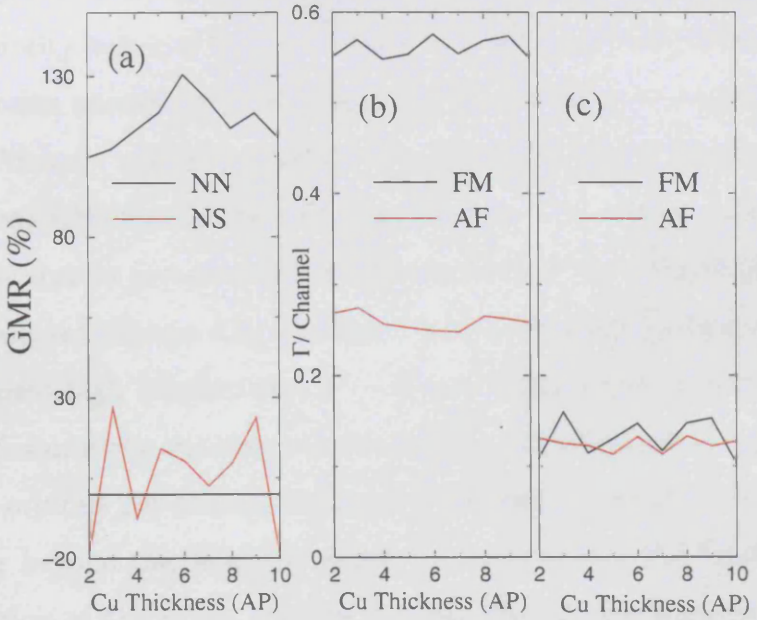

Figure 6.2: GMR ratio (a) and conductance in the FM and AF configurations (b and c) for the disorder-free system $Cu/[Co_7/Cu_{10}]_{\times 10}/Pb$. NN refers to the case in which Pb is in the normal state, NS to the case in which Pb is in the superconducting state. (b) shows the conductances in the NN case and (c) in the NS case. Note the dramatic suppression of the spin-polarization of the current when superconductivity is introduced.

shows results for the GMR ratio in the normal and superconducting states as a function of the Cu thickness, obtained by summing over $5{\cdot}10^3$ $k_{||}$ points, and clearly demonstrates a dramatic superconductivity-induced suppression of GMR. Figure 6.2b and 6.2c show results for the individual conductances per open channel and demonstrate that the GMR ratio suppression arises because Γ_{NS}^{FM} is drastically reduced compared with Γ_{NN}^{FM} and equals Γ_{NS}^{AF}.

To understand this effect, consider the simplest model of spin-dependent boundary scattering shown in figure 6.3, namely the Krönig-Penney potential introduced in Chapter 4. In the limit of delta-function ferromagnetic layers, it reduces to the model used to describe the N/F/S experiment of [22]. Fig 6.3a (6.3b) shows a cartoon of a majority (minority) spin, scattering from a series of potential barriers in successive FM aligned layers. Since the minority spins see the higher barrier, one expects $T_{FM}^{\downarrow} \prec T_{FM}^{\uparrow}$. Figures 6.3c and 6.3d show the scattering potentials for anti-ferromagnetically aligned layers, for which $T_{AF}^{\uparrow} = T_{AF}^{\downarrow} < T_{FM}^{\uparrow}$. For such an ideal structure, GMR arises from the fact that $T_{FM}^{\uparrow} \gg T_{FM}^{\downarrow}$ and $T_{AF}^{\uparrow}$. In the presence of a single superconducting contact this picture is drastically changed. For ferromagnetically aligned layers, figure 6.3e shows an incident majority electron scattering from a series of low barriers, which Andreev reflects as a minority hole and then scatters from a series of high barriers (figure 6.3f). The reverse process occurs for an incident minority electron, illustrating the rigorous result that the Andreev reflection coefficient is spin-independent. Figures 6.3g and 6.3h illustrate Andreev reflection in the anti-aligned state. The crucial point illustrated by these sketches is that in presence of a S contact for both the aligned (figures 6.3e and 6.3f) and anti-aligned (figures 6.3g and 6.3h) states the quasi-particle scatters from N (=4 in the figures) high barriers and N (=4) low barriers and therefore, one expects $\Gamma_{NS}^{FM} \sim \Gamma_{NS}^{AF}$. Of course the rigorous results of figure 6.2, obtained using an *spd* Hamiltonian with 36 orbitals per atomic site (*spd*×2 for spin ×2 for particle-hole degrees of freedom) go far beyond this heuristic argument, nevertheless the figure clearly shows that the reduction of the GMR ratio in entirely due to the suppression of the high transmission majority channel in the ferromagnetic configuration.

Having shown that GMR is suppressed by adding a superconducting contact in the case of perfectly crystalline systems, it is reasonable to ask if this effect survives in presence of disorder. Despite the use of the highly efficient recursive Green's function

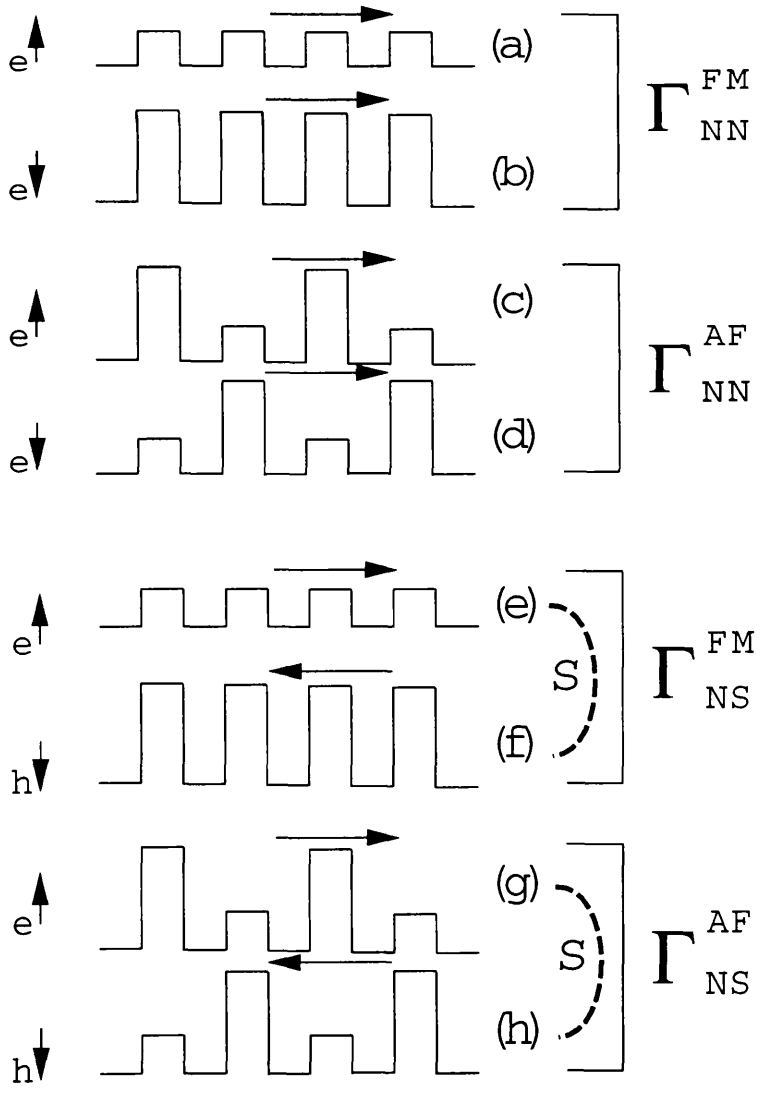

Figure 6.3: Cartoon of the different scattering processes. Figures (a), (b), (c) and (d) describes the transmission of spin electrons $e^{\uparrow(\downarrow)}$ in a NN system. Figures (e), (f), (g) and (h) describe the NS case. Note that in the FM case a majority (minority) spin electron $e^{\uparrow}$ ($e^{\downarrow}$) is Andreev reflected as a minority (majority) hole $h^{\downarrow}$ ($h^{\uparrow}$). In the antiferromagnetic (AF) case the path of the incoming electrons and out-coming holes is identical for both spins. The total number of large barriers is the same in the AF and FM case, and this produces GMR suppression.

technique to exactly evaluate the scattering matrix of a multilayer, currently available computing resources restrict such a calculation to systems with translational invariance parallel to the planes. To demonstrate that the suppression of CPP GMR is a generic feature of N/F/S hybrids and to study the effect of elastic impurity scattering, I now examine the reduced two band (s-d) model introduced in the previous chapter with a Hamiltonian matrix

$$H_{\mathrm{BG}} = \begin{pmatrix} H_0 - h & \underline{\Delta} \\ \underline{\Delta}^* & -H_0^* - h \end{pmatrix} . \tag{6.4}$$

In this model $H_0 \pm h$ is the spin-Hamiltonian for the normal system with h the exchange coupling, and $\underline{\Delta} = \Delta \mathcal{I}$ with Δ the superconducting order parameter. The tight-binding parameters are the ones presented in table 5.1 for Cu and Co and the superconducting gap is assumed to be $\Delta = 10^{-3}$eV. I consider as a model of disorder the simple Anderson model of Chapter 5 with a uniform distribution of random potential with width W =0.6eV. Figure 6.4 shows results for the GMR ratios in the normal and supercon-

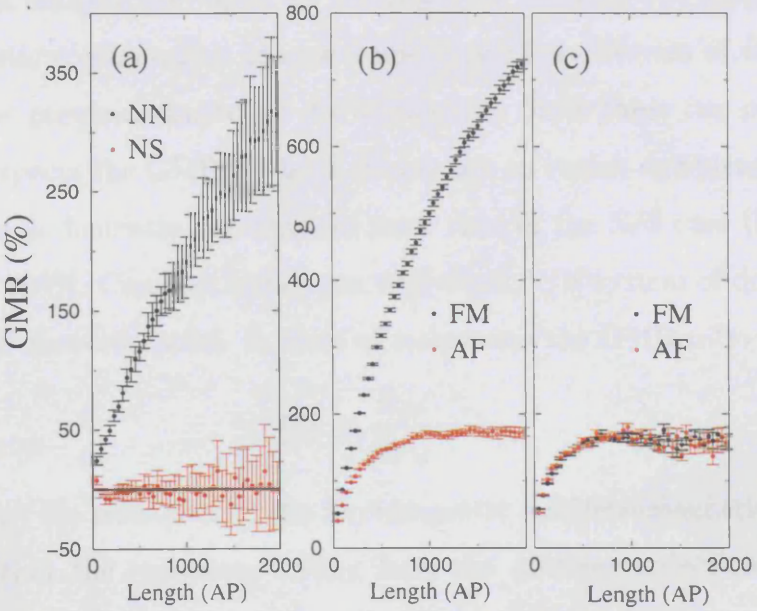

Figure 6.4: GMR (a) and reduced spin conductances g of Cu/Co multilayers calculated with the s-d two bands model, in the case of normal contacts (b) and with one N contact replaced by a superconducting (c) contact. The Co and Cu thicknesses are fixed and are respectively 15 and 8 atomic planes. Every point on the graph corresponds to an additional double bilayer Co/Cu/Co/Cu. The on-site energy fluctuates randomly according with a uniform distribution of width $W = 0.6$, and the error bars are the standard deviation of the mean over 10 random configurations. The unit cell is a square with 5×5 atomic sites, and I consider 25 $k-$points in the Brillouin zone. The horizontal line denotes GMR=0.

ducting case and demonstrates that the suppression of CPP GMR by superconductivity survives in the presence of disorder. The same argument used for completely ballistic

multilayers can be also used in the present case. If one assumes that all the transport is diffusive on the length scale of the individual layer thickness, the resistor network model can be applied. The cartoon of figure 6.3 can be re-interpreted by substituting the scattering potential with resistances in series, and elementary circuit analysis shows immediately that the GMR vanishes.

I have investigated a broad range of disorders and system sizes and find GMR suppression induced by superconductivity in all cases even though for some particular choices the suppression is not complete. As an example figure 6.5 shows the GMR ratio for a disorder with a uniform distribution of random potential of width W =0.4eV. In this case while the transport of the minority spins is almost diffusive, the one of the majority spins is quasi-ballistic. If one assumes the picture in which an N/S system can be mapped onto an equivalent N/N system with double size [129], it is clear that the difference between the conductances in the ferromagnetic and antiferromagnetic configuration is entirely equivalent to the difference between the conductances in the antiferromagnetic configuration of type I and type II multilayers of the first example discussed in the previous chapter in the section 5.5. Since these two conductances are different one expects the GMR in the N/S case not to vanish completely. Nevertheless I can use a simple heuristic argument to show that in the N/S case the GMR cannot be larger than 100%. Consider in fact the equivalent N/N system of double length and use the resistor network model. In term of resistances the GMR ratio is simply

$$\mathrm{MR} = \frac{R_{\mathrm{AF}}}{R_{\mathrm{FM}}} - 1 \,, \tag{6.5}$$

with R_{FM} (R_{AF}) the resistance of the ferromagnetic (antiferromagnetic) configuration. Suppose now that the resistance arising from the Andreev reflection can be written simply by adding in series the resistance of the incoming electron and outgoing hole (equivalent NN system). The GMR ratio becomes

$$\mathrm{MR} = \frac{2r_{\mathrm{AF}}}{r^{\uparrow}_{\mathrm{FM}} + r^{\downarrow}_{\mathrm{FM}}} - 1 \,, \tag{6.6}$$

with r^{σ} the spin-dependent resistance of the multilayer. Since $r^{\uparrow}_{\mathrm{FM}} < r_{\mathrm{AF}} < r^{\downarrow}_{\mathrm{FM}}$ one can immediately conclude that the GMR ratio in the case of superconducting contacts has an upper bound of 100%. This last result is still not consistent with the experiments of Michigan State University which show GMR ratio up to 150%. It is therefore clear that

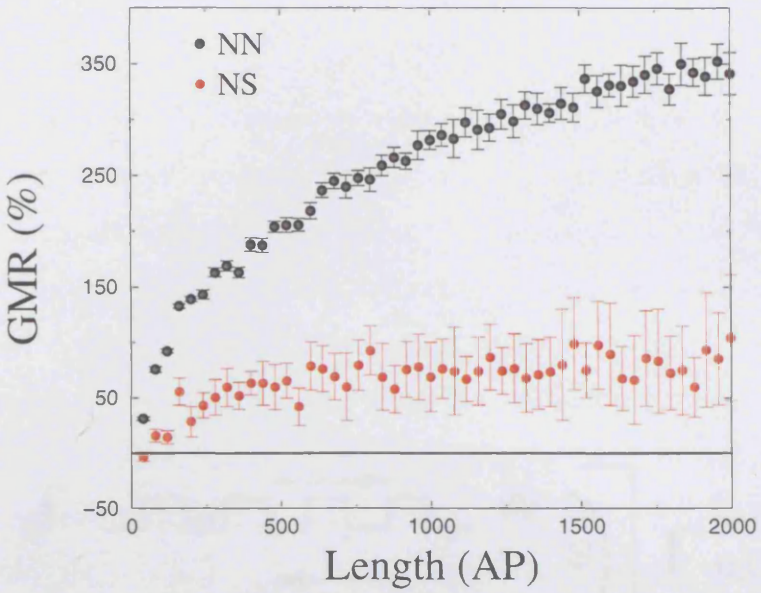

Figure 6.5: GMR of Cu/Co multilayers calculated with the s-d two bands model, in the case of normal contacts and with one N contact replaced by a superconducting contact. The Co and Cu thicknesses are fixed and are respectively 15 and 8 atomic planes. Every point on the graph corresponds to an additional double bilayer Co/Cu/Co/Cu. The on-site energy fluctuates randomly according with a uniform distribution of width $W = 0.4$, and the error bars are the standard deviation of the mean over 10 random configurations. The unit cell is a square with 5×5 atomic sites, and I consider 25 $k-$points in the Brillouin zone. The horizontal line denotes GMR=0.

some extra mechanism at the interface between the multilayer and the superconductor must occur. Here I propose that spin-flip at the interfaces can account for such a discrepancy. Consider in fact the cartoon of figure 6.6, where now I describe the Andreev reflection in presence of spin-flip at the interface. If a majority electron is Andreev reflected and spin-flipped, the corresponding outgoing hole will possess an up spin, and therefore propagate in the majority band. In this way the high transmission majority band is restored and the GMR ratio will not be suppressed. It is important to note that in this case the electrons responsible for the GMR signal are the ones which undergo to spin-flip at the interface. This situation is exactly opposite to the case in which no superconductors are present. The experimental study of the GMR in samples in which the superconductivity of the contacts can be switched on and off arbitrarily, is of great interest in order to to confirm this prediction. In the next section I will show that spin-flip at the interface may be considered also to explain the characteristic I-V curve of ballistic F/S junctions.

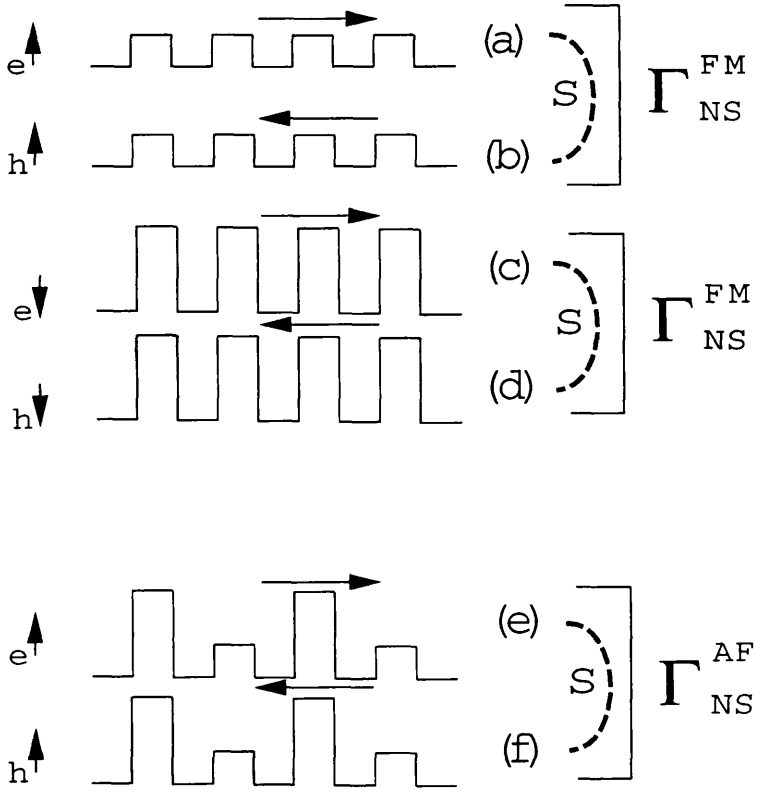

Figure 6.6: Cartoon of Andreev reflection in presence of spin-flip at the N/S interface. Figures (a-d) describe the FM configuration and figures (e-f) the AF configuration. Note that a majority spin electron is reflected like a majority spin hole, if spin-flip occurs at the interface (figures a and b). This produces high transmission in the majority spin-channel and therefore large GMR.

6.3 NS Ballistic Junctions

In the last twenty years the measurement of the spin-polarization of the current in ferromagnetic metals raised up some confusion due to the misleading idea of comparing polarization values inferred from different experiments. In particular the direct comparison of the polarization obtained from tunneling junctions and from devices where the direct current is measured shows very different results. The key point of all these measurements is that the quantity which is measured is the spin-polarization of a complicate structure, usually involving several different materials and interfaces. I have shown in the previous chapters that, when transport is phase-coherent, all the structure is important and the measured polarization may change simply as a result of changing the non-magnetic elements of the structure. For instance in magnetic multilayers based on Ni, the spin-polarization of the current in the ferromagnetic configuration may be switched from positive to negative, by using Pd ($P_{\mathrm{Ni/Pd}} = -0.34$) instead of Cu ($P_{\mathrm{Ni/Cu}} = 0.17$) as non-magnetic metal. Therefore the quantity to compare directly with experiments is the spin-polarization of the current of the specific device.

One recent and successful way to obtain information on the spin polarization of a system is by using ballistic F/S junctions and by measuring the change of the conductance due to the switching on of the superconductivity [22, 120, 121]. In the typical experimental setup a small constriction (usually 30nm long and 3-10nm thick) is made between a superconducting metal and another metal that can be either ferromagnetic or normal. The system is then cooled below the critical temperature for the superconductor and the I-V curve at small biases is measured. As a reference usually also the I-V curve for the equivalent F/N junction is measured at the same temperature. This is achieved by applying a magnetic field higher than the critical field of the superconductor. The quantity which is of interest is the normalized conductance $g(V)$ (not to be confused with the reduced conductance g defined in Chapter 5) as a function of the bias voltage V

$$g(V) = \frac{\Gamma_{\mathrm{FS}}(V) - \Gamma_{\mathrm{FN}}(V)}{\Gamma_{\mathrm{FN}}(0)} , \tag{6.7}$$

where $\Gamma_{\mathrm{FS}}(V)$ ($\Gamma_{\mathrm{FN}}(V)$) is the measured differential conductance for the F/S (F/N) junction. Experimentally, although the individual conductances fluctuate from sample to sample by up to one order of magnitude, the quantity $g(V)$ is constant. This is

a demonstration that the transport is ballistic and that the fluctuations of the conductance depend only on the size of the constriction (which can vary from sample to sample). Finally a fit of $g(V)$ is performed by using a modification of the Blonder-Tinkham-Klapwijk theory [130] with spin-dependent delta-like scattering at the interface, and hence the polarization is evaluated. Usually a remarkable good agreement with the experimental data is achieved particularly in the low bias region, where the fit is focused.

This kind of experiments is easily accessible to the scattering technique developed in this thesis. I have reproduced the I-V curves found in the experiments in order to obtain some informations on the scattering processes at the F/S interfaces. It is important to note that with the only exception of the superconducting gap (which is assumed to be the one of the bulk superconductor) there are not free parameters because all the tight-binding coefficients are fixed by an accurate fitting of the band structure for the bulk materials. Since $g(V)$ is measured for small bias, it is important to have a very accurate fit of the band structure in a narrow energy region close to the Fermi energy. I have performed such a fit for Cu, Co and Pb (the superconductor used in the references [22, 120]) by using a modified version of a fitting routine included in the tight-binding package OXON [131]. Details of this fitting procedure and the resulting band structures are discussed in appendix D.

The calculation of the conductance in the F/S and F/N cases uses the same technique of the previous section and of Chapter 2. Here I considered perfectly translational invariance across the entire structure (which means perfect lattice match at the interface) and I have taken only 30×30 $k_{\|}$-vectors in the transverse Brillouin zone, which gives roughly the same number of transverse modes of a constriction with a diameter of 10nm. I have consider Cu/Pb and Co/Pb constrictions and the hopping between different materials is, as usual, the geometric mean of the hoppings of the bulk materials. I calculate the conductance as a function of the energy $\Gamma(E)$ and then integrate in order to obtain the differential conductance at finite temperature. This last quantity respectively for the F/S and F/N case is calculated as follows [130]

$$\Gamma_{\mathrm{FS}}(V) = \int_{-\infty}^{+\infty} \left(-\frac{\partial f_0}{\partial E}\right) \Gamma_{\mathrm{FS}}(E) dE \,, \tag{6.8}$$

$$\Gamma_{FN}(V) = \int_{-\infty}^{+\infty} \left(-\frac{\partial f_0}{\partial E}\right) \Gamma_{FN}(E) dE \,, \tag{6.9}$$

where f_0 is the Fermi distribution. This is obtained by assuming that the effect of the temperature and the bias is only to change the occupation of the reservoir according to the Fermi distribution.

The calculated I-V curve for Cu/Pb is shown in figure 6.7 together with the experimental data from reference [22]. The agreement is surprisingly good particularly for low

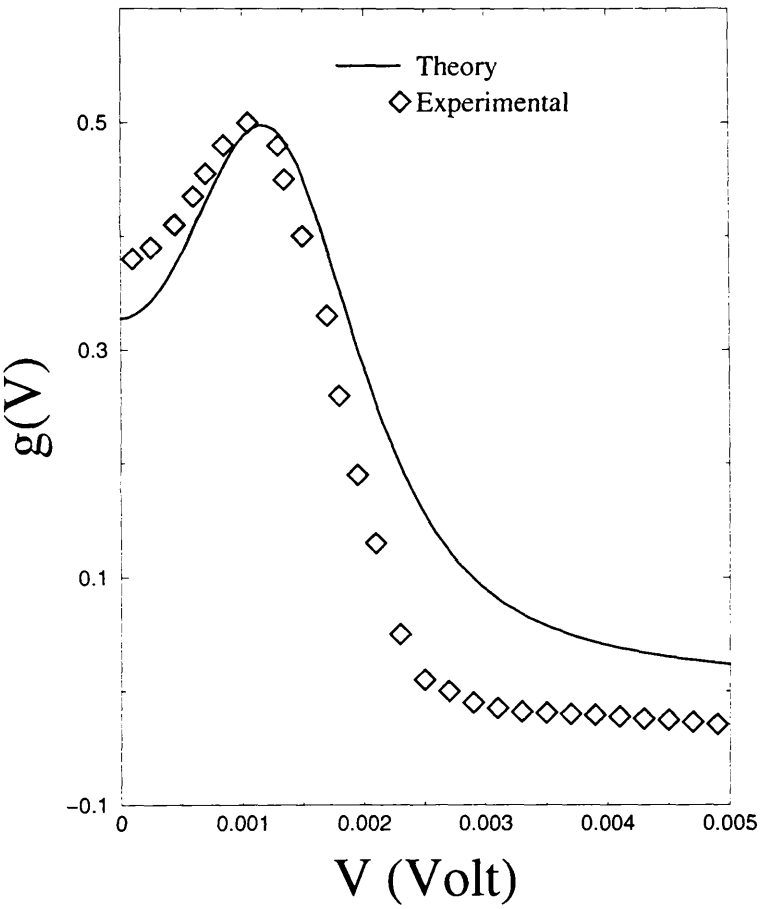

Figure 6.7: I-V curve for a Cu/Pb ballistic junction at 4.2°K. The solid line represents the calculated curve and the squares the experimental data from reference [22]. Note that the agreement is remarkably good particularly at low bias.

bias. Note that the experimental data show a negative $g(V)$ for large biases which is in contradiction with the elementary expectation of $g(V) \sim 0$ for $eV > \Delta$. Nevertheless this seems to be consistent with the experimental error on the determination of $g(V)$ [132] and therefore the agreement of the theoretical curve may be considered almost perfect over the whole voltage range. Better agreement can be obtained by reducing the

superconducting gap Δ below the bulk value for Pb. This is reasonable if one considers that in the constriction region size effects can suppress the superconductivity.

This surprisingly good agreement indicates that the scattering technique is the appropriate description of this kind of structures. In particular it is important to point out that, at least for the case of Cu/Pb, an accurate description of the hopping at the interface seems not to be crucial and all the transport is largely determined by the bulk band structures of the constituent materials. Since the lattice mismatch between Cu and Pb is very similar to the one between Co and Pb, one may expect that the same good agreement can be found also for Co/Pb interfaces. Figure 6.8 shows the I-V curve for a Co/Pb junction, where it is easy to see that such an expectation is largely not satisfied. In particular at zero bias the normalized conductance $g(V)$ is negative, which is the result of a strong under-estimation of Γ_{FS} with respect to the experiments. It is quite unlikely that such a disagreement is related with a very different quality of

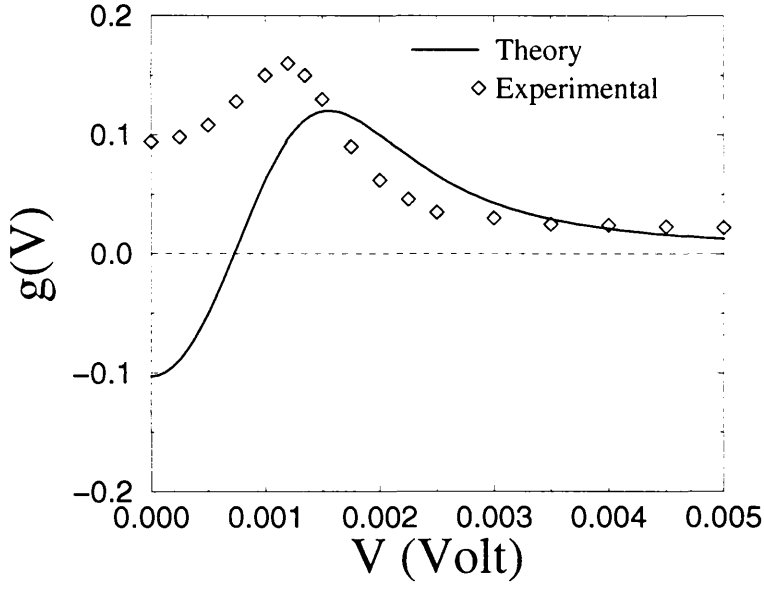

Figure 6.8: I-V curve for a Co/Pb ballistic junction at 4.2°K. The solid line represents the calculated curve and the squares the experimental data from reference [22]. Note that at low bias the calculated curve presents a $g(V)$ value with an opposite sign with respect to what found in experiments.

the junction in the the Co/Pb case with respect to Cu/Pb or to a bad fit of the band structure of Co, and therefore this must be connected with the magnetic state. One possible explanation is to postulate large spin-flip scattering at the interface. Like Nb in the case of the contacts for GMR measurements, Pb is a heavy material and spin-

orbit scattering can be large. Spin-orbit scattering is not a spin-conserving process and therefore induces spin-flip at the interface. This. as explained in the previous section, restores the high transmission in the majority channel. giving rise to a global enhancement of the conductance. Note that this process can be also present in the case of Cu/Pb junctions (because due solely to Pb) without producing any change of the resistance.

Another possibility is to assume an enhancement of the magnetization at the interface as recently found by several groups for different materials [69, 133]. If this enhancement is present, the band structure will be locally distorted and a better match between the Fermi surfaces of electrons with different spins is possible. This creates a global enhancement of the conductance in the F/S case and eventually $g(V)$ can be positive at low bias. Figure 6.9 shows $\Gamma_{FN}(0)$ and $\Gamma_{FS}(0)$ for Co/Pb as a function of the exchange coupling h of the first Co monolayer at the interface with Pb. It is clear that for a small range of exchange coupling $g(0)$ can indeed be positive with a maximum obtained for an exchange coupling of $h = 1.85eV$ (the bulk value is $h \sim 0.9eV$). The I-V curve corresponding to $h = 1.6eV$ is presented in figure 6.10 and shows that good agreement with experiments can be achieved. This is the central result of this section because it shows that I-V curves similar to the experimental ones can be obtained by making a detailed prediction of the materials characteristic of the F/S interface.

In summary I have shown that the description of ballistic N/S and F/S junctions is a powerful tool for the understanding of the scattering processes occurring at the interfaces. The scattering technique gives excellent agreement with the experimental data in the case of N/S junctions, but largely under-estimate the conductance in the case of F/S junctions. This may be due to the presence of spin-flip scattering, consistently with GMR measurements, or to a strong local distortion of the band structure of the magnetic metal. A completely self-consistent description of the interface can solve this ambiguity and give a complete solution of this fascinating problem.

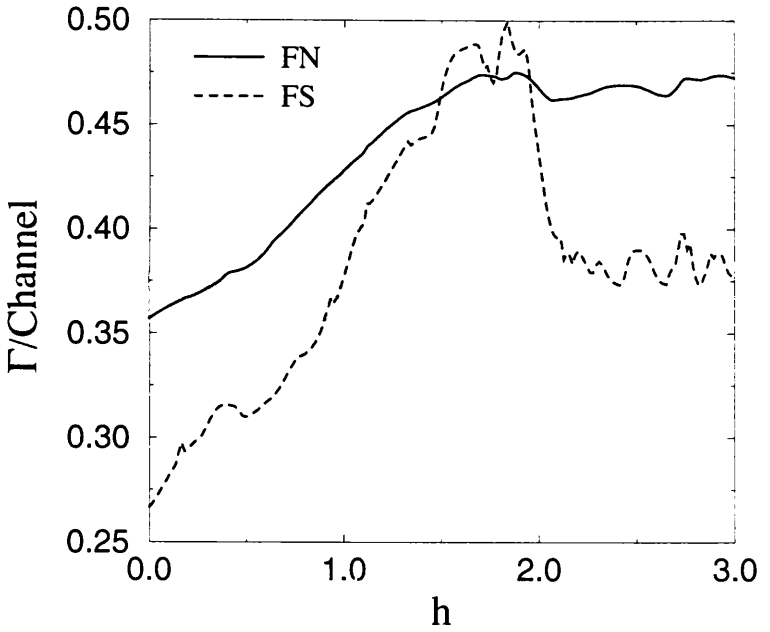

Figure 6.9: $\Gamma_{FN}(0)$ and $\Gamma_{FS}(0)$ at 4.2°K for a Co/Pb ballistic junction as a function of the exchange coupling of the first Co monolayer at the interface with Pb. Note that for a small window of exchange coupling $\Gamma_{FN}(0) < \Gamma_{FS}(0)$ and therefore $g(0) > 0$.

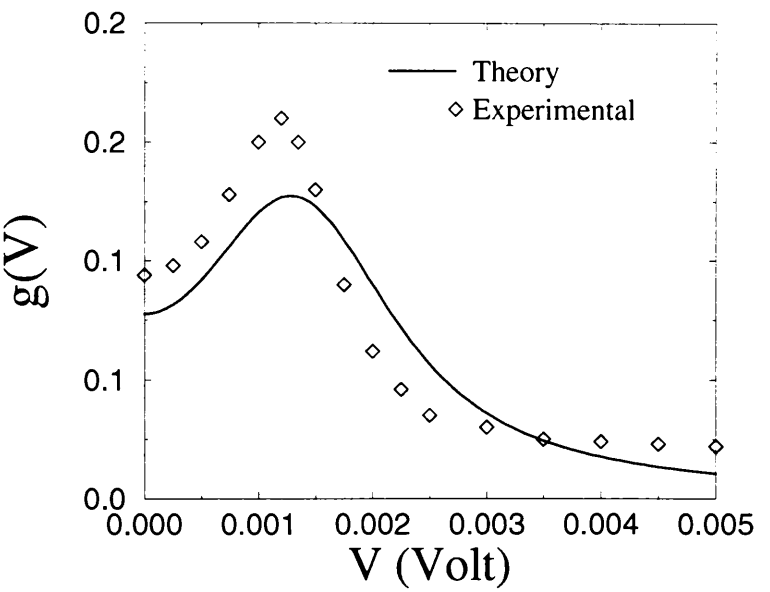

Figure 6.10: I-V curve for a Co/Pb ballistic junction at 4.2°K when a monolayer with an exchange energy of $h = 1.6$eV is added at the F/S interface. The solid line represents the calculated curve and the squares the experimental data from reference [22].

7 Carbon Nanotubes

7.1 Introduction

In this chapter I will concentrate on a new class of materials which in the last ten years raised up great enthusiasm for their amazing mechanical and electronical properties, namely carbon nanotubes. Carbon nanotubes [134, 135, 136] are narrow seamless graphitic cylinders, which show an unusual combination of a nanometer-size diameter and millimeter-size length. This topology, combined with the absence of defects on a macroscopic scale, gives rise to uncommon electronic properties of individual single-wall nanotubes [137, 138], which depending on their diameter and chirality, can be either metallic, semiconducting or insulating [139, 140, 141].

Here I will focus attention only on metallic nanotubes and in particular on the so-called "armchair" nanotubes. An armchair nanotube is a graphite tube in which the hexagon rows are parallel to the tube axis. If n is the number of carbon dimers along the nanotube circumference the tube will be labeled as (n, n) nanotube. One of the most important properties of the armchair nanotubes is that they behave like a mono-dimensional metal and this is directly connected with their structure. The electronic wave-length in fact is quantized around the circumference of the tube because of the periodic boundary conditions. This gives rise to mini-bands along the tube axis and the tube is metallic or insulating whether or not one or more mini-bands cross the Fermi energy. In the case of armchair nanotubes two mini-bands along the tube axis cross the Fermi energy [142, 143, 144], therefore, according to scattering theory [24], the conductance is expected to be $2G_0$, where $G_0 = 2e^2/h \sim (12.9\ \mathrm{k}\Omega)^{-1}$ is the quantum conductance. Direct evidence of the de-localization of the wave function along the tube axis has been already shown [145, 146], while a direct measurement of the conductance quantization for single-wall nanotubes is still missing (for an introduction to electronic transport in carbon nanotubes see reference [147]).

The situation for multi-wall nanotubes is rather different. A multi-wall nanotube consists of several single-wall nanotubes inside one another, forming a structure reminiscent of a "Russian doll". A section of a double-wall (5,5)@(10,10) armchair nanotube is presented in figure 7.1. Recent measurements [44] of the conductance in multi-wall nanotubes have raised a significant controversy due to the observation of unexpected

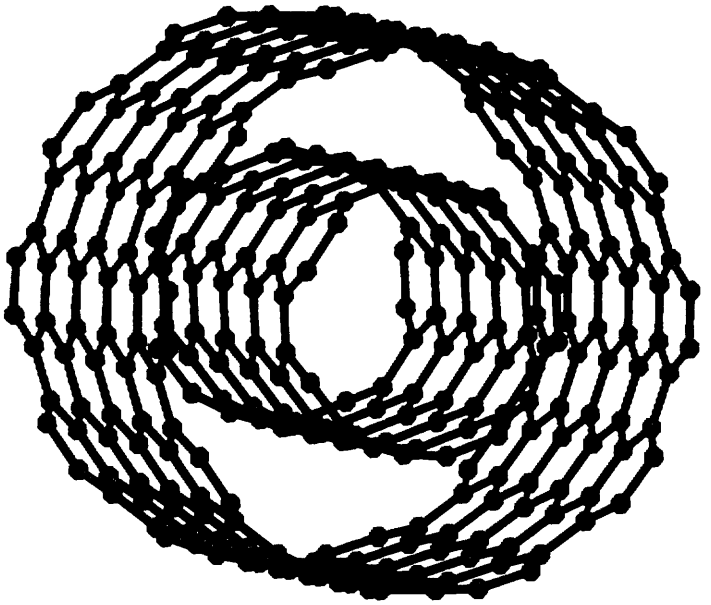

Figure 7.1: Section of a (5,5)@(10,10) "armchair" nanotube.

conductance values and of ballistic transport at temperatures far above room temperature. In these experiments several multi-wall nanotubes are glued to a gold tip, which acts as the first electrode, with a colloidal silver paint. The second electrode is made by a copper bowl containing mercury, which provides a gentle contact with the nanotube. The tip is lowered into the mercury and the two-probe conductance is measured as a function of the immersion depth of the tubes into the mercury. The main feature of the experiments is that at room temperature the conductance shows a step-like dependence on the immersion depth, with a value of $0.5\,G_0$ for low immersion and $1\,G_0$ when the tip is further lowered. The value of $0.5\,G_0$ usually persists for small immersion depths ($\leq$ 40nm) and is completely absent in some samples, while the value $1\,G_0$ is found for very long immersion depths, up to 0.5μm. Nevertheless some anomalies have been found with conductances of $0.5\,G_0$ lasting for more than 500nm [44].

While the ballistic behaviour up to high temperature can be explained by the almost complete absence of backward scattering [148], the presence of such conductance values is still not completely understood. In the absence of inter-tube interactions, if one assumes that m of the nanotubes forming the multi-wall nanotube are metallic

and in contact with both the electrodes, then a conductance of $2mG_0$ is expected for the multi-wall nanotube. This means that even in the extreme case in which only one tube is metallic and in contact with the electrodes a conductance of $2G_0$ must be measured. Therefore the values $0.5\,G_0$ and $1\,G_0$ are largely unexpected. One possible explanation, provided by the authors of the experiments, is that only the outermost tube is responsible for the transport and that the anomalous conductance is the result of scattering to impurities. Nevertheless both these hypotheses may be challenged. The first is based on the assumption that, since mercury does not wet the innermost tubes, it does not provide an efficient electrical contact with the innermost part of the multi-wall nanotube. This may not be the case because the interaction between the different walls may be large and the motion of electrons across the structure efficient. As far as the second hypothesis is concerned, it has been shown recently [149] that disorder averages over the tube's circumference, leading to an electron mean free path that increases with the nanotube diameter. Therefore single impurities affect transport only weakly, particularly in the nanotube forming the outermost shell, which has the largest diameter.

In this chapter I address these puzzling measurements and show that the structural properties of multi-wall nanotubes can explain their peculiar transport. The electronic band structure of multi-wall carbon nanotubes [150, 151, 152], as well as single-wall ropes [153, 154] is now well documented. More recently, it has been shown that pseudo-gaps form near the Fermi level in multi-wall nanotubes [152] due to inter-wall coupling, similar to the pseudo-gap formation in single-wall nanotube ropes [153, 154]. Here I demonstrate that the unexpected transport properties of multi-wall nanotubes arise from the inter-wall interaction. This interaction may not only block some of the quantum conductance channels, but also redistribute the current non-uniformly over the individual tubes. When only the outermost tube is in contact with one of the voltage/current electrodes, then this forms a preferred current path and, because of inter-tube interaction, the conductance of the whole system will typically be smaller than $2G_0$.

The chapter is organized as follows. In the next section I will briefly describe how to calculate the transport in infinite armchair single-wall and multi-wall nanotubes.

Since the unit cell must include two atomic planes the hopping matrix turns out to be singular, and a special trick must be used to solve the dispersion equation and built up the retarded Green's function. I will illustrate this procedure by using the decimation diagrams introduced in Chapter 5.

In the following section I will discuss the transport in infinite multi-wall nanotubes and understand which are the effects of the inter-tube interaction both on the dispersion and on the wave-function of the tube. Then I present the results for transport of inhomogeneous multi-wall nanotubes, giving an explanation of the experiments of reference [44]. In this part I will consider different scenarios regarding the structure of the electrical contacts.

Finally I will extend the analysis given in the previous sections for the zero-temperature limit to room temperature, in the limit in which the multi-walled scattering region is replaced by a continuous of states. In this classical limit, if only the outer-most tube forms an electrical contact with the metallic electrodes, the conductance is expected to be $1G_0$. A reduction of this value is expected in the case in which there is strong scattering between the single-walled and the multi-walled regions.

The last section is dedicated to the investigation of possible spin injection in carbon nanotubes. At present very few studies has been made both theoretical and experimental [41]. Nevertheless the absence of spin-mixing scattering and the low dimension of the tubes paves the way for the injection of spin-electrons into carbon nanotubes with extremely long spin life-time. This may open new hopes for spin-filtering devices and maybe quantum computation.

Most of the material of this section has been already published in references [42, 43].

7.2 Singularity of H_1

In this section I describe a trick necessary to calculate the retarded Green's functions of the carbon nanotubes. In this case two atomic planes must be included in the unit cell and therefore the matrix H_1 is singular. As indicated in Chapter 2, this is a problem since the dispersion relation expressed by equation (2.27) is not well defined.

The tight-binding parameterization of carbon nanotubes is determined by *ab initio* calculations for simpler structures [155]. The electronic structure and superconducting properties of the doped C_{60} solid [156], the opening of a pseudo-gap near the Fermi

level in a rope consisting of (10,10) nanotubes [154] and in (5,5)@(10,10) double-wall nanotubes [152] are some of the problems successfully tackled by this technique. The band structure energy functional is augmented by pairwise interactions describing both the closed-shell interatomic repulsion and the long-range attractive van der Waals interaction. This reproduces correctly the interlayer distance and the C_{33} modulus of graphite. Independent checks of this approach can be carried out by realizing that the translation and rotation of individual tubes are closely related to the shear motion of graphite. One expects that the energy barriers in tubes lie close to the graphite value which, due to the smaller unit cell, is easily accessible to *ab initio* calculations [157, 158].

For infinite nanotubes, both single-wall and multi-wall, the unit cell that I have used comprises two atomic planes. This is because two adjacent planes are identical but rotated by π/n degrees where n is the coordination number of the tube. Therefore the matrices H_0 and H_1 are respectively of the form

$$H_0 = \begin{pmatrix} H_0' & H_1' \\ H_1'^{\dagger} & H_0'' \end{pmatrix} , \tag{7.1}$$

$$H_1 = \begin{pmatrix} 0 & 0 \\ H_1'' & 0 \end{pmatrix} . \tag{7.2}$$

The previous expressions describe a system in which the inequivalent atomic planes are described by the matrices H_0' and H_0'', and H_1' describes the coupling between the H_0' plane and the H_0'' plane, while H_1'' describes the coupling between the H_0'' plane and the H_0' plane. Such a structure can be represented by the decimation diagrams of figure 7.2. In order to obtain a non-singular matrix H_1 I have decided to use the decimation technique introduced in Chapter 2 for the scatterer. The main idea in fact is to decimate all the degrees of freedom of the unit cell which are not coupled with degrees of freedom of the next unit cell and hence to define a new non-singular H_1 matrix. For this purpose consider the figure 7.2. The procedure consists in decimating all the planes described by H_0'' yielding a new intra-plane matrix H_0^* and a new inter-plane matrix H_1^*. Note that the new matrices H_0^* and H_1^* have dimension which is a half of the dimension of the starting matrices H_0 and H_1 of equations (7.1) and (7.2). In performing this procedure one should be careful to decimate the H_0'' planes both on the left- and on the right-hand side of H_0' in order to obtain a new periodic structure.

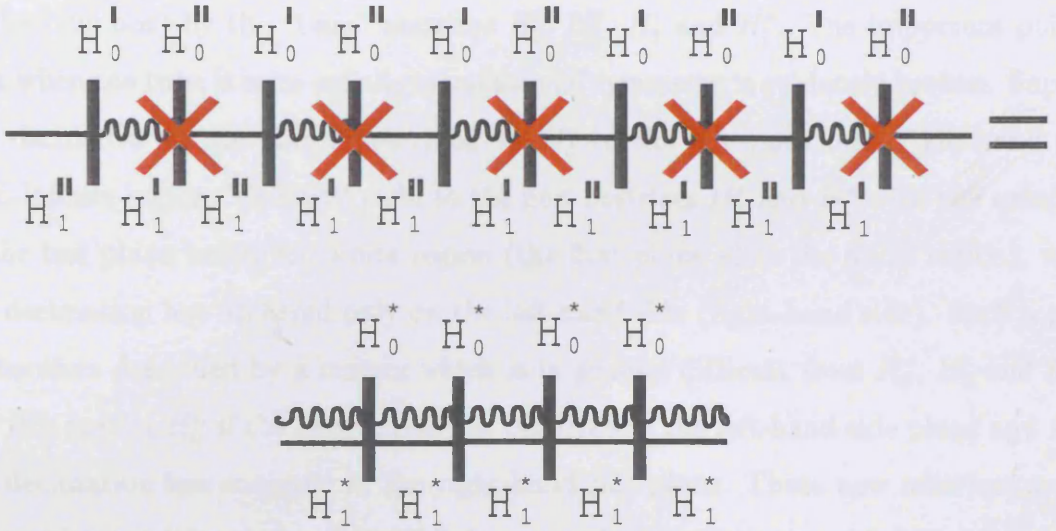

Figure 7.2: Decimation diagrams for the carbon nanotubes unit cell. This procedure enables to construct a non-singular coupling matrix H_1.

The rules to perform such a decimation are illustrated in figure 7.4a and 7.4b where the new matrices H_0^* and H_1^* are defined. Note that the new structure defined by these new matrices is periodic and that the coupling matrix H_1^* is non-singular.

Finally special attention must be used when a finite scatterer is attached to semi-infinite carbon nanotubes described by the new matrices H_0^* and H_1^*. To illustrate this point consider the decimation diagrams of figure 7.3 where I take two semi-infinite nanotubes attached to a scattering region. The aim is to describe the two semi-infinite

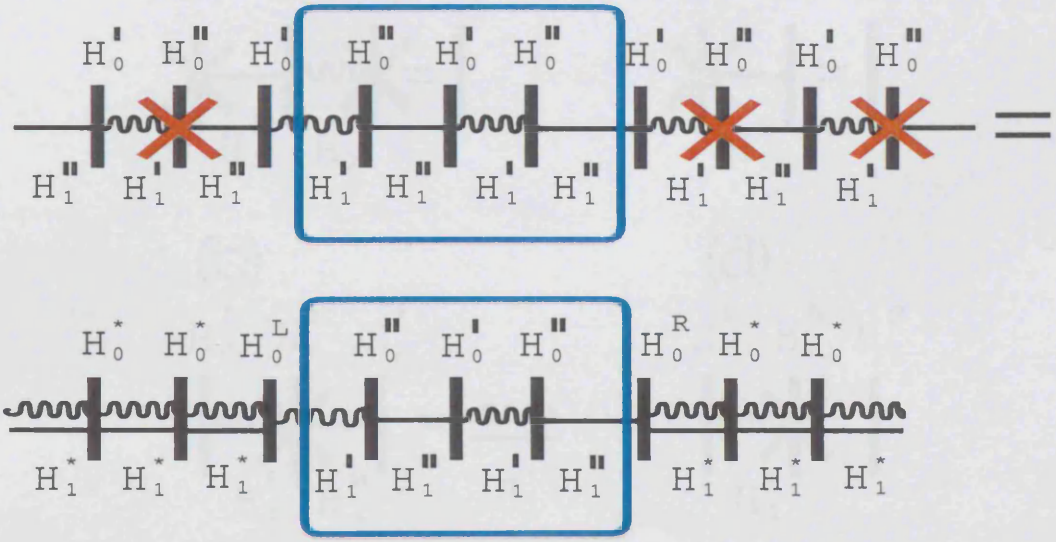

Figure 7.3: Decimation diagrams for two semi-infinite carbon nanotubes attached to a finite scattering region (also a carbon nanotube). The purpose is to describe the semi-infinite parts by the renormalized matrices H_0^* and H_1^* and the finite part by the "bare" matrices H_0', H_0'', H_1' and H_1''.

nanotubes by the new matrices H_0^* and H_1^* and a finite middle region (the one included

in the blue box) by the "bare" matrices H_0', H_0'', H_1' and H_1''. The important point is that when the tube is semi-infinite translational symmetry is evidently broken. Suppose one decimates all the planes described by H_0'' in the left-hand side (right-hand side) semi-infinite region. This will yield to the new matrices H_0^* and H_1^* with the exception of the last plane before the finite region (the first plane after the finite region), where the decimation has occurred only on the left-hand side (right-hand side). Such a plane is therefore described by a matrix which is in general different from H_0^*, H_0' and H_0''. I call this matrix H_0^{L} if the decimation has occurred in the left-hand side plane and H_0^{R} if the decimation has occurred in the right-hand side plane. These new matrices are the ones which must be used to attach finite scattering regions to semi-infinite nanotubes. I illustrate this point in figure 7.3 by using the decimation diagrams. In the figure the upper part describes the structure and the position of the planes to decimate, and the lower part the result of the decimation.

To conclude in figure 7.4 I summarize all the decimation rules introduced in this section.

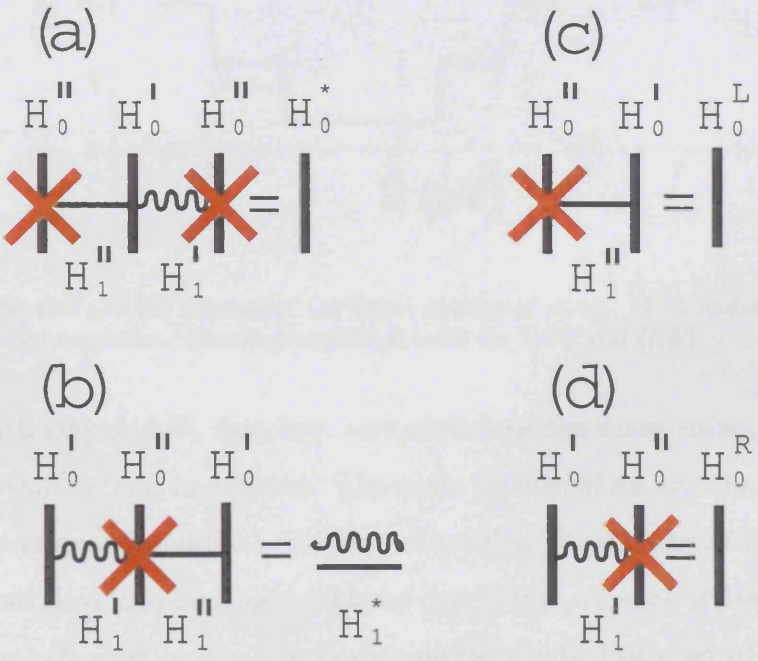

Figure 7.4: Summary of all the decimation rules introduced in this section: (a) new on-site matrix H_0^*, (b) new non-singular coupling matrix H_1^*, (c) last left-hand side matrix of the left-hand side lead H_0^{L}, (d) first right-hand side matrix of the right-hand side lead H_0^{R}.

7.3 Conductance in infinite multi-wall nanotubes

For an homogeneous system the total transmission coefficient $T(E)$ assumes integer values corresponding to the total number of open scattering channels at the energy E. For individual (n, n) armchair tubes, this integer is further predicted to be even [142, 143, 144], with a conductance of $2G_0$ near the Fermi level. As an example, the results for the conductance $G(E)$ and the density of states of the $(10, 10)$ nanotube are shown in Fig. 7.5. In this section I combine the scattering technique with the procedure

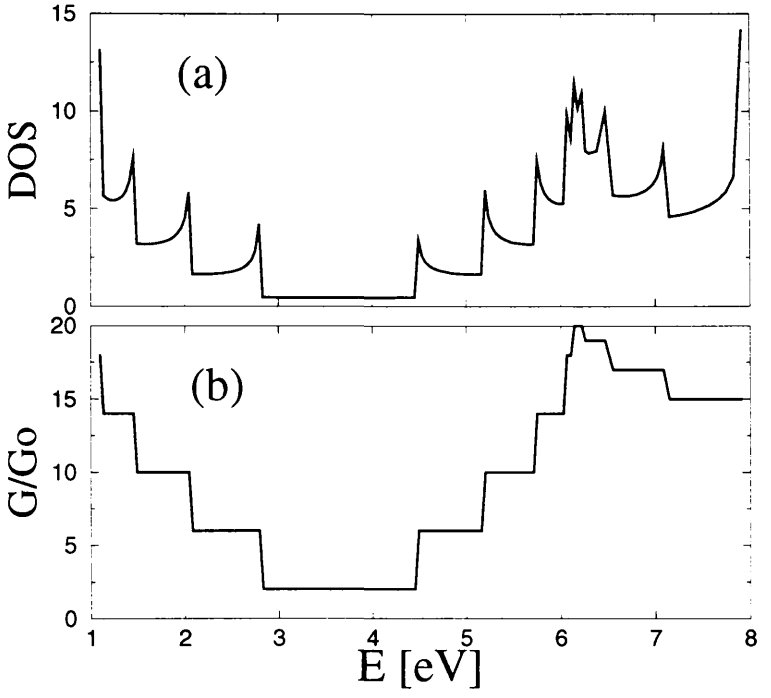

Figure 7.5: Single-wall (10,10) nanotube. (a) Local density of states. (b) Conductance as a function of energy. Note the mono-dimensional character of both the DOS and $G(E)$.

for dealing with singular H_1 matrices, and introduce the main transport properties of infinite multi-wall carbon nanotubes. The main feature of an armchair nanotube is its true mono-dimensional metallic behaviour. Note that the density of state shows mono-dimensional van Hove singularities which are due to the presence of dispersion-less mini-bands. This is reflected in the energy-dependent conductance which shows a typical step-like behaviour. Such steps appear whenever the energy crosses a new mini-band, and therefore correspond to the van Hove singularities in figure 7.5. It is crucial to note that in an infinite system every scattering channel gives the same contribution G_0 to the conductance independently from its dispersion and group velocity. The situation

is rather different in an inhomogeneous system, where scattering of electrons from low dispersion to high dispersion bands of different materials, can give rise to strong backward scattering and therefore to a reduction of the conductance. At the Fermi energy of an armchair nanotube (in this case $E = E_F = 3.6$eV) only two scattering channels are present resulting in a conductance $2G_0$. This value remains constant in an energy interval of approximately 1.5eV, above which other mini-bands start to cross the Fermi energy.

Consider now multi-wall nanotubes. As observed in the introduction, in the absence of inter-tube interactions, different tubes behave as conductors in parallel and the conductances are simply additive. Therefore, since the position of the Fermi energy does not change with the tube diameters one expects a conductance $2mG_0$ for a multi-wall nanotubes comprising m walls. Note also that the width of the energy region around the Fermi energy where the conductance is $2G_0$, depends only weakly on the tube diameters. The situation changes drastically when inter-tube interaction is switched on. In figures 7.6 and 7.7 I present the density of states and the conductance respectively for a (10,10)@(15,15) and for a (5,5)@(10,10)@(15,15) multi-wall nanotube. In the

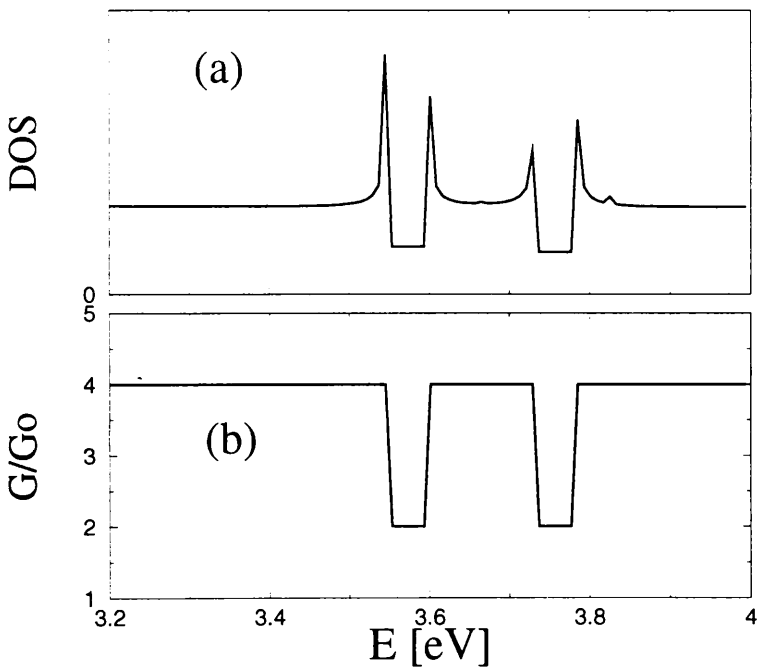

Figure 7.6: (a) Local density of states for a double-wall (10,10)@(15,15) nanotube. (b) Conductance as a function of energy for the same nanotube.

figures I restricted the energy window to the region where the single-wall armchair

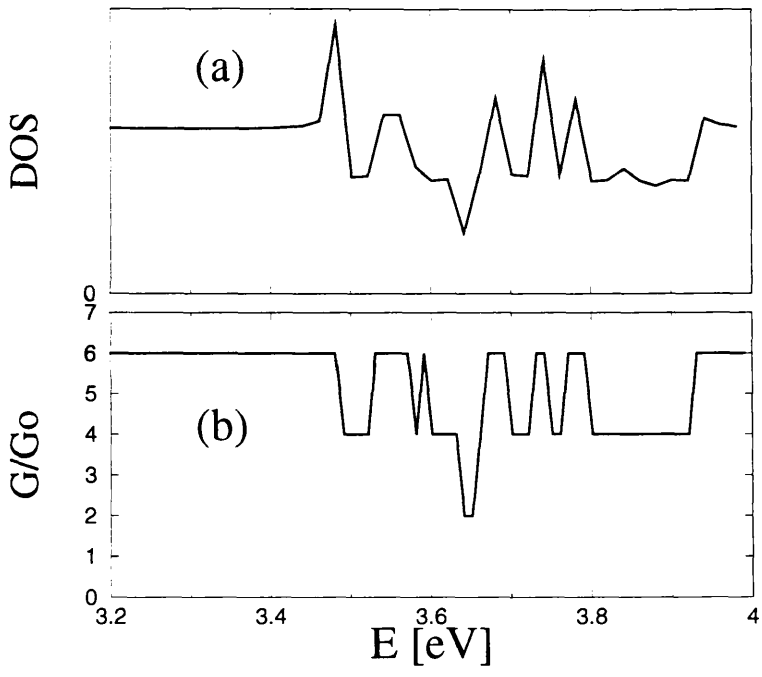

Figure 7.7: (a) Local density of states for a triple-wall (5,5)@(10,10)@(15,15) nanotube. (b) Conductance as a function of energy for the same nanotube.

nanotubes present conductances of $2G_0$. The main feature of both the figures is the presence of pseudo-gaps [152] which lower the conductance from the expected value $2mG_0$. In the case of a double-wall nanotube, this results in two regions where the conductance passes from $4G_0$ to $2G_0$, while in triple-wall nanotube the values $6G_0$, $4G_0$ and $2G_0$ are possible. Nevertheless both these results are still not consistent with the experimental observations of $1G_0$ and $0.5G_0$ [44].

It is important to note that the presence of energy pseudo-gaps not only lowers the conductance but also gives rise to two important effects. First it changes drastically the dispersion of the mini-bands close to the gaps. At the edge of the gaps in fact the dispersion passes from a linear to an almost dispersion-less parabolic-like structure. This is shown in figure 7.8 where I present the band structure along the direction of the tube axis for a double-wall (10,10)@(15,15) nanotube in contrast with the band structure of a single-wall (15,15) nanotube.

Secondly the amplitude of the wave-function across the nanotubes may not be uniformly distributed. Far from the gaps, where the effects of the inter-tube interaction are weak, the wave-function is expected to have a uniform distribution across the different walls composing the nanotube. This is what is found in the case of non-interacting

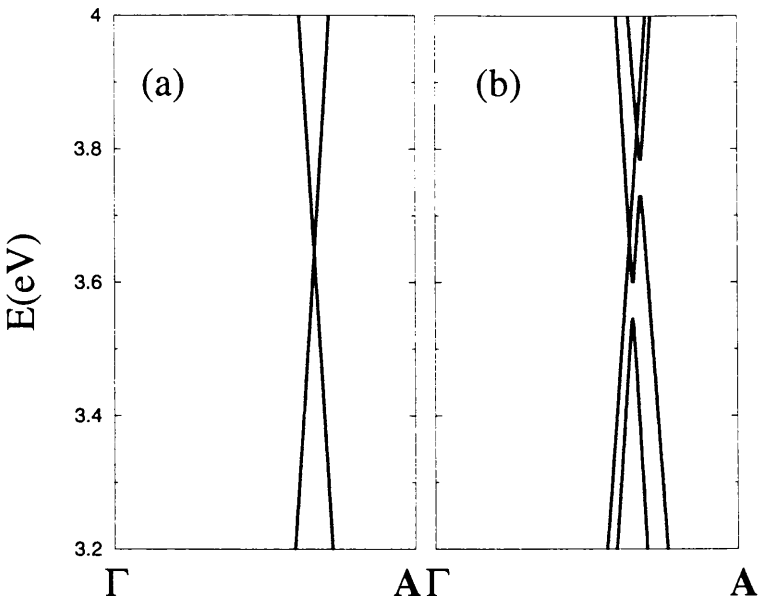

Figure 7.8: (a) Band structure along the tube axis for a (15,15) nanotube. (b) Band structure along the tube axis for a (10,10)@(15,15) nanotube.

walls, whereas in the vicinity of a pseudo-gap, the distribution changes dramatically and the amplitude may be enhanced along some walls and reduced along some others. To demonstrate this effect in figure 7.9 I present the partial conductance across the two walls composing a (10,10)@(15,15) nanotube and across the three walls composing a (5,5)@(10,10)@(15,15) nanotube. The partial conductance is defined as the projection of the total conductance for an infinite multi-wall tube onto the degrees of freedom describing the individual walls. This is identical to what done for the partial conductance over the atomic orbitals presented in Chapter 3. From the figure it is very clear that the amplitude of the wave-function (which is proportional to the partial conductance) is not uniform across the structure and depends critically on the energy. Both the change in the dispersion and the non-uniform distribution of the amplitude of the wave-function across the tubes have drastic effects on the transport of heterogeneous systems, because it creates strong inhomogeneities along the structure, and therefore strong backward scattering. This aspect, which occurs in a multi-wall nanotube when one of the innermost walls closes, will be discussed in the next section.

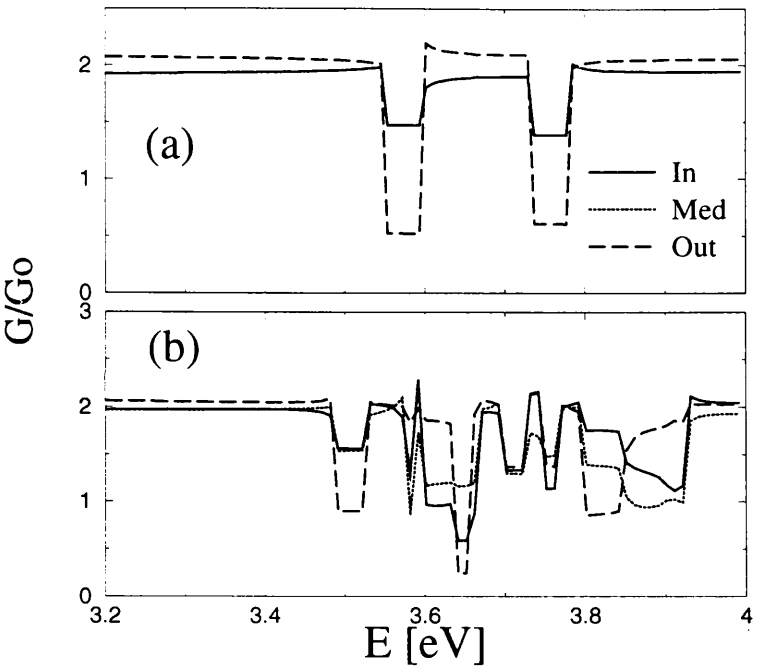

Figure 7.9: Partial conductance of (a) (10,10)@(15,15) and (b) (5,5)@(10,10)@(15,15) nanotube. The solid line, dotted and dashed lines represent the partial conductance respectively onto the innermost, the medium (only in the case of (5,5)@(10,10)@(15,15)) and the outermost tube. Note that within the pseudo-bandgaps the conductance does not distribute uniformly onto the different tubes.

7.4 Transport in inhomogeneous multi-wall nanotubes

In this section I will use the ideas developed above to describe the experiments of reference [44]. Note that for inhomogeneous systems, where multi-wall nanotubes are contacted to the voltage/current probes, the conductance quantization in units of $2G_0$ which I found also for multi-wall nanotube in presence of inter-wall interaction is evidently violated and fractional values of the conductance are allowed. One of the difficulties of the experiments, which use gold as one electrode and mercury as the other, is that not all the tubes make contact with the electrodes. I have considered two different scenarios and have found that agreement with the experiments is obtained when one assumes that only the outermost tube is in contact with the gold electrode, whereas the number of walls in contact with the mercury depends on the depth at which the tube is immersed into the liquid. This latter assumption may seem surprising, because the mercury does not wet the inner tubes. Nevertheless I believe that at equilibrium, the inter-tube interaction allows a uniform distribution of the chemical potential across the cross-section of the whole structure and therefore in the linear-response regime,

the scattering problem reduces to a semi-infinite single-wall nanotube (the one in direct contact with gold) attached to a scattering region in which a variable number of walls are present (see fig.7.10a). Moreover a close analysis of the inter-tube matrix elements shows that these are of the same order of magnitude as the intra-wall ones. This means that electron transport between different walls may be efficient, as well as the electron feeding of the innermost walls from the electrons reservoirs. Consider

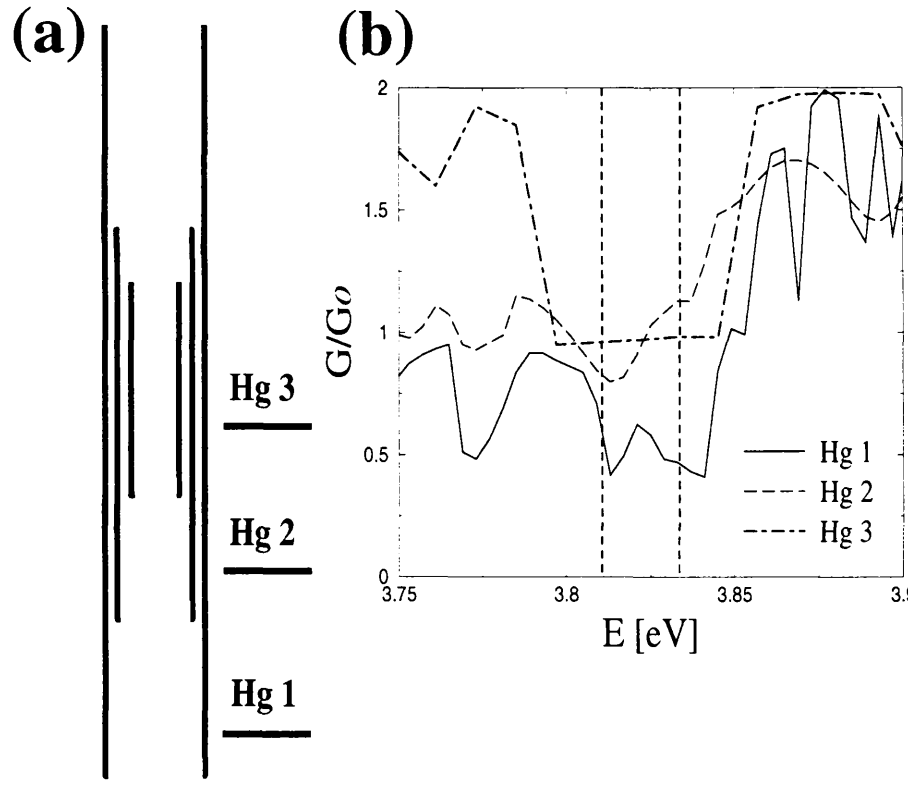

Figure 7.10: (a) Schematic geometry of the system in which only the outermost tube is contacted with the gold electrode for different immersion depths. The perfect contact of the outermost tube with the gold electrode is simulated by considering a semi-infinite single-walled carbon nanotube lead. (b) Conductance as a function of energy for the system of (a).

first the case in which only the outermost tube makes contact with the gold electrode. I argue that the step-like dependence of the conductance on the immersion depth is due to the fact that the scattering region makes contact with the mercury reservoir via a multi-wall semi-infinite nanotube whose number of walls varies and depends on the immersion of the structure. For small immersion depths (such as Hg1 in fig.7.10a), only the outermost tube is in contact with mercury, because it is the only one with an end below the mercury level. A further lowering of the gold tip (to depths such as Hg2

and Hg3 in figure 7.10a) will sequentially place more inner walls into electrical contact with the mercury, thereby changing the conductance. Note that the conductance of such a structure cannot be larger than that of the single-wall nanotube, which is the only tube in contact with the gold electrode.

In figure 7.10b I present the conductance as a function of energy for the inhomogeneous structure described in figure 7.10a. In all three cases, the simulated structure makes contact with the upper Au reservoir via a (15,15) nanotube, which forms the upper external lead, whereas the lower external lead contacting the Hg comprises either a single-, double- or triple-wall nanotube. The solid curve corresponds to a structure formed from a 200 atomic plane (AP) (~250Å) (5,5)@(10,10)@(15,15) triple-wall region, below which is attached to a 200 AP (10,10)@(15,15) double-wall region. The ends of the outer (15,15) nanotube are connected to semi-infinite (15,15) nanotubes, which form the external leads. The dashed curve corresponds to a structure formed from a 200 AP (5,5)@(10,10)@(15,15) triple-wall region. The upper end of the outer tube is attached to a semi-infinite (15,15) nanotube, which forms the external lead contacting the Au reservoir. The lower end of the (10,10) and (15,15) nanotubes continues to infinity, and forms a (10,10)@(15,15) external contact to the Hg reservoir. Finally the dot-dashed line shows the conductance of a (5,5)@(10,10)@(15,15) nanotube, which at the lower end makes direct contact with the Hg and at the upper end, the outer tube continues to infinity, thereby forming a (15,15) external contact to the Au reservoir. These situations correspond to immersion of the tube into the mercury at positions Hg1, Hg2 and Hg3 respectively, where either one wall and two walls are in electrical contact with the mercury.

In all the simulations, the ends of the finite-length tubes are left open and I do not include capping layers. I believe that the capping layers are not crucial to the description of the transport properties of inhomogeneous multi-wall nanotubes, since these are mainly determined by the mis-match of wave-vectors between different regions. Figure 7.10b shows clearly that in an energy window of about 0.03eV (indicated by vertical dashed lines), the conductance for the first structure is approximately $0.5G_0$, while for the latter two is of order $1G_0$. Note that such energy window is larger than both the bias used in the experiments and room temperature. This suggests that these results are quite robust and will survive both at room temperature and moderate

biases. This remarkable result is in excellent agreement with the recent experiments of reference [44].

The scattering in such an inhomogeneous structure arises from the reasons pointed out in the previous section. In the energy window considered in fact the infinite (5,5)@(10,10)@(15,15) presents a large pseudo-gap with conductance $4G_0$. One therefore expects that at both the interfaces of the (5,5)@(10,10)@(15,15) region with respectively the (10,10)@(15,15) region and the (15,15) tube, the mismatch of either the transverse components of the wave-function $\phi_{k_\perp}$ and the longitudinal $k_\perp$-vectors will be large. This gives rise to the strong suppression of the conduction observed in the experiments [44]. In figure 7.11 I present the conductance as a function of immersion depth in mercury for the structure described above. The conductance is calculated at zero-temperature in the zero bias limit and the energy has been set in the middle of the marked region of figure 7.10b (3.825eV). For comparison I superimpose the experimental results of reference [44], which show a very good agreement with the calculation.

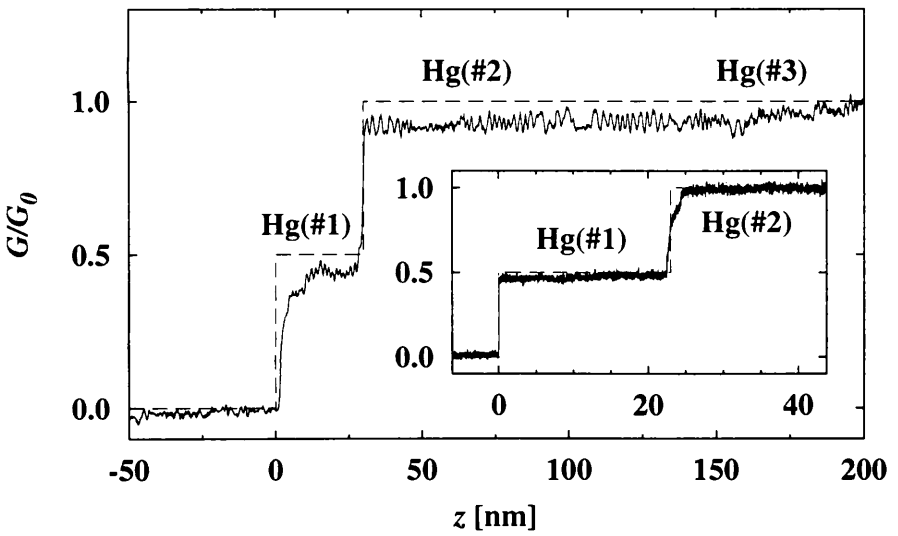

Figure 7.11: Conductance G of a multi-wall nanotube as a function of immersion depth z in mercury. Results predicted for the multi-wall nanotube discussed in figure 7.10a, given by the dashed line, are superimposed on the experimental data of reference [44].

I now consider a second possible scenario, in which three tubes are in direct contact with the gold electrode. In this case the electrons are fed from gold into the structure directly along all the tubes. This contact can be simulated by a semi-infinite (5,5)@(10,10)@(15,15) nanotube with uniform chemical potential across the tubes. The

structure considered is presented in figure 7.12a. In this case the upper bound of the

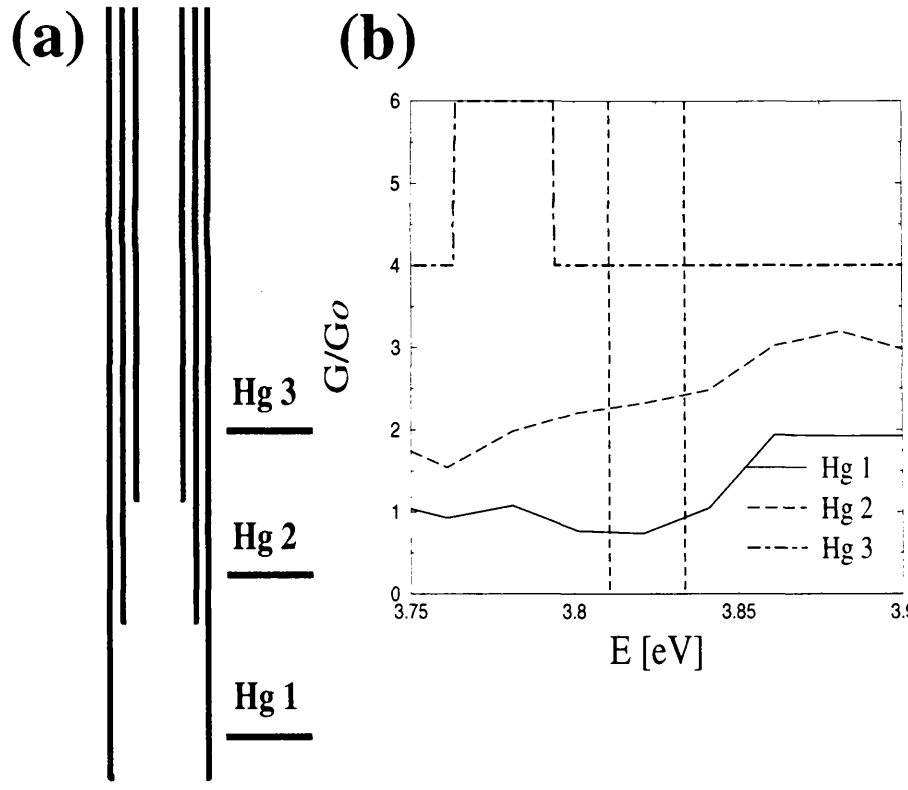

Figure 7.12: (a) Schematic geometry of the system in which three tubes tubes are contacted with the gold electrode for different immersion depths. The perfect contact of the outermost tube with the gold electrode is simulated by considering a semi-infinite triple-walled carbon nanotube lead. (b) Conductance as a function of energy for the system of (a).

conductance is no longer fixed by the single-wall tube to be $2G_0$ but can be as large as $6G_0$ and depends on the number of walls contacting the mercury. In figure 7.12b I show the conductance as a function of energy respectively for a 200 AP (10,10)@(15,15) nanotube sandwiched between a (15,15) and a (5,5)@(10,10)@(15,15) nanotube leads, for (10,10)@(15,15) nanotube lead in contact with a (5,5)@(10,10)@(15,15) nanotube lead, and for an infinite (5,5)@(10,10)@(15,15) nanotube. This again corresponds to the different levels of immersion Hg1, Hg2 and Hg3 in (figure 7.12a). Note that in the case in which the (5,5)@(10,10)@(15,15) nanotube is in direct contact with both the gold and the mercury electrodes its conductance corresponds to the number of open scattering channels for the infinite triple-wall system.

Figure 7.12 shows that if all the three tubes are electrically connected to the gold electrode, a much larger increase in the conductance occurs when a new wall is lowered

below the mercury level, although this is still smaller than the value of $2G_0$, obtained for completely isolated tubes. In this case, corresponding to the different value of the immersion depth, I expect the conductance to be respectively $1G_0$, $2G_0$ and $4G_0$.

The large difference between the transport of the structures in figures 7.10a and 7.12a is therefore crucially dependent on the number of tubes which make a direct contact with the gold electrode. At the moment a complete description of the nanotube/metal interface is not available, and deserves further investigation both experimentally and theoretically.

7.5 Room temperature transport: the classical limit

In this section I will extend the results obtained at zero-temperature for a multi-walled scattering region with up to three walls, to the case of room temperature and a scattering region with a large number of walls. I will evaluate the conductance in the classical limit by using the framework of quantum transport through a quantum dot coupled to two external contacts. This mimics a single-wall carbon nanotube in which a large multi-walled region is encapsulated and corresponds to the first scenario discussed in the previous section. Note that in this case the coupling to the scattering region is not through a scattering potential like in the typical case of quantum dots, but is given by the intertube interaction, whose effects have been discussed previously.

Consider first the general expression for the current within the Landauer-Büttiker formalism (see for example [159])

$$I = \frac{2e}{h} \int \bar{T}(E)[f_1(E) - f_2(E)]dE \,, \tag{7.3}$$

where $\bar{T}(E)$ is the transmission function obtained by summing all the the transmission probabilities $T_{nm}(E)$ and $f_1(E)$ ($f_2(E)$) is the Fermi function for the contact 1 (2) which is at the chemical potential μ_1 (μ_2). All the information regarding the scattering region and its coupling with the external contacts is included in the definition of the transmission function. As stated earlier, the scattering region is described as a system with a large number of discrete energy levels E_m whose widths are smaller than the typical level spacing. In this limit the transmission function can be written in the

Lorentzian form [160, 161, 162],

$$\bar{T}(E) = \sum_m \frac{\Gamma_L^m(E)\Gamma_R^m(E)}{(E - E_m)^2 + \left(\frac{\Gamma_L^m(E)\Gamma_R^m(E)}{2}\right)^2} , \tag{7.4}$$

where $\Gamma_L^m(E) + \Gamma_R^m(E)$ is the linewidth of the m-th resonance and is proportional to the transmission probability $T(E)$ from both the left- and right-hand side contacts through the relation $\Gamma(E) = \hbar\nu T(E)$ with ν the attempt frequency [163]. Suppose now that the linewidths are independent on the energy of the resonant states. In this case the total current through the structure is simply given by

$$I = \frac{2e}{h}\sum_m \int\int \frac{\Gamma_L\Gamma_R\,\delta(E' - E_m)}{(E - E')^2 + \left(\frac{\Gamma_L+\Gamma_R}{2}\right)^2}[f_1(E) - f_2(E)]dEdE' , \tag{7.5}$$

which can be re-written in the following form by introducing the density of states of the scattering region $\sum_m \delta(E - E_m) = \rho(E)$

$$I = \frac{2e}{h}\sum_m \int\int \frac{\Gamma_L\Gamma_R\,\rho(E')}{(E - E')^2 + \left(\frac{\Gamma_L+\Gamma_R}{2}\right)^2}[f_1(E) - f_2(E)]dEdE' . \tag{7.6}$$

The integration over E can be performed by taking the low-bias limit in which $[f_1(E) - f_2(E)]$ reduces to $-\frac{\partial f}{\partial E}(\mu_1 - \mu_2)$. The integration over E' is then simply the integration of a Lorentzian curve, once $\rho(E)$ is taken to be constant, ρ_0. After both integrations the conductance G becomes,

$$G = \frac{2e}{\hbar}\rho_0\frac{\Gamma_L\Gamma_R}{\Gamma_L + \Gamma_R} . \tag{7.7}$$

Finally by using the definition of attempt frequency and the relation between the transmission probability and the resonance linewidth, I obtain the expression for the conductance in the classical limit,

$$G = \left(\frac{1}{G_L} + \frac{1}{G_R}\right)^{-1} , \tag{7.8}$$

where G_L (G_R) is the conductance of left-hand (right-hand) contact, determined solely by the transmission into the scattering region. Equation (7.8) expresses the ohmic conductance of two contacts coupled to a region with a large number of discrete states. Note that this does not involve any dissipation and the transport is completely ballistic.

I now apply the above formula to the case of the multi-wall nanotube described earlier. In the case that the contacts are two semi-infinite single-wall carbon nanotubes with no scattering potential between them and the multi-walled region, then $G_L =$

$G_R = 2G_0$ and the total conductance is expected to be $1G_0$. This is the upper bound of the conductance and is obtained in the case that the transmission from the nanotube contacts to the multi-walled region is perfect. Nevertheless the non-uniform distribution of the wave function along the different tubes in the case of multi-walled nanotubes can generate backward scattering, which in general reduces the transmission. This is what was found in the previous sections. However the limiting case of $G_L = G_R = 2G_0$ can be obtained for some energies, when the mixing of the wave-functions belonging to different tubes is minimal.

Bearing in mind that the results of the previous sections have been obtained at zero temperature, they seem to suggest that agreement with the experiments is achieved if only few tubes make contact with the metallic electrodes, and if the transmission from the nanotube leads to the multi-walled scattering region is not perfect.

7.6 Is spin injection possible?

This last section is dedicated to a different aspect of the physics of carbon nanotubes. In fact I will briefly investigate the possibility of spin-injection into nanotubes. This is a completely new field and to date only one experiment [41] conducted on a multi-wall nanotube sandwiched between two cobalt contacts has shown that the current in a nanotube can be spin-polarized by proximity with magnetic metals. In this experiment an hysteretic behaviour of the resistance is detected and explained as a spin-valve effect. From the experimental data the authors estimate (by using the elementary Julliere theory for spin tunneling [17]) that the spin-diffusion length of the nanotube is about 130nm. Nevertheless this value can largely underestimate the true spin-diffusion length of the nanotube, since a paramagnetic region is very likely to be present at the Co/Nanotube interface, and therefore large spin-flip scattering may be present solely at the interface.

In this section I am not going to present any calculation, but only to give some reasons to believe that spin-injection into nanotubes is possible, and that in principle very large GMR can be obtained. The main idea is based on a paper by Tersoff [164] in which the contact resistance between a metal and a carbon nanotube is investigated. Consider first the Fermi surface of an armchair single-wall carbon nanotube. It can be derived easily from the Fermi surface of a graphite sheet and consists only of two points

symmetric with respect to the Γ point (see figure 7.13). Such a Fermi wave-vector can be calculated and is simply given by $k_F = 2\pi/3z_0$ with $z_0 = d_0\sqrt{3}/2$ and d_0 the C-C bond distance (d_0=1.42 Å). In contrast the Fermi surface of a magnetic transition metal consists of two spheres with different radii for the different spins. In a simple free-electron model with exchange field, in which the energy is given by

$$E^\sigma = \frac{\hbar^2 k^2}{2m} + \sigma\Delta/2\,, \tag{7.9}$$

with $\sigma = -1$ ($\sigma = +1$) for majority (minority) spins and Δ the exchange energy, the spin-dependent wave-vectors are respectively $k_F^\uparrow = \sqrt{2m(E_F + \Delta/2)}/\hbar$ and $k_F^\downarrow = \sqrt{2m(E_F - \Delta/2)}/\hbar$. The transport through an interface between such a magnetic metal and the nanotube is determined by the overlap between the corresponding Fermi surfaces. Three possible scenarios are possible.

First the Fermi-wave vector of the carbon nanotube is smaller than both $k_F^\uparrow$ and $k_F^\downarrow$ (see figure 7.13a). In this case in the magnetic metal there is always a k-vector that perfectly matches the Fermi-wave vector of the nanotube for both spins. Therefore both spins can be injected into the tube and the total resistance will be small and spin-independent.

Second the Fermi-wave vector of the carbon nanotube is larger than both $k_F^\uparrow$ and $k_F^\downarrow$ (see figure 7.13b). In this case there are no available states in the metallic contact whose wave-vectors match exactly the Fermi wave-vector of the carbon nanotube. Therefore in the zero-bias zero-temperature limit the resistance is infinite and spin-independent. Nevertheless as one increases the temperature or/and the bias, transport may be possible because of inelastic scattering at the interface. In fact electrons can be scattered out of the Fermi surface into states with large longitudinal momentum. At temperature T the fraction of electrons with energy above E_F is simply proportional to the Fermi distribution function and is spin-independent. Nevertheless, because of the exchange energy, spin-up electrons possess higher total momentum than the spin-down, and therefore there is a larger probability to find spin-up states with a longitudinal momentum that matches the one of the nanotube than spin-down states. This gives a temperature-induced spin-dependent resistance. Hence one should expect that the increasing of the temperature will largely decreases the resistance for spin-up electrons, leaving almost unchanged the one for spin-down.

Finally if the Fermi wave-vector of the carbon nanotube is larger than $k_F^{\downarrow}$ but smaller than $k_F^{\uparrow}$ (see figure 7.13c), only the majority electrons can enter the nanotube and the system becomes fully spin-polarized. In this situation a spin-valve structure made by magnetic contacts and carbon nanotube as spacer is predicted to show an infinite GMR at zero temperature, similar to the case of the half-metals [80, 85]. The increase of the temperature will produce a degradation of the polarization because also the spin-down electrons may occupy high energy states with large longitudinal momentum. Both the spins can be injected and the spin-polarization depends on the number of occupied states with longitudinal momentum matching the one of the nanotube.

Two important aspects must be pointed out. First all these considerations are based on the assumption of perfectly crystalline systems. This may not be true in reality and the effects of breaking the translational invariance must be considered. From a qualitative point of view disorder will smear the Fermi surface and eventually produce some states with large longitudinal momentum. This will improve the conductance through the nanotube, even if its spin-polarization will be in general dependent on the nature of disorder. An enhancement of conductance of nanotubes connected to gold electrodes with increasing disorder has been recently observed experimentally [165].

Second, in contacts made from transition metals the simple parabolic band model introduced here is largely non-realistic. The details of the band structure can play a very important rôle and the polarization of the current injected into the nanotube will also depend on the coupling between the nanotube and the metal. Some attempts of describing realistic nanotube/metal contacts have been recently made [166], although a fundamental *ab initio* description is still absent.

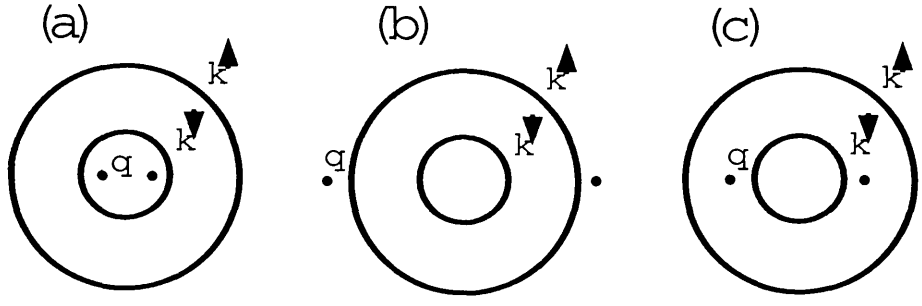

Figure 7.13: Fermi surfaces of an armchair carbon nanotube and of a magnetic transition metal. The Fermi surface of the nanotube consists in two points $k_F^{\rightarrow} = q$, symmetric with respect to the Γ point. The Fermi surface of a transition magnetic metal consists of two spheres (for up and down spins) whose different diameters depend on the exchange field. The three possible scenarios discussed in the text: (a) $q < k_F^{\downarrow} < k_F^{\uparrow}$, (b) $k_F^{\downarrow} < k_F^{\uparrow} < q$, (c) $k_F^{\downarrow} < q < k_F^{\uparrow}$.

8 Conclusions and Future Work

The discovery of GMR in magnetic metal multilayers [1, 2] has brought the electron spin to the attention of the scientific community as an important degree of freedom for electronic devices. Since then, a large amount of work has been done both to understand the characteristics of spin transport and to fabricate new sensitive devices. Several systems have been studied, including ferromagnetic multilayers, spin valves, tunneling junctions and superconductor/ferromagnet junctions. The aim of this thesis was to study the transport of these various systems and to understand their material characteristics and dependencies. An efficient scattering technique has been developed, which makes use of a real space Green's functions calculation and a "decimation" algorithm. The use of this technique, in combination with realistic *spd* tight-binding models, allowed the investigation of transport in several metallic systems. The main results of this work are as follows.

I have analysed the material characteristics which give rise to large GMR ratios in disorder-free systems, and identified the main effects of disorder. From this analysis Co-based multilayers emerge as the best candidates for devices design. The large energy separation between the two spin sub-bands of Co, much larger than in Ni, is the key element to understanding this behavior. Nevertheless, it is clear that when the transport is phase coherent, the whole structure is important and the rôle of the non-magnetic metals used is crucial. In particular I have shown that spin-polarization of the current in a magnetic multilayer can be reversed only by changing the non-magnetic spacer. In view of this, Ni-based multilayers can also present large GMR ratios, in particular if *d*-conductors (Pd, Pt, Rh and Ir) are used as spacers.

Similar results were obtained during the study of magneto-tunneling junctions. In this case the polarization of the tunneling current was shown to depend on the material forming the insulator. Moreover, in the case of disorder-free insulators such a polarization can be either +1 or -1 for very thick barriers and can be reversed by changing the insulator.

All this suggests that the spin-polarization of a magnetic structure does depend on all the elements forming the structure and not only on the magnetic elements.

In magnetic multilayers the GMR ratio and also the spin-conductance are oscillating functions of the layer thicknesses. I have studied this problem using both the *spd* tight-binding model and a simple free-electron like effective mass model with Krönig-Penney potential to represent band offsets. The main result was to show that the conductance oscillations depend both on the Fermi surfaces of the materials forming the multilayer and on the multilayer structure itself.

Disorder was introduced in the calculations by considering a reduced *s-d* tight-binding model. Several models of disorder were considered and the competition between the enhancement of the spin-asymmetry of the conductance, and the reduction of the mean free path due to disorder were analyzed. Moreover the coherent approach to transport, going beyond the largely employed resistor network model, enabled recent experiments, in which the GMR ratio changes when the order of the layers is changed, to be explained.

The interplay between superconductivity and ferromagnetism was also investigated. I have shown that the use of superconducting contacts in CPP GMR measurements drastically suppresses GMR. This, in strong contradiction to most of the experiments, pointed out the rôle of spin-flip scattering at the interface with the superconductor. I have predicted that in the absence of spin-flip scattering at the interface, the GMR ratio vanishes when superconducting contacts are used. This prediction deserves further experimental investigation.

With the same technique, realistic F/S and N/S ballistic junctions have been studied. Detailed *I-V* curve were calculated and in some cases the agreement with the experiments is remarkably good. The main problem with these calculations is that the results are very sensitive to the interface and hence an accurate model is fundamental. This is particularly true in the case of materials with very different bulk properties (lattice spacing, band structure...), and more sophisticated techniques to model the interface will be welcome.

Finally the transport in Carbon nanotubes was investigated. The great interest in the electronic properties of Carbon nanotubes is due to their peculiar one-dimensional properties. These can be used for spin-injection and several other future applications.

In this thesis I have concentrated on the transport of multi-wall nanotubes, and investigated the effects of inter-tube interaction on the transport. An explanation of the unexpected conductance quantization in units of e^2/h is given, solving an old controversy of the physics of nanotubes.

Several aspects deserve further investigation.

The study of the I-V curves of ballistic junctions highlighted the limit of the scattering approach. In the case of heterojunctions made from very different materials a simple description of the interface is not satisfactory. In this thesis the coupling between different materials has been taken as the geometric mean of the coupling of the individual materials. This can be largely improved with a self-consistent description of the interface including both *ab initio* methods and molecular dynamics simulations. Moreover, recently several measurements on ballistic point-contacts made from magnetic metals have been carried out [167, 168, 169]. The modeling of these is of great interest, but tight-binding methods with parameterization based on bulk materials are not adequate. In a typical point-contact device very few atoms form the contact, the lattice spacing may be very different from the bulk and the local magnetic moment can vary from atom to atom. The description of all these aspects deserves a fundamental approach and a combination of *ab initio* methods and molecular dynamics simulations seems to be the most powerful way forward. Finally the same problem is encountered in the study of metallic contacts with Carbon nanotubes. This is a very important issue from both the fundamental and device design point of view. A detailed description of the C-Metal bond does not exist at the moment. This is expected to be crucial for molecular electronics design and to understand the possibility of spin-injection into carbon nanotubes.

Probably the largest challenge for the future is to transfer the present knowledge of spin-transport in metallic system to semiconductors. This large field is called "spintronics" [170, 171]. The use of semiconductors presents several advantages. From a fundamental point of view the electronic properties of semiconductors are much more controllable than those of metals and manipulations are possible both at the struc-

tural and electronic level. From the point of view of applications spin-transport in semiconductors can be readily transfered to present electronic device, which are almost exclusively based on semiconductors. Several important breakthroughs have already been made in both these directions.

Hybrid semiconductor-metal devices have been produced. In particular metallic ferromagnetic thin films can be exchange coupled through semiconductors [172], and spin-polarized current can be injected into semiconductors by proximity with metallic magnetic contacts [173]. Nevertheless, hybrid structures are not completely satisfactory. On the one hand they involve materials with very different resistances and usually the spin-dependent component is small compared with the spin-independent one. On the other hand large electric fields at the interfaces can be present. This creates large spin-flip scattering at the interfaces, reducing the spin-polarization of the current.

The production of magnetic semiconductors based on low-temperature MBE techniques [174, 175] has been demonstrated. (Ga,Mn)As can be deposited with a Curie temperature of 110°K and this can be used in combination with non-magnetic semiconductors to build up future devices. Spin-injection into semiconductors by using magnetic semiconductors has also been demonstrated [176], opening the way to new "all-semiconductor" devices.

Finally the spin lifetime in semiconductors has been shown to be very long ($\sim$100ns) [177, 178, 179] and electrons can be drifted over long distances ($\sim 100\mu$m) without losing their spin direction [180]. The importance of this result is twofold. On the one hand it shows that in semiconductors the two spin-fluid picture is largely applicable and that spin-polarization can be conserved over long distances. This is crucial for constructing efficient spin-valve-like systems with high sensitivity. On the other hand the long spin lifetime paves the way for more exotic spin-systems, such as q-bit elements for quantum computation.

From a theoretical point of view a lot of further work needs to be done. As far as the materials are concerned the origin of ferromagnetism in diluted magnetic semiconductors must be understood. The RKKY interaction seems to be responsible for ferromagnetism but at present there are no calculations of GaAs doped with Mn. For

this purpose *ab initio* calculations are crucial and perhaps tne only reliable way to fully understand these materials. Transport is also of interest and both tight-binding methods and simple effective mass models could be used.

Probably the most difficult challenge is the study of the spin dynamics in normal and magnetic semiconductors [181]. Several mechanisms to explain the spin-decoherence in semiconductors are known from the early sixties [182] and mainly involve spin-orbit scattering [183, 184] and electron-hole exchange interactions [185]. The analysis of these models from the viewpoint of the recent experiments involving heterostructures and a quantitative approach, is the next big step.

To conclude, I believe that although a great deal of progress has been made in the past ten years towards the comprehension and use of spin dynamics in condensed matter, our understanding is still insufficient. A major challenge has been set for the future and only the combination of physics, chemistry, engineering and material science will enable the spintronics dream to become a viable reality.

A Explicit Calculation of retarded Green function for a double infinite system

In this appendix I present the explicit calculation leading to the equation (2.29) for the Green function of a double infinite system. The starting point is the equation (2.28)

$$g_{zz'} = \begin{cases} \sum_{l=1}^{M} \phi_{k_l} e^{ik_l(z-z')} \mathsf{w}_{k_l}^{\dagger} & z \geq z' \\ \sum_{l=1}^{M} \phi_{\bar{k}_l} e^{i\bar{k}_l(z-z')} \mathsf{w}_{\bar{k}_l}^{\dagger} & z \leq z' \end{cases} , \tag{A.1}$$

with w_k and $\mathsf{w}_{\bar{k}}$ two vectors to be determined. The expression of equation (A.1) to be a Green function must be continuous for $z = z'$ and must satisfy the Green equation

$$[(E - H)g]_{zz'} = \delta_{zz'} . \tag{A.2}$$

The first condition yields immediately to the relation

$$\sum_{l=1}^{M} \phi_{k_l} \mathsf{w}_{k_l}^{\dagger} = \sum_{l=1}^{M} \phi_{\bar{k}_l} \mathsf{w}_{\bar{k}_l}^{\dagger} , \tag{A.3}$$

while the second gives

$$\sum_{l=1}^{M} \left[(E - H_0)\phi_{k_l} \mathsf{w}_{k_l}^{\dagger} + H_1 \phi_{k_l} e^{ik_l} \mathsf{w}_{k_l}^{\dagger} + H_{-1} \phi_{\bar{k}_l} e^{-i\bar{k}_l} \mathsf{w}_{\bar{k}_l}^{\dagger} \right] = 1 . \tag{A.4}$$

The task is now to re-write the vectors w's as a function of the known vectors ϕ's and their dual $\tilde{\phi}$'s. First note that by adding and subtracting to the (A.4) the expression

$$\mathcal{W} = \sum_{l=1}^{M} \left[H_{-1} \phi_{k_l} e^{-ik_l} \mathsf{w}_{k_l}^{\dagger} \right] , \tag{A.5}$$

it is possible to re-write the (A.4) in the following compact form

$$\sum_{l=1}^{M} H_{-1} \left[\phi_{k_l} e^{-ik_l} \mathsf{w}_{k_l}^{\dagger} - \phi_{\bar{k}_l} e^{-i\bar{k}_l} \mathsf{w}_{\bar{k}_l}^{\dagger} \right] = -1 , \tag{A.6}$$

where the definition of ϕ_k of equation (2.23) has been used. Now consider the continuity equation (A.3) and multiply the left-hand side by the dual vector $\tilde{\phi}_{k_h}$ and the right-hand side by $\tilde{\phi}_{\bar{k}_h}$. It yields respectively to two expressions that relate w_k to $\mathsf{w}_{\bar{k}}$

$$\sum_{l=1}^{M} \left[\tilde{\phi}_{k_h}^{\dagger} \phi_{\bar{k}_l} \mathsf{w}_{\bar{k}_l}^{\dagger} \right] = \mathsf{w}_{k_h}^{\dagger} , \tag{A.7}$$

$$\sum_{l=1}^{M} \left[\tilde{\phi}_{\bar{k}_h}^{\dagger} \phi_{k_l} \mathsf{w}_{k_l}^{\dagger} \right] = \mathsf{w}_{\bar{k}_h}^{\dagger} . \tag{A.8}$$

If now one substitutes the equations (A.7) and (A.8) into the equation (A.6) and uses the continuity equation (A.3), the following fundamental relation is obtained

$$\sum_{l=1}^{M}\sum_{j=1}^{M} H_{-1}\left[\phi_{k_l}e^{-ik_l}\tilde{\phi}^{\dagger}_{k_l} - \phi_{\bar{k}_l}e^{-i\bar{k}_l}\tilde{\phi}^{\dagger}_{\bar{k}_l}\right]\phi_{\bar{k}_j}\mathsf{w}^{\dagger}_{\bar{k}_j} = 1\ , \tag{A.9}$$

from which it follows immediately

$$\left[\sum_{l=1}^{M} H_{-1}\left(\phi_{k_l}e^{-ik_l}\tilde{\phi}^{\dagger}_{k_l} - \phi_{\bar{k}_l}e^{-i\bar{k}_l}\tilde{\phi}^{\dagger}_{\bar{k}_l}\right)\right]^{-1} = \sum_{j=1}^{M}\phi_{\bar{k}_j}\mathsf{w}^{\dagger}_{\bar{k}_j} = \sum_{j=1}^{M}\phi_{k_j}\mathsf{w}^{\dagger}_{k_j}\ . \tag{A.10}$$

In the second equality of the equation (A.10) I have used the continuity equation (A.3). Note that the equation (A.10) expresses explicitly the vectors w's in term of the known quantities ϕ, $\tilde{\phi}$ and H_{-1}. Therefore w's may be computed by simply multiplying the (A.10) for the correct dual vectors. By doing so I obtain

$$\mathsf{w}^{\dagger}_{\bar{k}_h} = \tilde{\phi}^{\dagger}_{\bar{k}_h}\mathcal{V}^{-1}\ , \tag{A.11}$$

$$\mathsf{w}^{\dagger}_{k_h} = \tilde{\phi}^{\dagger}_{k_h}\mathcal{V}^{-1}\ , \tag{A.12}$$

with $\mathcal{V}$ the operator defined in Chapter 2

$$\mathcal{V} = \sum_{l=1}^{M} H_{-1}\left[\phi_{k_l}e^{-ik_l}\tilde{\phi}^{\dagger}_{k_l} - \phi_{\bar{k}_l}e^{-i\bar{k}_l}\tilde{\phi}^{\dagger}_{\bar{k}_l}\right]\ . \tag{A.13}$$

The equation (A.13) concludes the demonstration. In fact by substituting the expressions for $\mathsf{w}_{\bar{k}}$ and w_k into the starting Ansatz (A.1), one obtains the final expression for the Green function of an infinite system

$$g_{zz'} = \begin{cases} \sum_{l=1}^{M}\phi_{k_l}e^{ik_l(z-z')}\tilde{\phi}^{\dagger}_{k_l}\mathcal{V}^{-1} & z \geq z' \\ \sum_{l=1}^{M}\phi_{\bar{k}_l}e^{i\bar{k}_l(z-z')}\tilde{\phi}^{\dagger}_{\bar{k}_l}\mathcal{V}^{-1} & z \leq z' \end{cases}\ . \tag{A.14}$$

B Current Operator and the Rotation in the Degenerate Space

I this appendix I discuss the construction of the current operator and the rotation needed to diagonalize it in the case in which the vectors ϕ_k's are degenerate. Let start by considering the current matrix at the position z. It can be easily expressed as the time derivative of the density matrix at the same point z

$$\mathcal{J}_z(t) = \frac{\partial}{\partial t}\psi_z(t)\psi_z(t)^\dagger \,, \tag{B.1}$$

where $\psi_z(t)$ is the value of the time-dependent wave-function at the position z satisfying the time-dependent Schrödinger equation

$$i\frac{\partial}{\partial t}\psi_z(t) = H_0\psi_z(t) + H_1\psi_{z+1}(t) + H_{-1}\psi_{z-1}(t) \,. \tag{B.2}$$

By explicitly evaluating the time derivative in equation (B.1), and by using the Schrödinger equation and its complex conjugate, the current matrix can be written in the following transparent form

$$\mathcal{J}_z = \mathcal{J}_0 + \mathcal{J}_{z-1\to z} + \mathcal{J}_{z+1\to z} \,, \tag{B.3}$$

where $\mathcal{J}_0$, $\mathcal{J}_{z-1\to z}$ and $\mathcal{J}_{z+1\to z}$ are defined respectively as

$$\mathcal{J}_0 = -i\left[H_0\psi_z\psi_z^\dagger - \psi_z\psi_z^\dagger H_0\right] \,, \tag{B.4}$$

$$\mathcal{J}_{z-1\to z} = -i\left[H_{-1}\psi_{z-1}\psi_z^\dagger - \psi_z\psi_{z-1}^\dagger H_1\right] \,, \tag{B.5}$$

$$\mathcal{J}_{z+1\to z} = -i\left[H_1\psi_{z+1}\psi_z^\dagger - \psi_z\psi_{z+1}^\dagger H_{-1}\right] \,. \tag{B.6}$$

In the calculation of the relations above I simplified the time-dependent component of the wave-function and expressed the current matrix by mean of the column vectors introduced in Chapter 2 through the time-independent Schrödinger equation (2.21). Note that $\mathcal{J}_0$ does depend only on the value of the wave-function at the position z, while $\mathcal{J}_{z-1\to z}$ and $\mathcal{J}_{z+1\to z}$ depend also respectively on its value at the position $z-1$ and $z+1$. Now evaluate the expectation value of the current by taking the trace of the current matrix. It is easy to show that

$$J_z = \mathrm{Tr}\ \mathcal{J}_z = J_{z-1\to z} + J_{z+1\to z} \,, \tag{B.7}$$

with

$$J_{z-1\to z} = -i\left[\psi_z^\dagger H_{-1}\psi_{z-1} - \psi_{z-1}^\dagger H_1 \psi_z\right] = 2\Im\left(\psi_z^\dagger H_{-1}\psi_{z-1}\right) , \tag{B.8}$$

$$J_{z+1\to z} = -i\left[\psi_z^\dagger H_1\psi_{z+1} - \psi_{z+1}^\dagger H_{-1}\psi_z\right] = -2\Im\left(\psi_{z+1}^\dagger H_{-1}\psi_z\right) . \tag{B.9}$$

In the calculation of the equations (B.8) and (B.9) I used the circular property of the trace Tr AB = Tr BA. Note that the expectation value of $\mathcal{J}_0$ vanishes. The relations (B.8) and (B.9) have a clear interpretation. $\mathcal{J}_{z-1\to z}$ and $\mathcal{J}_{z+1\to z}$ represent the current matrices for electrons propagating respectively to the right (right-moving) and to the left (left-moving). Note that in the case of a translational-invariant system ψ_z can be written in the Bloch form of equation (2.22)

$$\psi_z = n_k^{1/2} e^{ikz}\phi_k . \tag{B.10}$$

If now one substitutes the (B.10) into the (B.8-B.9) it is easy to show that $J_z = 0$ as expected from the translational invariance.

The final part of this appendix is dedicated to show that the states of the form $\psi_z = n_k^{1/2} e^{ikz}\phi_k$ diagonalize the current. As anticipated in the Chapter 2 this is not strictly valid in the case of different ϕ_k corresponding to the same k. Nevertheless in such a case I will show that there is always a rotation in the degenerate space that diagonalizes the current.

Consider for instance the right-moving current (all the following arguments can be applied to the left-moving counterpart), and a Bloch state

$$\psi_z = \sum_l \alpha_l e^{ik_l z}\phi_{k_l} , \tag{B.11}$$

and calculate the expectation value of the current for such a state. It easy to show that this yields to the equation

$$J_{z-1\to z} = -i\sum_{l,l'} \alpha_l\alpha_{l'}^\star \left[\phi_{k_{l'}}^\dagger H_{-1}\phi_{k_l} e^{-ik_l} - \phi_{k_{l'}}^\dagger H_1\phi_{k_l} e^{ik_{l'}}\right] = -i\sum_{l,l'} \alpha_l\alpha_{l'}^\star \left[\phi_{k_{l'}}^\dagger (H_{-1}e^{-ik_l} - H_1 e^{ik_{l'}})\phi_k \right. \tag{B.12}$$

If one now assumes that the off-diagonal matrix elements vanish (ϕ_k's diagonalize the current), then the states (B.11) diagonalize the current and curry unitary flux if the normalization constant is taken to be

$$\frac{1}{\nu_l^{1/2}} = \alpha_l = \frac{1}{[-i\phi_{k_l}^\dagger (H_{-1}e^{-ik_l} - H_1 e^{ik_l})\phi_{k_l}]^{1/2}} , \tag{B.13}$$

with ν_l defining the group velocity. Note that the states (B.11) with the normalization constant (B.13) are the ones introduced in Chapter 2, which guarantee the unitarity of the S matrix.

The final step is to demonstrate that $\psi_z = e^{ikz}\phi_k$ diagonalizes the current. To achieve this, consider the Schrödinger equation evaluated on such a Bloch state and its complex conjugate

$$(E - H_0)\,\phi_{k_l} = \left(H_1 e^{ik_l} + H_{-1}e^{-ik_l}\right)\phi_{k_l}\,, \tag{B.14}$$

$$\phi^\dagger_{k_l}\,(E - H_0) = \phi^\dagger_{k_l}\left(H_1 e^{ik_l} + H_{-1}e^{-ik_l}\right)\,. \tag{B.15}$$

By multiplying the first equation by $\phi^\dagger_{k_{l'}}$ to the left and the second by $\phi_{k_{l'}}$ to the right one obtains the relation

$$\phi^\dagger_{k_{l'}} H_{-1}\phi_{k_l} e^{-ik_l} + \phi^\dagger_{k_{l'}} H_1 \phi_{k_l} e^{ik_l} = \phi^\dagger_{k_{l'}} H_{-1}\phi_{k_l} e^{-ik_{l'}} + \phi^\dagger_{k_{l'}} H_1 \phi_{k_l} e^{ik_{l'}}\,. \tag{B.16}$$

The (B.16) is identically satisfied if $k_l = k_{l'}$, also if $\phi_{k_l} \neq \phi_{k_{l'}}$. This occurs when one or more wave-vectors k_l are degenerate (ie there are many ϕ_{k_l}'s for the same k_l). In the case this does not happen few algebraic manipulations yield to the relation

$$\phi^\dagger_{k_{l'}} H_{-1}\phi_{k_l} e^{-ik_{l'}} = \phi^\dagger_{k_{l'}} H_1 \phi_{k_l} e^{ik_l}\,. \tag{B.17}$$

The last equality shows the cancellation of the off-diagonal terms in the expression of the expectation value of the right-going current (B.12). This means that in the case in which there is no degeneracy in k, the states ϕ_{k_l} diagonalize the current. Nevertheless in the case in which degeneracy is present one can perform a unitary rotation in the degenerate space and construct a new basis φ in which the current is diagonal. To show explicitly how to obtain this rotation consider a set of vectors ϕ^μ_k $(\mu = 1, ..., N)$ corresponding to the same wave vector k and construct the "reduced" $N \times N$ current matrix, whose matrix elements are

$$(J^{\mathrm{R}})_{ij} = \phi^{i\,\dagger}_k [i(H_{-1}e^{-ik} - H_1 e^{ik})]\phi^j_k\,. \tag{B.18}$$

Since $H_{-1} = H_1$ the "reduced current" is an hermitian matrix. Therefore it has always a diagonal form. Moreover the transformation matrix $\mathcal{U}$ which diagonalizes J^{R}, is a unitary matrix. If $\mathcal{D}$ is the diagonal form of J^{R} I can write such a unitary transformation as

$$\mathcal{D} = \mathcal{U}^{-1} J^{\mathrm{R}} \mathcal{U}\,. \tag{B.19}$$

It follows that the transformation $\mathcal{U}$ also transforms the basis ϕ_k^μ into a "rotated" basis φ_k^μ which diagonalize the current (note that the "reduced current" is simply the total current introduced above calculated onto a subset of the total Hilbert Space). By evaluating the equation (B.19) the explicit definition of φ_k^μ is obtained

$$\varphi_k^j = \sum_{l=1}^{N} \varphi_k^l \mathcal{U}_{lj} \,. \tag{B.20}$$

The equation (B.20) completes the demonstration.

In this appendix I have shown that the Bloch states $\psi_z = e^{ikz}\phi_k$ diagonalize the current in the case the vectors ϕ_k are not degenerate in k. Moreover in the case in which this condition is not satisfied it is always possible to perform a rotation in the degenerate space and to obtain a new set of vectors φ in which the current is diagonal.

C Projector of the Retarded Green function onto the corresponding Wave-function

In this appendix I want to show that the projector that maps the retarded Green function for the double infinite system on the corresponding wave-function projects also the total retarded Green function (system = scatterer + leads) on the corresponding total-wave function. Consider the total Hamiltonian

$$H = H_0 + H_{\text{scat}} \,, \tag{C.1}$$

where H_0 describes the leads and H_{scat} describes the scattering region. The Schrödinger equation and the Green equation for the leads (without any scattering region) are respectively

$$(E - H_0)\psi_0 = 0 \,, \tag{C.2}$$

$$(E - H_0)g_0 = \mathcal{I} \,, \tag{C.3}$$

with g_0 the Green function, E the energy and $\mathcal{I}$ the identity matrix. The corresponding equations for the whole system (scatterer + leads) are

$$[E - (H_0 + H_{\text{scat}})]\psi = 0 \,, \tag{C.4}$$

$$[E - (H_0 + H_{\text{scat}})]G = \mathcal{I} \,. \tag{C.5}$$

Furthermore ψ, ψ_0 and g_0, G are related by the respective Dyson equations

$$\psi = (\mathcal{I} - g_0 H_{\text{scat}})^{-1}\psi_0 \,, \tag{C.6}$$

$$G = (\mathcal{I} - g_0 H_{\text{scat}})^{-1} g_0 \,. \tag{C.7}$$

Define now the projector P in such a way that

$$\psi_0 = g_0 \cdot P \,. \tag{C.8}$$

If one now uses the Dyson equation for ψ (C.6) together with the definition of P, it follows immediately

$$\psi = (\mathcal{I} - g_0 H_{\text{scat}})^{-1} g_0 \cdot P = G \cdot P \,, \tag{C.9}$$

where I used the Dyson equation for G (C.7). The equation (C.9) completes the demonstration and shows that P also maps G onto ψ.

D Tight-Binding Parameters and band fit at the Fermi energy

In this appendix I tabulate all the parameters used throughout the thesis. The first table corresponds to the on-site energies and the second contains the corresponding hopping integrals. They are taken from reference [84].

Metal	E_s (eV)	E_p (eV)	$E_d^{\uparrow}$ (eV)	$E_d^{\downarrow}$ (eV)
Co	5.551	14.025	-2.23	-0.66
Ni	4.713	11.699	-2.114	-1.374
Cu	2.992	10.594	-2.746	-2.746
Ag	2.986	9.127	-4.65	-4.65
Au	0.329	10.081	-3.82	-3.82
Pd	5.764	11.457	-2.05	-2.05
Pt	1.849	11.523	-2.61	-2.61
Ir	2.844	11.728	-2.211	-2.211
Rh	6.737	11.903	-1.84	-1.84
Pb	-8.220	2.146	14.947	14.947
Al	-1.868	5.852	15.233	15.233
INS	-4.756	3.655	-15.640	-15.640

Table 4.1: On-site energies from reference [84]. INS is a model insulator.

Metal	$ss\sigma$	$sp\sigma$	$pp\sigma$	$pp\pi$	$sd\sigma$	$pd\sigma$	$pd\pi$	$dd\sigma$	$dd\pi$	$dd\delta$
Co	-1.23	1.856	3.23	-0.019	-0.517	-0.553	0.38	-0.573	0.405	-0.092
Ni	-1.177	1.75	2.877	0.155	-0.455	-0.465	0.382	-0.478	0.349	-0.084
Cu	-1.02	1.578	2.679	0.258	-0.421	-0.449	0.245	-0.354	0.245	-0.054
Ag	-0.895	1.331	2.143	0.088	-0.423	-0.531	0.207	-0.429	0.239	-0.046
Au	-0.909	1.323	2.431	-0.224	-0.642	-0.871	0.258	-0.676	0.357	-0.062
Pd	-1.083	1.541	2.329	-0.073	-0.665	-0.893	0.289	-0.709	0.392	-0.072
Pt	-1.066	1.523	2.541	-0.335	-0.843	-1.165	0.333	-0.933	0.48	-0.08
Ir	-1.163	1.65	2.548	-0.408	-0.987	-1.376	0.383	-1.144	0.573	-0.092
Rh	-1.184	1.62	2.321	-0.126	-0.763	-1.038	0.326	-0.858	0.464	-0.083
Pb	-0.37	-0.557	1.464	-0.089	0.725	-1.384	0.134	-1.847	1.345	-0.365
Al	-0.793	-1.267	2.333	-0.139	1.129	-2.212	0.42	-2.314	1.006	-0.067
INS	0.068	-0.129	0.110	0.053	0.248	-0.156	-0.063	-0.012	0.002	0.003

Table 4.2: Hopping integrals from reference [84]. INS is a model insulator.

All the tight-binding parameters are expressed in eV and the on-site energies are chosen in order to have the Fermi energy $E_F = 0$eV. In Chapter 6 I used a different set of

parameters for Co, Cu and Pb. These have been obtained with a fitting algorithm which allows to accurately fit a specific energy region. In what follows I will discuss the fitting algorithm and present the computed band structure and the new set of parameters.

The fitting code used for fitting band structures coming from *ab-initio* LDA calculations is included in a large tight-binding package called OXON (OXford Order N) [131]. The code can perform a multi-parameter fit in which all the tight-binding parameters can be varied. Alternatively there is the flexibility to perform the fit only varying smaller subsets of parameters. The inputs for the fitting algorithm are the eigenvalues $E_n(k)$ calculated for arbitrary k-points in the Brillouin zone. Such eigenvalues do not need to be taken at high symmetry points in the Brillouin zone. Nevertheless it can be useful to perform the fit at high symmetry points because it allows to check the correct molteplicity of the bands. This may also improve the convergence of the fit. If I call the provided eigenvalues $E_n(k)$ (the values one wants to fit) the function which is minimized during the fit is the following

$$f(E_n, \vec{\gamma}) = \sum_n \alpha_n [E_n(k) - E_c(k, \vec{\gamma})]^2 \,, \tag{D.1}$$

where $\vec{\gamma}$ is the m-dimensional vector ($m = 13$ in the case of *spd* Hamiltonian with Slater-Koster parameterization [81]) including the fitting parameters ($\vec{\gamma}$ =(E_s,E_p,E_d, ssσ,spσ.....)), α_n is the weight assigned to the different eigenvalues and $E_c(k, \vec{\gamma})$ are the computed eigenvalues. At a fixed k-point the bands must be fitted starting from the lower energy (it is not possible to fit arbitrary taken $E(k)$ points). If one wants to have a good fit near the Fermi energy the weight must be large for eigenvalues close to the Fermi energy (~ 1) and small elsewhere. The fit is not unique. The function $f(E_n, \vec{\gamma})$, at least for $3d$ transition metals, possesses a large number of local minima and the convergence not always is easy to achieve. To avoid falling down into local minima it is useful to start from an initial set of parameters as close as possible to the final one. If the starting set is not particularly accurate the fit results to be very long. In all the fit that I performed I used as starting set of parameters the one tabulated in reference [84].

The following standard prescription has been followed in all the fits. Firstly I calculate the band structure by varying only a single parameter every run. This is

useful to get confidence with the band structure and to understand which are the branches of the band structure modified by each individual parameter. Usually only few parameters are important at the Fermi energy and may be useful to fit them independently. Secondly I performed several multi-parameter fits starting from the new set obtained during the previous runs. Finally I compared the new band structures obtained with the ones that I wanted to fit and, if the agreement was not satisfactory, I performed new multi-parameter fits.

The band structures I used as fitting bands come from LDA calculations, namely from the Siesta code (Spanish Initiative for Electronic Simulations with Thousands of Atoms) for Co and Cu, and from reference [84] for Pb. I usually considered 4 symmetry points (Γ, L, X, W) in the fcc Brillouin zone, fitting 6 eigenvalues for each points. The f function is thus evaluated over 24 eigenvalues.

The aim of the fit was to have a good description of the band structure within 4 eV around the Fermi energy. The eigenvalues in that energy window are calculated with a weight $\alpha_n = 1$ and the weight is continuously decreased going toward higher and lower energy. It has been usually convenient to neglect completely the description of the low energy branch of the parabolic s-band at the Γ point, and to adjust it later by varying the ssσ parameter (it does not affect largely the region around the Fermi energy). The main aspects that I reproduced are the correct curvature of the band and the correct position of the band crossing at the Fermi energy. Examples of the band structures for Cu, for the majority band of Co and for Pb are presented in figures D.1, D.2 and D.3. It is clear that the agreement with the LDA band structures is quite good. The minority band of Co gives more problems because of the strong d-component and the presence of almost dispersionless bands at the Fermi energy. I reasonably reproduced the minority band of Co by making a complete new fit with respect to the majority band. The majority and the minority bands of Co do not differ only in the different on-site energy of the d-bands, but all their tight-binding parameters are allowed to be different. This is justified because I am not interested in properties of the bands at all energies (ie the total magnetic moment) but only locally in the properties of the Fermi surface. The new set of parameters are tabulated in the next two tables. Note that for Pb a good description of the band structure can be obtained allowing a very large value of E_d. This is consistent with the well known sp-characters of the conduction

electrons of Pb at the Fermi energy.

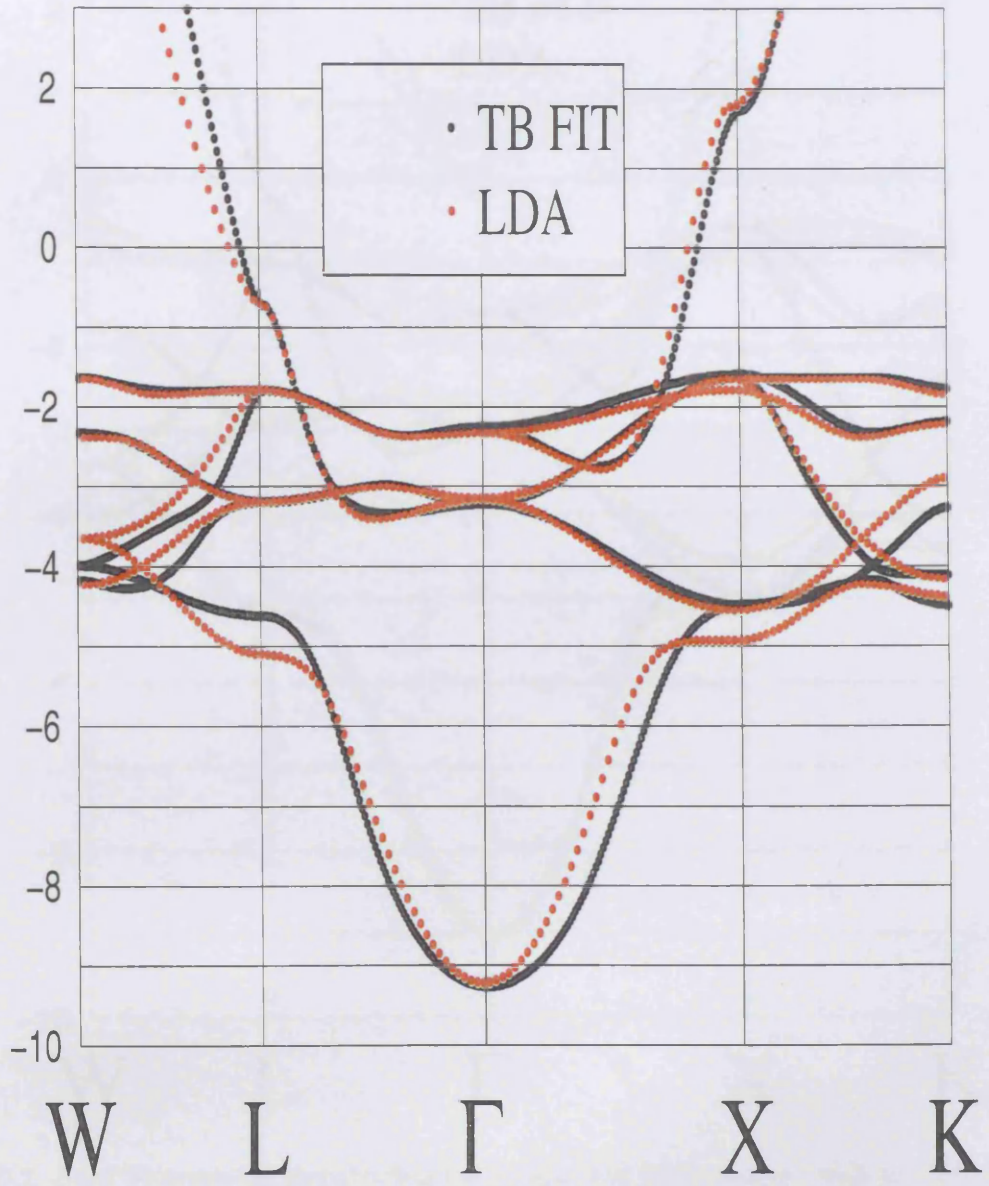

Figure D.1: Band Structure for fcc Cu. The band obtained with the tight-binding fit (black line) are compared with the ones obtained with *ab initio* methods (red line).

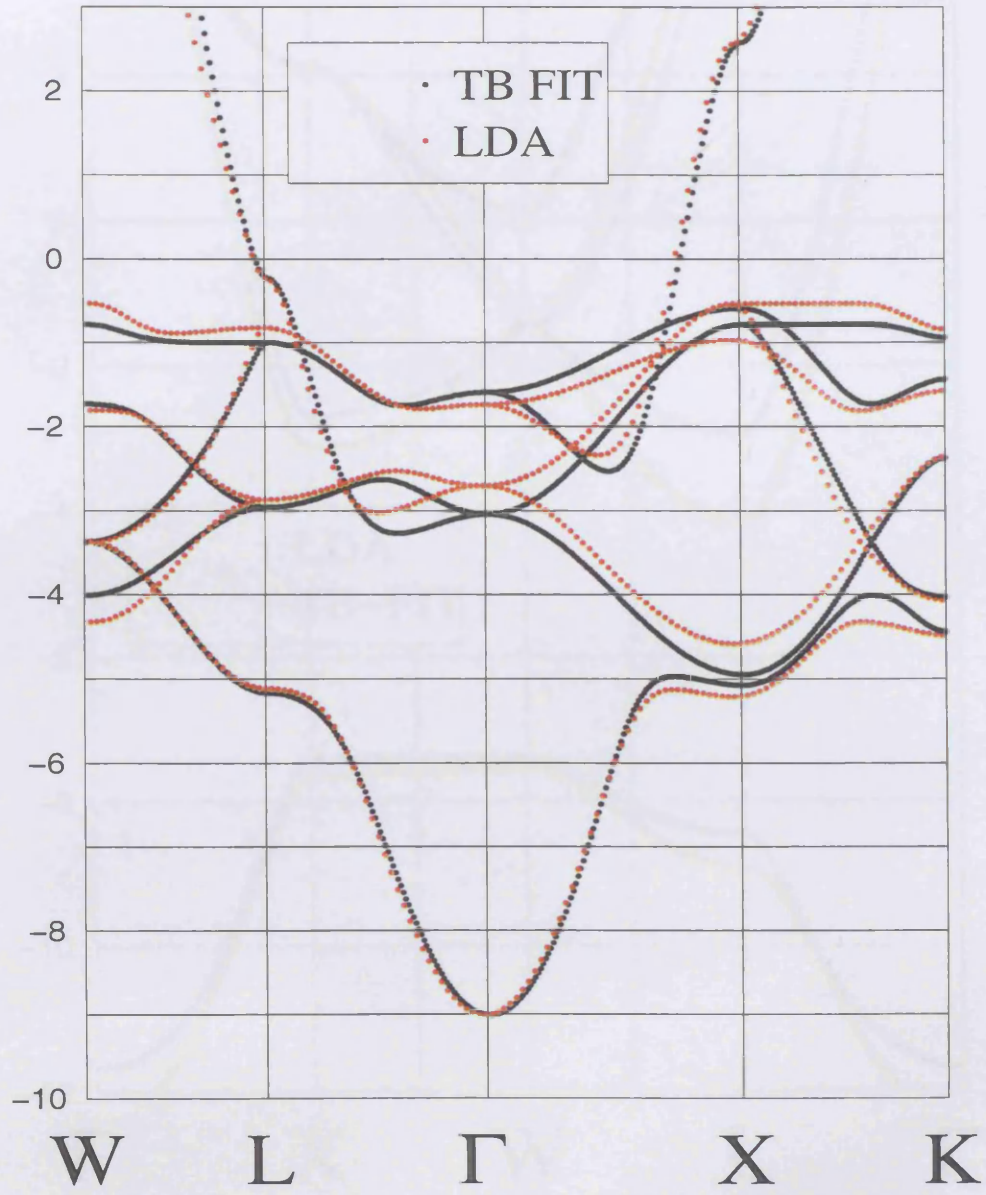

Figure D.2: Band Structure for majority band of fcc Co. The band obtained with the tight-binding fit (black line) are compared with the ones obtained with *ab initio* methods (red line).

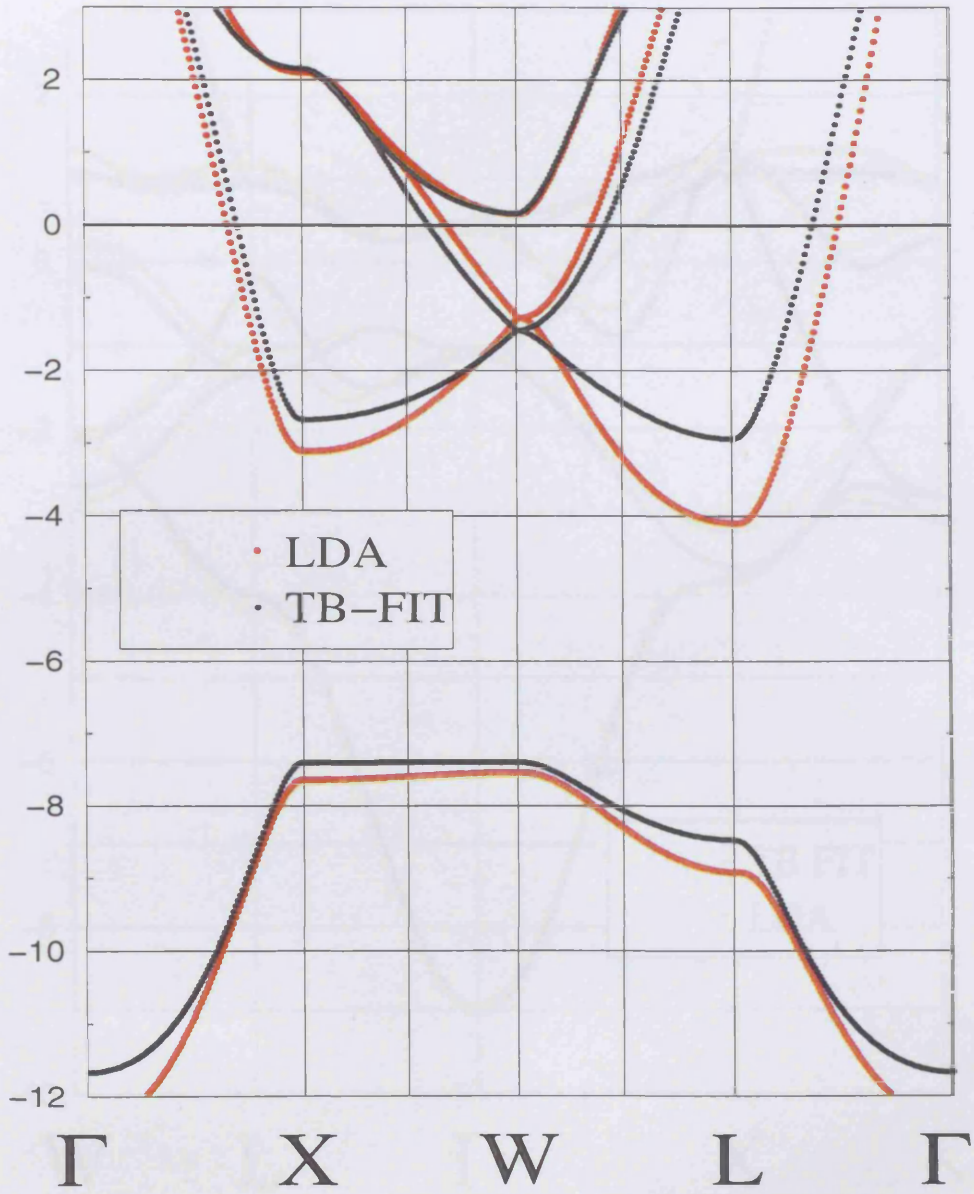

Figure D.3: Band Structure for fcc Pb. The band obtained with the tight-binding fit (black line) are compared with the ones obtained with *ab initio* methods (red line).

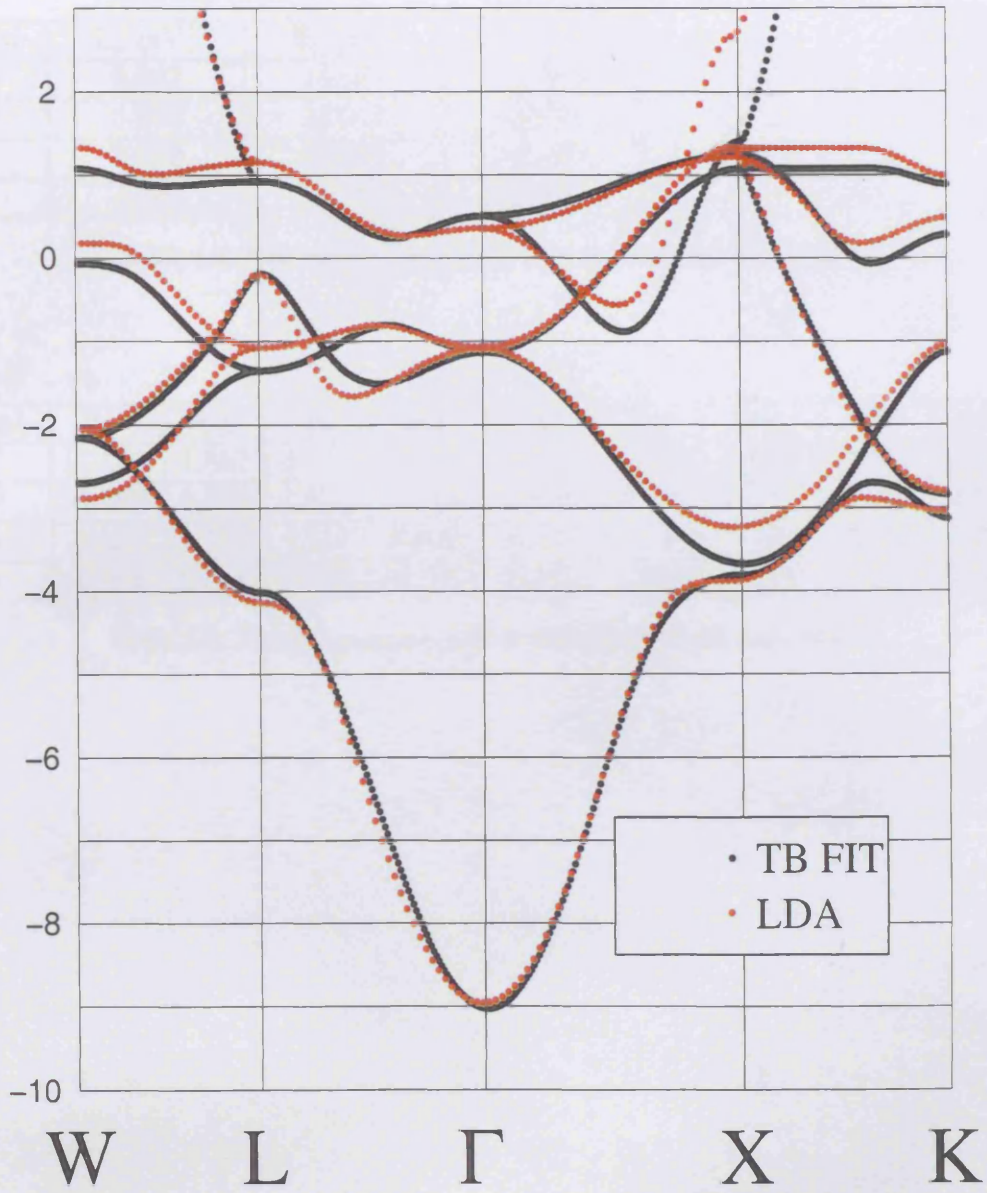

Figure D.4: Band Structure for minority band of fcc Co. The band obtained with the tight-binding fit (black line) are compared with the ones obtained with *ab initio* methods (red line).

Metal	E_s (eV)	E_p (eV)	E_d (eV)
Co$^{\uparrow}$	6.652	14.874	-2.388
Co$^{\downarrow}$	5.678	14.015	-0.661
Cu	2.992	10.594	-2.746
Pb	-8.461	1.899	23.401

Table 4.3: New on-site energies fitted from *ab-initio* calculations

Metal	ssσ	spσ	ppσ	ppπ	sdσ	pdσ	pdπ	ddσ	ddπ	ddδ
Co$^{\uparrow}$	-1.225	1.807	3.150	-0.399	-0.646	-0.769	0.403	-0.557	0.384	-0.066
Co$^{\downarrow}$	-1.303	1.904	3.074	-0.702	-0.608	-0.702	0.318	-0.507	0.325	-0.087
Cu	-1.022	1.578	2.217	-0.609	-0.427	-0.741	0.504	-0.355	0.206	-0.047
Pb	-0.276	0.611	1.143	-0.066	-0.079	1.698	-0.208	-1.007	2.977	-0.057

Table 4.4: New hopping integrals fitted from *ab-initio* calculations

E General Transfer Matrix Approach to the Band Structure of an Arbitrary 1D Periodic Potential

In this appendix I introduce an efficient and easy way to calculate the band structure for an arbitrary periodic Krönig-Penney potential. Consider the periodic potential of figure E.1 where only a period is plotted. It is composed by four regions respectively labelled with A, B, C and D. Each region N is characterized by an effective mass m_N, a potential V_N and a length l_N.

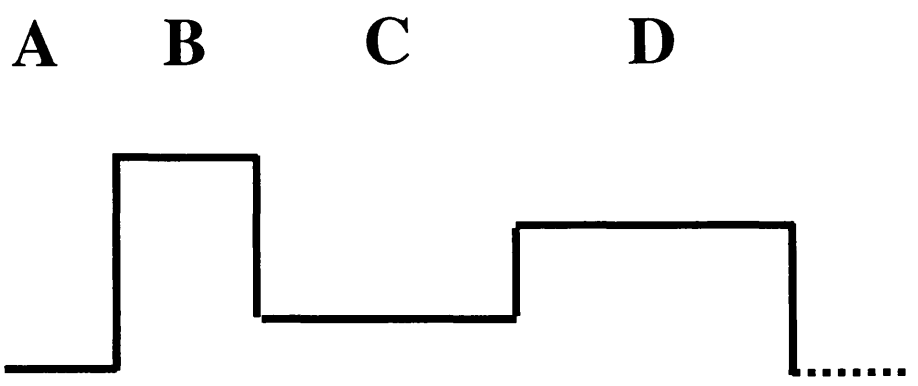

Figure E.1: Krönig-Penney potential considered in the calculation.

I consider a monodimensional case reminding that in Chapter 4 I have shown that this is sufficient to describe the conductance for a 3D superlattice. The Hamiltonian to be considered therefore is

$$H(z) = -\frac{\hbar^2}{2}\frac{\mathrm{d}}{\mathrm{d}z}\frac{1}{m^*(z)}\frac{\mathrm{d}}{\mathrm{d}z} + \frac{\hbar^2 k_{||}^2}{2m^*(z)} + V(z)\ . \tag{E.1}$$

In each of the four regions the wave-function is simply a linear combination of plane-waves of the form

$$\psi_N(z) = a_N e^{ik_N z} + b_N e^{-ik_N z}\ , \tag{E.2}$$

where the wave-vector k_N is simply $k_N = \sqrt{2m_N(E - V_N)}/\hbar$ and E is the energy. The total wave-function must be continuous, therefore the wave-functions defined in the different regions (E.2) must be matched at the interfaces. Moreover the condition of current conservation across the structure provides the following relation between the first derivatives

$$\left.\frac{1}{m_N}\frac{d\psi_N}{dz}\right|_{z=z_0} = \left.\frac{1}{m_M}\frac{d\psi_M}{dz}\right|_{z=z_0}\ , \tag{E.3}$$

where I assumed that the boundary between the region N and M is located at $z = z_0$. Note that the condition (E.3) reduces to the usual continuity of the first derivative in the case the effective masses are the same $m_N = m_M$.

The continuity of the wave-function and the condition (E.3) provide six equations and to completely define the system the two following Bloch conditions must be considered

$$\psi_N(z_0 + L) = e^{iqL}\psi_N(z_0) \,, \tag{E.4}$$

$$\frac{1}{m_N}\frac{d\psi_N}{dz}\bigg|_{z=z_0+L} = \frac{1}{m_M}\frac{d\psi_M}{dz}\bigg|_{z=z_0} e^{iqL} \,, \tag{E.5}$$

where $L = l_\mathrm{A} + l_\mathrm{B} + l_\mathrm{C} + l_\mathrm{D}$ is the total length of a period and q is the quasi-momentum. The resulting eight equations can be written in a convenient matricial form

$$\mathcal{M}\nu = 0 \,. \tag{E.6}$$

The vector ν is a column vector

$$\nu = \begin{pmatrix} c_\mathrm{A} \\ c_\mathrm{B} \\ c_\mathrm{C} \\ c_\mathrm{D} \end{pmatrix} \,, \tag{E.7}$$

with

$$c_\mathrm{N} = \begin{pmatrix} a_\mathrm{N} \\ b_\mathrm{N} \end{pmatrix} \,. \tag{E.8}$$

The matrix $\mathcal{M}$ is a 4×4 block matrix

$$\mathcal{M} = \begin{pmatrix} \hat{M}_\mathrm{A} & -\hat{M}_\mathrm{B}\hat{e}^{ik_\mathrm{B}l_\mathrm{A}} & 0 & 0 \\ 0 & \hat{M}_\mathrm{B}\hat{e}^{ik_\mathrm{B}(l_\mathrm{A}+l_\mathrm{B})} & -\hat{M}_\mathrm{C}\hat{e}^{ik_\mathrm{C}(l_\mathrm{A}+l_\mathrm{B})} & 0 \\ 0 & 0 & \hat{M}_\mathrm{C}\hat{e}^{ik_\mathrm{C}(l_\mathrm{A}+l_\mathrm{B}+l_\mathrm{C})} & -\hat{M}_\mathrm{D}\hat{e}^{ik_\mathrm{D}(l_\mathrm{A}+l_\mathrm{B}+l_\mathrm{C})} \\ \hat{e}^{iqL} & 0 & 0 & \hat{M}_\mathrm{D}\hat{e}^{ik_\mathrm{D}(l_\mathrm{A}+l_\mathrm{B}+l_\mathrm{C}+l_\mathrm{D})} \end{pmatrix} \,, \tag{E.9}$$

where the following 2×2 matrices have been introduced

$$\hat{M}_\alpha = \begin{pmatrix} 1 & 1 \\ \frac{k_\alpha}{m_\alpha} & -\frac{k_\alpha}{m_\alpha} \end{pmatrix} \,, \tag{E.10}$$

$$\hat{e}^{i_\alpha\alpha} = \begin{pmatrix} e^{ik_\alpha\alpha} & 0 \\ 0 & e^{-ik_\alpha\alpha} \end{pmatrix} \,. \tag{E.11}$$

The secular equation for such a system can be explicitly calculated by solving $\det\mathcal{M} = 0$. Nevertheless, for numerical purposes it is convenient to map the calculation of the determinant of $\mathcal{M}$ onto an eigenvalue problem involving only 2×2 matrices. This can

be achieved by writing explicitly the equation (E.6) in term of the two-dimensional column vectors c_N and the matrices $\hat{M}_\alpha$ and $\hat{e}^{ik_\alpha a}$. The equation (E.6) is therefore written as a system of four 2×2 matricial equations, which can be reduced by recursive substitution to the equation

$$\left[\hat{\mu}_D(l_D)\hat{\mu}_C(l_C)\hat{\mu}_B(l_B)\hat{\mu}_A(l_A) - \mathcal{I}e^{iqL}\right] c_A = 0 \,, \tag{E.12}$$

where $\mathcal{I}$ is the 2×2 identity matrix and $\hat{\mu}_\alpha(a) = \hat{M}_\alpha \hat{e}^{ik_\alpha a} \hat{M}_\alpha^{-1}$ or explicitly

$$\hat{\mu}_\alpha(a) = \begin{pmatrix} \cos(k_\alpha a) & i\frac{m_\alpha}{k_\alpha}\sin(k_\alpha a) \\ i\frac{k_\alpha}{m_\alpha}\sin(k_\alpha a) & \cos(k_\alpha a) \end{pmatrix} . \tag{E.13}$$

The equation (E.12) concludes the demonstration. In fact for a given energy E the quasi-momentum q can be calculated by calculating the eigenvalues of the following matrix

$$\hat{S}(E) = \hat{\mu}_D(l_D)\hat{\mu}_C(l_C)\hat{\mu}_B(l_B)\hat{\mu}_A(l_A) \,. \tag{E.14}$$

Such eigenvalues have a form e^{iqL} and the dispersion calculated as $q = q(E)$ can be evaluated for both real and imaginary q. Note that, in complete analogy with respect to the general solution of the dispersion relation in the tight-binding case (see Chapter 2 in particular equation (2.24)), the dispersion is calculated like $q = q(E)$ and not like in the usual band structure approach $E = E(q)$.

The final result of equation (E.12) can be generalized either to the case of arbitrary potential and to energies below the barriers (one or many). In the first case it is possible to divide the system in regions where both the potential and the effective mass are constant. Suppose these regions are A_1, A_2, A_3, ...A_N. Following the same procedure described above I define in every region a matrix $\hat{\mu}_{N_m}(l_{N_m})$ (which depends only on the effective mass, the potential and the length of such a region) and the dispersion relation is calculated like in equation (E.12) where this time $S(E)$ is given by the product

$$\hat{S}(E) = \hat{\mu}_{A_N}(l_{A_N})\ldots\ldots\hat{\mu}_{A_3}(l_{A_3})\hat{\mu}_{A_2}(l_{A_2})\hat{\mu}_{A_1}(l_{A_1}) \,. \tag{E.15}$$

Note that if in the region N_m the energy is below the barrier, then $k_{N_m} \to i|k_{N_m}|$ and the matrices $\hat{\mu}_{N_m}(l_{N_m})$ become simply

$$\hat{\mu}_{N_m}(l_{N_m}) = \cosh(|k_{N_m}|l_{N_m}) \begin{pmatrix} 1 & i\frac{m_{N_m}}{|k_{N_m}|}\tanh(|k_{N_m}|l_{N_m}) \\ -i\frac{|k_{N_m}|}{|m_{N_m}|}\tanh(|k_{N_m}|l_{N_m}) & 1 \end{pmatrix} . \tag{E.16}$$

The expression (E.16) is particularly useful from a computational point of view because all the eventual large divergences are factorized out of the matrix in the prefactor $\cosh(|k_{N_m}|l_{N_m})$.

Finally the above treatment can be further generalized to the calculation of the S matrix for a non-periodic potential. I this case the Bloch conditions (E.4-E.5) are no longer applicable but a relation between the coefficient vectors (E.8) of the first c_{A_1} and the last c_{A_N} region of the potential can be calculated

$$c_{A_N} = e^{-ik_{A_N}L}\hat{M}^{-1}_{A_N}\hat{\mu}_{A_N-1}(l_{A_N-1}).....\hat{\mu}_{A_2}(l_{A_2})\hat{M}_{A_1}c_{A_1} = S'(E)c_{A_1}\ , \tag{E.17}$$

where $L = l_{A_1} + l_{A_2} + ... + l_{A_N}$. If now one considers electrons traveling from the right-hand side to the left-hand side of the potential the transmission t and reflection coefficient r are defined by the equations

$$c_{A_1} = \begin{pmatrix} 0 \\ t \end{pmatrix}\ , \tag{E.18}$$

$$c_{A_N} = \begin{pmatrix} r \\ 1 \end{pmatrix}\ , \tag{E.19}$$

and are related to the matrix elements of the matrix S' of equation (E.17) through the relations

$$r = \frac{S'_{21}}{S'_{22}}\ , \tag{E.20}$$

$$t = \frac{1}{S'_{22}}\ . \tag{E.21}$$

Note that also in this case the divergent terms can be factorized out of the matrices.

References

[1] M.N. Baibich, J.M. Broto, A. Fert, F. Nguyen Van Dau, F. Petroff, P. Etienne, G. Creuzet, A. Friederich and J. Chazelas, Phys. Rev. Lett. **61**, 2472 (1988)

[2] G. Binasch, P. Grünberg, F. Sauerbach and W. Zinn, Phys. Rev. **B 39**, 4828 (1989)

[3] D.M. Edwards, J. Mathon, R.B. Muniz and M.S. Phan, Phys. Rev. Lett. **67**, 493 (1991)

[4] P. Bruno, Phys. Rev. **B 52**, 411 (1995)

[5] J. Mathon, M. Villeret, R.B. Muniz, J. d'Albouquerque e Castro and D.M. Edwards, Phys. Rev. Lett. **74**, 3696 (1995)

[6] J. Mathon, M. Villeret, A. Umerski, R.B. Muniz, J. d'Albouquerque e Castro and D.M. Edwards, Phys. Rev. **B 56**, 11797 (1997)

[7] G.A. Prinz, Physics Today, 58, April 1995. See also the rest of the special Issue on Magnetoelectronics (April 1995)

[8] H.A.M. van den Berg, W. Clemens, G. Gieres, G. Rupp, W. Schelter and M. Vieth, IEEE Trans. Magn. **32**, 4624 (1996)

[9] W. Clemens, H.A.M. van den Berg, G. Rupp, W. Schelter, M. Vieth and J. Wecker, J. Appl. Phys. **81**, 4310 (1997)

[10] See http://ssdweb01.storage.ibm.com/oem/mrheads/mainmrheads.html

[11] N.F. Mott, Adv. Phys. **13**, 325 (1964)

[12] R. Meservey and P.M. Todrow, Phys. Rep. **238**, 173 (1994)

[13] W.P. Pratt Jr., S.-F. Lee, J.M. Slaughter, R. Loloee, P.A. Schroeder and J. Bass, Phys. Rev. Lett. **66**, 3060 (1991)

[14] M.A.M. Gijs, S.K.J. Lenczowski and J.B. Giesbers, Phys. Rev. Lett. **70**, 3343 (1993)

[15] M.A.M. Gijs and G.E.W. Bauer, Adv. Phys. **46**, 285 (1997)

[16] J-Ph. Ansermet, J.Phys.: Cond. Matter **C 10**, 6027 (1998)

[17] M. Julliere, Phys. Lett. **50A**, 225 (1975)

[18] J.S. Moodera, L.R. Kinder, T.M. Wong and R. Meservey, Phys. Rev. Lett. **74**, 3273 (1995)

[19] E.Yu. Tsymbal and D.G. Pettifor, Phys. Rev. **B 58**, 432 (1998)

[20] A.M. Bratkovsky, cond-mat/9712170

[21] J.M. De Teresa, A. Barthèlèmy, A. Fert, J.P. Contour, R. Lyonnet, F. Montaigne, P. Seneor and A. Vaurès, Phys. Rev. Lett. **82**, 4288 (1999)

[22] S.K. Upadhyay, A. Palanisami, R.N. Louie and R.A. Buhrman, Phys. Rev. Lett. **81**, 3247 (1998)

[23] A.F. Andreev, Zh. Eksp. Teor. Fiz. **46**, 1823 (1964)

[24] R. Landauer, Philos. Mag. **21**, 863 (1970)

[25] M. Büttiker, Y. Imry, R. Landauer and S. Pinhas, Phys. Rev. **B 31**, 6207 (1985)

[26] M. Buttiker, IBM J. Res. Dev., **32**, 317 (1988)

[27] S. Sanvito, C.J. Lambert, J.H. Jefferson and A.M. Bratkovsky, Phys. Rev. **B 59**, 11936 (1999)

[28] J.M. Gallego, D. Lederman, S. Kim and I.K. Schuller Phys. Rev. Lett. **74**, 4515 (1995)

[29] S. Sanvito, C.J. Lambert, J.H. Jefferson and A.M.Bratkovsky, J. Phys.C: Condens. Matter **10**, L691 (1998)

[30] S. Sanvito, C.J. Lambert and J.H. Jefferson, J. Magn. Magn. Mater **197**, 101 (1999)

[31] S. Sanvito, C.J. Lambert and J.H. Jefferson, J. Magn. Magn. Mater **201-203**, 105 (1999)

[32] W. Schwarzacher and D.S. Lashmore, IEEE Trans. Magn. **32**, 3133 (1996)

[33] T. Valet and A. Fert, Phys. Rev. **B 48**, 7099 (1993)

[34] A. Fert, J.-L. Duvail and T. Valet, Phys. Rev. **B 52**, 6513 (1995)

[35] D. Bozec, M.A. Howson, B.J. Hickey, S. Shatz and N. Wiser, cond-mat/9906410

[36] W.-C. Chiang, Q. Yang, W.P. Pratt Jr., R. Loloee and J. Bass, J. Appl. Phys. **81**, 4570 (1997)

[37] S. Sanvito, C.J. Lambert and J.H. Jefferson, Phys. Rev. **B 60**, 7385 (1999)

[38] S. Sanvito, C.J. Lambert and J.H. Jefferson, submitted Phys. Rev. Lett., see also cond-mat/9903190

[39] F. Taddei, S. Sanvito, C.J. Lambert and J.H. Jefferson, Phys. Rev. Lett. **82**, 4938 (1999)

[40] F. Taddei, S. Sanvito, C.J. Lambert and J.H. Jefferson, in preparation

[41] K. Tsukagoshi, B.W. Alphenaar and H. Ago, Nature **401**, 572 (1999)

[42] S. Sanvito, Y.-K. Kwon, D. Tománek and C.J. Lambert, submitted to Phys. Rev. Lett., also cond-mat/9808154

[43] S. Sanvito, Y.-K. Kwon, D. Tománek and C.J. Lambert, "Quantum Transport in inhomogeneous quantum nanotubes" (to appear in *Science and Application of Nanotubes*, Kluwer Academic Publishing/Plenum Press)

[44] S. Franck, P. Poncharal, Z.L. Wang and W.A. de Heer, Science **280**, 1744 (1998)

[45] E.N. Economou, *Green's Functions is Quantum Physics*, (Springer-Verlag, New York, 1983)

[46] V.C. Hui, PhD dissertation, Lancaster University, (1990)

[47] C.J. Lambert, V.C. Hui and S.J. Robinson, J. Phys.: Condens. Matter, **5**, 4187 (1993)

[48] R.E. Camley and J. Barnas, Phys. Rev. Lett. **63** 664 (1989)

[49] K.M. Schep, P.J. Kelly and G.E.W. Bauer, Phys. Rev. Lett. **74**, 586 (1995)

[50] K.M. Schep, P.J. Kelly and G.E.W. Bauer, Phys. Rev. **B 57**, 8907 (1998)

[51] P. Zahn, I. Mertig, M. Richter and H. Eschrig, Phys. Rev. Lett. **75**, 2996 (1995)

[52] P. Zahn, J. Binder, I. Mertig, R. Zeller and P.H. Dederichs, Phys. Rev. Lett. **80**, 4309 (1998)

[53] E.Yu. Tsymbal and D.G. Pettifor, Phys. Rev. **B 54**, 15314 (1996)

[54] J. Mathon, Phys. Rev. **B 55**, 960 (1997)

[55] M.A.M. Gijs, M.T. Johnson, A. Reinders, P.E. Huisman, R.J.M. van de Veerdonk, S.K.J. Lenczowski and R.M.J. van Gansewinkel, Appl. Phys. Lett. **66**, 1839 (1995)

[56] S.S.P. Parkin, R. Bhadra and K.P. Roche, Phys. Rev. Lett. **66**, 2152 (1991)

[57] D.J. Monsma, J.C. Lodder, Th.J.A. Pompa and B. Dieny, Phys. Rev. Lett. **74**, 5260 (1995)

[58] W.P. Pratt Jr., S.-F. Lee, P. Holody, Q. Yang, R. Loloee, J. Bass and P.A. Schroeder, J. Magn. Magn. Mater. **126**, 406 (1993)

[59] E.E. Fullerton, D.M. Kelly, J. Guimpel, I.K. Schuller and Y. Bruynseraede, Phys. Rev. Lett. **68**, 859 (1992)

[60] H. Kubota, M. Sato and T. Miyazaki, J. Magn. Magn. Mater. **167**, 12 (1997)

[61] K.D. Bird and M. Schlesinger, J. Electrochem. Soc. **142**, L65 (1995)

[62] H. Sato, T. Matsudai, W. Abdul-Razzaq, C. Fierz and P.A. Schroeder, J. Phys.: Condens. Matter **6**, 6151 (1994)

[63] S.-Y. Hsu, P. Holody, R. Loloee, J.M. Rittner, W.P. Pratt Jr. and P.A. Schroeder, Phys. Rev. **B 54**, 9027 (1996)

[64] S.D. Steenwyk, S.Y. Hsu, R. Loloee, J. Bass and W.P. Pratt Jr., J. Magn. Magn. Mater. **170**, L1 (1997)

[65] P. Holody, W.C. Chiang, R. Loloee, J. Bass, W.P. Pratt Jr. and P.A. Schroeder, Phys. Rev. **B 58**, 12230 (1998)

[66] S.F. Lee, W.P. Pratt Jr., R. Loloee, P.A. Schroeder and J. Bass, Phys. Rev. **B 46**, 548 (1992)

[67] W.-C. Chiang, W.P. Pratt Jr., M. Herrold and V. Baxter, Phys. Rev. **B 58**, 5602 (1998)

[68] T. Kai, Y. Ohashi and K. Shiiki, J. Magn. Magn. Mat. **183**, 292 (1998)

[69] A. Dinia, S. Zoll, M. Gester, D. Stoeffler, J.P. Jay, K. Ounadjela, H.A.M. van den Berg and H. Rakoto, Eur. Phys. J. **B 5**, 203 (1998)

[70] J.L. Leal and M.H. Kryder, J. Appl. Phys. **83**, 3720 (1998)

[71] K. Wellock, J. Caro and B.J.Hickey J. Magn. Magn. Mat. **198-199**, 27 (1999)

[72] A. Dinia, M. Stoffel, K. Rahmouni, G. Schmerber and H.A.M. van den Berg, J. Magn. Magn. Mat. **198-199**, 67 (1999)

[73] H. Yanagihara, K. Pettit, M.B. Salamon, E. Kita, S.S.P. Parkin, J. Appl. Phys. **81**, 5197 (1997)

[74] J.C. Slonczewski, Phys. Rev. **B 39**, 6995 (1989)

[75] T.-S. Choy, J. Chen and S. Hershfield, cond-mat/9903118

[76] J.M. MacLaren, X.-G. Zhang, W.H. Butler and X. Wang, Phys. Rev. **B 59**, 5470 (1999)

[77] K. Wang, S. Zhang, P.M. Levy, L. Szunyogh and P. Weinberger, J. Magn. Magn. Mater. **189**, L131 (1998)

[78] E.Yu. Tsymbal and D.G. Pettifor, J. Phys.: Condens. Matter **9**, L411 (1997)

[79] J. Mathon, Phys. Rev. **B 56**, 11810 (1997)

[80] A.M. Bratkovsky, Phys. Rev. **B 56**, 2344 (1997)

[81] J.C. Slater and G.F. Koster, Phys. Rev. **94**, 1498 (1954)

[82] P.B. Allen, J.Q. Broughton and A.K. McMahan, Phys. Rev. **B 34**, 859 (1986)

[83] P.-O. Löwdin, J. Chem. Phys. **18**, 365 (1950)

[84] D.A. Papaconstantopoulos, *Handbook of the Band Structure of Elemental Solids*, (Plenum, New York, 1986). See also the web site http://cst-www.nrl.navy.mil/bind/

[85] A.M. Bratkovsky, JETP Letter **65**, 453 (1997)

[86] S.S.P. Parkin, Phys. Rev. Lett. **67**, 3598 (1991)

[87] J.A. Borchers, J.A. Dura, J. Unguris, D. Tulchinsky, M.H. Kelley, C.F. Majkrzak, S.Y. Hsu, R. Loloee, W.P. Pratt Jr. and J. Bass, Phys. Rev. Lett. **82**, 2796 (1999)

[88] J.M. Gallego, D. Lederman, S. Kim and I.K. Schuller, Phys. Rev. Lett. **74**, 4515 (1995)

[89] S. Kim, D. Lederman, J.M. Gallego and I.K. Schuller, Phys. Rev. **B 54**, R5291 (1996)

[90] D. Lederman, J.M. Gallego, S. Kim and I.K. Schuller, J.Magn. Magn. Mater **183**, 261 (1998)

[91] S. Kim, PhD Dissertation, (University of California, San Diego, 1996)

[92] L.L. Henry, M. Oonk, R. Loloee, Q. Yang, W-C Chang, W.P. Pratt Jr and J. Bass, J. Appl. Phys. **79**, 6129 (1996)

[93] J. Mathon, M. Villeret and H. Itoh, Phys. Rev. **B 52**, R6983 (1995)

[94] S. Krompiewski and U. Krey, Phys. Rev. **B 54**, 11961 (1996)

[95] S. Krompiewski, M. Zwierzycki and U. Krey, J.Phys.:Condens. Matter **9**, 7135 (1997)

[96] J. Mathon, Phys. Rev. **B 54**, 55 (1996)

[97] R. de L. Krönig and W.G. Penney, Proc. R. Soc. A **130**, 499 (1931)

[98] F. Szmulowicz, Eur. J. Phys. **18**, 393 (1997)

[99] M.G. Burt, J.Phys.:Condens. Matter **11**, R53 (1999)

[100] E.O. Kane, J. Phys. Chem. Solids **1**, 249 (1957)

[101] A. Blondel, J.P. Meier, B. Doudin and J.Ph. Ansermet, Appl. Phys. Lett. **65**, 3019 (1994)

[102] L. Piraux, S. Dubois, A. Fert and L. Belliard, Eur. Phys. J. **B 4**, 413 (1998)

[103] I. Mertig, R. Zeller and P.H. Dederichs, Phys. Rev. **B 47**, 16178 (1993)

[104] V.S. Stepanyuk, R. Zeller, P.H. Dederichs and I. Mertig, Phys. Rev. **B 49**, 5157 (1994)

[105] D. Bozec, M.J. Walker, B.J. Hickey, M.A. Howson and N. Wiser, Phys. Rev. **B 60**, 3037 (1999)

[106] P.W. Anderson, D.J. Thouless, E. Abrahams and D.S. Fisher, Phys. Rev. **B 22**, 3519 (1980)

[107] O.K. Andersen and O. Jepsen, Physica **B 91**, 317 (1977)

[108] N. Papanikolaou, R. Zeller, P.H. Dederichs and N. Stefanou, Phys. Rev. **B 55**, 4157 (1997)

[109] B. Voegeli, A. Blondel, B. Doudin and J.Ph. Ansermet, J. Magn. Magn. Mater **151**, 388 (1995)

[110] C.W.J. Beenakker, Rev. Mod. Phys. **69**, 731 (1997)

[111] B. Kramer and A. MacKinnon, Rep. Prog. Phys. **56**, 1469 (1993)

[112] E.Yu. Tsymbal and D.G. Pettifor, J. Phys.C: Condens. Matter **8**, L569 (1996)

[113] M. Büttiker, Phys. Rev. **B 3**, 3020 (1986)

[114] C.H. Marrows, PhD dissertation, University of Leeds, (1997)

[115] C.H. Marrows, M. Perez and B.J. Hickey, Preprint University of Leeds

[116] S.Y. Hsu, A. Barthélémy, P. Holody, R. Loloee, P.A. Schroeder and A. Fert, Phys. Rev. Lett. **78**, 2652 (1997)

[117] C. Vouille, A. Barthélémy, F. Elokan Mpondo, A. Fert, P.A. Schroeder, S.Y. Hsu, A. Reilly and R. Loloee, Phys. Rev. **B 60**, 6710 (1999)

[118] M.J.M. de Jong, C.W.J. Beenakker Phys. Rev. Lett. **74**, 1657 (1995)

[119] D.V. Baxter, S.D. Steenwyk, J. Bass and W.P. Pratt Jr, J. Appl. Phys. **85**, 4545 (1999)

[120] S.K. Upadhyay, R.N. Louie and R.A. Buhrman, Appl. Phys. Lett. **74**, 3881 (1999)

[121] R.J. Soulen, J.M. Byers, M.S. Osofsky, B. Nadgorny, T. Ambrose, S.F. Chang, P.P. Broussard, C.T. Tanaka, J. Nowak, J.S. Moodera, A. Barry and J.M.D. Coey, Science **282**, 85 (1998)

[122] N. Allsopp, V.C. Hui, C.J. Lambert and S.K. Robinson, J. Phys. C: Condens. Matter **6**, 10475 (1994)

[123] C.J. Lambert, J. Phys. C: Cond. Matter **3**, 6579 (1991)

[124] Y. Takane and H. Ebisawa, J. Phys. Soc. Jpn **61**, 2858 (1992)

[125] C.J. Lambert and R. Raimondi, J. Phys. C: Condens. Matter **10**, 901 (1998)

[126] V.I. Fal'ko, C.J. Lambert and A.F. Volkov, JETP Letter **69**, 532 (1999)

[127] V.I. Fal'ko, C.J. Lambert and A.F. Volkov, cond-mat/9901051

[128] P.G. De Gennes, *Superconductivity of Metals and Alloys*, (W.A. Benjamin, Inc. New York 1966)

[129] C.W.J. Beenakker, Phys. Rev. **B 46**, 12841 (1992)

[130] G.E. Blonder, M. Tinkham and T.M. Klapwijk, Phys. Rev. **B 25**, 4515 (1982)

[131] OXford Order N tight-binding Package. Department of Materials, Oxford University (Prof. D. Pettifor)

[132] R.A. Buhrman, Private comunication

[133] M. Böhm and U. Krey, cond-mat/9810256

[134] S. Iijima, Nature **354**, 56 (1991)

[135] M.S. Dresselhaus, G. Dresselhaus and P.C. Eklund, *Science of Fullerenes and Carbon Nanotubes* (Academic Press Inc., 1996 San Diego), and references therein

[136] R. Saito, G. Dresselhaus and M.S. Dresselhaus, *Physical Properties of Carbon Nanotubes* (Imperial College, 1998 London), and references therein

[137] S. Iijima and T. Ichihashi, Nature **363**, 603 (1993)

[138] D.S. Bethune, C.H. Kiang, M.S. de Vries, G. Gorman, R. Savoy, J. Vazquez and R. Beyers, Nature **363**, 605 (1993)

[139] J.W. Mintmire, B.I. Dunlap and C.T. White, Phys. Rev. Lett. **68**, 631 (1992)

[140] R. Saito, M. Fujita, G. Dresselhaus and M.S. Dresselhaus, Appl. Phys. Lett. **60**, 2204 (1992)

[141] N. Hamada, S. Sawada and A. Oshiyama, Phys. Rev. Lett. **68**, 1579 (1992)

[142] L. Chico, L.X. Benedict, S.G. Louie and M.L. Cohen, Phys. Rev. **B 54**, 2600 (1996)

[143] W. Tian and S. Datta, Phys. Rev. **B 49**, 5097 (1994)

[144] M.F. Lin and K.W.-K. Shung, Phys. Rev. **B 51**, 7592 (1995)

[145] S.J. Tans, M.H. Devoret, H. Dai, A. Thess, R.E. Smalley, L.J. Geerligs and C. Dekker, Nature **386**, 474 (1998)

[146] M. Bockrath, D.H. Cobden, P.L. McEuen, N.G. Chopra, A.Z. ettl, A. Thess and R.E. Smalley Science **275**, 1922 (1997)

[147] C. Dekker, Physics Today May 1999, 22 (1999)

[148] T. Ando and T. Nakanishi, J. Phys. Soc. Jpn. **67**, 1704 (1998)

[149] C.T. White and T.N. Todorov, Nature **393**, 240 (1998)

[150] R. Saito, G. Dresselhaus and M.S. Dresselhaus, J. Appl. Phys. **73**, 494 (1993)

[151] Ph. Lambin, L. Philippe, J.C. Charlier and J.P. Michenaud, Comput. Mater. Sci. **2**, 350 (1994)

[152] Y.-K. Kwon and D. Tománek, Phys. Rev. **B 58**, R16001 (1998)

[153] P. Delaney, H.J. Choi, J. Ihm, S.G. Louie and M.L. Cohen, Nature **391**, 466 (1998)

[154] Y.-K. Kwon, S. Saito and D. Tománek, Phys. Rev. **B 58**, R13314 (1998)

[155] D. Tománek and M. A. Schluter, Phys. Rev. Lett. **67**, 2331 (1991)

[156] M. Schluter, M. Lannoo, M. Needels, G.A. Baraff and D. Tománek, Phys. Rev. Lett. **68**, 526 (1992)

[157] J.-C. Charlier, X. Gonze and J.-P. Michenaud, Europhys. Lett. **28**, 403 (1994)

[158] M.C. Schabel and J.L. Martins, Phys. Rev. **B 46**, 7185 (1992)

[159] S. Datta, *Electronic Transport in Mesoscopic Systems*, (Cambridge University Press, Cambridge 1985)

[160] A. Chaplik and M. Entin, Zh. Éksp. Teor. Fiz. **67**, 208 (1974) [Sov. Phys. JETP **40**, 106 (1974)]

[161] M. Azbel, Solid State Commun. **45**, 527 (1983)

[162] W. Xue and P.A. Lee, Phys. Rev. Lett. **38**, 3913 (1988)

[163] H. Van Houten, C.W.J. Beenakker and A.A.M. Staring, *Coulomb-Blockade Oscillations in Semiconductor Nanostructures*, in "Single Charge Tunneling", Edited by H. Grabert and M.H. Devoret, Plenium Press, New York, 1992

[164] J. Tersoff, Appl. Phys. Lett. **74**, 2122 (1999)

[165] A. Bachtold, M. Henny, C. Terrier, C. Strunk, C. Schönenberger, J.-P. Salvetat, J.-M. Bonard and L. Forro, Appl. Phys. Lett. **73**, 274 (1998)

[166] M.P. Anantram, S. Datta and Y. Xue, cond-mat/9907357

[167] N. Garcia, M. Muñoz and Y.-W. Zhao, Phys. Rev. Lett. **82**, 2923 (1999)

[168] G. Tatara, Y.-W. Zhao, M. Muñoz and N. Garcia, Phys. Rev. Lett. **83**, 2030 (1999)

[169] T. Ono, Y. Ooka, H. Miyajima and Y. Otani, Appl. Phys. Lett. **75**, 1622 (1999)

[170] Apparently the word "spintronics" has been invented by Bell Labs Lucent Technology scientists, in relation with systems "in which the direction an electron **spin** is pointing is just important as its charge". See http://public1.lucent.com/press/0798/980731.bla.html

[171] J.Gregg, W. Allen, N. Viart, R. Kirschman, C. Sirisathitkul, J.-P. Schille, M. Gester, S. Thompson, P. Sparks, V. Da Costa, K. Ounadjela and M. Skvarla, J. Magn. Magn. Matter **175**, 1 (1997)

[172] P. Walser, M. Schleberger, P. Fuchs and M. Landolt, Phys. Rev. Lett. **80**, 2217 (1998)

[173] S. Gardelis, C.G. Smith, C.H.W. Barnes, E.H. Linfield and D.A. Ritchie, Phys. Rev. **B 60**, 7764 (1999)

[174] H. Ohno, Science **281**, 951 (1998)

[175] H. Ohno, F. Matsukura, T. Omiya and A. Akiba, J. Appl. Phys. **85**, 4277 (1999)

[176] M. Oestreich, J. Hübner, D. Hägele, P.J. Klar, W. Heimbrodt, W.W. Rühle, D.E. Ashenford and B. Lunn, Appl. Phys. Lett. **74**, 1251 (1999)

[177] J.M. Kikkawa, I.P. Smorchkova, N. Samarth and D.D. Awschalom, Science **277**, 1284 (1997)

[178] J.M. Kikkawa and D.D. Awschalom, Phys. Rev. Lett. **80**, 4313 (1998)

[179] D.D. Awschalom and J.M. Kikkawa, Physics Today, 33, June 1999

[180] J.M. Kikkawa and D.D. Awschalom, Nature **397**, 139 (1999)

[181] L.J. Sham, J. Magn. Magn. Matter **200**, 219 (1999)

[182] J. Fabian and S. Das Sarma, J. Vac. Sci. Technol. **B 17**, 1708 (1999) and references therein

[183] R.J. Elliott, Phys. Rev. **96**, 266 (1954)

[184] M.I. D'yakonov and V.I. Perel', Sov. Phys. Solid State **13**, 3023 (1972)

[185] G.L. Bir, A.G. Aronov and G.E. Pinkus, Sov. Phys. JETP **42**, 705 (1976)